UNIVERSITY OF READING

Department of Meteorology

On the development, characterisation and applications of a balloon-borne atmospheric turbulence sensor

Graeme John Marlton

A thesis submitted for the degree of Doctor of Philosophy

April 2016

Declaration

I confirm that this is my own work and the use of all material from other sources has been properly and fully acknowledged.

Graeme Marlton

Abstract

This thesis describes the development, characterisation and use of a dataset of measurements made using 51 radiosondes equipped with accelerometers to measure atmospheric turbulence. Atmospheric turbulence, especially Clear-Air Turbulence (CAT) is hazardous to aircraft as it cannot be observed in advance. Pilots and passengers rely on CAT forecasts, which at best, are correct 60-70% of the time. The reason for this moderate performance in turbulence forecasts is due to a lack of quantitative unbiased observations needed to improve the turbulence theory. This work seeks to improve understanding of turbulence through a standardised method of turbulence observations that span the entire troposphere. To achieve this a sensing package is developed to measure the acceleration of the radiosonde as it swings due to its carrier balloon being agitated by turbulence. The accelerometer radiosonde is then compared against multiple turbulence remote sensing methods to characterise its measurements. From a comparison with a Doppler lidar in the boundary layer a relationship in terms of the eddy dissipation rate, a meteorological measure of turbulence, is found. A further relationship is found when compared with the spectral width of an Mesospheric Stratospheric and Tropospheric (MST) radar. The full dataset of accelerometer sonde ascents is analysed and with information from instrumental comparisons a standard deviation of 5 m s^{-2} is defined as a threshold for significant turbulence. The dataset spans turbulence generated in meteorological phenomena such as jet streams, clouds and in the presence of convection. The analysis revealed that 77% of observed turbulence could be explained by the aforementioned phenomena. In jet streams turbulence generation was often caused by horizontal processes such as deformation. In the presence of convection turbulence is found to form when CAPE > 150 J kg^{-1}. Deeper clouds were found to be more turbulent due to the increased intensity of in-cloud processes. The accelerometer data were used to verify the skill of turbulence diagnostics, in order to assess which diagnostics are best at forecasting turbulence. It was found that turbulence diagnostics featuring the wind speed, deformation and relative vorticity advection predicted turbulence best. This work provides a new, safe and inexpensive method to retrieve in-situ information about the turbulent structure of the atmosphere. It can inform the aviation industry on where turbulence is generated and assess which are the most skilful diagnostics to predict this.

Acknowledgements

I would like to take this opportunity to thank the people and organisations who have assisted me over the last three and a half years. The project would not have been possible without the NERC studentship which funded the PhD and the Royal Society support which funded the radiosondes and sensors.

Next I would like to thank my supervisors Giles Harrison, Keri Nicoll and Paul Williams who have provided excellent advice, opportunities and adventures over the course of my PhD. I would also like to thank the meteorology department's technicians: Andrew Lomas whom designed and manufactured the finished sensors, Ian Read for providing electronics support, and finally Mike Stroud, for assisting me with launching the majority of radiosondes and accompanying me to NERC MST radar site, and John Lally for providing data from the ACTUAL lidar based at Reading. Whilst at Hyytiala, Keri and I enlisted the help of the radiosonde operators Pasi Vanttaja and Jarkko Pilkottu. The ARM technicians Patrick Dowell and Mark Smith provided invaluable support, food and company during our stay. Ewan O'Connor's assistance in interpreting the data collected there was much appreciated. For the campaign at the MST radar site I would like to thank Dave Waring and Les Dean for preparing the field site for the campaign, Hugo Ricketts for providing a second sounding kit, and David Hooper and Chris Lee, for providing support in interpreting the MST radar data. I would like to thank Janet Barlow and Miguel Teixeira for the advice and guidance given during my monitoring committee meetings. Finally I must thank Stephen Gill, who paid careful attention to my welfare.

I would like to thank my parents who have supported me throughout my education, especially with a spare laptop and proof reading a few chapters. On the subject of proof reading, I would like to thank Simon Thomas, Emma Hopkin, Will Maslanka and Lenka Novak for each proof reading a chapter. I have been very fortunate to be in a very sociable department and have made many friends across the years. I have lived in a brilliant house of friends during my PhD who have been with me through thick and thin. I would like to take a moment to mention a good friend of mine, Robert Barrington Gill, who had a dream of becoming an air traffic controller. Sadly he is no longer with us, but he would have found this project very interesting.

Measure what is measurable, and make measurable what is not so.

Galileo Galilei

Contents

List of Figures

List of Tables

List of Acronyms

Acronym	Definition
AMDAR	Aircraft Meteorological DAta Relay
ARM	The Atmospheric Radiation Measurement program
BAECC	Biogenic Aerosols and their Effects on Cloud and Climate
BOAC	British Overseas Airways Company
CAPE	Convective Available Potential Energy (J kg^{-1})
CAT	Clear-Air Turbulence
DBS	Doppler Beam swing method
DELICAT	Demonstration of LIdar based Clear Air Turbulence
DEVG	Derived Equivalent Vertical Gust (m s^{-1})
ECMWF	European Center for Medium range Weather Forecast
EL	Equilibrium Level (of Convection) (m)
ERA	ECMWF ReAnalysis
FAA	Federal Aviation Administration
FFT	Fast Fourier Transform
GPS	Global Positioning System
GTG	Graphical Turbulence Guidance system
HSRL	High Spectral Resolution Lidar
IFS	Information Forecast System
IOP	Intense observation period
JMA	Japanese Meteorological Agency
JRA	Japanese ReAnalysis
LCL	Lifting condensation Level (m)
LED	Light Emitting Diode
LES	Large Eddy Simulation
LFC	Level of free convection (m)
LWC	Liquid Water content (g kg^{-1})
MST	Mesopheric Stratospheric and Tropospheric
NCAR	National Centre of Atmospheric Research
NCEP	National Centre for Environmental Prediction

Acronym	Definition
NCSU	North Carolina State University
NERC	Natural Environment Research Council
NOAA	National Oceanic and Atmosphere Administration
NWP	Numerical Weather Prediction
PANDORA	Programmable Analogue aNd Digital Operational Radiosonde Accessory
PDF	Probability Density Function
PIREP	PIlot REPort
RMSE	Root Mean Square Error
RUAO	Reading University Atmospheric Observatory
SIGWX	Significant Weather Chart
TKE	Turbulent Kinetic Energy (J kg^{-1})
UHF	Ultra High Frequency
ULTURB	Upper Level TURBulence algorithm
US	United States (of America)
UTC	Coordinated Universal Time
UTLS	Upper Troposphere and Lower Stratosphere
VHF	Very High Frequency
WAFC	World Area Forecast Center
WMO	World Meteorological Organisation

List of Mathematical Notation

Symbol	Definition	Unit
α	Pendulum dampening coefficient	
α_k	Kolomogorov's constant	0.55
β	Balloon rubber coefficient	0.909
ϵ	Eddy dissipation rate	m^2s^{-3}
ϵ_{Brown}	Brown dddy dissipation rate	m^2s^{-3}
ϵ_D	Eddy Dissipation Rate from structure functions	m^2s^{-3}
ϵ_M	Eddy Dissipation Rate from turbulence closure theory	m^2s^{-3}
ϵ_r	Molecular weight ratio of H_2O to dry air	0.622
ϵ_{SI}	Eddy Dissipation Rate from spontaneous imbalance	m^2s^{-3}
η	MST Radar coefficient	4ln2
γ	Pendulum angle to the vertical in the plane of swing	deg
λ	Wavelength	m
κ_{ka}	Ka-band attenuation coefficient for liquid water	dB $km^{-1}g^{-1}m^3$
κ_X	X-band attenuation coefficient for liquid water	dB $km^{-1}g^{-1}m^3$
μ	Kinematic viscosity	$m^2\ s^{-1}$
μ_r	Shear modulus of balloon rubber	300 kPa
ν	One way half width of radar beam	deg
∇_H	Divergence	s^{-1}
$\nabla_H T$	Horizontal temperature gradient	K m^{-1}
Φ	Brown turbulent index	s^{-1}
ϕ_p	Pendulum angle to the vertical in the Y plane	deg
ψ	Off vertical beam angle	deg
ρ	Density	kg m^{-3}
ρ_l	Density of liquid water	1000 kg m^{-3}
σ_{br}	Spectral width component due to beam broadening	m s^{-1}
σ_m	Standard deviation of Z axis magnetometer voltage	mV
σ_{ms}	MST measured spectral width	m s^{-1}
σ_t	MST derived spectral width due to turbulence	m s^{-1}
σ_v	Standard deviation of vertical velocity	m s^{-1}

Symbol	Definition	Unit
σ_Z	Standard deviation of Z axis accelerometer	m s^{-2}
θ	Potential temperature	K
θ_b	Radar beam width	deg
θ_p	Pendulem angle to the vertical in the X plane	deg
θ_z	Potential temperature gradient	K m^{-1}
ξ	Relative vorticity	s^{-1}
ξ_r	MST beam broadening coefficient	m s^{-1}
ζ	Absolute vorticity	s^{-1}
ζ_r	MST beam broadening coefficient	m deg
A	DEVG description term	
A_{ka}	Attenuation coefficient of atmospheric gases in the Ka-band	dB km^{-1}
A_X	Attenuation coefficient of atmospheric gases in the X-band	dB km^{-1}
$\hat{a}$	Non dimensional wave amplitude	
a	Vertical acceleration of aircraft	g
a_w	Wave amplitude	m
B	LWC temperature correction factor	dB
$b_{1...4}$	Marroquin turbulence index coefficients	
C_k	Proportionality between Ozmidov and thorpe length scales	
C_m	MST Radar ϵ coefficient	
$CCAT$	CCAT turbulence index	s^{-3}
CP	Colson Panofsky turbulence index	knots^2
$c_{1...5}$	DEVG aircraft dependent coefficients	
c_p	Specific heat capacity of dry air	1004 J kg^{-1} K^{-1}
c_s	Phase shift of wave	m s^{-1}
D	Turbulent structure function	m s^{-1}
D_{cor}	Correction structure function	m s^{-1}
D_m	Turbulent structure function across model level	m s^{-1}
D_{ref}	Reference structure function	m s^{-1}
D_S	Shearing deformation	s^{-1}

Symbol	Definition	Unit
D_T	Stretching deformation	s^{-1}
DEF	Magnitude of deformation	s^{-1}
DUT	Dutton turbulence index	s^{-2}
E	Standard error of MST corrected spectral width	$m\ s^{-1}$
$ET1$	Ellrod Turbulent index 1	s^{-2}
$ET2$	Ellrod Turbulent index 2	s^{-2}
e	Vapour pressure	hPa
e_s	Saturated vapour pressure	hPa
F	Frontogenesis function	$m^2s^{-3}K^{-2}$
F_χ	Gaussian hyper confluent geometric function	
f	Coriolis parameter	s^{-1}
g	Acceleration due to gravity	$9.81\ m\ s^{-2}$
H	Aircraft altitude	ft
K_{ka}	Di-electric constant of Ka-band radar	
K_h	Thermal diffusivity	m^2s^{-1}
K_m	Kinematic diffusivity	m^2s^{-1}
K_X	Di-electric constant of X-band radar	
$KX1$	Knox turbulence index	s^{-2}
k	Wave number	m^{-1}
k_0	Lower wave number limit of the radar observable inertial sub-range	m^{-1}
k_1	Upper wave number limit of the radar observable inertial sub-range	m^{-1}
L	Fluid channel length scale	m
L_0	Upper length scale of the lidar's observable inertial sub-range	m
L_1	Lower length scale of the lidar's observable inertial sub-range	m
L_B	Buoyancy length scale	m
L_T	Thorpe length scale	m
l	String length between balloon and radiosonde	m
l_x	String length between balloon and radiosonde in x plane	m
l_y	String length between balloon and radiosonde in y plane	m

Symbol	Definition	Unit
M	MST radar beam width	m
MDD	Median Drop Diameter	mm
m	Mass	kg
N	Brunt-Vaisala frequency	s^{-1}
N_r	Refractive index	ppm
N_s	Sample count	
$NAVA$	Negative absolute vorticity advection	s^{-2}
$NCSU1$	NCSU turbulence index 1	s^{-3}
n	Refractive index	
n_m	Number of moles	mol
Pr	Prandtl number	
PV	Potential Vorticity	$\mathrm{m}^2\mathrm{s}^{-1}\mathrm{K\ kg}^{-1}$
P	Pressure	hPa
P_0	Reference pressure at surface	1000 hPa
q	Specific humidity	$\mathrm{g\ kg}^{-1}$
ΔR	Radar range gate size	m
R^*	Ideal gas constant	$8.314\ \mathrm{Pa\,K}^{-1}\,\mathrm{mol}^{-1}$
R_d	Gas constant of dry air	$287\ \mathrm{J\ K}^{-1}\mathrm{kg}^{-1}$
Re	Reynolds number	
RH	Relative humidity	%
RH_s	Pseudo relative humidity	%
Ri	Richardson Number	
RVA	Relative vorticity advection	s^{-2}
r	Radius of a weather balloon	m
r_0	Relaxed internal radius of a weather balloon	m
r_s	Saturation mixing ratio	$\mathrm{g\ kg}^{-1}$
r_{sonde}	Radius of radiosonde from origin	m
S	Velocity spectrum	$\mathrm{m}^2\mathrm{s}^2$
$s_{x..z}$	Displacement of virtual radiosonde from balloon	m
T	Temperature	K
T_{BV}	Brunt-Vaisala period	s
T_d	Dew point Temperature	K
T_v	Virtual temperature	K

Symbol	Definition	Unit
T_zDEF	Flow deformation × vertical temperature gradient	K $\mathrm{m^{-1}s^{2}}$
t	Time (in seconds unless stated otherwise)	s
t_0	Relaxed thickness of a weather balloon rubber	0.21 mm
t_d	Dwell time of remote sensing observation	m
U	Magnitude of horizontal wind	m $\mathrm{s^{-1}}$
$U\phi$	Wind speed × directional shear	m $\mathrm{s^{-1}}$ deg
U_{air}	Aircraft air speed	m $\mathrm{s^{-1}}$
U_H	Dutton's horizontal wind gradient	$\mathrm{s^{-1}}$
U_z	Magnitude of horizontal wind shear variation with height	$\mathrm{s^{-1}}$
$UDEF$	Wind speed × DEF turbulence index	m $\mathrm{s^{-2}}$
u	Zonal wind component	m $\mathrm{s^{-1}}$
V	Voltage	V
V_w	Doppler adjusted wave velocity	m $\mathrm{s^{-1}}$
V_x	Radial velocity of off vertical beam in x direction	m $\mathrm{s^{-1}}$
V_y	Radial velocity of off vertical beam in y direction	m $\mathrm{s^{-1}}$
V_z	Radial velocity of the vertical beam	m $\mathrm{s^{-1}}$
v	Meridional wind component	m $\mathrm{s^{-1}}$
v_r	Radial velocity	m $\mathrm{s^{-1}}$
v_{sonde}	Velocity of radiosonde relative to balloon	m $\mathrm{s^{-1}}$
w	Vertical wind component	m $\mathrm{s^{-1}}$
X''_{accel}	Acceleration experience by virtual radiosonde along x axis	m $\mathrm{s^{-2}}$
X''_{sonde}	Acceleration experience by virtual radiosonde in x plane	m $\mathrm{s^{-2}}$
Y''_{accel}	Acceleration experience by virtual radiosonde along y axis	m $\mathrm{s^{-2}}$
Y''_{sonde}	Acceleration experience by virtual radiosonde in y plane	m $\mathrm{s^{-2}}$
Z	Geopotential Height	m
Z_{acc}	Observed acceleration along accelerometer z axis	m $\mathrm{s^{-2}}$
Z_{calc}	Calculated acceleration along accelerometer z axis	m $\mathrm{s^{-2}}$
Z''_{accel}	Acceleration experience by virtual radiosonde along z axis	m $\mathrm{s^{-2}}$
Z''_{sonde}	Acceleration experience by virtual radiosonde in z plane	m $\mathrm{s^{-2}}$
Z_{ka}	Ka-band Radar reflectivity	dBZ

Symbol	Definition	Unit
Z_X	X-band Radar reflectivity	dBZ
z	Height	m
z_r	Radar range gate distance	m

Chapter 1

Introduction

Turbulence occurs all around us, whether it is water flowing over rocks in a quaint stream, or in Jupiter's violent atmosphere, it is present in all fluids. For most, turbulence means an uncomfortable flight to or from their holiday destination. Despite its common occurrence, turbulence is one of the least well understood atmospheric processes. First in this introduction the formation of turbulence in a fluid will be discussed. If a fluid has regions of differing velocities, eddies or vortices are generated by localised regions of vorticity. When these vortices are stretched or deformed turbulence occurs (Lesieur, 2012). (This can only occur if the viscosity of the fluid is low enough to allow this to happen.) All fluids have a viscosity μ which is a measure of how much shear stress needs to be applied to the fluid to make it deform. For example if golden syrup which has a high viscosity of 100 kg m^{-1} s^{-1}, and water that has a lower viscosity of 1×10^{-3} kg m^{-1} s^{-1} [1], is then passed down a channel, water would be expected to have a more turbulent flow. Reynolds (1894) experimented by passing fluids down channels at various velocities and viscosities and found that turbulence occurred under some conditions and not others. From this the Reynolds number, Re, an indicator of turbulence, was derived

$$Re = \frac{\rho U L}{\mu}, \tag{1.1}$$

where ρ is the density, U is the velocity of the fluid μ is the kinematic viscosity and L is the length scale, which is the diameter of the channel. It was found that a Re of 2000 would cause turbulence. Turbulence can be formed along a boundary or between two fluids of different velocities as shown in panels a) and b) of figure 1.1 respectively. The interaction of vertical motions of different fluids can generate turbulence while interacting

---

[1] Values at room temperature

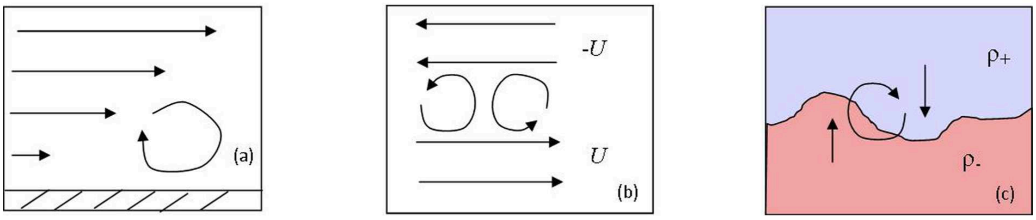

Figure 1.1 Diagrams showing the formation of turbulence between, a) a fluid flow and a boundary, b) two fluids of differing velocities and c) two thermally unstable fluids.

to reach their neutral buoyancy, as shown in panel (c). As stated, turbulence is formed by the generation of deformed vortices and eddies. These eddies break down, transferring their energy into a greater number of smaller eddies which further break down into even smaller eddies forming a constantly devolving cascade of eddies of different sizes. At very small eddy sizes ($<$ 1 mm for air) the molecular viscosity begins to dominate and their energy is dissipated as heat. This was discussed by Richardson (1920) who later wrote this short poem in Richardson (1922):

"Big whirls have little whirls, which feed on their velocity, and little whirls have lesser whirls, and so on to viscosity."

A mathematical way to think about the creation and dissipation of turbulence is to perform a spectral analysis of a velocity time series of a turbulent fluid to analyse its horizontal structure. This produces a velocity power spectrum similar to the idealised spectrum shown in figure 1.2. There are three distinct sections to the spectrum, the low frequency production range contains large scale non turbulent eddies or waves generated by an instability. The next section is called the inertial sub-range, is the frequency range where turbulence occurs as eddies cascade down to smaller eddies. As the turbulent kinetic energy is transferred down to a larger number of smaller eddies with smaller velocity perturbations, a spectral slope is present. Finally, at very high frequencies in the viscous sub range, the eddies dissipate as molecular viscosity begins to dominate. Kolmogorov (1941), derived from a dimensional analysis that the power spectral density $S(k)$ between the production range and the viscous sub-range was given by

$$S(k) = \alpha_k \epsilon^{\frac{2}{3}} k^{-\frac{5}{3}}, \tag{1.2}$$

where k is the wave number in spectral space and ϵ is the eddy dissipation rate, which is the rate at which turbulent energy created in the production range is dissipated in the viscous sub range. Finally α_k is the Kolomogorov constant equal to 0.55. Equation 1.2 has a -5/3 power term which is the power law of the spectral slope across the inertial sub-range seen in figure 1.2. ϵ is often used as a measure of turbulence intensity, this is because intense turbulence has larger eddies and hence a larger Turbulent Kinetic Energy (TKE), thus more TKE will dissipate as the spectral slope is fixed. It should be noted that TKE is conserved in the inertial sub-range and it is just redistributed to a larger amount of smaller eddies, only dissipating when in the viscous sub-range.

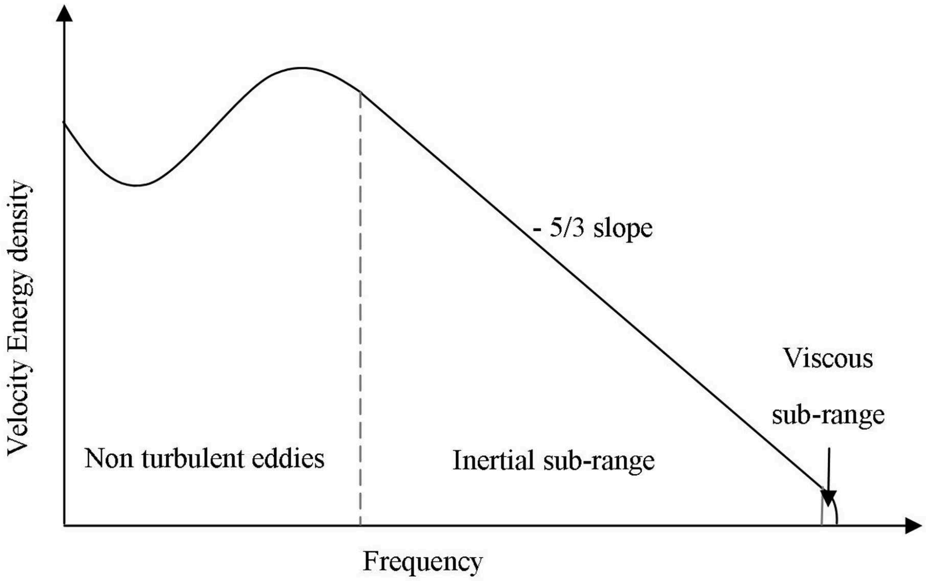

Figure 1.2 A diagram showing a hypothetical vertical velocity spectra plotted against frequency, the the outer scale, inertial sub-range and viscous sub-range have been marked.

In this brief introduction to turbulence some of the basic mechanisms of how turbulence may form in a fluid and how it dissipates have been covered. In the next section the different sources of turbulence in the Earth's atmosphere will be discussed.

1.1 Turbulence in the Earth's atmosphere

The Earth's atmosphere is a fluid in constant motion and is turbulent. Turbulence is generated in the atmosphere by a variety of different meteorological conditions. Turbulence is often seen in the atmosphere in the form of Kelvin Helmholtz billow clouds (Browning, 1971) shown in figure 1.3. Here the wind speed above and below the cloud

Figure 1.3 A photograph of a Kelvin Helmholtz billow cloud, the picture is from `http://www.amusingplanet.com/2013/07/kelvin-helmholtz-clouds.html`

differ significantly causing a distinct wave pattern to form. The waves form from vortices or eddies, becoming turbulent and cascade to smaller eddies until they dissipate. Hence such clouds are only present over a period of 20 minutes before the structure dissipates. High wind shear and low thermal stability have been shown to cause turbulence in the atmosphere and have led to the Richardson number criterion (Richardson, 1920) for turbulence, which is further discussed in chapter 2.

Figure 1.4 shows the major sources of turbulence generation within the atmosphere. In the atmospheric boundary layer turbulence forms as air thermally and dynamically interacts with the Earth's surface (Kaimal and Finnigan, 1994), similar to the example shown in panel a) of figure 1.1. Turbulence is also produced in the wake of objects such as buildings and trees (Counihan et al., 1974). Another part of the Earth's surface which is a source of turbulence is mountains. As air advects over mountains it is forced upwards, meaning that air passing over the mountain is less buoyant than the surrounding air, causing it to sink after passing over the mountain. The perturbed air sinks to a region where it is more buoyant due to its gathered momentum and begins to oscillate forming a gravity wave (Holton, 2004). At high altitudes above the mountain, the air is also perturbed forming a gravity wave with a vertical wavelength of several km that propagates down stream of the mountain. This wave can amplify and break if it reaches a critical level, which Holton (2004) refers to as a height at which the velocity of the mean

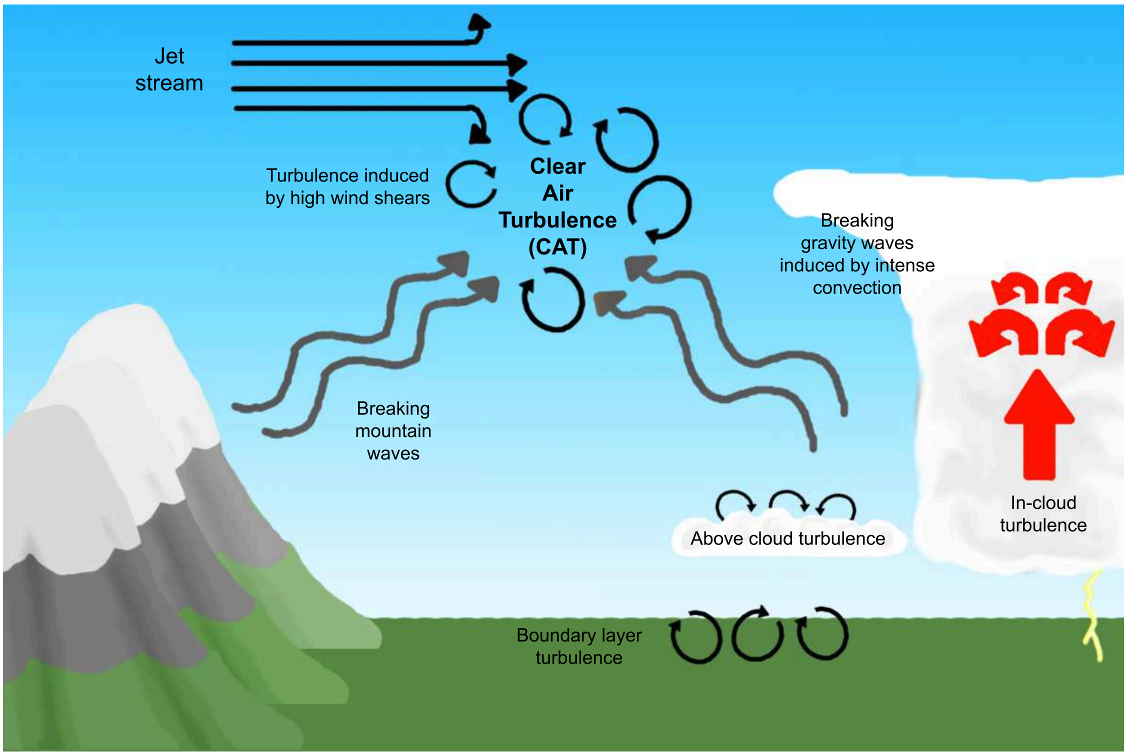

Figure 1.4 A diagram showing the different sources of turbulence in the atmosphere. See text for more in-depth descriptions for each turbulence source.

background flow reaches zero. Like a breaking wave on a beach, the wave breaks down causing turbulence. Similar to objects in the boundary layer, turbulent wakes can also be formed in the immediate region downstream of mountains (Lester, 1994)

Clouds are also sources of turbulence. In stratiform clouds turbulence can occur at the cloud top due to radiative cooling making the air thermally unstable (Shao et al., 1997). In larger frontal clouds, vertical motion combined with frontal dynamics create many turbulence generation mechanisms, also important for the growth of hydrometeors (Houze Jr et al., 1976). Turbulence is also present in violent cumulonimbus clouds due to the large convective up-draft (Meischner et al., 2001), which is so intense it generates gravity waves that propagate away from the convective cell meaning turbulence can be observed in clear air some 100km away (Lane et al., 2012).

The final source of atmospheric turbulence is the jet stream, a fast moving region of air in the mid to upper troposphere and lower stratosphere. Because of the substantial wind speeds turbulence has been observed in high wind shear regions between the jet core and the background flow (Kennedy and Shapiro, 1975), (Shapiro, 1976), (Kennedy and Shapiro, 1980). Turbulence has also been observed along regions of the jet stream where deformation was present (Mancuso and Endlich, 1966), (Ellrod and Knapp, 1992).

Deformation is the reshaping of a fluid within a flow and often occurs in the atmosphere near the exits of jet streams, along ridges of high pressure between two lows, along upper level fronts and in regions of confluence (Ellrod and Knapp, 1992). In these cases the interaction with air of different velocities in a horizontal sense enables the formation of turbulence. Furthermore, convergence can also yield turbulence as air is forced upwards or downwards due to the confluence of air, forming regions of instability in the atmosphere Koch and Dorian (1988).

The aforementioned meteorological sources of turbulence fall into two main categories of turbulence, the first is Clear Air Turbulence (CAT). This is turbulence that occurs in clear-air usually associated with turbulence from the jet stream or from breaking gravity waves from a mountain or local atmospheric disturbance. The second is in-cloud turbulence, occurring inside and near cloud boundaries. Aircraft have experienced turbulence since the earliest days of powered flight (Pick and Bull, 1926). Pilots can avoid in-cloud turbulence by circumnavigating the cloud, however clear-air turbulence is more difficult to avoid. This is due to there being no visual sign of the turbulence in advance, the first sign of CAT is typically the response of the aircraft as it passes through a turbulent patch (McLean Jr, 1987). In the next section the risks to aircraft flying through turbulence will be explored.

1.2 Risks of turbulence to aviation

A study of aviation accidents over the US between 1982 and 1984 by McLean Jr (1987) showed that 24% of commercial aviation accidents were caused by turbulence. It was estimated that there were 81 injuries to flight crews and passengers of which 24 were listed as serious. Figures from Golding (2002) show that between 1984 and 1997 there were 342 cases of major turbulence reported over the US, in which 769 reported injuries, 80 of those were serious and 3 people died. Injuries commonly occur to passengers who are not wearing seat belts and from items in the cabin being thrown around against the fuselage. Flight attendants have an increased risk as they are often dispensing refreshments. McLean Jr (1987) also comments that smaller aircraft are more likely to be in a fatal accident as they are more prone to total loss of control in severe turbulence. The chances of a commercial airline crashing due to severe turbulence is incredibly rare but such accidents do happen. One such incident was in 1966 where a BOAC B727 crashed near Mount Fuji in Japan after encountering mountain wave turbulence. The turbulence was so intense, that the tail plane of the aircraft was ripped off, causing it to crash with the loss of all 133 people on board (BBC Archive, 1966). McLean Jr (1987) reported three commercial aircraft fatally crashing over the US between 1968 and 1974 being attributed to structural failure of aircraft in turbulence. There are 3-4 reported cases in the media each year of severe Clear-air turbulence, causing injury to passengers and crew, resulting in emergency landings to seek medical assistance. A recent example of this was a flight from Miami to Milan in January 2016, which encountered severe turbulence causing the aircraft to make an emergency landing where 3 passengers and 4 flight attendants were hospitalised (CNN News, 2016). Figure 1.5 (a) shows the inside of a Singapore airline flight after it encountered severe CAT en-route to London. (b) shows the loss of an aircraft engine after encountering turbulence.

Turbulence causes damage to aircraft both internally and externally, as well as injuring passengers and crew. This leads to claims being made by passengers which are estimated to be US$ tens of millions a year and the loss of several thousand flight attendant staffing hours due to injuries (Sharman et al., 2006). Golding (2002) estimates the annual cost of turbulence to the airline industry to the order of US$ 100 million. These costs are expected to rise in the coming decades as turbulence is predicted to increase in frequency and intensity across the Atlantic flight corridor due to climate change (Williams and Joshi, 2013). As discussed, aircraft can avoid in-cloud turbulence, but CAT they cannot. The aviation industry relies on turbulence forecasts to predict where significant CAT may be present, which are discussed in the next section.

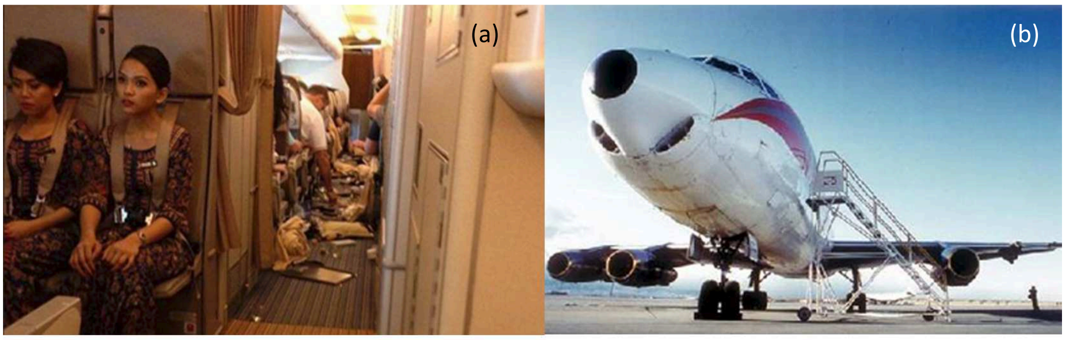

Figure 1.5 (a) A scene of damage and destruction on a Singapore Airline flight to London which encountered severe CAT (Alan Cross) and (b) aircraft missing an engine after an encounter with CAT (courtesy DELICAT).

1.3 Turbulence forecasts

CAT forecasts are mainly based on empirical forecasts which, for example look at deformation(Ellrod and Knapp, 1992), or a combination of many (Sharman et al., 2006). There are two leading turbulence forecasting packages, the first is the Graphical Turbulence Guidance (GTG) system described in Sharman et al. (2006), that uses a weighted combination of several diagnostics which are adjusted based on their performance in the few hours leading up to the forecast run time. The second is the ULTURB which uses the Lighthill-Ford theory of spontaneous imbalance to predict regions where breaking gravity waves may form, as if they are radiated from a rotating shallow fluid flow (McCann et al., 2012). These turbulence forecast systems are able to predict significant turbulence approximately 60% of the time for the GTG and approximately 70% for the ULTURB system. World Area Forecast Centers (WAFC) which provide global forecasts for aviation use the Ellrod turbulent indices (Ellrod and Knapp, 1992) which are further described in chapter 2. In order to develop these forecasts, observations of turbulence are required to compare forecast data with. The main source of turbulence observations are from commercial airline pilot reports (Schwartz, 1996). However, these are subjective as the report has biases to the size of aircraft and pilot experience, also they are not quantitative. Aircraft Meteorological DAta Relay (AMDAR) (Painting, 2003) has successfully managed to remove this bias by making automated turbulence measurements which produce an ϵ value derived from an aircraft's accelerometer using algorithms developed by Cornman et al. (1995). There is still further bias due to observation density, especially involving severe turbulence encounters as if one aircraft reports severe turbulence, other aircraft will then avoid that airspace, limiting an observation to one per severe event.

With each aircraft turbulence report, the temperature, pressure and wind speed along the flight route is also provided. Although useful, it makes it difficult to build up a vertical profile of the structure of the atmosphere. Scientific campaigns have flown instrumented aircraft on intense observation routes through jet streams (Shapiro, 1978) and thunderstorms (Meischner et al., 2001) to learn more about the turbulent structure. These flights, whilst providing a wealth of information concerning turbulence profiles in both the vertical and horizontal, are few and far between, mainly due to financial cost of such flights. Alternative methods for probing atmospheric turbulence are to use remote sensing methods or an untethered balloon platform, which is the main method discussed within this thesis. Remote sensing methods such as Doppler lidar techniques

(O'Connor et al., 2010) can be used to detect turbulence, but are limited to the boundary layer. Doppler cloud radars can observe turbulence within clouds (Meischner et al., 2001), (Bouniol et al., 2004) and finally wind profilers can also make observations of turbulence across a large vertical range of 20 km (Dehghan et al., 2014), but are distributed sparsely across the globe.

Balloons have been used to carry instrumentation to measure the profile of the atmosphere since the late 18th century. One of the first of these flights was a manned flight made by J. A. C. Charles, using a hydrogen filled balloon constructed by the Roberts Brothers in France on 1st December 1783. Charles ascended above 2000m where he recorded an air temperature of -5^{o}C (Pfotzer, 1972). During the next 100 years these pioneers yearned for more observations from greater altitudes. In 1862 two British aeronauts lost conciousness at a height of 10km and were lucky to escape with their lives. Because of increased costs and safety limitations to such ascents, unmanned flights began to be made (Hoinka, 1997). These unmanned flights recorded observations using a meteograph, an instrument which recorded: pressure, temperature and humidity on to a clockwork drum, allowing the recovery of data for analysis (Renard, 1903). Following developments in radio and electronics during the 1920s, Robert Bureau, replaced the clockwork system with an electronic system which relayed information over a radio link to a ground station. He made the first flight on the 7th January 1929, and soon coined the phrase ”radiosonde”. Within the next decade companies [2] across the globe began mass producing radiosondes for meteorological organisations. Since then radiosondes have been developed to utilise the current technologies of the age. A standard radiosonde can measure: temperature T, relative humidity RH, Pressure P, height z and u and v wind components derived from its position.

Alone a radiosonde does not carry instrumentation to directly measure turbulence. Gavrilov et al. (2005) and Clayson and Kantha (2008) showed information concerning turbulence may be inferred from the inversions identified in a radiosonde's potential temperature, θ, profile, in a similar method used to identify overturns in ocean currents (Thorpe, 1977). However turbulence detected using this method has not been substantially compared with other turbulence observations. Anderson (1957) flew accelerometers on balloons and used the data from the accelerometer during descent on parachute to make observations of turbulence. This showed how the addition of a motion sensor to a platform such as this can yield turbulence measurements. This data was combined

---

[2] One such individual was Professor Vilho Vaisala. The company which still bears his name began commercial production of radiosondes in 1936.

with meteorological data from a radiosonde launched at the same time to give a database of turbulence encounters with corresponding meteorological information. As a balloon and radiosonde ascend through the atmosphere the balloon is perturbed by turbulence causing the radiosonde to swing underneath. Harrison and Hogan (2006) and Harrison et al. (2009) flew a magnetometer motion sensor on a standard meteorological radiosonde to measure the swing of the magnetometer in turbulence. This allowed vertical profiles of meteorological data and motion data from the balloon's interaction with turbulence to be obtained. Furthermore, radiosondes can be flown in almost all weather conditions and have an excellent vertical range of up to 30 km. The radiosondes are disposable and are safer for sampling atmospheric hazards than aircraft. One example was when in situ measurements of volcanic ash were made using a disposable balloon-borne aerosol sensor during a precautionary protective flight ban over Europe (Harrison et al., 2010).

1.4 Thesis objectives

Anderson (1957), Harrison and Hogan (2006) and Harrison et al. (2009) demonstrated that motion sensors fitted on standard meteorological balloons can observe turbulence. Thousands of radiosondes are launched globally around the world daily, this coupled with the widespread availability and low cost motion sensors such as accelerometers, provides great potential for an extensive network of turbulence measurements. These equipped radiosondes can provide profiles that can be used to increase our understanding of atmospheric turbulence. Hence the main aims of this project are to further develop an adapted radiosonde to make standardised observations of turbulence using motion sensors, then using this turbulence sonde, make standardised turbulence observations in different meteorological conditions and assess turbulence forecast skill. Thus this thesis has four main objectives which are listed below, and form the main basis for each of the thesis chapters:

(a) To further develop a balloon borne turbulence sensor that can be used to make standardised measurements of atmospheric turbulence

The magnetometer device used in Harrison and Hogan (2006) and Harrison et al. (2009) is first characterised to detect the swing of the radiosonde when the balloon is agitated by turbulence. An accelerometer device is then prototyped to observe the radiosonde's swing in turbulence. Extensive spectral analysis and comparisons between the two instruments are made, as well as modelling of the balloon radiosonde system to more fully understand the interaction. A decision is made to use the accelerometer motion device, as it shows the best response to turbulence, however, in order to allow a meaningful measurement of turbulence to be inferred, a comparison with other turbulence detection methods is needed which informs the second objective.

(b) Compare turbulence measurements from the accelerometer sonde against those from remote sensing techniques.

It is important to understand how the accelerometer sonde reacts to turbulence, so that results from the sensor can be used to infer meaningful information about turbulence. To achieve this, comparisons between the accelerometer radiosonde and turbulent observations made using a Lidar, a Doppler cloud radar and an MST wind profiler will be undertaken to characterise the device. This will allow a meaningful analysis of a larger accelerometer sonde dataset to be undertaken.

(c) Analyse observations of the turbulent structure of the atmosphere in different meteorological conditions.

An analysis of over 50 accelerometer sondes is carried out, where data is sub-set by different meteorological conditions to allow the turbulent structure and reasons for turbulence generation within each phenomena to be identified. By identifying turbulence in different meteorological conditions the dataset can be used to evaluate the skill of CAT diagnostics in clear air conditions in the final objective:

(d) Use the dataset of standardised turbulence observations to assess the skill of turbulence forecasts.

Here an appropriate model will be selected and the accelerometer sonde dataset will be compared with 23 commonly used CAT diagnostics. First some turbulence diagnostics will be compared with accelerometer sonde case studies, before a full comparison is made using the full dataset, to find the most skilful diagnostics.

1.5 Thesis structure

Each objective here forms the basis of a chapter in this thesis. In Chapter 2, previous and current turbulence observation techniques are reviewed, as well as a review of the different turbulence diagnostics which will be used in chapter 6. In chapter 3 the magnetometer motion sensing device for a radiosonde developed by Harrison and Hogan (2006) is firstly examined. From there, the development of the accelerometer device is documented and the motion of the radiosonde beneath the balloon is modelled to help further understand the balloon radiosonde system. In chapter 4 the accelerometer sonde is compared against multiple remote sensing methods of turbulence. Chapter 5 shows the results from 51 accelerometer sonde ascents in different meteorological conditions. Finally chapter 6 shows the comparison of the turbulence sonde data with turbulence diagnostics. An overview of the findings will be discussed in chapter 7, the conclusions chapter, along with some extended discussion of results. Appendices include information on the calculation of various quantities used in the thesis, which are too much of a digression from the main text.

Chapter 2

A review of turbulence measurements and predictions

This chapter consists of two parts. The first part discusses methods to observe atmospheric turbulence using both in-situ and remote sensing methods. In the second part of the chapter, methods to predict turbulence using the output from numerical weather prediction models are discussed.

2.1 In-situ methods to detect turbulence

In-situ turbulence measurements are turbulence observations made by an instrument or object placed into a turbulent flow. At the ground this is easy to achieve with the use of micro meteorology instruments such as sonic anemometers and fine wire platinum resistance thermometers, which measure the structure of the turbulent flow (Kaimal and Finnigan, 1994). These instruments can be placed on masts or suspended from tether balloons (Readings, 1973) to enable the lowest reaches of the atmosphere to be sampled. For the in-situ detection of turbulence detrimental to aircraft, measurements are needed at higher altitudes. This yields two observing platforms: aircraft and untethered balloons. In this section the various methods in which turbulence observations can be made will be discussed along with their merits and disadvantages.

2.1.1 Pilot reports

Pilot reports have been used to report turbulence for nearly 90 years. One of the earliest standardised sets of turbulence pilot reports were made around Cranwell, Lin-

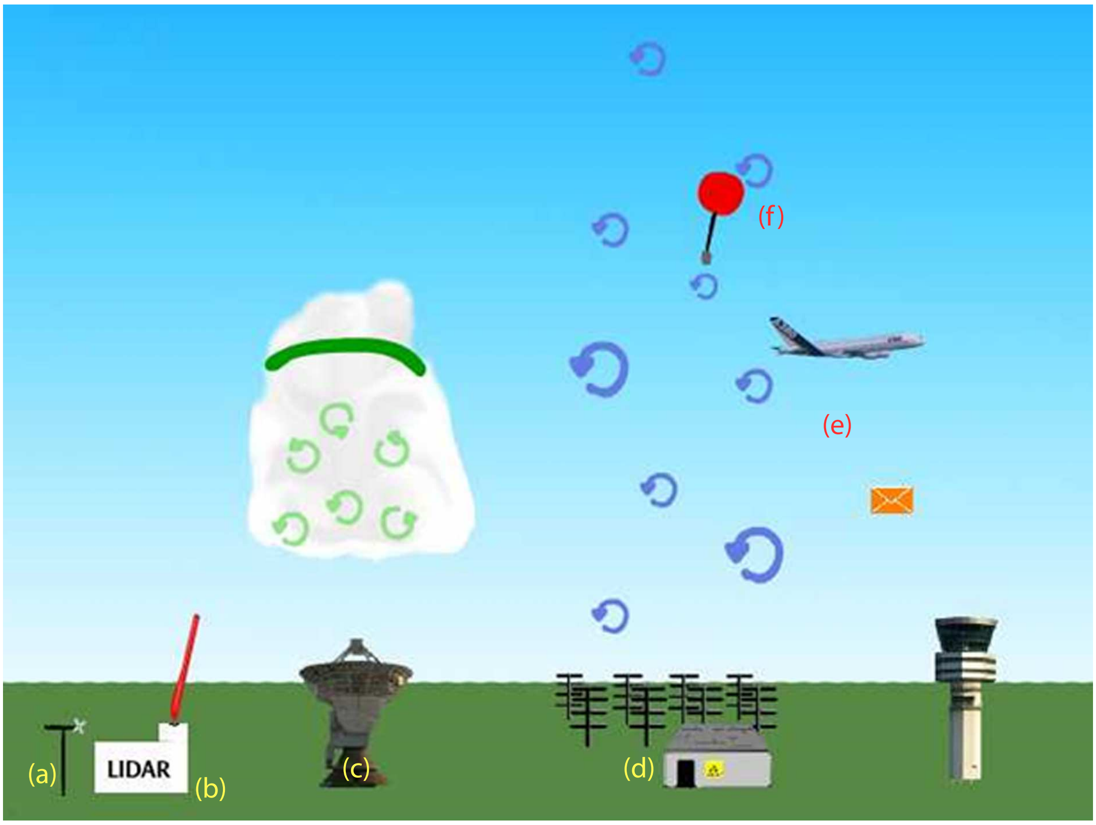

Figure 2.1 A diagram showing multiple methods to detect turbulence using, surface instrumentation (a), remote sensing techniques of lidar (b), cloud radar (c) and wind profilers (d) and also in-situ measurements from balloons (f) and aircraft (e).

colnshire, between 1925 and 1926 (Pick and Bull, 1926). Pilots were asked to report ”bumpiness” on a scale of: 0 - for no bumps to 5 - for exceptionally bumpy. Four months of data taken at heights of up to 3000ft (1 km) were collected. From this, comparisons were made by examining the air mass present over the UK. Initial conclusions showed that air of equatorial origin was more ”bumpy”. Although the scale used was somewhat vague and quintessentially British, it did lay foundations for more technical descriptive observations of turbulence.

In the 1970s aviation authorities began requiring that all encounters with turbulence were to be reported, and so PIlot REPorts (PIREPs) began to be logged. A PIREP contains: height, position, aircraft type, sky and weather conditions, air temperature, wind data and turbulence information. This is transferred in a standard format by radio to air traffic control, allowing controllers to make real time decisions in response to turbulence and icing (Federal Aviation Association, 2010). The turbulence criteria have moved from scales of bumpiness to more descriptive measures as shown in table 2.1

All aircraft from leisure craft to the largest civilian aircraft transmit this information during flight. This, over many years, generated a large dataset of global turbulence

Turbulence Intensity	Aircraft Response	Cabin Experience
Null	Aircraft flies smoothly	Objects remain where they're placed
Light	Slight changes in altitude, pitch, roll and yaw	Passengers may feel slight strain against seatbelts. Unsecured objects may move slightly, no difficulty walking
Moderate	Erratic changes in altitude, pitch, roll and yaw, however aircraft stays in control	Passengers feel definite strain on seatbelts, loose objects may move about.
Severe	Large abrupt changes in altitude, pitch, roll and yaw. Aircraft may be momentarily out of control	All loose objects are thrown about and passengers are violently forced against restraints.
Extreme	Aircraft is violently tossed about and is impossible to control, risk of structural damage.	All unsecured objects are thrown around the aircraft.

Table 2.1 Table showing PIREP turbulence intensities and aircraft response and cabin conditions from Lester (1994).

reports, which has been utilised by many for verification purposes in the development of new turbulence diagnostics (Ellrod and Knapp, 1992) and Sharman et al. (2006) for example. However one must consider how good a PIREP report is as a measure of turbulence. Firstly a PIREP is not based on a quantitative measure of turbulence. The report is a scale of how the aircraft is reacting to turbulence in flight, adding another consideration into the reliability of such a dataset, as different aircraft react to different turbulence intensities in different ways. An analogy for this is a small fishing boat and a large container ship in a rough sea. The small fishing boat will be rocked around whilst the container ship would only bob gently up and down. Similarly with aircraft, a small four seater aircraft may report severe turbulence whilst a large aircraft may only report light turbulence. A second uncertainty arising with PIREPs is the pilot compiling the report. Pilots with differing experiences may report turbulence differently, for example an inexperienced pilot may report moderate turbulence as severe. Schwartz (1996) suggested reasons as to why pilots may not be completing or being untruthful in the completion of pilot reports. One suggestion was that, in light to moderate cases, it was not worth reporting. Alternatively it was suggested this could be to minimise ground inspection times or to minimise any legalities that may arise out of an extreme turbulence encounter. However there have been no case studies provided to substantiate this claim. A final point is that, when moderate or greater turbulence is recorded, air traffic control re route aircraft around the problem area limiting information about an extreme turbulence event to one encounter. This is not particularly useful if one wishes to use this data to evaluate new turbulence predictors.

In conclusion whilst being one of the longest records of aviation turbulence PIREPs appear to have many biases based on pilot experience, aircraft type and a tendency to observing moderate and light turbulence more than severe turbulence. Pilot and aircraft bias could be removed by making automated observations of turbulence aboard the aircraft which is discussed in the next section.

2.1.2 Instrumented aircraft measurements

Automated observations of turbulence can be made by instrumenting an aircraft, which can either sample the turbulent structure of the air or be equipped with motion sensing equipment. The advantage is it minimises human error and potentially provides a more quantitative aircraft independent measure of turbulence. However consideration is needed to remove the bias that is the aircraft response, which varies with aircraft design.

The ability for aircraft to begin logging information concerning the structure of the atmosphere began in the 1960s with MacCready (1962), who flew hot wire anemometers and an accelerometer on a glider. Data was recorded on magnetic tape, then analysed spectrally to calculate the eddy dissipation rate ϵ using a -5/3 law. In other work turbulence can also be calculated from horizontal and vertical wind velocities measured by an aircraft, although one underlying problem was reliably obtaining u,v and w from the aircraft without contamination from aircraft manoeuvres (Reiter and Burns, 1966). These problems were overcome with the development of devices known as inertia platforms (Axford, 1968), which allowed an aircraft's pitch, yaw, roll, and angle of attack to be known. This, combined with wind vanes mounted on a boom at the front of the aircraft, and knowledge of the aircraft speed, allows the horizontal and vertical velocity perturbations to be accurately calculated. Nicholls (1978) used this system to make observations of turbulence within the marine boundary layer. -5/3 laws were fitted to the horizontal and vertical velocity spectra, indicating that ϵ could be calculated. Similar experiments were also carried out by Brown et al. (1983) who found a -5/3 law in pressure fluctuations along a nose cone. Meischner et al. (2001) made aircraft observations of eddy dissipation rate through the top of thunderstorms. The eddy dissipation rate was calculated by using the spatial structure function

$$D = \frac{1}{2}[(v(t) - v(t - \Delta t))^2 + (w(t) - w(t - \Delta t))^2]^{1/2}, \tag{2.1}$$

where v is the perpendicular wind speed to the aircraft and w is the vertical wind speed. Δt is the time period over which the function is computed. Paluch and Baumgardner (1989) showed that ϵ can be calculated using

$$\epsilon^{\frac{1}{3}} \approx \frac{D^{1/2}}{1.652(U_{air}\Delta t)}, \tag{2.2}$$

where U_{air} is the air speed of the aircraft. The values of ϵ were compared against an "MRI turbulence meter" which, upon further investigation yielded a product patent by Maccready (1966). The patent describes an elegant analogue device in which a voltage proportional to $U_{air}^{2/3}$ is band pass filtered at both frequencies above and below the inertial sub-range. The output from the filter is then scaled by a factor based on the properties of the circuit to yield real time values of ϵ. Unfortunately there have not been any published calibrations of the device so its effectiveness is not known.

This showcase of measurements illustrates that a quantitative measure of turbulence can be found by adding specialist instruments to an aircraft. Whilst removing pilot error, there still remains the question of how much the aircraft size affects the measurement. As mentioned before, larger aircraft are less likely to be perturbed by given turbulence than a light aircraft, which may have a slight effect on derived quantities despite compensation from inertial navigation systems or the modern day equivalent of GPS (Lester, 1994). The majority of these aircraft had been modified to carry a boom to support the sensors. Thus turbulence observations were made in limited places and in conditions predetermined by the scientific campaign. If more regular observations are required then aircraft-independent automated observations requiring minimal adaptation to the aircraft are needed.

2.1.3 Automated aircraft measurements of turbulence

Attempts to begin making wide spread automated observations of meteorological conditions experienced by aircraft began in 1970's backed by the WMO. It wasn't until 1991 that Aircraft Meteorological DAta Relay (AMDAR), a global project began operating (Painting, 2003). Participating airlines in the project relayed real time meteorological information for data assimilation in numerical weather prediction models across the world.

AMDAR enabled aircraft are also able to yield up to three turbulence metrics dependent on aircraft. Each measurement is derived from the aircraft's inertial navigation system vertical accelerometer. The simplest of the three metrics used is the peak vertical acceleration from the accelerometer over a given period. It is a quantitative measurement and is very aircraft dependent (Lester, 1994) (Painting, 2003) if one considers the boat analogy.

Derived equivalent vertical gust (DEVG)

Derived equivalent vertical gust is an aircraft independent measure of turbulence. It is a measure of the vertical gust that the aircraft would have to experience near the surface inducing the same vertical acceleration as if in turbulence (Sherman, 1985). Curran (1973) performed an experiment between a Vulcan bomber (a large delta wind aircraft) and a Canberra fixed wind twin jet aircraft (figure 2.2). The two aircraft flew along similar flight paths through turbulence recording different vertical accelerations, but the derived equivalent vertical gust from each was very similar, hence demonstrating DEVG can be an aircraft independent measure.

DEVG is calculated by taking the mass, air speed and vertical acceleration into account as well as various coefficients pertaining to the aircraft in question. The coefficients for calculating the DEVG have been calculated for a range of different aircraft and are designed to include information such as wing shape and span. The DEVG for an aircraft

Figure 2.2 Left: English Electric Canberra, courtesy of RAF (Crown Copyright) Right: A Vulcan aircraft over Wilstead, Bedfordshire, courtesy of Mr P. Marlton. The two aircraft are very different in both shape and size, the Canberra has a wing area of 89 m^2 and the Vulcan has a wing area of 368 m^2.

is given by (Painting, 2003)

$$DEVG = \frac{10Am|\Delta a|}{U_{air}}, \tag{2.3}$$

where m is the mass of the aircraft, Δa is the magnitude of vertical acceleration from g and U_{air} is the airspeed of the aircraft. A is given by

$$A = \overline{A} + c_4 \left(\overline{A} - c_5\right) \left(\frac{m}{\overline{m}} - 1\right), \tag{2.4}$$

where $\overline{m}$ is the reference weight of the aircraft and $\overline{A}$ is given by

$$\overline{A} = c_1 + \frac{c_2}{c_3 + H}. \tag{2.5}$$

where H is the height of the aircraft in ft, and coefficients c_1 to c_5 are the aircraft dependent coefficients. For AMDAR aircraft, the coefficient data has been calculated for a range of aircraft, meaning the accelerometer data can be combined to give aircraft independent values of turbulence. DEVG data calculated in this way has been used in the verification of turbulence forecast using Boeing 747 aircraft (Gill, 2014).

Eddy dissipation rate ϵ

Another aircraft independent measure of turbulence would be to calculate ϵ from the aircraft accelerometer data. As discussed in this chapter ϵ has previously been calculated before using accelerometers (MacCready, 1962) and using variations in wind speed (Maccready, 1966), however aircraft independence had not been accounted for. A method proposed in Cornman et al. (1995) was to use the vertical accelerometer data to calculate the Eddy Dissipation Rate. The accelerometer data had a band-pass filter applied to the data to filter out the high frequency effects of aircraft vibration. The low frequency edge of the band-pass filter was to remove motion caused by aircraft manoeuvring. The mean square of the filtered accelerometer data was combined with the aircraft velocity and an aircraft response function. The aircraft response function contains information as to how the aircraft responds in the vertical to changes in acceleration under different conditions. For use on AMDAR, the aircraft response functions are saved within look up tables for a variety of situations and manoeuvres (Painting, 2003). This is a somewhat more complex and universally applicable system to that in Maccready (1966) due to the use of accelerometers and that the aircraft type have been factored in. ϵ observed in this manner has been used by Sharman et al. (2014).

The three methods show how on board accelerometer data can be used to provide a gauge of turbulence. The first method is of little use as there is no aircraft independence, especially if a large database of observations is needed. The latter two are aircraft independent and have been shown that they can be used to provide a good turbulence database.

Turbulence category	Aircraft vertical acceleration magnitude (g)	DEVG for B737 ($\mathrm{m\ s^{-1}}$)	ϵ for B737 ($\mathrm{m^2 s^{-3}}$)
Light	0.2-0.5	1.66-4.17	0.001-0.027
Moderate	0.5-1	4.17-8.34	0.027-0.125
Severe	1-2	8.34-16.68	0.125-0.343
Extreme	>2	>16.68	> 0.343

Table 2.2 Adapted from Lane et al. (2012), aircraft vertical acceleration magnitude from Lester (1994), the DEVG calculated from the vertical accelerations for a B737 and the approximate ϵ for a B737.

The Eddy dissipation rate and derived equivalent vertical gust are related as they are different derivatives of the same vertical measures of acceleration whilst maintaining an amount of aircraft independence. Using the bin edge and centre values (not shown) in table 2.2 it is possible to find a relationship between DEVG and ϵ as shown in figure 2.3. As ϵ spans at least three orders of magnitude and was log base 10 transformed, the relationship between the $log_{10}(\epsilon)$ and the DEVG had a exponential trend hence the fitted curve in red. Using this relationship it is then possible to use the DEVG to calculate the vertical acceleration a range of aircraft would experience by rearranging equation 2.3 and using coefficients from different aircraft listed in table 1 of appendix 1 in Painting (2003).

Figure 2.4 shows hypothetically how different aircraft may encounter the same intensity of turbulence but have a very different reaction to it. All but the Kingair 100 are large commercial airliners, whereas the Kingair is a small aircraft usually used for research flights. Using these estimations the turbulent motion experienced by the Kingair could be up to 5 times worse, as the predicted vertical accelerations are larger, although it should be noted that these are hypothetical calculations. It also highlights how the use of raw accelerometer data is not a standardised method of building a large turbulence database from many different flights.

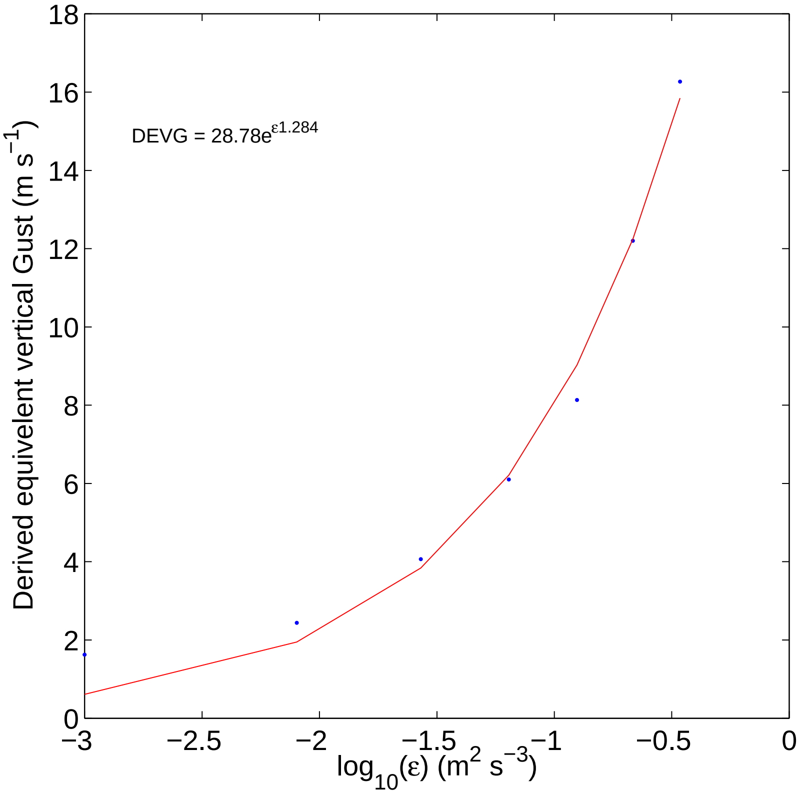

Figure 2.3 Eddy dissipation rate (m^2s^{-3}) plotted against a derived equivalent vertical gust ($m\ s^{-1}$) using data from table 2.2.

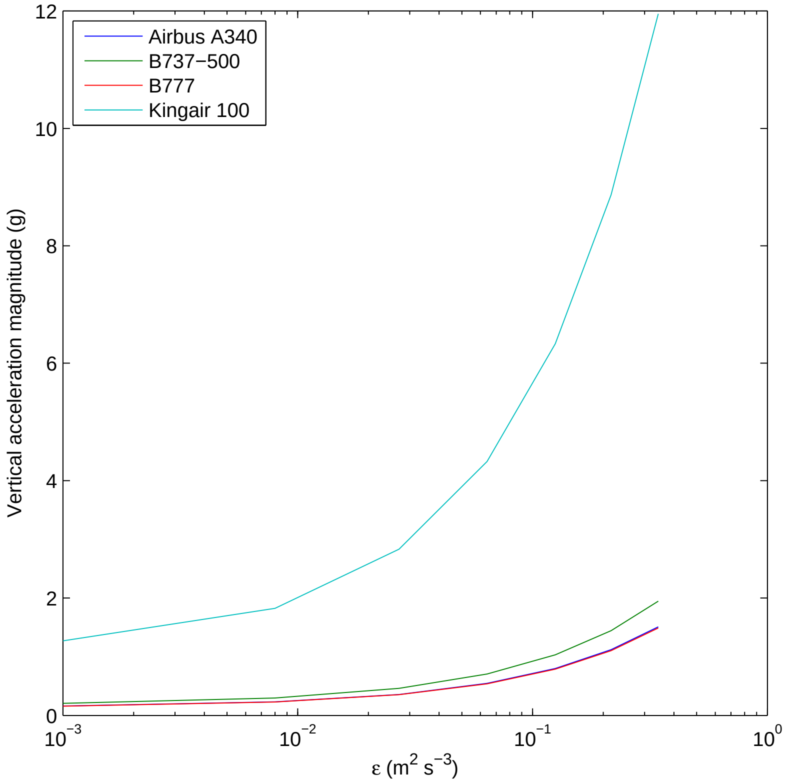

Figure 2.4 Eddy dissipation rate (m^2s^{-3}) plotted against magnitude of vertical acceleration (g) for an Airbus A340, B737-500, B777 and Kingair 100.

2.1.4 Free balloon measurements of turbulence

Balloons have been used as measurement platforms for many atmospheric quantities in the mid troposphere since the late 1700s (Pfotzer, 1972). In 1929 a radio transmitter was added to a weather balloon allowing meteorological data to be relayed back to a ground station. In 1950 the US government commissioned gust-sondes to provide information on gust loads for aircraft. Anderson (1957) used this data to perform a comparison against meteorological conditions. The device consisted of a pressure switch and a vertically orientated accelerometer. Given the similar nature of this work to the current project a more in-depth summary of this work is provided. Anderson (1957) comments that the balloon platform was unstable, probably due to the ubiquitous turbulence in the atmosphere. Hence only the accelerometer data was logged after the balloon had burst and was descending by parachute. The parachute was designed to provide a high level of stability so when the device did encounter turbulence it evoked a response in the accelerometer. The gust-sondes were launched an hour before a standard meteorological radiosonde was launched. The reasoning for this was to combine standard meteorological ascent data from the radiosonde with the descent data from the gust sonde. The gust sondes were launched from four locations across the United States, and over a year 828 gust sondes were launched. Turbulent air was associated with a descent distance of 100ft or more where accelerometer variability was detected. This yielded a qualitative measure of turbulent or non turbulent regions of air. Meteorological and turbulence data were combined to give a data set comprising of 300m slices of the atmosphere. From here the investigator found relationships between the Richardson number, vertical wind shear and other meteorological quantities. For example stating that turbulence is statistically more likely at wind speeds greater than 16 m s^{-1}. Although the data analysis was carried out mechanically using some 30,000 punched records, it was successful in highlighting conditions in the free atmosphere in which turbulence was observed. The main limitations of the experiment were that the dataset was underused, possibly due to technical limitations such as not comparing the observations to larger synoptic scale features. Furthermore the meteorological knowledge of the time was still some what limited. For example papers regarding the jet stream were only being published 5 years before this experiment (Lewis, 2003). It was an experiment before its time as the surrounding theory had not yet been understood to provide better explanations for the results. Yet it shows how a network of instrumented balloons can be used to make observations of turbulence.

Reiter (1962) suggested that the way forward for making observations of turbulence was to either use balloon borne platforms or smoke tracers. The next generation of turbulence measurements to be made with balloons started with a theory originating from oceanography. Thorpe (1977) described a method in which turbulent length scales could be identified by looking for overturns in ocean density profiles. Figure 2.5 shows two hypothetical density profiles. In the turbulent profile it can be seen that density does not monotonically increase with depth. Thorpe (1977) suggested that noting the vertical distance each point had to be moved in order to yield a monotonic profile could yield a displacement. For a given inversion a Root mean square was taken of the individual displacements to give a turbulent length scale. This turbulent length scale L_T, has become known as a Thorpe length scale and the method to obtain it is known as the Thorpe analysis.

Gavrilov et al. (2005) showed that the Thorpe analysis could be used on high resolution balloon measurements of potential temperature, θ given by

$$\theta = T\left(\frac{P_0}{P}\right)^{\frac{R_d}{c_p}}, \tag{2.6}$$

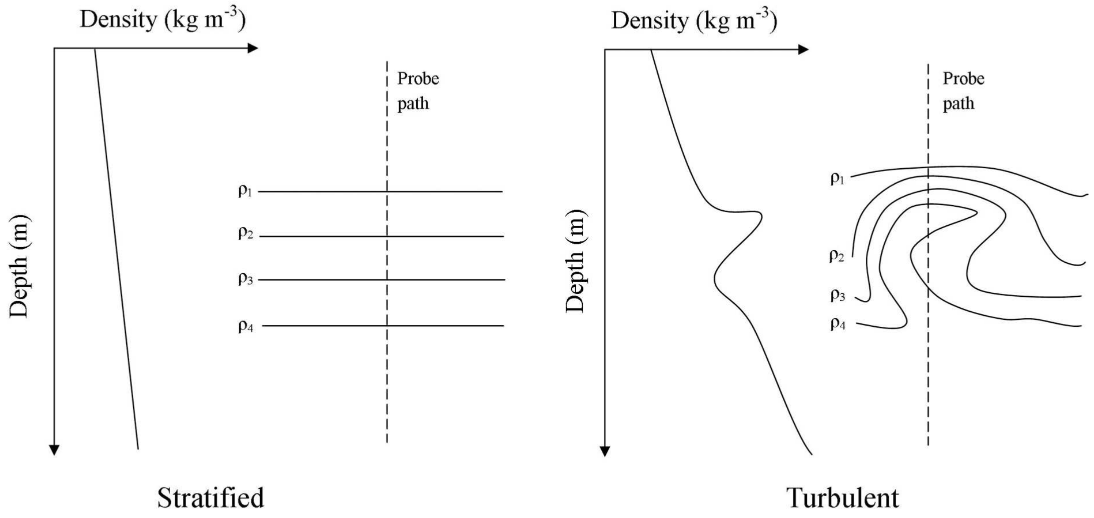

Figure 2.5 Left: a hypothetical density profile of a stratified fluid with a sketch of isopycnals (lines of constant density) showing the density structure of the probed fluid. Right: A hypothetical density profile of a turbulent fluid with a sketch of isopycnals showing the density structure of the probed fluid.

where T is temperature P is pressure, P_0 is a reference pressure at the Earth's surface taken to 1000 hPa, R_d is the gas constant of dry air, and c_p is the specific heat capacity of dry air. In one particular campaign, 10 balloons were flown, each logging temperature and pressure at a vertical resolution of 0.1 m. Calculations of ϵ were made using

$$\epsilon = C_k L_T^2 N^3, \tag{2.7}$$

where L_T is the Thorpe length scale, N is the Brunt-Vaisala frequency and C_k is 1.132 and is the proportionality squared between the Ozmidov and Thorpe length scales, and can vary by an order of magnitude (Clayson and Kantha, 2008). For one of the ascents, an ϵ of order 10^{-2} $\mathrm{m^2s^{-3}}$ was calculated in a shear region of a jet stream. These measurements were made by a small number of specialised balloons. Clayson and Kantha (2008) proposed that this technique could be used on a large dataset of standard high resolution radiosondes. Most operational radiosondes relay data every 1 second at 5 m $\mathrm{s^{-1}}$ equating to a 5 m vertical resolution suitable to perform a Thorpe analysis. It was speculated that large archives of standard radiosonde soundings could be used to generate climatologies of turbulence data. Figure 2.6 shows an extensive radiosonde station network across the globe. This could make the Thorpe analysis ideal for continuous observations of turbulence once a few problems with the method are addressed. The first is the implication of instrumental noise, which needs to be differentiated from actual inversions in the measurements. The second is the need to cross reference these derived measurements with other in-situ or remote sensing methods.

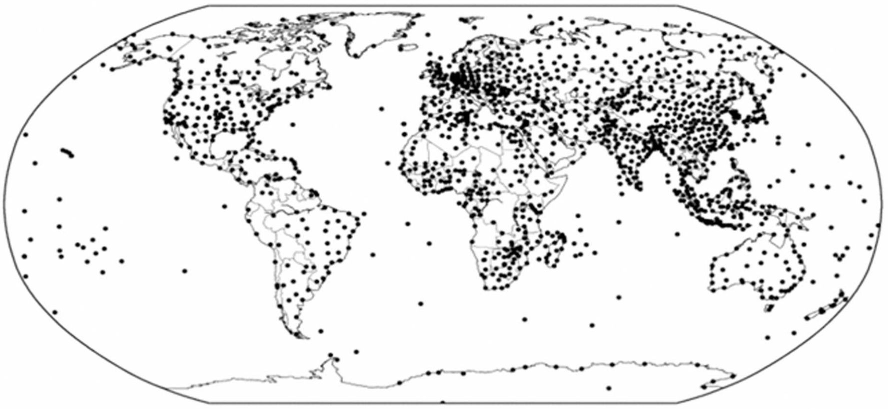

Figure 2.6 A world map showing the position of regular radiosonde stations from `https://www.ncdc.noaa.gov/`.

The first problem was addressed by Wilson et al. (2010) who improved the method by approximating the effect of instrumental noise on the calculation of overturns in the θ profile. Using the new method a Thorpe length scale was only selected if it was statistically significantly different from one generated by instrumental noise. Wilson et al. (2013) then performed another analysis of radiosonde data using a pseudo potential temperature profile accounting for moist and saturated air. A qualitative comparison was performed between a MST radar's[1] aspect sensitivity (see section 4.3.1 for more information) and selected Thorpe lengths. Use of the qualitative measure of aspect sensitivity can be used to infer turbulence and Wilson et al. (2013) has cited sources in which case studies similar to that shown have had turbulence present. Nonetheless it is not a quantitative measurement which is desirable if the Thorpe analysis is to used for turbulence observation.

There are few cases in which the Thorpe method has been compared with other observation techniques. One such case was undertaken by Kantha and Hocking (2011) where radiosondes were launched near a MST wind profiler. ϵ was calculated from the radiosonde's Thorpe lengths and from the MST radar. For a single ascent there was some degree of agreement between the derived profiles of ϵ from both the radar and radiosonde. However when examining all data collected over the campaign it is difficult to draw conclusions as both methods recorded similar values of ϵ, furthermore there is little evidence to show either metric's response to turbulence. Following on, both methods are not mutually independent. The MST radar's ϵ is estimated by

$$\epsilon = \frac{C_m \sigma_t^2}{T_{BV}}, \tag{2.8}$$

where C_m in this case is 3.81 (Kantha and Hocking, 2011), σ_t is the MST radar's spectral width as described in section 4.3.1. T_{BV} is the Brunt-Vaisala period which needs deriving from radiosonde data. ϵ derived from the Thorpe analysis in equation 2.7 also uses the Brunt-Vaisala frequency which is derived from the same data. A better test would have been to compare the Thorpe analysis ϵ with the radar's spectral width. In conclusion the Thorpe analysis shows some promise in its ability to provide a large turbulence dataset from standard radiosonde measurements. However there is little work showing comparisons with other in-situ measurements or remote sensing methods, suggesting the dataset may not be as reliable as measurements made by actual in-situ or remote sensing measurements.

---

[1] Mesospheric, Stratospheric and Tropospheric radar, these radars are capable of making wind and turbulence observations in the troposphere and lower stratosphere

In 2003 an artist by the name of Simon Faithful released a weather balloon with a downward pointing camera called "30 km" [2] . As the balloon soared through the atmosphere it wobbled which inspired Professor R. Giles Harrison to want to quantify the wobble on the radiosonde beneath the balloon. The wobble had been noted almost 50 years before by Anderson (1957) who used descent data for their experiments. Harrison and Hogan (2006) subsequently developed a magnetometer based turbulence device that interfaced with the radiosonde, which can detect its orientation with respect to the Earth's magnetic field. On free balloon flights in regions where turbulence was expected, there was heightened variability from the magnetometer. A small number of radiosondes were flown near a boundary layer Doppler lidar and a relationship between the vertical velocity variance and the magnetometer variance was found. This effectively provided the first verified balloon measurements of turbulence verified using an independent method. The advantages of this method over the Thorpe analysis are that it is a physical measurement of turbulence as opposed to approximating it from standard instrumentation. Further advantages over the work of Anderson (1957) were:

- The motion sensor and radiosonde were on the same measurement platform. Allowing better comparisons of meteorological data on an ascent to ascent basis.
- The variability of the magnetometer also gave a quantitative measurement meaning it was more than just a binary turbulence indicator.

Following the success of that campaign more magnetometers were commissioned for this current project and a further analysis will be under taken in chapter 3.

In concluding this review, it has been shown that reliable turbulence measurements can be made by surface instruments near the ground. However making reliable observations in the free troposphere and above is more difficult. Many research aircraft have made measures of turbulence in terms of ϵ by using specially adapted booms and sensors, which is good for science campaigns requiring turbulence information for particular case studies. Pilot reports are a current method of widespread qualitative observations of turbulence, however there is a degree of subjectiveness regarding these observations. Hence automated turbulence reports using AMDAR could provide both aircraft and pilot independent reports of turbulence. However as aircraft are re-routed around known severe turbulence patches, a bias still occurs. Balloons with the addition of accelerometers were first used to make turbulence observations in the 1950's, unfortunately further

---

[2] This art piece was part of a larger project called "Defying Gravity", where a series of objects were taken to the edge of space on a balloon, including a chair.

experiments using current knowledge of the time were never implemented. Instead work began using the Thorpe analysis to derive turbulence metrics from standard radiosonde data theoretically providing an ϵ, although there is little evidence showing agreement with other turbulence observation techniques. Recently motion sensors flown on-board meteorological radiosondes are able to provide atmospheric turbulence measurements.

2.2 Remote sensing methods to detect turbulence

Remote sensing methods predominantly use the Doppler property of electromagnetic radiation to retrieve information concerning air motion in the atmosphere. Different wavelengths are used to observe different atmospheric targets. Lidars for example operate in the nm wavelength (visible light) and target aerosols in the atmosphere. Cloud radars operate in the mm-cm range using hydrometeors as their targets. Wind profilers operate between 30 cm and 6m wavelengths using the refractive properties of air to deduce atmospheric motion. In this section established remote sensing methods of turbulence detection are described.

2.2.1 Doppler lidar measurements

Doppler lidars started being used in meteorology in the 1970s. Köpp et al. (1984) were one of the first to begin verifying wind measurements made from a Doppler lidar,

Figure 2.7 A pulsed Doppler lidar at the Reading University Atmospheric Observatory.

comparing the results with traditional wind measurements from radiosondes. By the 1990s multiple methods had been described to use continuous wave lidar to measure ϵ. Banakh et al. (1999) showed three methods how to achieve this. The first was using spectral width, which is the half power half width of the Doppler velocity distribution detected by the lidar over a given time period of magnitude 10 ms for example. A spectral width can be used to infer turbulence information. Intense turbulence yields a wider spread of velocities and a wider spectral width as shown in figure 2.8. By combining the spectral width cubed and scaling by a length scale, ϵ could be found. Theoretically the wider the spectral width the more intense the turbulence observed. Caution must be taken as contamination of the spectral width from velocities perpendicular to the beam can occur (O'Connor et al., 2010).

A second proposed method was to use velocity information from a fixed point over 2 minutes to calculate ϵ from structure functions, similar to those shown in section 2.1.2. These showed that by performing an analysis of the lidar's velocity series spectrum turbulence velocity information could indeed be inferred. The third method uses retrievals from a conical scan of velocities combined with further structure functions to generate an ϵ. Due to the nature of each probing technique like for like comparisons could not be made.

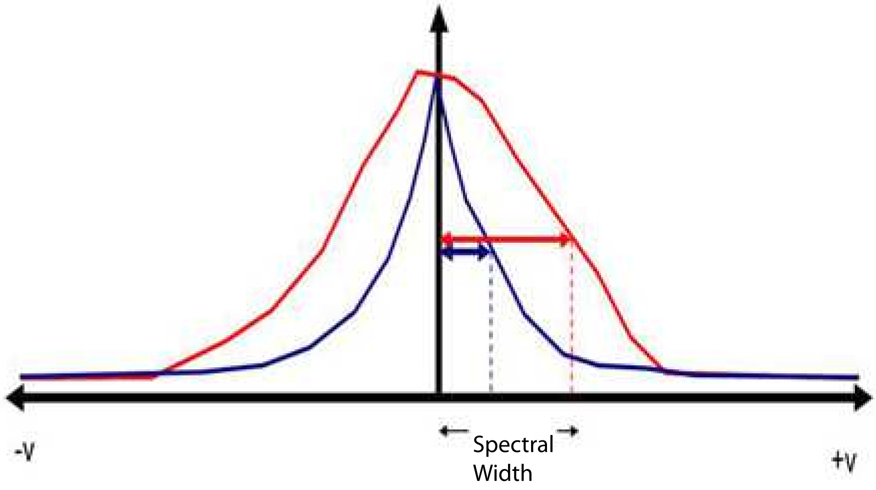

Figure 2.8 A diagram showing the hypothetical spectral widths for both non turbulent (blue) and turbulent (red) air.

O'Connor et al. (2010) proposed a simpler method where the standard deviation of the vertical velocity from a lidar could be used to make turbulence observations. Using Kolomogrov's equation (equation 1.2) and integrating over two wave numbers dictating the smallest and largest eddies observable by the lidar, the standard deviation of the mean velocity could be related to ϵ with two length scales which are a function of the horizontal wind speed. A full derivation is featured in section 4.1. O'Connor et al. (2010) also proposed a scheme for the calculation of the error in such measurements. The method is a derivative of Kolomogrov's theory and was shown that a -5/3 law could be fitted to the velocity spectra providing an alternative calculation of ϵ. A collocated sonic anemometer supported by a tether balloon made observations of ϵ. These were compared with the lidar derived values of ϵ and a good level of agreement was found.

The lidar provides a good estimate of ϵ, but it suffers from being a near visible laser meaning clouds and low visibility severely limit its sampling range. The lidar's vertical range is further limited by the amount of aerosol present, ultimately limiting its use to the boundary layer, due to the high concentrations of aerosol that the beam backscatters off. High spectral resolution lidars (HSRL) are unaffected by this problem and make measurements higher in the atmosphere (Shipley et al., 1983), but are unable to make velocity measurements. This does not negate the HSRL as a turbulence observation device, as in some situations the tropospheric aerosol backscatter can be used as a tracer to see turbulent structures in the atmosphere. The DELICAT project attached a high spectral resolution lidar to an aircraft to make in-flight turbulence measurements by observing aerosol fluctuations ahead of the aircraft (Vrancken et al., 2010). The aim is to introduce a clear-air turbulence avoidance system for aircraft, but the system is still in an experimental stage. In conclusion whilst ground based Doppler lidar provides reliable estimates of ϵ verified with in-situ measurements, it is somewhat limited by its vertical range for mid atmospheric observations of turbulence.

2.2.2 Doppler cloud radar measurements

During the second world war, Robert Watson Watt, one of the forefathers of radar, created a method to detect opposition aircraft approaching the United Kingdom. At the time the radar operators noticed a problem with clouds affecting the detection abilities of the radar system. Radar meteorology came into being on 21st November 1941, when a radar tracked the passage of a thunderstorm off the south-east coast of the UK (Hitschfeld, 1986). Dopplerisation of weather radar occurred in the 1950's allowing radar data to observe atmospheric motions within clouds. Rogers and Tripp (1964) utilised a Doppler cloud radar to make observations of turbulence in a snow cloud. A RMSE of the detected Doppler velocity was calculated to estimate the radial velocity variance. However investigators discuss how there are no comparisons with other in-situ measurements of turbulence. Meischner et al. (2001) calculated the ϵ using a scanning radar's spectral width, care was taken to remove the effects of antenna rotation, velocity spread of hydrometeor fall velocities and wind shear affects. A comparison with an aircraft, discussed in section 2.1.2, was undertaken and in the majority of cases both ϵ from the radar and aircraft showed agreement in thunderstorms, giving confidence in this method.

Bouniol et al. (2004) proposed a method to calculate ϵ from high temporal resolution zenith pointing radar. This method is similar to that of O'Connor et al. (2010) where the standard deviation in the vertical velocity at each point along the radial beam with time is taken. It does not take hydrometeor fall speeds into account and suggests this method may be unsuitable for heavy precipitating clouds. In this experiment no calibration was made against another measurement system so its accuracy cannot be accessed. Shupe et al. (2012) showed that independent measures of ϵ from a mast based sonic anemometer and aircraft data in boundary layer stratocumulus showed good agreement with radar observations of ϵ.

In conclusion cloud radar can be used to probe information about in-cloud turbulence processes. Two methods have been shown, the spectral width method was shown to calculate ϵ using scanning radar in thunderstorms. The second method has only been used in non-precipitable clouds, meaning turbulence in more convective clouds may not be accurately resolved. Despite this the second method has been used to resolve ϵ in the cloudnet data base (Illingworth et al., 2007).

2.2.3 Wind profiler measurements

Wind profilers operate at VHF and UHF radio frequencies using clear air echoes to make observations of wind velocities in the atmosphere. Basic operating principles of how a wind profiler operates will be described before discussing various methods to extract turbulence information from the profiler. The clear air echo is caused by small discontinuities in the refractive index of the atmosphere. The refractive index of the atmosphere is given by (Ottersten, 1969)

$$n = 1 + \frac{0.373e}{T^2} + \frac{77.6 \times 10^{-6}p}{T}, \tag{2.9}$$

Figure 2.9 The 46.6 MHz NERC Mesospheric Stratospheric and Tropospheric Radar at Aberystwyth, West Wales, United Kingdom.

where e is the vapour pressure of water vapour in hPa. Equation 2.9 is sufficient for use in the troposphere and stratosphere, at higher altitudes extra terms are needed to represent electron density within the ionosphere. The two non-unity terms in equation 2.9 refer to the wet and dry terms of the atmosphere. Given that a typical value of $n = 1.000290$ and only differs slightly in the atmosphere, it is often rewritten as

$$N_r = (n - 1) \times 10^6. \tag{2.10}$$

The return power to the radar is related to the vertical gradient of N_r, the larger the vertical gradient of N_r the higher the return power. The wind profilers emit a pulsed signal, the time period of return yields the height window and the Doppler frequency shift of the signal allows the radial velocity along the beam to be calculated. Wind profilers use a minimum of two off-vertical and one vertical beam directions to calculate the 3D wind vector at each height. There are three main wind profiler operating bands, which are summarised in table 2.3.

The 1000 MHz profiler, despite being affected by precipitation has been used as a boundary layer wind profiler (Ecklund et al., 1988). They provide a useful overlap with

Frequency (MHz)	Wavelength (m)	Operating height (km)	Effects of hydrometeors.
50	6	20	None - except very heavy precipitation but clear-air echo wind measurements dominate.
400	0.75	10	Yes - fall speeds of moderate hydrometeors dominate wind measurements.
1000	0.3	3	Yes - all precipitation dominates wind measurements.

Table 2.3 Table showing common operating frequencies of wind profilers, their wavelengths, operating heights and how they are effected by hydrometeors. From data available at `<http://mst.nerc.ac.uk/intro_wind_prof.html>`

the larger 50 MHz wind profilers which only begin sampling the atmosphere from heights of 2 km. They also provide an additional advantage over Doppler lidars which require aerosols to make a retrieval, limiting their use to the boundary layer. A 1000 MHz wind profiler makes clear-air observations up to 3 km. Campistron et al. (2002) used the Doppler spectral width from both vertical and off vertical beams from a boundary layer wind profiler to calculate ϵ. The calculation of ϵ for wind profilers is more complex due to the larger pulse volume sizes than that of cloud radars and lidars. To achieve this equation 1.2 had to be calculated for a volume. White et al. (1999) derived an expression which allowed ϵ to be calculated from the spectral width using a double integral approximation to represent the pulse volume. Campistron et al. (2002) used this approximation and made a good comparison with ϵ calculated from the wind velocities of a co-located aircraft (Lohou et al., 1998). Both methods observed turbulence of the same magnitude however without confidence intervals it is unsure how close they are to a one to one relationship.

The spectral width technique to derive turbulence is essentially similar for all three types of wind profiler. Spectral width derived values of ϵ were made by Sato and Woodman (1982) using a 430 MHz radar, but were not verified by in-situ measurements. Most turbulence measurements made using wind profilers have been made with 50 MHz wind profilers, commonly known as MST radars. The beam width is such that the pulse volume's dimensions are of order 100 m, meaning that ϵ yet again is tricky to calculate. Labitt (1981) attempted to address the volume problem by using a Gaussian hyper confluent geometric function to calculate ϵ, although no in-situ data was available to verify this.

Hocking (1983) derived methods using the spectral width to obtain ϵ from the radars' spectral width. At first, artefacts which may affect beam broadening were highlighted, which have since been mathematically described in Dehghan and Hocking (2011). He then showed that through an integration of equation 1.2 ϵ could be calculated using

$$\epsilon = \frac{3.5\overline{(v_r'^2)}^{3/2}}{\left(L_B^{2/3} - (\lambda/2)^{2/3}\right)^{3/2}}, \tag{2.11}$$

where v_r' is the Reynolds average velocity perturbation, which is equivalent to spectral width. The two length scales shown in the denominator represent the sampling scales of the pulse volume. The smallest eddies the radar can observe are half the radar wavelength λ. The largest eddies were suggested to be that of the buoyancy length scale

$$L_B = \left(\frac{2\pi}{0.62}\right)\epsilon^{1/2}N^{-3/2}, \tag{2.12}$$

given in Weinstock (1978) who proposed that the inertial sub-range could be truncated to have a buoyancy driven range below certain wave numbers. Hocking (1983) then combined equation 2.11 and 2.12 , taking into account that $L_B >> \lambda$ and hence removing λ to give

$$\epsilon = C_m\overline{v_r'^2}N, \tag{2.13}$$

where C_m is a constant which has been listed between 0.4 and 0.5, this equation is of similar form to the equations used in 2.8 where $C_m = 3.81$. A review by Hocking (1999) showed that ϵ could be calculated using the methods shown above or by using

$$\epsilon = C_m\frac{\left(\sigma_v^2\right)^{3/2}}{L_B}, \tag{2.14}$$

where C_m is constant. It was also shown after an analysis of the method shown by Labitt (1981) that the L_B could be interchanged for a length scale which is the largest of the pulse length or width. This in effect gives two methods of calculating ϵ but the crux of the methodologies appears in selecting a suitable C_m and a length scale whether from that of the radar pulse dimensions, or from the buoyancy length scale which is a function of N. Hocking (1999) showed if the effects of buoyancy sub range were taken into account then equation 2.13 should be used. ϵ was calculated from a MST radar using 2.13 and compared with ϵ from a light aircraft in Dehghan et al. (2014). A correlation was found between the two but only over a range of ϵ up to 10^{-3} ($\mathrm{m^2s^{-3}}$), furthermore the errors on both techniques give a high uncertainty. Another analysis (Dehghan et al., 2014) was made using data from commercial aircraft, where no correlation was found, although the aircraft derived ϵ was significantly larger than the radars'. This discrepancy could be due to the value of T_{BV} used, Dehghan et al. (2014) reported both a climatological value T_{BV} or that derived from a nearby radiosonde profile were used. The climatological value would remove any variability, but not accurately represent the thermodynamic state of the atmosphere.

Worthington et al. (1999) showed that by looking at the difference in return power between the vertical beam and an off-vertical beam one may be able to make qualitative observations of turbulence. The difference in power of the two beams is called the aspect sensitivity and is small if looking at regions of the atmosphere that may have been recently mixed by turbulence. Aspect sensitivity is large if stratification is present as Fresnel reflections (Hooper and Thomas, 1995) may reflect off-vertical beams away from the receivers. Wilson et al. (2013) used aspect sensitivity when comparing the Thorpe length analysis to a radar.

In conclusion, MST radars have the vertical range to make turbulence observations using the spectral width, but struggle converting the spectral width into ϵ as there is some reliance in the selection of an appropriate length scale derived from either the Brunt-Vaisala frequency or the radar pulse dimensions. Comparisons with in-situ measurements are inconsistent, indicating that the current underlying theories for the derivation of ϵ from a MST radar need further refinement.

As a final remark for the remote sensing of turbulence, the three main methods shown here can be used to infer some information about atmospheric turbulence. The Doppler lidar is well placed making good observations of turbulence, confirmed by in-situ measurements. The narrow beam of the lidar which uses atmospheric aerosol in suspension as its target minimises contamination to derived ϵ. Its main limitations are its height range. Turbulence within clouds can be observed by radars, scanning radars were shown making coherent observations of turbulence if allowances were made for hydrometeor fall speeds and shearing. The zenith method suffers as the drop size and fall speed are not taken into account. Finally wind profilers have been shown to make observations of turbulence with their spectral width, which for high frequency wind profilers can be turned into an ϵ. For the low frequency wind profilers the relationship between the spectral width and ϵ involves using the Brunt-Vaisala frequency, not making it a strictly independent turbulence metric. Comparisons with in-situ measurements highlight how this method may be insufficient for calculating ϵ. In the next section turbulence diagnostics, which have been developed using some of the aforementioned turbulence observation methods will be discussed.

2.3 Turbulence diagnostics

In weather forecasting, turbulence diagnostics are calculated using the output of a numerical weather prediction model. Turbulence diagnostics are metrics calculated which have shown to be indicative of turbulence that can affect aircraft. In this section the history of these diagnostics will be discussed and a list compiled of common diagnostics currently used to predict turbulence. Whilst appendices of turbulence diagnostics have already been published (Sharman et al. (2006), Williams and Joshi (2013) and Reap (1996)) this section will include a brief discussion of how these have come into being.

Reynolds (1883) first pondered if a criterion could be derived to calculate under which conditions a fluid was likely to succumb to turbulent flow. Initially he concluded that the density, viscosity and velocity of the fluid played a vital role in producing turbulence. Over a decade later Reynolds (1894) defined a dimensionless number, known as the Reynolds number

$$Re = \frac{\rho U L}{\mu}, \tag{2.15}$$

where L is the length scale of the fluid channel or tube and μ is the kinematic viscosity, where ρ is the density of the fluid and U represent the velocity of the fluid. This was one of the first examples of a turbulence diagnostic for a fluid. From experiments with water at room temperature in glass tubes Reynolds (1894) suggested a Re of 2000 could cause turbulence in the water.

2.3.1 The Richardson number

As knowledge of the atmosphere increased over the decades Richardson (1920) derived a relationship between the thermal stability of the atmosphere and the vertical wind shear. It was proposed that if the vertical wind shear with height squared was greater than the static stability, then turbulence would form, hence

$$Ri = \frac{\frac{g}{T}\frac{\partial \theta}{\partial z}}{\left(\frac{\partial u}{\partial z}\right)^2 + \left(\frac{\partial v}{\partial z}\right)^2}, \tag{2.16}$$

would imply the presence of turbulence if less than one. Where the numerator is the static stability term and is equivalent to the Brunt-Vaisala frequency N^2. The denominator is the vertical wind shear term. Often associated with turbulence are Kelvin Helmholtz waves. They occur at a critical point just before turbulence forms, a critical number of 0.25 was introduced as more work on the subject evolved (Miles, 1961). The Richardson number has been used in multiple field campaigns to infer turbulence from radiosonde measurements (Anderson (1957) , Clayson and Kantha (2008) , Wilson et al. (2011) etc.). Kronebach (1964) wrote one of the first CAT prediction systems which automatically calculated the Richardson number from radiosonde soundings. A contour map for each height level was produced and values of $Ri < 1$ were considered turbulent for the next 12 hours. A comparison with pilot reports from the US military were used to evaluate the performance, 49% of the turbulence reported during the verification period was found to be associated with Ri <1. Reiter et al. (1967) discovered that the length scales over which the Ri was calculated could affect the critical values of Ri. In short many have researched the usefulness of the Richardson number as a turbulence predictor, which has been shown to give low values when mesoscale phenomena, associated with turbulence are sampled (Endlich, 1964). The Richardson number is calculated using the numerical output of numerical weather prediction models allowing the calculation of a turbulence forecast.

The Richardson number has been used to form a basis for other turbulence diagnostics. The Colson Panofsky index

$$CP = \Delta z^2 U_z^2 \left(1 - \frac{Ri}{0.25}\right), \tag{2.17}$$

where Δz is the vertical grid spacing (Colson and Panofsky, 1965) and U_z is the magnitude of horizontal wind shear variation with height, given by

$$U_z = \sqrt{\left(\frac{\partial u}{\partial z}\right)^2 + \left(\frac{\partial v}{\partial z}\right)^2}. \tag{2.18}$$

The Colson Panofsky index was derived from examining the energy and length scales required to produce turbulence that could affect aircraft. The index was successful in forecasting aircraft encounters with turbulence over North America. Knox (1997) discussed using a turbulence diagnostic which included the relative vorticity, Coriolis parameter and Richardson number

$$KX1 = f\left(f\left(1 - \frac{1}{Ri}\right) + \xi\right). \tag{2.19}$$

Where f is the Coriolis parameter and ξ is the relative vorticity given by

$$\xi = \frac{\partial v}{\partial x} - \frac{\partial u}{\partial y}. \tag{2.20}$$

This was shown to provide a criterion for turbulence within anti-cyclonic flows, typically associated with ridges of high pressure between adjacent low pressure systems. Kaplan et al. (2006) used both equation 2.19 and another Richardson number based metric called the North Carolina State University version 1(NCSU1)

$$NCSU1 = \frac{|\nabla \xi|}{|Ri|} \left(u\frac{\partial u}{\partial x} + v\frac{\partial v}{\partial y} \right). \tag{2.21}$$

The turbulence diagnostic was constructed after examining meteorological conditions leading to cases of severe turbulence. The reasoning was to form a turbulence diagnostic which combined advection of the wind velocity along the curvature of the jet stream, which had been associated with turbulence, combined with the Richardson number, an already existing indicator of turbulence. Brown (1973) discussed how the rate of change in the logarithm of the Ri was used with poor effect to predict turbulence. It was summarised that the poor performance of this turbulence diagnostic was caused by the method of calculation. To derive the rate of change of $\log(Ri)$ the wind direction needed recalculating in terms of the geostrophic wind axis. Brown (1973) recalculated the Richardson number tendency as

$$\Phi = \left(0.3\zeta^2 + D_s^2 + D_T^2\right)^{1/2}, \tag{2.22}$$

where Φ is the Richardson number tendency and is known as the Brown index. ζ is the absolute vorticity $(f + \xi)$, $D_s = \partial u/\partial y + \partial v/\partial x$ is the shearing deformation and $D_T = \partial u/\partial x - \partial v/\partial y$ is the stretching deformation. Deformation is a property of the horizontal flow of a fluid and describes how the change in a velocity field of a fluid can cause the sharpening of other properties in the fluid such as the temperature gradient. It is an important factor within the life cycle of extra tropical cyclones. A second turbulent diagnostic

$$\epsilon_{Brown} = \Phi \frac{\frac{\Delta U}{\Delta z}}{24}, \tag{2.23}$$

was also derived in Brown (1973). It was successfully tested against observations of turbulence made by pilots.

2.3.2 Deformation based turbulence diagnostics

The previous section showed how turbulence could be predicted using metrics based on the deformation of the horizontal flow. Ellrod and Knapp (1992) began examining both fields of the shearing and stretching deformation for their suitability as a turbulent predictor. It was found that the predicted areas contained both large negative and positive values which over predicted turbulence. The two deformation terms were combined and the magnitude of the deformation was used . It was also observed that moderate turbulence events occurred in regions of high vertical wind shear, which was combined to yield the Ellrod T1 index:

$$ET1 = \frac{\Delta U}{\Delta z}\sqrt{D_s^2 + D_T^2}. \tag{2.24}$$

As well as deformation occurring around the exits and entrances of jet streams and along fronts, convergence also causes turbulence. Convergence occurs where air is forced either upwards or downwards due to incompressibility causing turbulence. Hence Ellrod and Knapp (1992) employed a second diagnostic

$$ET2 = \frac{\Delta U}{\Delta z}\left(\sqrt{D_s^2 + D_T^2} - \nabla_H\right) \tag{2.25}$$

where ∇_H is the convergence term. The diagnostics were verified against pilot reports and found to predict 71% of turbulence cases. The convergence term is sometimes referred to as the divergence term, and has been used as a turbulence diagnostics by Sharman et al. (2006) and Williams and Joshi (2013). It is given by

$$\nabla_H = \left(\frac{\partial u}{\partial x} + \frac{\partial v}{\partial y}\right). \tag{2.26}$$

Reap (1996) used three years of pilot reports and compared them against many dynamical meteorological outputs. Results showed the top performing diagnostic to be

$$UDEF = U|DEF|, \tag{2.27}$$

Where $DEF = \sqrt{D_s^2 + D_T^2}$. Amongst others which are discussed further in 2.3.4

$$TDEF = \frac{dT}{dz}|DEF| \tag{2.28}$$

was found to be another good predictor of turbulence. Deformation plays a vital role in frontogenesis and Koch et al. (2005) showed that turbulence and gravity waves were detected in an upper level front. Sharman et al. (2006) included the frontogenesis function in a suite of turbulence diagnostics where the frontogenesis function was given by

$$F = \frac{D|\nabla\theta|}{Dt}. \tag{2.29}$$

This was calculated on each θ level within the model and an alternative provided for calculation upon pressure surface levels.

2.3.3 Vorticity based diagnostics

In the previous section the turbulence diagnostics discussed have examined deformation of a horizontal flow. Vorticity is an important quantity connected to synoptic scale meteorology and hence can also be used as a turbulence diagnostic. ξ, the relative vorticity has already been used in previous discussed turbulence diagnostics (see equation 2.21 for example). It is useful for providing information about the curvature of a jet stream. Sharman et al. (2006) suggests using the magnitude of Potential Vorticity (PV) and the horizontal gradient of PV . There have been a couple of case studies by Knox (2001) and Shapiro (1978) however the findings were limited to a handful of case studies where turbulence was observed with changes of PV. Sharman et al. (2006) also proposed that negative vorticity advection was a turbulence diagnostic used widely by aviation, however there was no evidence to back this up.

2.3.4 Miscellaneous diagnostics

Reap (1996) showed lapse rates, wind speeds and their derivatives performed favourably within their analysis. It is easy to see why, for example, the lapse rate has always been used as a measure of stability in meteorological text books such as Ambaum (2010) and Wallace and Hobbs (2006). The horizontal gradient of the temperature field can also be used Audrey et al. (2011). The jet stream is one of the major causes of turbulence, hence having the magnitude of the horizontal wind and its vertical shear could be used as a basic diagnostic for identifying turbulence. Further to this Williams and Joshi (2013) used the directional wind shear with height times the horizontal wind velocity. Vogel and Sampson (1996) undertook a study comparing the Ellrod T1 (equation 2.24) index with

$$CCAT = \frac{g}{T}\frac{\xi + f}{f}\left(U \cdot \nabla\frac{dT}{dz}\right) \tag{2.30}$$

However it was found that the Ellrod T1 index out performed it for the data collected. The Ellrod T1 was also suggested for being computationally simpler to calculate. Dutton (1980) analysed 11 different meteorological quantities from a NWP model. A multiple linear regression analysis was used to yield a set of quantities which best predicted turbulence reported by pilots. The most effective combination of diagnostics is given by,

$$DUT = 1.25U_H + 0.25\left(\frac{dU}{dz}\right)^2 + 10.5. \tag{2.31}$$

Where U_H was given in Dutton (1980) as

$$U_H = \frac{1}{U^2}\left(uv\frac{\partial u}{\partial x} - u^2\frac{\partial u}{\partial y} + v^2\frac{\partial v}{\partial x} - uv\frac{\partial u}{\partial y}\right). \tag{2.32}$$

2.3.5 Non empirical turbulence diagnostics

The reason for using empirical turbulence diagnostics was that turbulence cannot be explicitly resolved at grid scales used by operational weather forecasts. In this section diagnostics which are based on a theory of wave breaking are discussed as well as turbulence diagnostics which calculate a metric in terms of ϵ.

Marroquin (1998) computed ϵ using

$$\epsilon_M = K_m\left(\frac{b_1}{b_3}\sqrt{\frac{\partial u}{\partial z}^2 + \frac{\partial v}{\partial z}^2} - \frac{b_2}{b_3}\frac{N^2}{Pr}\right), \tag{2.33}$$

where K_m is the kinematic diffusivity constant, $b_{1..3}$ are constants given in Marroquin (1998) and Sharman et al. (2006). N is the Brunt-Vaisala frequency and Pr is the Prandtl number, which is the ratio of heat diffusion and viscous diffusion. The principle behind this diagnostic was to use TKE - ϵ closure theory often used in boundary layer meteorology. Frehlich and Sharman (2004) demonstrated a method of using 2nd order structure functions to estimate a value of ϵ using

$$\epsilon_D^{2/3} = \frac{3}{10}\frac{D_m}{D_{cor}D_{ref}}. \tag{2.34}$$

Where D_m is a structure function similar to equation 2.1. Instead a displacement vector across a model level is taken. D_{cor} is a correction factor and D_{ref} is the reference structure function of an idealised atmosphere. It was compared against pilot reports and it was shown that this diagnostic marginally out performed the Ellrod T1 turbulence diagnostic. Kopeć et al. (2011) developed a method to forecast clear-air turbulence by examining conditions where shallow convection associated with small cumulus clouds could cause gravity wave generation above the convection. Turbulence was predicted to occur in regions of wave breaking, where the wave breaking was defined by a critical value, such as when the background flow was 0 Holton (2004). A case study was shown from a radiosonde ascent however a comparison with aircraft data has yet to be made.

The final turbulence diagnostic to be discussed, was that developed by Knox et al. (2008). This turbulence diagnostic is based on Lighthill Ford theory. In summary it describes how a rotating shallow flow produces gravity waves due to spontaneous imbalance. Breaking gravity waves were shown in the previous section to be a cause of turbulence. Knox et al. (2008) proposed that it was unlikely that an entire gravity wave could be turbulent. So stated that turbulence could only be produced due to buoyancy or wind shear regions of a gravity wave. Hence an estimate of ϵ was given by

$$\epsilon_{SI} = \max\left(K_h\left(\hat{a}-1\right)N^2, K_m\left(\frac{\partial U}{\partial z}\right)^2\left(1+\hat{a}\sqrt{Ri}\right)^2\right), \tag{2.35}$$

where K_h is the eddy thermal diffusivity and

$$\hat{a} = \frac{N a_w}{|V_w - c_s|}, \tag{2.36}$$

is the non-dimensional wave amplitude. Here a_w is the actual wave amplitude and V_w and c_s are the Doppler adjusted wind velocity and phase shift respectively. However it is impossible to know the amplitude of every wave so a mean is taken of equation 23 of Knox et al. (2008) which represents the leading and second order Lighthill Ford radiation term. The authors stated some initial calibration was required against turbulence reports to provide a constant of proportionality. The performance of the turbulent diagnostic was compared against the Graphical Turbulence Guidance Sharman et al. (2006) system, a leading turbulence forecast system of the time, to find it significantly exceeded it in performance. McCann et al. (2012) used the same core equations as Knox et al. (2008) but modified the diagnostic to include turbulence generation from wind shear and stability. It was found to have a higher forecast skill than the original Lighthill Ford turbulence diagnostic and the second generation version of the GTG. Knox et al. (2008) also performed a scale analysis of the Lighthill Ford equations and the leading term was proportional to relative vorticity advection,

$$RVA = U \cdot \nabla \xi. \tag{2.37}$$

Hence relative vorticity advection can also be used as a proxy to identify regions of turbulence due to spontaneous imbalance as in Williams and Joshi (2013) .

Diagnostic	Symbol	Underlying theory	Units
Richardson number	Ri	Richardson number	
Colson Panofsky index	CP	Richardson number	knots^2
Knox 1997 index	$KX1$	Richardson number and vorticity	s^{-2}
Relative vorticity	ξ	vorticity	s^{-2}
North Carolina State University index 1	$NCSU1$	Richardson number and vorticity	s^{-3}
Brown index	Φ	Deformation and vorticity	s $^{-1}$
Brown eddy dissipation rate	ϵ_{Brown}	Deformation, vorticity wind shear	m^{2}s^{-3}
Ellrod's turbulence index 1	$ET1$	Deformation and wind shear	s^{-2}
Ellrod's turbulence index 2	$ET2$	Deformation, wind shear and convergence	s^{-2}
Horizontal divergence	∇_H	Divergence	s^{-1}
Deformation	DEF	Deformation	s-1
U	U	Wind speed	m s^{-1}
U × Deformation	$UDEF$	Deformation and wind speed	m s^{-2}
Thermal gradient × Deformation	$TDEF$	Deformation and thermal gradient	K m^{-1}s^{-1}
Frontogenesis function	F	Deformation	m^2 s^{-3} K^{-2}'
Potential vorticity	PV	Vorticity	m^{2}s^{-1}K kg^{-1}
Negative absolute vorticity advection	$NAVA$	Vorticity	s^{-2}
Vertical wind shear	U_z	Wind shear	s^{-1}
Horizontal temperature gradient	$\nabla_H T$	Temperature gradient	K m^{-1}
$U\times$ directional wind shear	$U\phi_z$	Wind shear	rad s^{-1}
CCAT	$CCAT$	Temperature gradient and vorticity	s^{-3}
Dutton empirical index	DUT	Wind shear gradients	s^{-2}
Marroquin eddy dissipation rate	ϵ_M	TKE-ϵ closure theory	m^{2}s^{-3}
Sharman eddy dissipation rate	ϵ_D	Turbulence structure functions	m^{2}s^{-3}
Eddy dissipation rate from spontaneous imbalance	ϵ_{SI}	Lighthill Ford theory of spontaneous imbalance	m^{2}s^{-3}
Relative vorticity advection	RVA	vorticity	s^{-2}

Table 2.4 A table summarising the turbulence diagnostics discussed with their corresponding symbol, underlying dynamical properties and units.

In this section it has been shown how a wide range of turbulence diagnostics can be used to detect turbulence from basic rules of thumb to those based on common properties of the atmosphere, which act as proxies for turbulence forecasting. Some turbulent diagnostics are able to determine if the atmosphere is theoretically likely to produce turbulence from suitable dynamic theory. The turbulence diagnostics discussed have been summarised in table 2.4. The next section will look at how a turbulence forecast is implemented.

2.4 Turbulence forecast systems

There are two main providers of global turbulence forecasts, the UK Met Office and the National Oceanic and Atmospheric Administration NOAA in Washington known as World Area Forecast Centres (WAFC). Between them they are charged with the production of aviation forecasts of icing, turbulence and other hazards. The WAFC produces both an automated gridded forecast and a SIGWX chart (Gill, 2014). A SIGWX chart is a weather chart showing regions of turbulence, jet streams, volumes of substantial cloud that could cause icing as well as ash hazards from volcanoes.

Figure 2.10 shows a SIGWX chart over northern Europe, jet streams are marked by black arrows with quivers showing the position and intensity of jet streams. Regions of clear air turbulence are contoured in black dashed lines and are numbered. The numbers

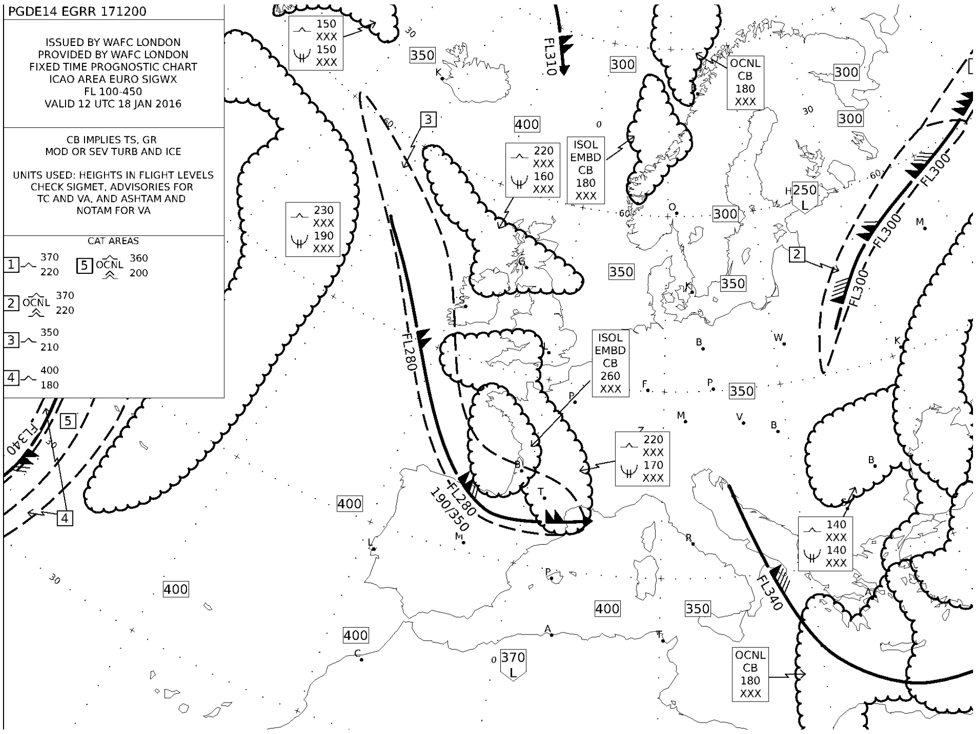

Figure 2.10 A SIGWX chart for Europe for 12 UTC on January 18th 2016. Retrieved from `www.aviationwxchartsarchive.com`.

correspond to a legend on the left providing more information about the vertical extent of the turbulence and its magnitude. A single hat stands for moderate turbulence whilst a double hat signifies severe turbulence. Regions of cloud that may give rise to turbulence and icing are surrounded by curly lines. Alternatively an automated forecast is generated which produces a gridded data set for different flight levels. Both turbulence forecasts are created from the Ellrod T1 turbulence index.

Figure 2.11 is an example of the automated turbulence forecast using the Ellrod T1 turbulence diagnostic. However the skill of a turbulence forecast using just one turbulence diagnostic has limitations. The Ellrod T1 index has shown a high skill level but is only good in conditions where turbulence is being caused by deformation. Sharman et al. (1999) first began to combine different turbulence diagnostics together. The system was fully described in Sharman et al. (2006) where multiple turbulence diagnostics were generated from the same forecast data and used to produce an estimate of turbulence severity. There were, however two problems that needed to be overcome. The first being that each turbulence diagnostic had different units, so needed rescaling on to a common scale. This was achieved by using a database of PIREP-turbulence diagnostic pairs to calculate turbulence diagnostic thresholds for each turbulence severity in table 2.1. Secondly each turbulence diagnostic is slightly different hence some may produce a more favourable

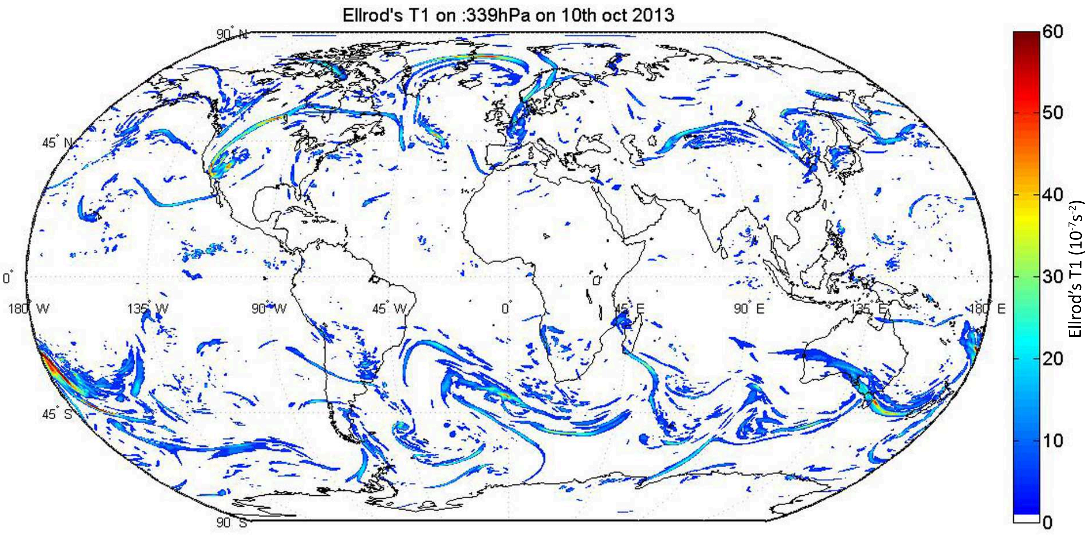

Figure 2.11 The Ellrod T1 index calculated from the ECMWF deterministic model on the 339 hPa pressure, equivalent to the 25000 ft flight level, for 11UTC on 10th October 2013.

forecast skill than others under different conditions. To achieve this a rapid update cycle was used, in which live PIREP reports were used to assess which turbulence diagnostics were performing best under the current conditions. The skill of each diagnostic in this short time period was used to provide weighting to allow a turbulence forecast to be made. This forecast system named Graphical Turbulence Guidance (GTG) was demonstrated to provide a better skill than using individual turbulence diagnostics (Sharman et al., 2006). Whilst not the first attempt to use multiple turbulence diagnostics (Reap, 1996) (Kaplan et al., 2006), it was the first combining the strength of many. In its first incarnation the only turbulence diagnostic which superseded it was that of Knox et al. (2008). The GTG system was operationally shown to produce accurate turbulence forecasts over the United States. Other work has demonstrated its ability to forecast turbulence over East-Asia (Kim et al., 2011). Gill and Buchanan (2014) in separate work using observations of DEVG have used multiple diagnostics to make predictions of turbulence, with the inclusion of convective parametrisations handling turbulence caused by convection.

2.5 Conclusions

In this chapter many different ways of detecting turbulence have been examined. Despite many methods to accurately calculate ϵ the main source of turbulence observations are still the qualitative PIREPs, followed by AMDAR aircraft data. Remote sensing observations of turbulence are seldom used to evaluate the turbulence diagnostics, this is probably due to the precision of the results obtained. The humble radiosonde has been explored as a method to make observations of turbulence. The Thorpe method may enable standard radiosondes to make proxy observations of turbulence, however the best results are obtained when adding a motion sensor. The advantage a motion sensing balloon has above all other methods is that it takes a complete vertical meteorological profile of the atmosphere, which is combined with corresponding turbulence information at the same location. A wide range of turbulence diagnostics have been discussed, it is apparent that better turbulence forecasts are produced using a combination of turbulence diagnostics. Alternatively diagnostics based on Lighthill Ford radiation of gravity waves have shown to provide just as skilled turbulence diagnostics.

Chapter 3

Developing a method to observe atmospheric turbulence with a radiosonde

In this chapter a method to use a radiosonde to make observations of atmospheric turbulence will be discussed. Examined first will be the physics of how the dynamical system that is the radiosonde and balloon reacts to turbulence. Two approaches will be discussed to determine the motion of the radiosonde, namely using a magnetometer or an accelerometer. Data from experimental tests and flights will show that the accelerometer gives a superior method of detecting the motion of a radiosonde. Finally an in-depth examination of the physics of a radiosonde is carried out using a mathematical model.

3.1 The physics of a weather balloon

Let us take a spherical helium balloon with radius r and suspend beneath it a radiosonde with mass m on a string of length l (Figure 3.1). It can be seen that this represents a pendulum system as a mass hanging under gravity is allowed to swing from a pivot. The balloon ascends through the atmosphere and its path is perturbed by wind shears and turbulence. Hence the pivot is not fixed, and the balloon and radiosonde can be thought of as a pendulum with a moving pivot. In the troposphere the radius of the balloon increases from 0.6 to 1.5 m, which equates to a cross-sectional area of 1.12 - 3.14 m^2. When compared to the cross-sectional area of the radiosonde of 7×10^{-3} m^2, it can be concluded the dynamic system is driven by the atmosphere's interaction with

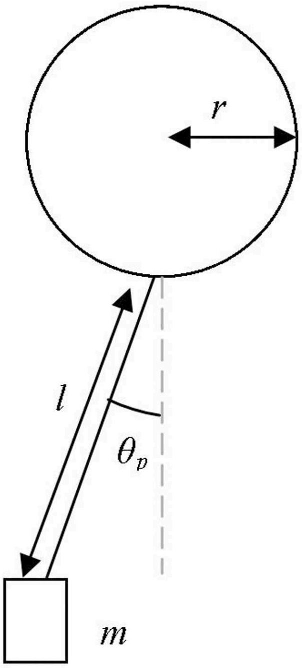

Figure 3.1 A schematic of the motion of a radiosonde beneath a balloon.

the balloon. This implies that one can learn about the atmospheric motion the balloon experiences by studying the motion of the radiosonde package. In this chapter, two methods will be explored to measure the motion of the radiosonde using a magnetometer and an accelerometer. However before embarking on an explanation of each sensing method, some brief attention will be given to how the sensors are integrated with the radiosonde.

3.2 The RS92 Radiosonde and the Programmable Analogue aNd Digital Operational Radiosonde Accessory

To date, radiosondes have been configured in the manufacturing stage to relay standard meteorological data back to the ground station. Few allow for the addition of extra sensors, despite the widespread use of ozone sensors. Therefore it is not a straight forward task to simply add additional sensors. Weber and Few (1978) replaced a radiosonde's existing humidity sensor with a novel instrument. Harrison (2005) and Harrison et al. (2012) developed a device which provides an interface to facilitate connection of additional sensors to a radiosonde. As well as providing a data connection, it provides a variety of supply voltages to power additional sensors from the radiosonde's battery. On board there is a micro-controller which can read analogue voltage outputs from sensors through analogue to digital converters or accept serial data from sensors in a digital format. The programmable micro-controller can be configured to select data channels to read from and perform simple statistical operations in its limited 1 kB memory. It can be programmed to format data, for example providing a flag to a particular line of data, before outputting up to four 16 bit channels to the radiosonde for transmission to the ground station. The data is relayed over the radiosonde's data link alongside the standard meteorological data without affecting it. Given the listed abilities of the system, the name Programmable Analogue aNd Digital Operational Radiosonde Accessory (PANDORA) is used. It is placed in a plastic housing and attached to the side of a radiosonde as shown in figure 3.2.

For this project, the Vaisala RS92 Radiosonde has been used, because it is Vaisala's current market radiosonde and is used globally by meteorological institutes. It has an aneroid pressure sensor and a capacitive thermometer. There are two heated capacitive humidity sensors, which are cycled every 30 seconds to allow the heating of one sensor, whilst measurements are taken from the other. GPS is used to calculate the horizontal wind components (Vaisala, 2013). Each measured quantity is relayed every second to the ground station, giving an approximate vertical resolution of 5m, assuming an ascent rate of 5 m s^{-1}. There is a socket which provides an interface allowing the connection of an ozone sensor. This socket is called the OIF92 port and is where the PANDORA system interfaces to the RS92 radiosonde. Through this connection, power is provided to the PANDORA system and sensor data is transferred to the sonde. However there is

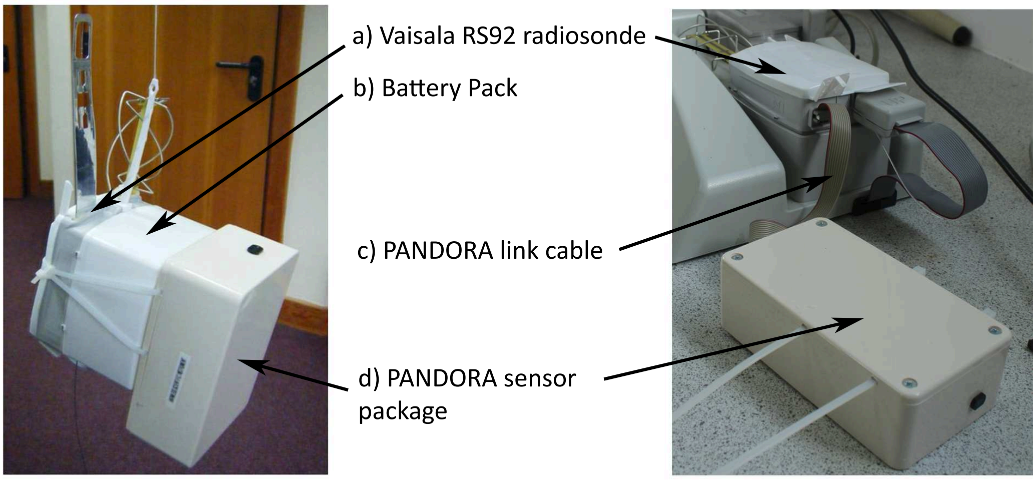

Figure 3.2 Left: PANDORA system attached to Vaisala RS92 radiosonde ready for flight. Right: PANDORA system attached to radiosonde on ground check station. The Radiosonde and the PANDORA system are labelled in the diagram.

only enough bandwidth in the RS92 radio link to transfer 64 bits of data each second, corresponding to four channels of data at 16 bit resolution. More data channels using a lower digital resolution can also be used, for example five 12 bit channels. After the ascent is completed, three files are extracted from the sounding system. The ”FRAWPTU.tsv” file contains the raw pressure, temperature and relative humidity data. The ”EDT.txt” file contains processed meteorological data including wind speed and GPS location. The ”SPECSENS.txt” file contains the four channels of time-stamped data from the PANDORA system.

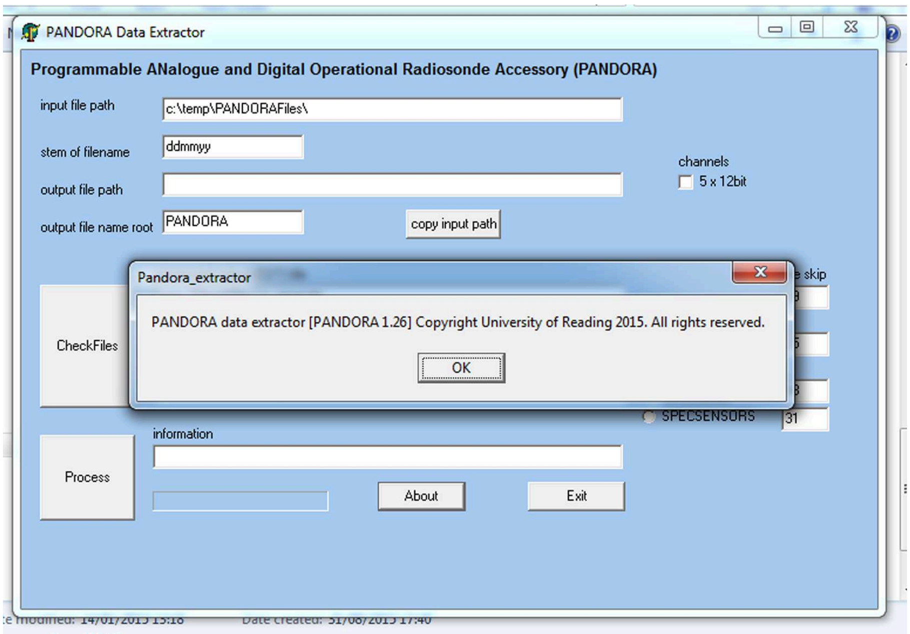
PANDORA Data Extractor

Programmable ANalogue and Digital Operational Radiosonde Accessory (PANDORA)

input file path: c:\temp\PANDORAFiles\

stem of filename: ddmmyy

output file path:

output file name root: PANDORA

channels ☐ 5 x 12bit

Pandora_extractor

PANDORA data extractor [PANDORA 1.26] Copyright University of Reading 2015. All rights reserved.

○ SPECSENSORS 31

information

Figure 3.3 A screen shot of the PANDORA extractor graphics user interface.

An additional piece of software called the PANDORA extractor (figure 3.3) is used to combine the files, which simply uses the time-stamps to interpolate the meteorological data from the FRAWPTU and EDT files onto the additional sensor values from the SPECSENS file. Hence up to four channels of additional sensor values and their corresponding heights and standard meteorological information are available for analysis.

3.3 Measuring the motion of a radiosonde with a magnetometer

A magnetometer is a device which responds to being placed within a magnetic field. A simple magnetometer has a transducer which provides an output proportional to the magnetic field. A variety of magnetometers are available, which are used to infer information about the vector components of a magnetic field. The Earth's magnetic field is a useful reference utilised by navigators for centuries as it can be assumed fixed on long time-scales. Harrison and Hogan (2006) attached magnetometers that detected the vector components of the Earth's magnetic field to a radiosonde. The magnetic field vectors then act as a proxy for the angle of the radiosonde's orientation. It was demonstrated that, as the radiosonde and balloon encountered turbulence, the magnetometer voltage output showed increased variability, as more intense turbulence induced larger swings in the radiosonde. Harrison et al. (2009) flew approximately 10 radiosondes with magnetometers and compared their variance with the vertical velocity variance determined from a boundary layer Doppler lidar. Given the success of this campaign, further magnetometer sensors were constructed initially for this project, of which approximately 30 magnetometer sensors were launched. Figure 3.4 shows the Hall effect magnetometer sensor board connected to PANDORA system within the sensor package housing. This section describes an investigation of the suitability of the method.

3.3.1 Data from preliminary flights

The first flights of this campaign were made on 27th October 2012 from Durlston Head, Dorset, UK (50.58^{o}N, 1.95^{o}W). The magnetometer radiosonde was suspended be-

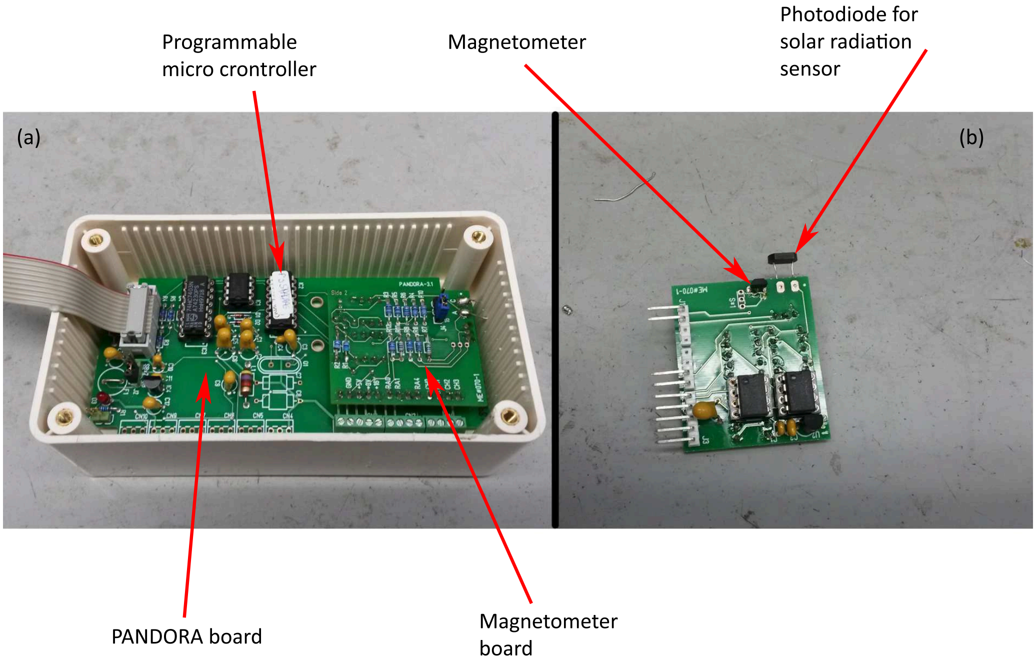

Figure 3.4 a) A picture showing the magnetometer board attached to the PANDORA board within the sensor housing. b) A picture of the underside of the magnetometer board, showing both the magnetometer and photodiode used for solar radiation observations described in section 3.6.

neath the balloon on the full 32 m string length. In Harrison et al. (2009) a magnetometer orientated in the vertical was found to show largest sensitivity to the swinging of the radiosonde. For these flights only a vertical orientated magnetometer is used. The magnetometer outputs a voltage proportional to its orientation, thus to infer if the balloon is in turbulence the variations of the voltage need examining. To calculate the variability in the magnetometer, σ_{mag}, the standard deviation was taken of the magnetometer voltage over an eight second moving window. A eight second window was used by Harrison et al. (2009) as this was the period over which a burst of 4Hz magnetometer measurements were collected before transmission. A continuation of the same sampling window was desired to provide some comparability with previous work. It is also short enough to provide a good vertical resolution of 50 m, yet large enough to provide enough samples to deduce the standard deviation accurately.

Figure 3.5 shows vertical profiles of standard meteorological quantities of temperature

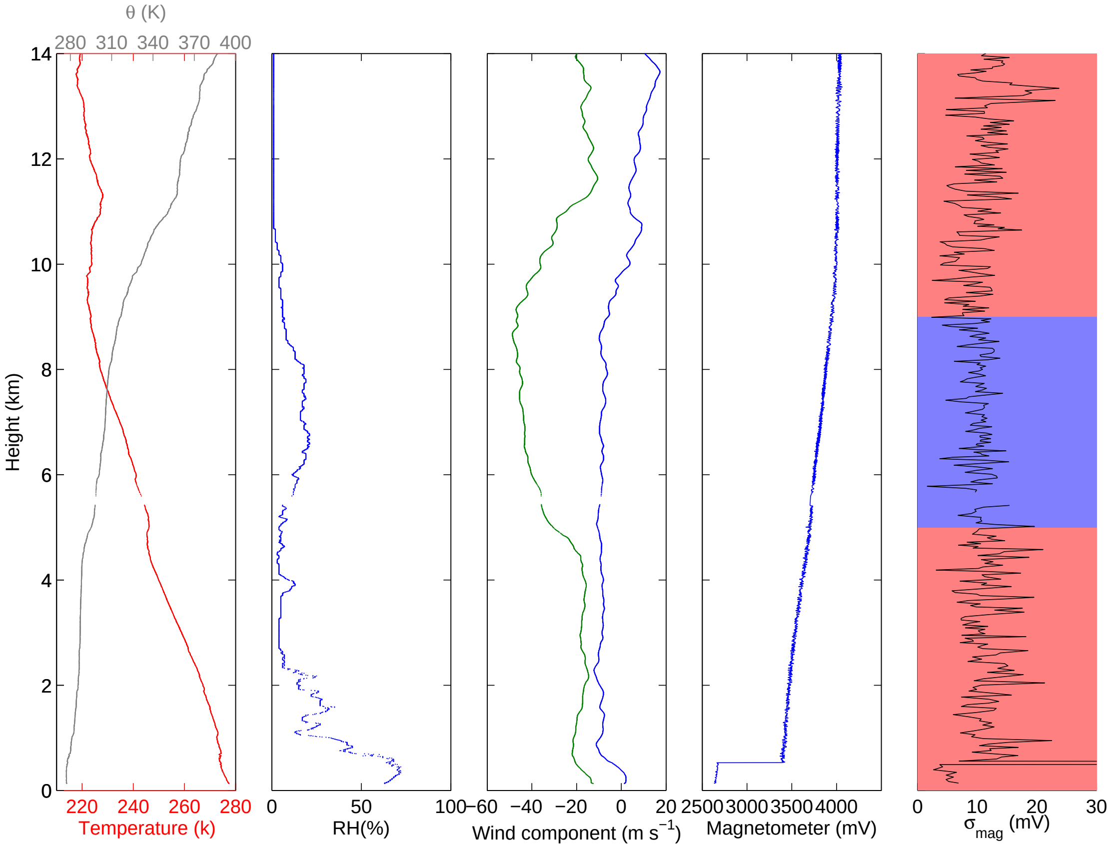

Figure 3.5 Vertical profiles of a) temperature and potential temperature θ (K) in red and grey respectively, b) relative humidity (%), c) u and v wind components (m s^{-1}) in blue and green respectively, d) magnetometer Voltage (mV) and e) the standard deviation of magnetometer voltage (mV) over 8 seconds, from an ascent made from Durlston Head at 11UTC on 27th October 2012. The shading in panel (e) is to highlight the jet (blue) and none jet (red) region of the atmosphere.

(T), relative humidity (RH), and the zonal (u) and meridional (v) wind components. Vertical profiles of raw magnetometer voltage and σ_{mag} are also shown. The prominent feature in the σ_{mag} profile is the 800 mV jump in magnetometer voltage at a height of approximately 500 m. One likely source of this jump is the radiosonde transmitter switching to "high power" mode. Whilst the radiosonde is being prepared for flight its radio transmitter operates in a low power mode to not just reduce power consumption, but also to protect the nearby receivers. After the radiosonde is launched, it switches to high power mode when it reaches a pressure 50 hPa less than at the surface. The second point to note is that the variability appears to permanently increase after the jump. Due to the sensitivity of the magnetometer, the influence of an increase in power of an electromagnetic source in close proximity could cause this variability. There is also a thermal drift in the magnetometer signal, inferred by visually inspecting the temperature profile and seeing similar patterns in both magnetometer and temperature data. This can cause the magnetometer voltage to drift by as much as 0.5 V over the course of the ascent. Harrison and Hogan (2006) documented both positive and negative thermal drifts from the magnetometer sensors, from those experiments the nature of the thermal drift is likely magnetometer dependent.

Despite these issues, the magnetometer still managed to make observations of turbulence similar to those shown in Harrison and Hogan (2006). A jet stream is present between 5 and 9 km, which is inferred by studying the wind profile in panel (c) of figure 3.5, which shows a large v wind component between 5 and 10 km. There is increased variability in σ_{mag} of 3.83 mV and 3.18 mV in the regions above and below (shaded red in panel (e) of figure 3.5) the jet, as opposed to the smaller σ_{mag} variability of 2.3 mV in the jet region (shaded blue in panel (e) of figure 3.5). The mean horizontal wind shears, which were calculated over a 200 m window were found to be 0.0103 s^{-1} and 0.0162 s^{-1} in the upper and lower red regions respectively and 0.008 s^{-1} in the blue jet stream section. This provides some evidence that wind shear is higher along the edges of the jet stream and hence generate turbulence. The σ_{mag} peak at 13 km could be caused due to inertia gravity waves breaking in the lower stratosphere, some evidence to support this is seen in the wave like structures in wind component at this height. The large variability in σ_{mag} at 2-4 km is harder to identify, it may be due to a tropopause fold; these occur when an intense jet stream usually flowing meridionally, as shown in figure 3.5, causes stratospheric air to be pulled under the jet core bringing stratospheric air down to 3-4 km. This is characterised by a dry layer and a low thermal gradient, both of which are observed at 4 km in panels (a) and (b).

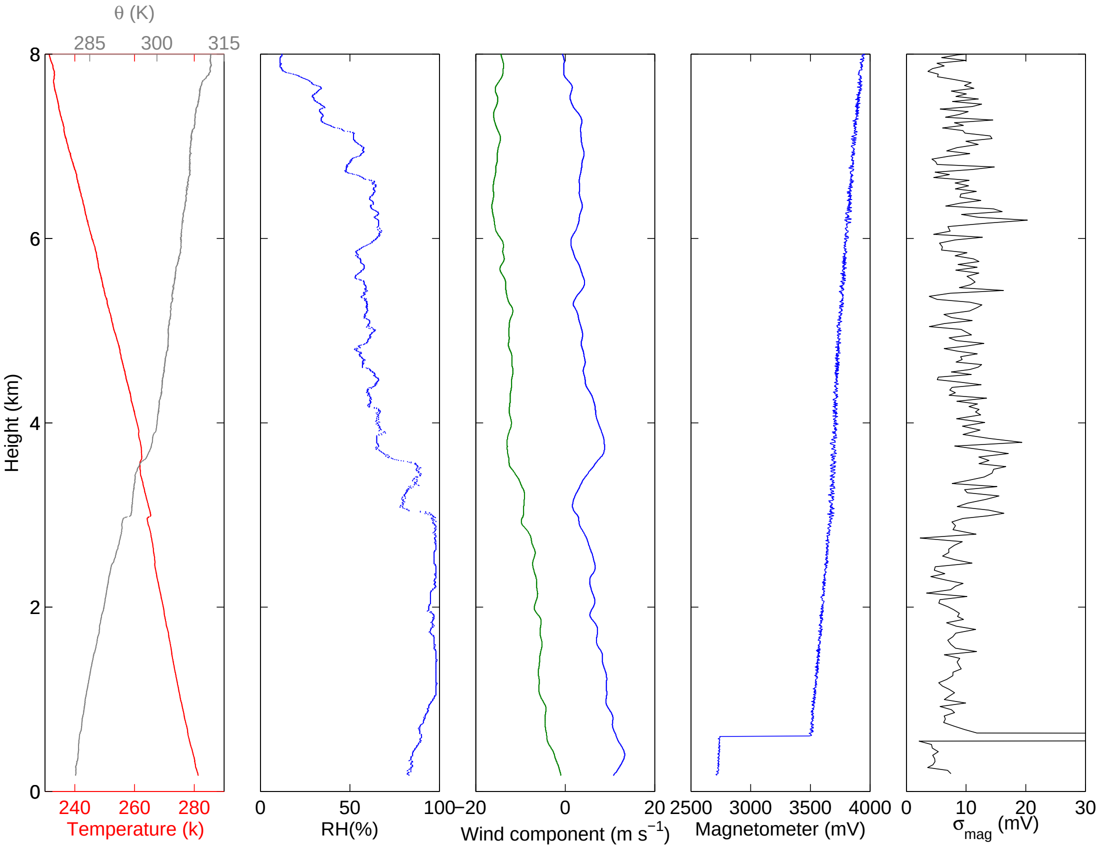

Figure 3.6 Vertical profiles of a) temperature and potential temperature (K) in red and grey respectively, b) relative humidity (%) , c) u and v wind components (m s^{-1}) in blue and green respectively, d) magnetometer Voltage (mV) and (e) the standard deviation of magnetometer voltage σ_{mag} (mV) over 8 seconds, from an ascent made from Durlston Head at 11UTC on 28th October 2012.

An ascent was made on the 28th October 2012 at the same site into different conditions, where a cloud layer was present and the jet stream had receded east from over the UK. The results of this are shown in figure 3.6. The jump in magnetometer output, caused by the increased radio transmitter power and the thermal drift are still present. In this ascent, there is reduced magnetometer variability within the cloud layer, which can be identified by a region of large relative humidity. Above the cloud layer there is increased magnetometer variability, which could be turbulence arising from a combination of latent heat transfer at the cloud top and wind shear at a similar height. The variability decreases a little but not significantly. This could occur if the air within and below the cloud is relatively stable to that above the cloud. From these two ascents, it has been demonstrated that some turbulence could be observed. The differences between what could be inferred as turbulent and calm air are difficult to define at times, hence the following need considering in regards to the sensor configuration beneath the radiosonde: Does the string length at which the radiosonde is suspended cause a dampening effect desensitizing the magnetometer variability to turbulence? Does the background variability change with temperature? And does the balloon experience any resonant oscillatory behaviour in addition to that caused by turbulence that could cause an increase in variability?

3.3.2 Setting a string length

As discussed in the previous section, one of the reasons there are only small changes in variability may be due to the string length between the radiosonde and balloon. The period of oscillation of a pendulum is given by

$$t = 2\pi\sqrt{\frac{l}{g}} \tag{3.1}$$

where g is the acceleration due to gravity and t is the period of oscillation. It is clear that an increase in the string length, l, is proportional to an increase in t. In turn this means the radiosonde will be making fewer oscillations per eight second sample. However, unlike a pendulum, the string between the balloon and radiosonde is not rigid and hence introduces further dampening. If the string was shortened it would minimise these effects of dampening and become more sensitive to motions induced by the balloon. A shorter string length may however cause some wake effects described in Luers and Eskridge (1998) whom suggested that it may cause a reduction in ventilation speed over the temperature and humidity sensors. The effect of the balloon's wake is unlikely to induce additional motions in the motion sensing package, as its cross sectional area is three orders of magnitude less than that of the weather balloon. A 4m string length was decided upon as it gave the sensing package enough clearance from the balloon, but would not be long enough to suffer from damping effects. A health and safety aspect also contributed in the choice of string selection, as it was foreseen that radiosondes would need launching in adverse conditions where a shorter string would yield a safer launch. Once a radiosonde is normally launched, the sensing package is allowed to unwind using the stock unwinder. In strong winds the balloon package may unwind too quickly and may collide with nearby objects. Mechanical unwinders and slower unwinders could have been used to remedy this hazard.

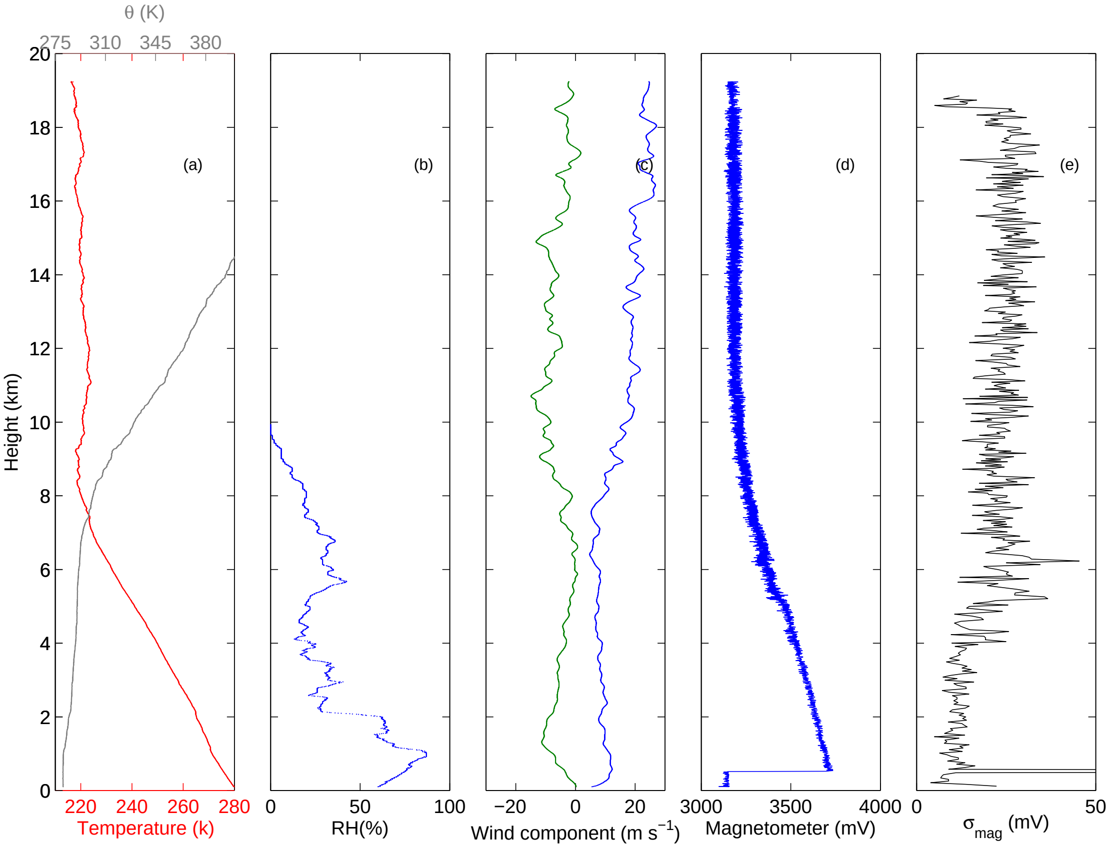

Figure 3.7 Vertical profiles of a) temperature and potential temperature (K) in red and grey respectively, b) relative humidity (%), c) u and v wind components (m s^{-1}) in blue and green respectively, d) Magnetometer Voltage (mV) and e) the standard deviation of magnetometer voltage (mV) over 8 seconds, from an ascent made from the RUAO at 11UTC on 4th December 2012, using the 4 m string configuration.

Figure 3.7 shows the standard meteorological profiles and the magnetometer data for the first flight with the shortened string. It can be seen that the magnetometer produces a larger σ_{mag} than seen in figures 3.5 and 3.6, most notably there are σ_{mag} spikes in excess of 30 mV. There is also a background increase in standard deviation with height and then a decrease just before the burst height. This may be due to the shortened string making the radiosonde package below more sensitive to motions induced at the balloon. This could be caused by instrument payload beneath entering a resonant oscillatory mode. The jump experienced when the radiosonde enters high power mode is still present, and a change in variability can be noticed. Before reaching further conclusions it was decided to examine another ascent to examine if the issues highlighted here are present in other ascents.

Figure 3.8 shows the meteorological and magnetometer data from a second ascent made on the 22nd February 2013 using the 4 m string configuration. It can be seen that the magnetometer variability is still increasing with height. There is also increased

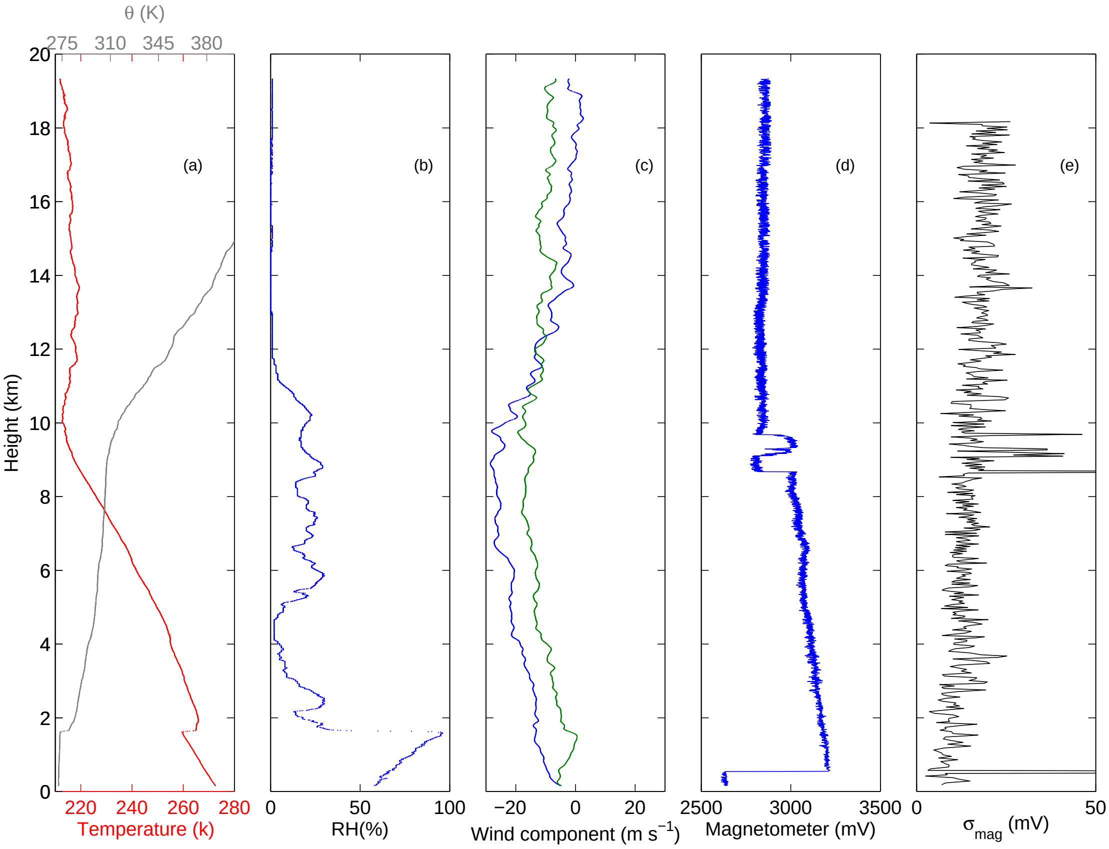

Figure 3.8 Vertical profiles of a) temperature and potential temperature θ (K) in red and grey respectively, b) relative humidity (%), c) u and v wind components (m s^{-1}) in blue and green respectively, d) magnetometer Voltage (mV) and e) the standard deviation of magnetometer voltage (mV) over 8 seconds, from an ascent made from the RUAO at 11UTC on 22nd February 2013, using a 4 m string configuration.

variability at 8-10 km where there are multiple step changes in the raw magnetometer data. The variability does not increase at the same rate with height as seen in figure 3.7 likely due to the fact that that each magnetometer has different voltage characteristics as shown in Harrison and Hogan (2006). The difference in baseline voltage can be seen between the two different magnetometers used in both figures 3.7 and 3.8, unless the output voltage drifts out of the 0-5V range of the PANDORA board it is not important as only the variability is used. It appears that a shortened string length does increase sensitivity but introduces a background trend in the magnetometer. Hence a couple of questions are raised which need further investigation: Firstly can the magnetometer produce repeatable results across multiple ascents? Secondly does the signal it presents as it is tilted change with temperature? Thirdly does a resonant oscillation in the balloon sensor package system make the results inconclusive?

3.3.3 Testing magnetometer under laboratory conditions

In order to examine the sensor-to-sensor variability between magnetometers a subsample of 10 magnetometers was selected at random. Each magnetometer was placed in a clamp and orientated at a range of angles between 0° and 90° to the vertical, the reference protractor could be measured to an accuracy of ± 2^o. They were placed vertically at the beginning and end of each tilt test to remove any background drift in each individual magnetometer. A drift of 2-3 mV was observed during each magnetometer test. This could be due to the changes in temperature shown in figure 3.8. However, the laboratory temperature is likely to remain constant over such short time scales. A geomagnetic drift would be unlikely observable due to the very long time over which these changes occur. Therefore the cause of the drift is still unclear.

The average background value for each magnetometer was subtracted from each magnetometer value to give a voltage difference with angle from vertical. The results from this experiment are shown in figure 3.9. It can be seen that the spread of voltage differences grow larger with angle from the vertical, concluding that magnetometer measurements

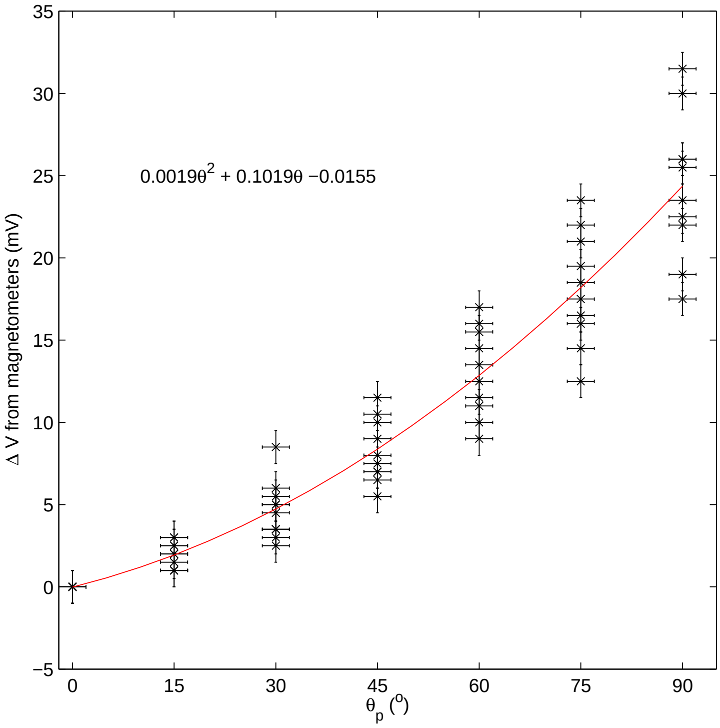

Figure 3.9 A plot showing tilt angle from vertical θ_p against voltage difference from background voltage ΔV recorded at the vertical for each magnetometer. The red line is a fitted second order polynomial to data from all magnetometers. Error bars are constructed from the accuracy of the reference protractor and from the resolution of the PANDORA logging system which is 1mV.

made during one ascent are not directly comparable with those of another ascent. Even with a 45^o degree swing there is a 10 mV difference in response. Secondly by examining figure 3.8 it can be shown that during the jump that occurs at 50 hPa above the surface there is a change in variability, which ultimately means that the results of this experiment may not be directly applicable to the in flight data. Each magnetometer took approximately five minutes to test but the background magnetometer values drifted indicating poor background stability. For a normal ascent speed of 5 m s^{-1}, five minutes corresponds to an atmospheric layer of 1.5 km which could affect measurements of turbulence over such a layer. An increase in sensitivity could cause the magnetometer variability to increase. A thermal drift or an increase in transmission power as seen in figure 3.7 could also cause an increase in sensitivity.

3.3.4 A spectral analysis of magnetometer data

If the balloon and instrument package enter into a resonant oscillatory motion, for example if the instrument package swings beneath the balloon like a conical pendulum as opposed to that of a normal pendulum (as currently assumed) the magnetometer may output different values. A method to explore this is to carry out a spectral analysis of the magnetometer data. To achieve this, a spectrogram approach is required where multiple spectra are calculated from a moving window. This creates successive power spectra at different heights allowing the detection of oscillations in the magnetometer data with height. Typically this could be achieved by using a spectra from a Fast Fourier Transform (FFT). However the use of a FFT is not straightforward in this application, as radiosonde data is on occasion intermittent due to poor signal quality. One spectral method that can deal with irregular data is the Lomb-Scargle periodogram (Lomb, 1976). It performs a spectral analysis by fitting sine waves in a least squares sense to the data, hence periodicities can be found even with missing data present, making it an ideal tool for this task[1].

The implementation of the Lomb-Scargle periodogram used here is based on that shown in Press (2007). In that implementation the amount of frequency bins produced is a function of the amount of input data parsed. Having a multiple amount of frequency bins would lead to a irksome analysis, as some windows have more data points than others. To alleviate this, frequency bins were calculated for an ideal data window where there were no missing data points. The spectra for a height window that had less than

---

[1] The Lomb-Scargle periodogram was originally developed for finding periodicities in irregular astronomical data

the correct amount of bins could be interpolated on to the correct amount of frequency bins. In cases where a small amount of frequency bins were present and interpolation was impossible for some ideal frequency bins, a null value was inserted. For this analysis a sixty second moving window was used, equating to a height window of 300m. The moving window was incremented in time by one second for every iteration.

As can be seen in the Lomb-Scargle spectrograms shown in figures 3.10 and 3.11 there is a dominant oscillation period of 0.3Hz for the majority of the ascents. On closer examination, when there is a peak in magnetometer variability the 0.3 Hz peak is not present. From this it is deduced that the radiosonde maybe entering an resonant oscillatory state and when encountering turbulence is made to break from the resonant oscillation. By considering equation 3.1 and setting l to 4 m, then the period of oscillation is 4 seconds, which equates to a frequency of 0.25 Hz, which is of a similar frequency to the detected oscillation. Given that this data only examines the magnetometer, a next prudent step was to check if this also occurs on other measurements made by the radiosonde. Two

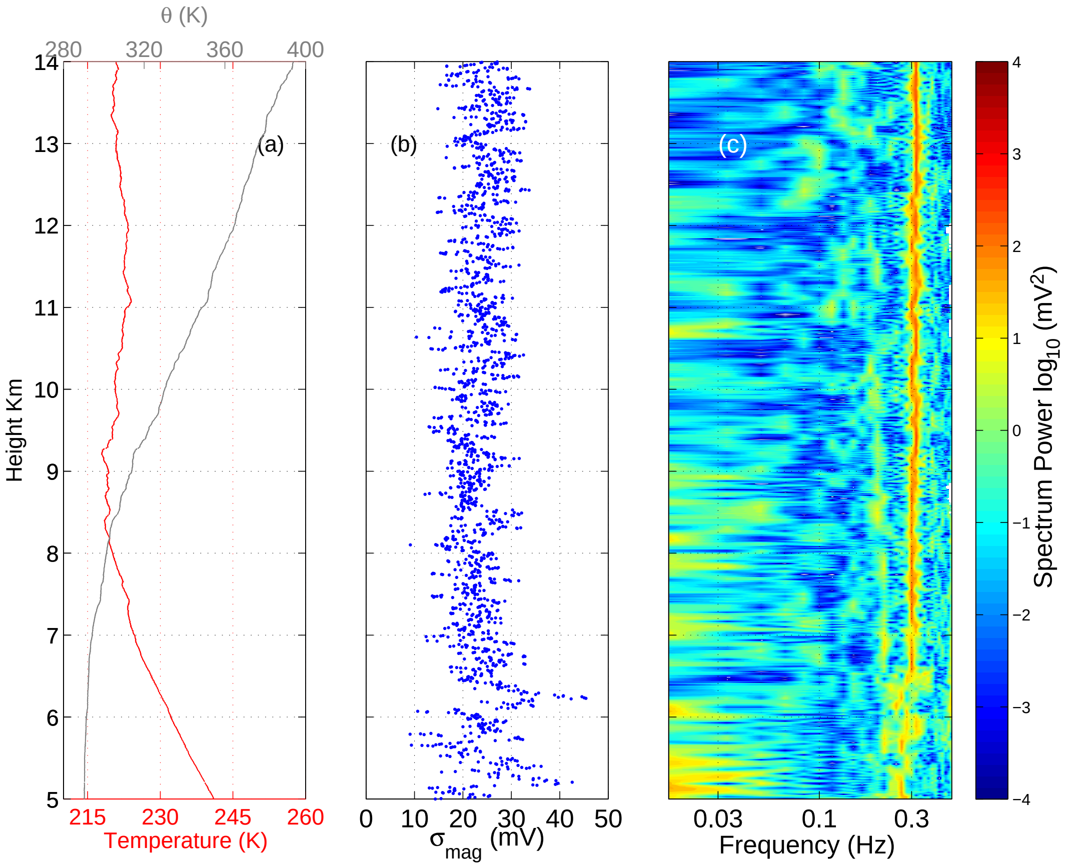

Figure 3.10 Vertical profiles of a) temperature and potential temperature θ (K) in red and grey respectively and b) standard deviation of magnetometer voltage σ_{mag} (mV) over 8 seconds. c) is a Lomb-Scargle spectrogram of the raw magnetometer (mV) over the same height, from an ascent from RUAO at 1100UTC on 4th December 2012.

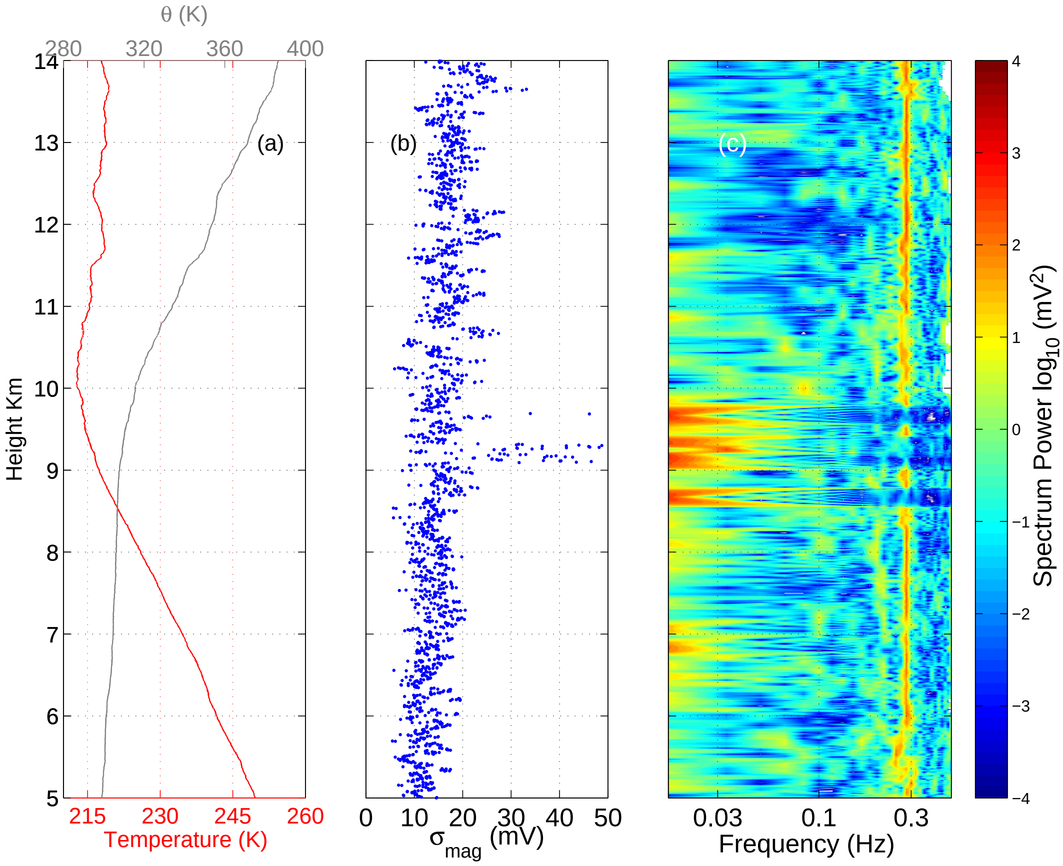

Figure 3.11 Vertical profiles of a) temperature and potential temperature (K) in red and grey respectively and b) standard deviation of magnetometer voltage σ_{mag} (mV) over 8 seconds. c) is a Lomb-Scargle spectrogram of the raw magnetometer (mV) over the same height, from an ascent from RUAO at 1100 UTC on 22nd February 2013.

other measurements which could measure some aspect of the radiosonde swing are available. The first is a photo diode which is used to infer whether the sonde is in cloud, this will be described in section 3.6. Secondly the raw GPS data from the radiosonde could also be used as the radiosonde manufacturers use an algorithm to minimise the effects of radiosonde swinging on GPS derived winds (private communication with Vaisala 2014). This will be further explored in section 3.4.3.

3.3.5 Suitability of a magnetometer

This project requires a motion sensor which can provide a standardised set of turbulence measurements. It was shown that the magnetometer device responds to atmospheric turbulence both in this thesis and in Harrison and Hogan (2006) and Harrison et al. (2009). Here it appears to be affected by the radiosonde's transmitter, the radiosonde and balloons resonant oscillation on the shorter string, and the varying sensitivity of each sensor. The resonant oscillatory effects of the radiosonde cause an increase in the variability of the magnetometer. This can be circumnavigated by using a longer string length, at the expense of less sensitivity and a hazardous launch. With qualitative results for each ascent, it makes a dataset of 20-30 ascents impossible to interpret.

3.4 Measuring the motion of a radiosonde with an accelerometer

Another method of measuring the motion of an object is to use an accelerometer. These devices are able to present a voltage output which is proportional to the acceleration experienced by a device, meaning that information about the motion of an object can be gained by looking at the variability in acceleration. Accelerometers are most commonly used in smart phones to enable gesture control and in-app interactions. They are also used for in-game interaction such as with the Nintendo Wii$^{\mathrm{TM}}$ gaming system. Most commercially available accelerometers are able to detect accelerations in three dimensions. Internally an accelerometer consists of a small microstructure mass supported by springs. Movement of the mass due to acceleration unbalances a differential capacitor, formed by a set of metal plates on both the mass and internal walls of the chamber encasing it. This produces a signal that is related to the movement of the mass. Post-processing on the accelerometer chip allows the direction and magnitude of the acceleration to be derived (Analog Devices, 2009). A voltage output proportional to the acceleration is then provided for each axis of the accelerometer. As discussed in chapter 2 accelerometers have been used by aircraft to make observations of turbulence, but only Anderson (1957) has used accelerometers on a weather balloon and parachute platform.

3.4.1 Selection and orientation configuration

Before flying the accelerometer on a radiosonde it is necessary to select an accelerometer with an appropriate range and orientation within the sensor package. From video footage of radiosondes in flight just after launch, a small swing of 30-40^o was observed. For prototyping the ADXL355 3 axis $\pm 3g$ accelerometer was used as this has a relatively high sensitivity and a suitable range. The accelerometer was placed within the sensing package with the three axes of the accelerometer aligned with the three principal dimensions of the sensor package as shown in figure 3.12

To see which accelerometer axes were most sensitive to the swing of the radiosonde, the accelerometer sensor package was attached to a radiosonde and suspended on a 4 m

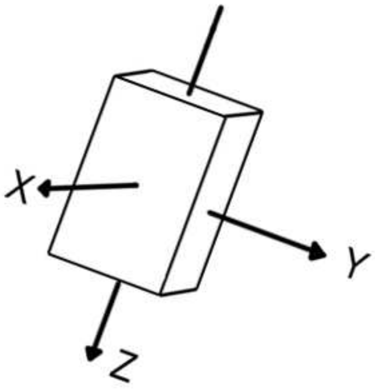

Figure 3.12 Diagram showing orientation directions of the 3-axis accelerometer relative to the sensing package position.

string from a mast. The radiosonde and sensing package was swung by hand beneath the mast. Each output from the three accelerometer axes were connected to a logging channel on the PANDORA system which was connected to the radiosonde. This allowed logged data to be relayed over the radiosonde's radio link for logging on the sounding system. This removes the need for a wired connection to the sensor package which could affect the swing. To infer the accelerations from the voltage output of the accelerometer some pre-calibration is required. The accelerometer can detect the static acceleration due to gravity g, which is used to calibrate the accelerometer output voltage in terms of mV g^{-1}. By rotating the accelerometer by 90^o along each axis, a voltage offset and sensitivity can be found by calibrating against gravity. Two experiments were carried out, the first looked at the stability of the sensors if the device was kept static, whereas the second examined the response of each axis of the accelerometer when swung. Furthermore a magnetometer device was also logged to see its response compared to the accelerometer on the fourth PANDORA channel.

In figure 3.13 it can be seen that the accelerometer shows a high level of stability when left at rest. The Z-orientated accelerometer detects a constant acceleration of 10 m s^{-2}, which is due to the accelerometer measuring the static acceleration due to gravity. The X and Y components remain constant, however they are slightly offset from zero, due to the radiosonde and instrumentation package not being a perfectly balanced object. Each respective axis is responding to a small vector component of the gravity acceleration vector. The stability of the accelerometer is very good with a standard deviation

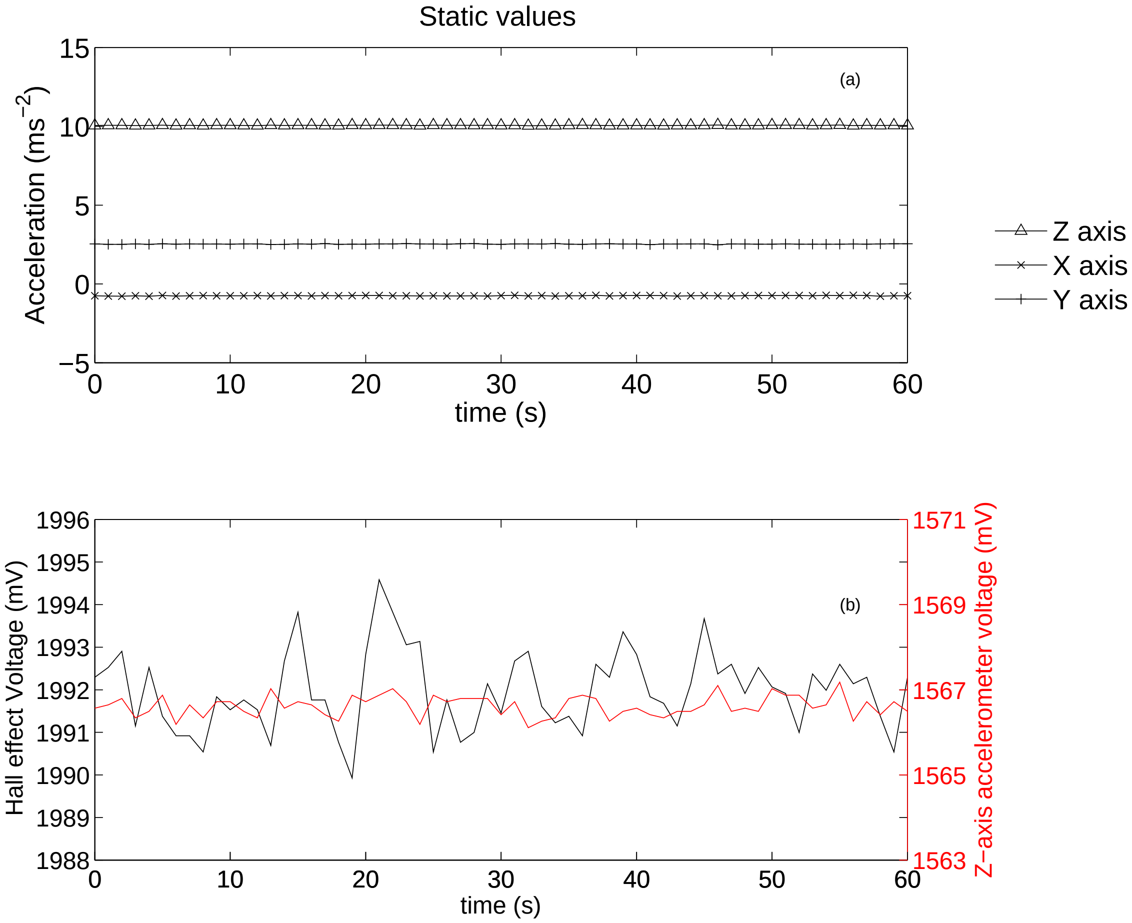

Figure 3.13 a) Time series of the X,Y and Z outputs of the accelerometer when the sensor package was at rest. b) A time series of magnetometer voltage (mV) logged from the same sensor package. The accelerometer's Z output voltage has been added to demonstrate its improved stability.

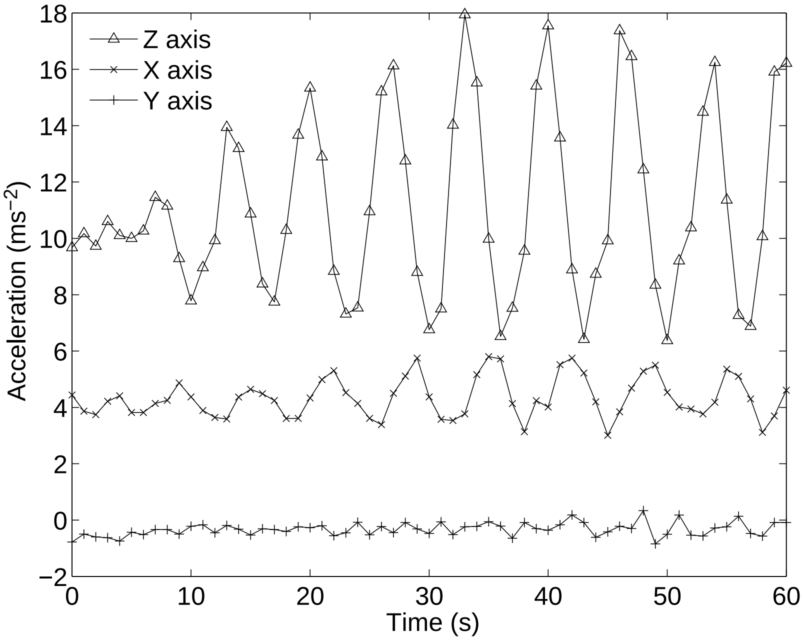

Figure 3.14 Time series of the X,Y and Z outputs of the accelerometer when the sensor package was swung with an approximate angular deflection of 30^o. Adapted from Marlton et al. (2015).

of approximately 0.01 m s^{-2}, when compared to that of the magnetometer, which has a standard deviation of approximately 1 mV shown in the bottom panel. The next experiment consisted of swinging the balloon in a pendulum fashion, for the largest swings the swing deflection was estimated to be approximately 30^o.

Figure 3.14 shows that the Z-axis has the largest response to the instrument package being swung. The X and Y components of the accelerometer do also show a response to the motion of the package, however the range is relative smaller compared with that of the Z-axis. The X and Y axis pick up a change in direction at the peak of the instrument package's swing. The Z-axis is sensing directional change as well as the centripetal component which is a function of v_{sonde}^2/l providing some limited information about the linear speed of the sensing package, v_{sonde}.

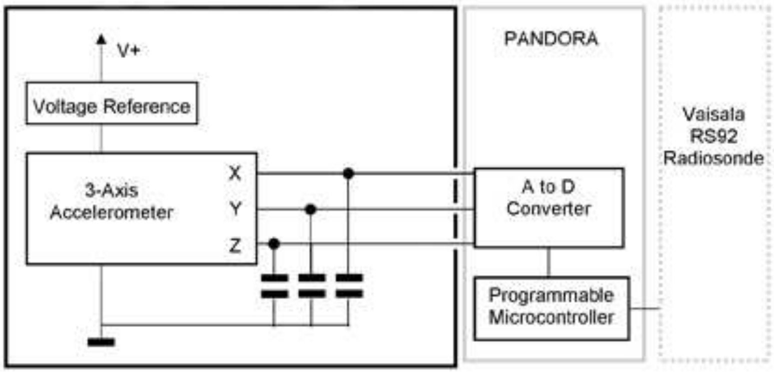

Figure 3.15 The configuration of the accelerometer: the accelerometer is powered by a voltage regulator and the output is modulated using capacitors across the outputs. Measurements are obtained by the PANDORA data acquisition system and are transferred to the commercially available Vaisala RS92 radiosonde. Adapted from Marlton et al. (2015).

The accelerometer was placed in the sensing package in the orientation shown in figure 3.12. The accelerometer was powered from a 3V voltage regulator powered from the 8V supply rail from the PANDORA system. The three outputs were connected to three of the PANDORA logging channels. 0.1 μF capacitors were added to each channel to implement noise reduction. The configuration of the accelerometer and its connection to the Vaisala RS92 radiosonde is shown in 3.15. The accelerometer was interfaced with the PANDORA board and placed in the sensor housing as shown in figure 3.16.

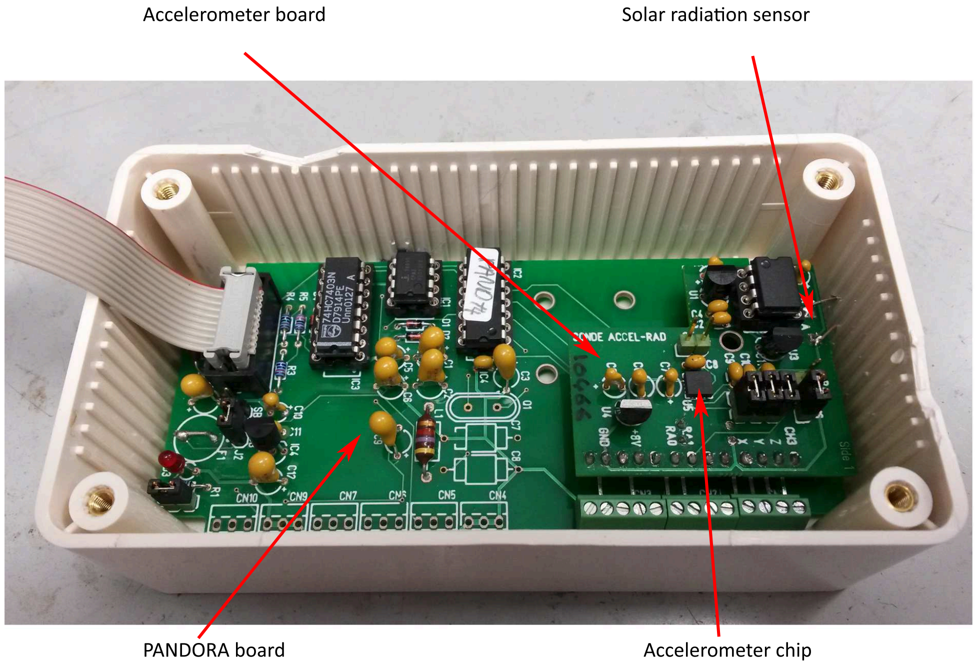

Figure 3.16 A picture of the accelerometer mounted on the accelerometer board interfaced with the PANDORA board within the sensor housing.

3.4.2 Accelerometer prototype flights

The first prototype accelerometer ascent was made on the 26th April 2013 from RUAO and shown in figure 3.17. All three of the accelerometer axes were logged for this ascent. A jet stream was present over Reading providing potential to make observations of atmospheric turbulence. The accelerometer device was suspended at a string length of 4 m. Although it was shown to have a resonant oscillatory effect on the balloon and instrument system, the 4 m string length was adopted as at the time the resonant oscillatory effects were not fully understood. Furthermore when jet streams are present, surface conditions can make it dangerous to launch balloons on the full string length.

The meteorological conditions depicted in panel (b) of figure 3.17 show a moderate jet stream with an intensity of 50 m s^{-1}. In panel (c) the z-axis accelerometer produces regions of increased variability at 3, 6 and 8 km. Given the accelerometer is being agitated by the motion of the balloon, increased variability in the accelerometer values compared to those recorded at 4 km for example, infer the balloon is passing through turbulence. Figure 3.18 shows also the standard deviations over 200 m for each of the accelerometer axis to highlight the changes in variability. Given this is a preliminary flight it is impetuous at this stage to quantitatively assign a value for significant turbulence so a qualitative

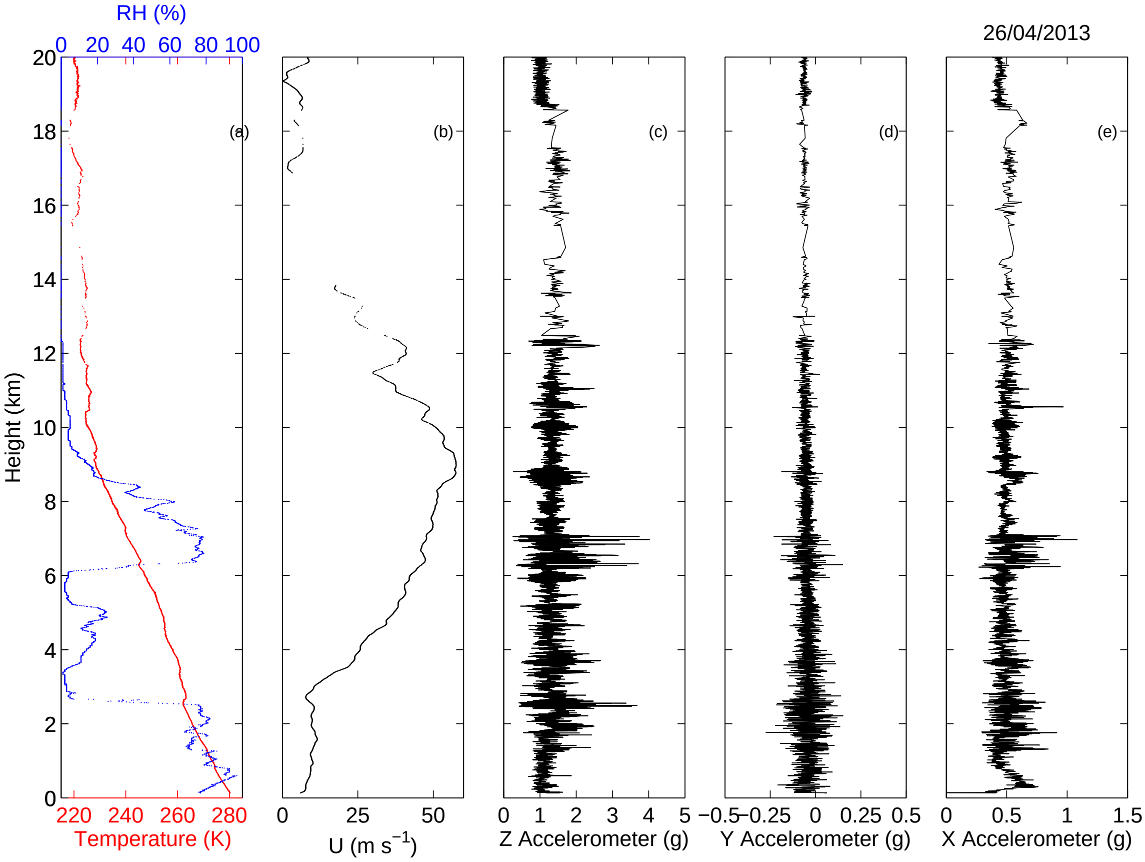

Figure 3.17 Vertical Profiles of (a) temperature (K) and Relative Humidity (%), b) wind speed U (m s^{-1}), (c) Z (d) Y (e) X axis of accelerometer in g, where (g=9.81 m s^{-2}) for an ascent from RUAO, on 26th April 2013.

interpretation is given. The turbulence at 3 km could be attributed to a potential cloud layer. The other two patches of turbulence are most likely associated with the jet stream. In panels (d) and (e) the X and Y axis also observed increased variability in each axis, however, as discussed in section 3.4.1, the variability in each axis is smaller than the Z axis. In the stratosphere there is some signal drop out which could be due to specular effects of stratified air. In chapter 2, it was briefly discussed how stratified air could reflect the MST radar signals from the ground, here the radiosonde's signal, which is of similar frequency to a wind profiler, could be deflected from the ground station in a similar way. However there is little turbulence detected by the accelerometer device in the stratosphere. The background value of g for the Z-axis accelerometer does drift slightly with height before returning to its normal 1g value. This drift is not as large as the drift on the magnetometer. Nonetheless it could be due to the resonant oscillatory effect of the balloon causing an additional centripetal force component to be detected along the Z-axis of the accelerometer. This resonant oscillatory effect does not seem to affect the balloon and instrument package's ability to detect turbulence. For example, at 8 km

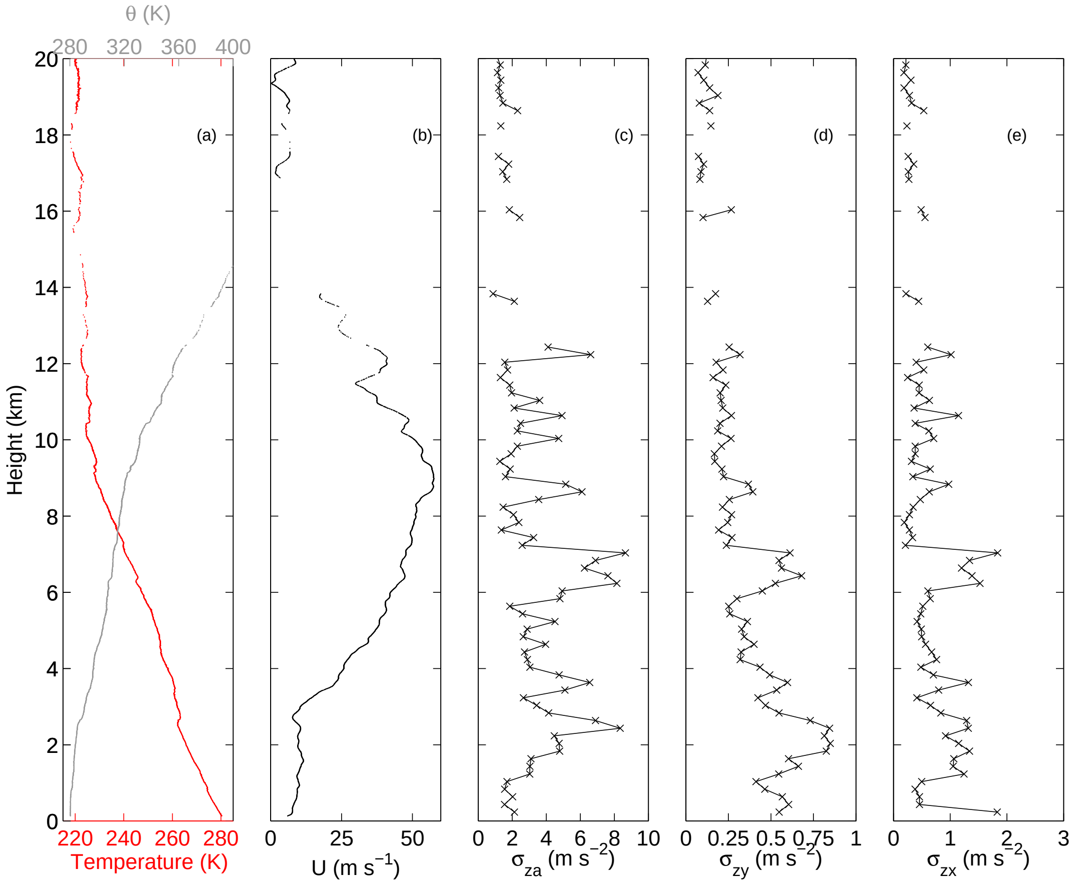

Figure 3.18 Vertical profiles of a) temperature and potential temperature θ (K) in red and grey respectively, (b) the horizontal wind speed U (m s^{-1}), (c) the standard deviation of the Z-axis σ_{za} (d) Y-axis σ_{ya} and (e) X-axis σ_{xa} accelerometer data (m s^{-2}) over 200 m height windows from an ascent made at RUAO on 26th April 2013.

accelerometer variability increases due to turbulence before returning to low variability about the background mean.

Figure 3.19 shows the correlations between the standard deviations of the three axis

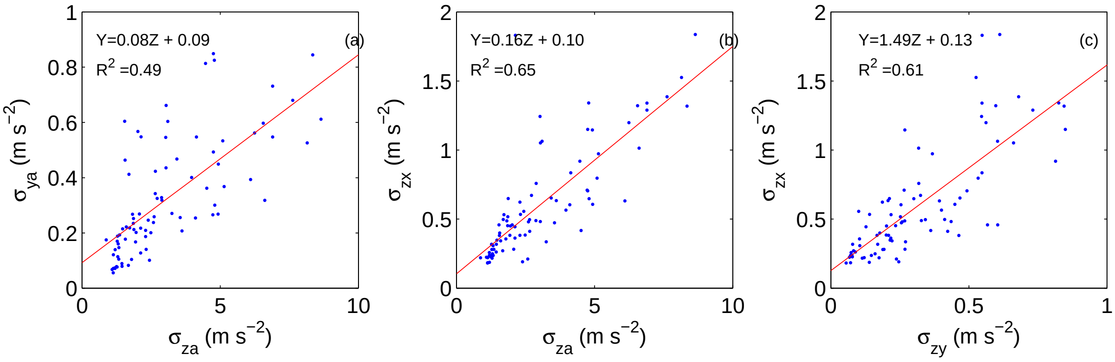

Figure 3.19 Comparisons in the standard deviation of accelerometer axes over 200 m for a) the Z-Y axes, b) the Z-X axes and c) the Y-X axes, for the ascent made on the 26th April 2013

of the accelerometer. All three orthogonal axis show a moderate correlation with each other, which adds confidence in that the turbulence that is agitating the balloon causing large swings in the radiosonde below. This also adds a level of redundancy as if there were to be a failure in the Z axis sensor channels, it would be possible to estimate the standard deviation in the Z-axis from theses relationships. It is hard however to deduce more information about the nature of the swing from the X and Y axes, this is predominantly due the fact that the directions these two axis refer too changes as the radiosonde is allowed to spin round the Z-axis. This may explain why the correlations in figure 3.19 are not perfect, it also adds reasoning to the use of the Z-axis of the accelerometer as it is always measuring the same component of the swing.

The accelerometer provides a lot more information than the magnetometer which effectively gives information about the orientation of the device. The accelerometer gives information about whether the radiosonde is swinging and about the magnitude of the swings. The small background shift in the Z accelerometer may be due to an resonant oscillatory effect between the radiosonde and balloon. By taking a standard deviation of the accelerometer output over a given height window of 200 m, it can be seen that the shift in background trends do not affect the variability of the accelerometer, hence enabling the resonant oscillation and the effects of turbulence on the sensing package to be separated. This is confirmed in panel (b) of figure 3.18 showing that the background standard deviation does not drift with height. This means that the accelerometer, despite being affected by a the potential background resonant oscillatory motion of the radiosonde, can still make turbulence observations. The $\pm 3g$ accelerometer is certified to be able to measure a minimal accelerometer range of $\pm 3g$. However, as shown in figure 3.17, the Z-axis sometimes exceeded this minimal range, so a ADXL325 $\pm 5g$ accelerometer was used for the remainder of the campaign. Offsets and sensitivities were recalculated for this larger range accelerometer in a identical fashion to that in section 3.4.1. The sensitivity characteristics of each accelerometer are summarised in table 3.1. The change in sign for the Z-axis sensitivity is due to the orientation of the accelerometer on the circuit board. The next step is to embark on a spectral analysis to see if the drift of the accelerometer is related to a resonant oscillation.

	ADXL355	ADXL325
Minimal range	± 3g	± 5g
Z-axis sensitivity	245 mV g^{-1}	-190±2 mV g^{-1}
Z-axis offset	-1300 mV	-1674±2 mV
Y-axis sensitivity	240 mV g^{-1}	193±2 mV g^{-1}
Y-axis offset	-1300 mV	-1643±2 mV
X-axis sensitivity	260 mV g^{-1}	185±2 mV g^{-1}
X-axis offset	-1300mv	-1683±1 mV

Table 3.1 Summary table of the specifications of the ADXL355 and ADXL325 accelerometers used in the prototyping. The ADXL325 coefficients were found by taking an average and standard error from seven ADXL325 accelerometers. For a more complete explanation of how the coefficients are applied to the voltage data refer to appendix C.

3.4.3 Spectral analysis of accelerometer data

A similar method undertaken in section 3.3.4 is applied here to perform a spectral analysis of the accelerometer data using Lomb periodograms. The aim is to see if any oscillations can be found within the accelerometer data that may yield more information about any potential resonent oscillatory states the balloon and radiosonde may enter during flight. Here, an analysis is performed on an ascent where both a magnetometer and accelerometer were logged. Due to addition of the magnetometer the Y-axis accelerometer data channel was sacrificed to allow magnetometer data to be relayed to the ground station. In this experiment the raw GPS wind data was also retrieved, and a spectral analysis was performed on the data for a complete analysis.

Figure 3.20 shows the standard meteorological profiles of temperature, relative humidity and wind speed. An intense jet stream was present between 4 and 12 km. Patches of intense turbulence are present in the high shear regions of the jet stream with the most intense turbulence at 7 km where the accelerometer exceeds its minimal 5g range. The background trend in increasing g is also detected indicating that the radiosonde is experiencing a resonant oscillatory effect. The u and v raw GPS data are shown in figure 3.21, there is noise present in the raw GPS data which could be either due to instrumental noise of the GPS instrument, or from the radiosonde swinging. The magnetometer data in panel (d) shows an increase in variability at the same height of 4-5 km when the background accelerometer value began deviating from a background trend of 1 g. Lomb periodograms were calculated for the raw u and v GPS components, the accelerometer and magnetometer. As in previous examples a moving sample window of 60 seconds was used.

The u and v periodograms in panels (a) and (b) of figure 3.22 show the existence of

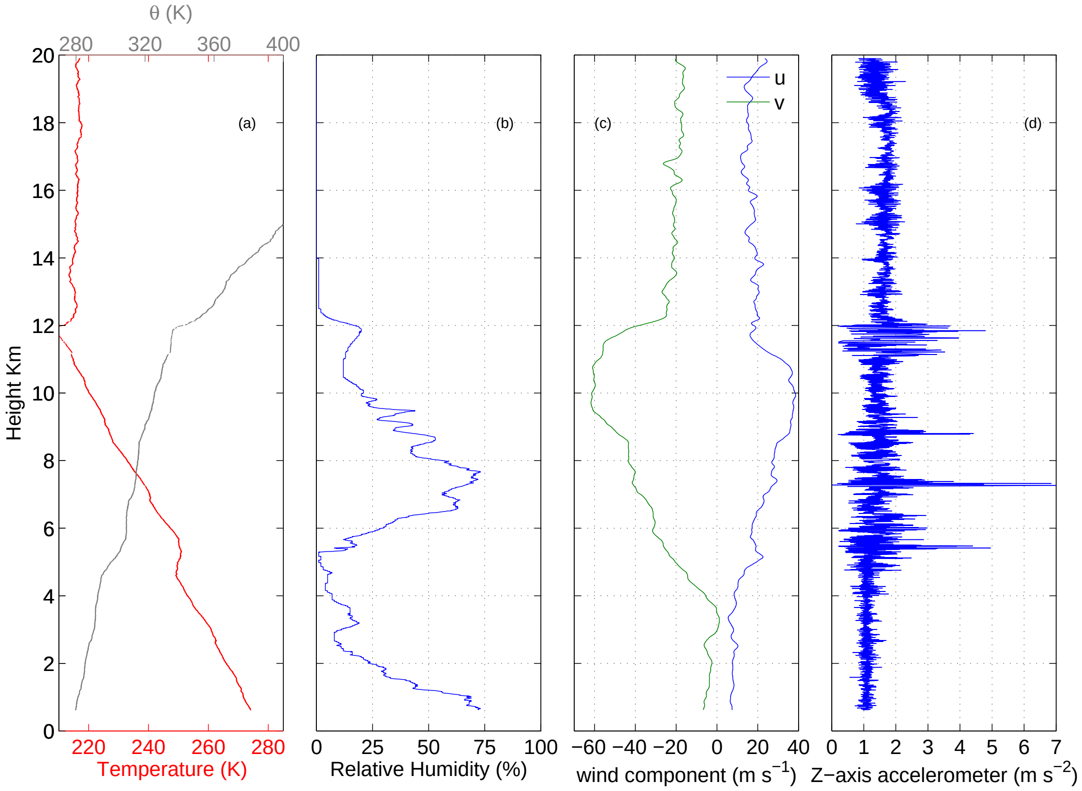

Figure 3.20 Vertical profiles of a) temperature and potential temperature θ (K) in red and grey respectively b) relative humidity c) u and v horizontal wind components in blue, and green respectively (m s^{-1}) and d) Z-axis accelerometer (g) for an ascent made on 14th January 2014 from RUAO.

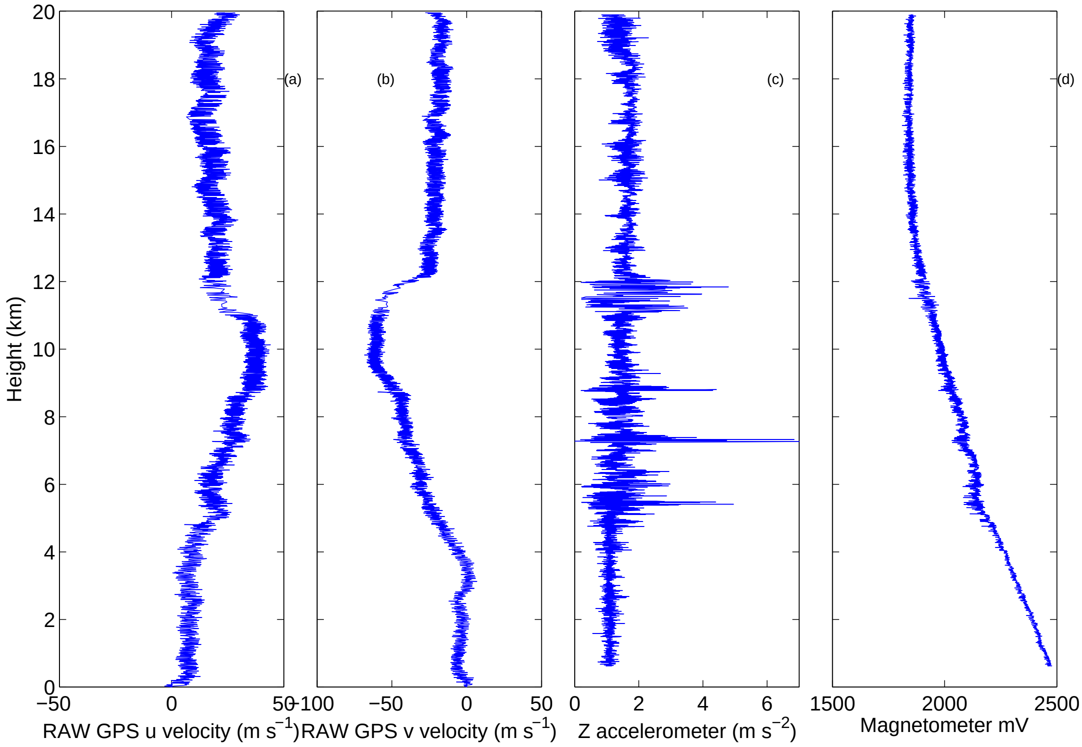

Figure 3.21 Vertical profiles of a) u raw GPS derived wind (m s^{-1}), b) v raw GPS derived wind (m s^{-1}), c) Z-axis accelerometer (g) and d) raw magnetometer output (mV), for an ascent made on 14th January 2014 from RUAO.

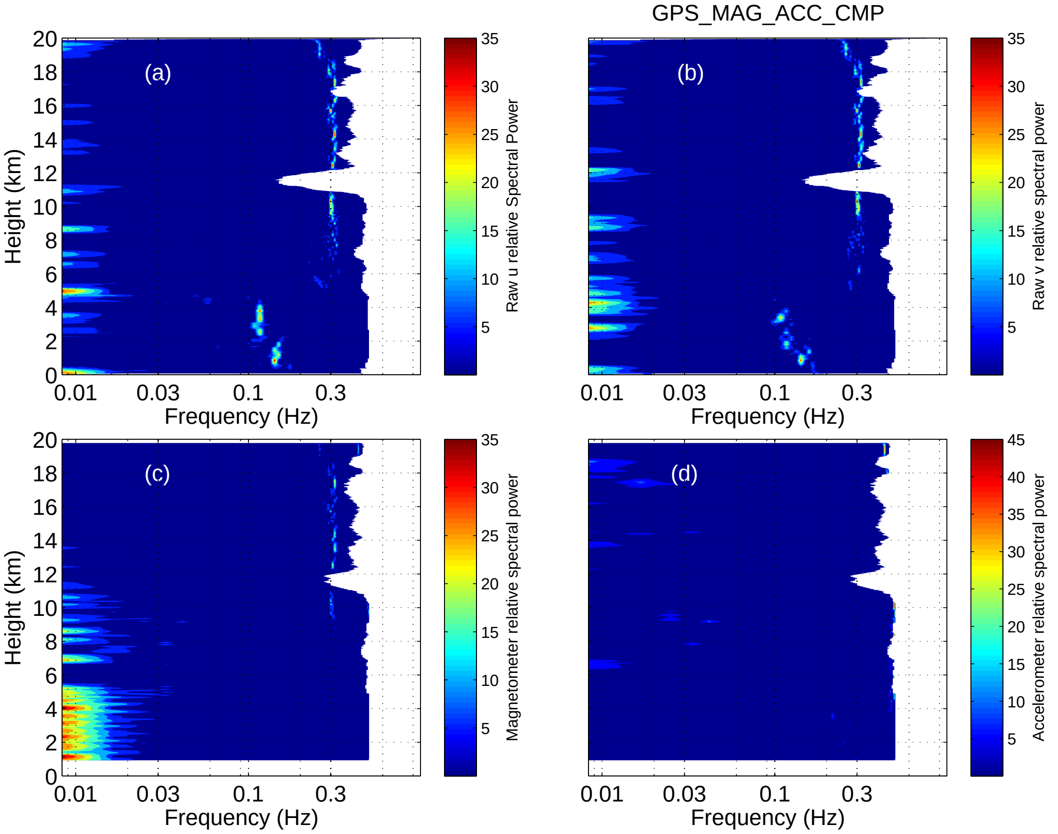

Figure 3.22 Lomb periodograms with height for a) u raw GPS data, b) v raw GPS data, c) magnetometer data and d) accelerometer data for an ascent from RUAO on 14th January 2014.

a 0.3 Hz oscillation of the same periodicity as that of the magnetometer shown in panel c). There is however no 0.3Hz oscillation observed in the Z-accelerometer data. One potential reason for this, is shown in figure 3.23, which shows the horizontal velocity and acceleration along the Z-axis of a theoretical pendulum allowed to swing in a 2D plane. It can be seen that for every oscillation in velocity there are two in the accelerometer signal, meaning that an oscillation of 0.3 Hz in the raw GPS would correspond to an oscillation in the accelerometer of 0.6 Hz which is above the Nyquist frequency of 0.5Hz. However the oscillation is occurring in both the x and y directions of the GPS indicating that the radiosonde is following a circular trajectory beneath the balloon such as that of a conical pendulum. The centripetal force and the force of gravity balance causing the mass to swing in a circular motion at a fixed angle θ_p from the vertical. As the two forces are balanced it means that the z-axis accelerometer may not exhibit the signs of a resonant oscillation. The period for the mass to complete one oscillation is given by

$$t = 2\pi\sqrt{\frac{l\cos(\theta_p)}{g}}. \tag{3.2}$$

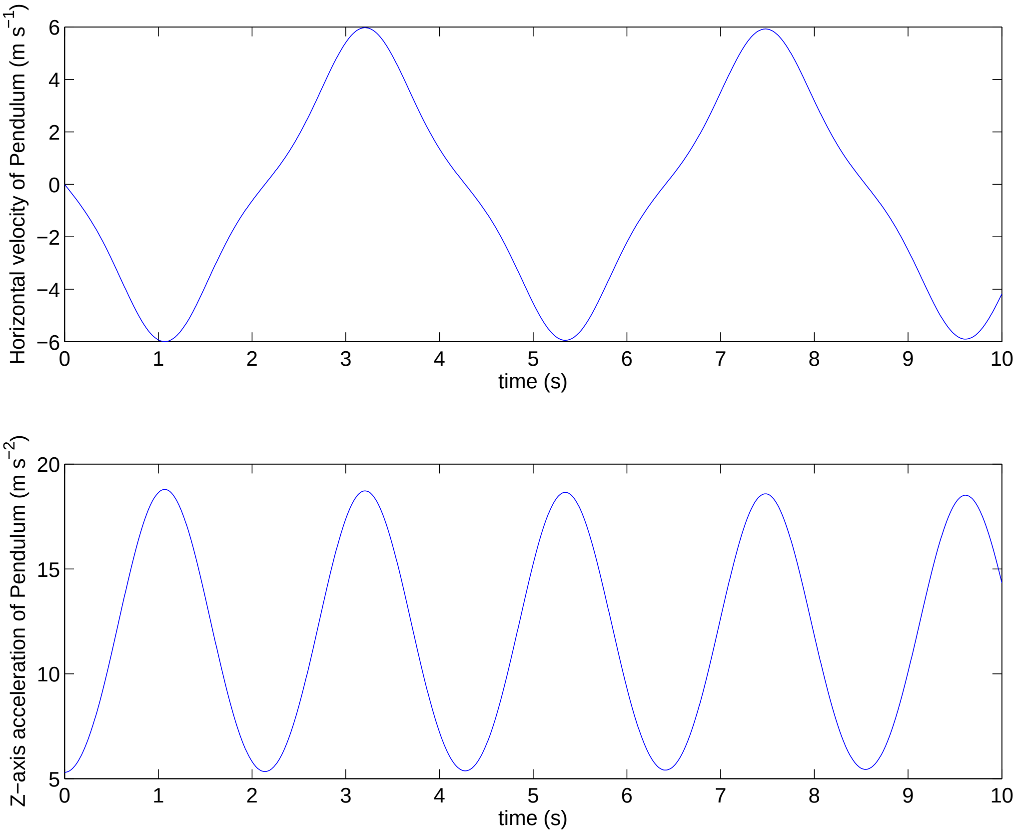

Figure 3.23 Top: Horizontal velocity (m s^{-1}) with time of a pendulum with a string length of 4 m swinging in a 2D plane. Bottom: Acceleration (m s^{-2}) along the Z-axis of the same pendulum.

Knowing the frequency and hence the time period of an oscillation allows θ_p to be calculated from the periodograms. Calculations showed $\theta_p = 60^o$ which is quite a significant angle for the radiosonde to be from the vertical. However by knowing θ_p, the centripetal acceleration can be calculated as r_{sonde}, the radius of the pendulum mass from the origin can be found. The period of oscillation is known and hence the velocity can be deduced. Knowing the angle at which the sensing package is orientated gives the orientation of the Z axis of the accelerometer. The calculated acceleration along the Z-axis of the accelerometer Z_{calc} is given by

$$Z_{calc} = g\cos(\theta_p) + \frac{v_{sonde}^2}{r_{sonde}}\sin(\theta_p). \tag{3.3}$$

The average peak frequency from the Lomb periodograms of the raw GPS u and v winds was calculated over a 500 m height window. The frequency was used to calculate the theoretical acceleration that one would expect the accelerometer to detect if it were a conical pendulum. The mean of the Z-axis accelerometer values from the radiosonde were taken over the same 500 m height window to give Z_{acc}. The two sets of data were plotted against each other as shown in figure 3.24.

Figure 3.24 shows that the predicted mean values of acceleration for the Z-axis accelerometer calculated from the periodograms is similar to observed values, hence concluding that the radiosonde has entered a resonant oscillatory mode where it behaves as a conical pendulum. Despite being at this large angle of swing of 60^o it appears that when the radiosonde encounters turbulence it is knocked out of this resonant oscillatory mode. Hence it does not seem to affect the accelerometer's ability to detect turbulence. However, what is not known is why the balloon and radiosonde enter this oscillatory motion. Another example is shown in figure 3.22 where raw GPS channels show larger peak frequencies about 0.1 Hz in the lower atmosphere at 2 km. This could be the radiosonde entering a different resonant oscillatory mode, however the catalyst for this is not known. Speculatively it may be an artefact of the string length used, as the balloon-radiosonde system may enter a resonance when the balloon is of a given size with the radiosonde a given distance beneath.

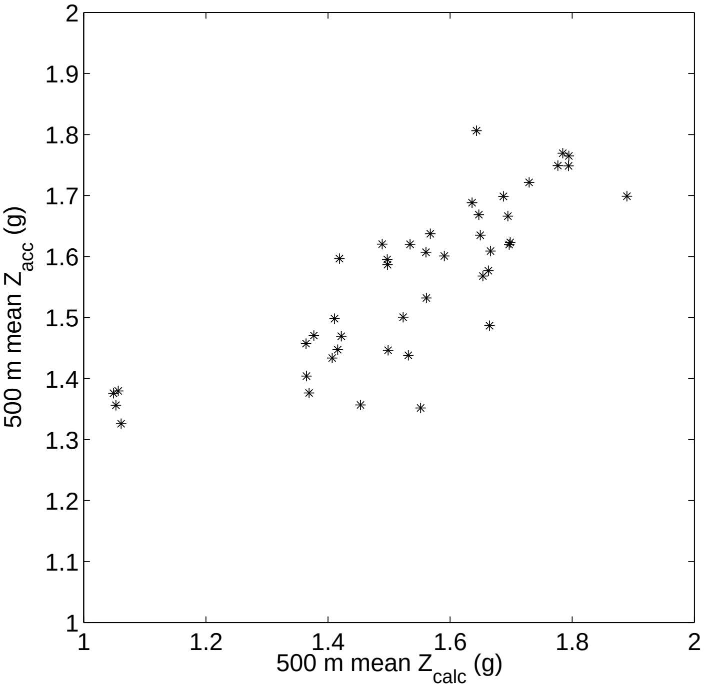

Figure 3.24 Estimate of the 500 m means of Z-axis acceleration estimated from the spectral analysis Z_{calc}, plotted against 500 m means of measurements from the Z-axis accelerometer Z_{obs}.

3.4.4 Suitability of the accelerometer

As shown in the previous sections the accelerometer provides a simple yet robust method of obtaining quantitative information regarding the variation in motion of the instrument package swinging beneath the radiosonde. Prototyping and testing have shown that the accelerometer appears to be stable even in the hostile conditions of the upper atmosphere. Furthermore the information about atmospheric turbulence can still be retrieved from the data even if the instrument package and balloon have entered a resonant oscillatory state. The accelerometer has many advantages over the magnetometer making it a more suitable method for turbulence detection. However such a discussion of results is not complete without a direct comparison of both magnetometer and accelerometer data from the same flight. In total three flights were carried out in this manner, during January 2014.

Figure 3.25 is a flight made during the 14th January 2014. A jet stream is present

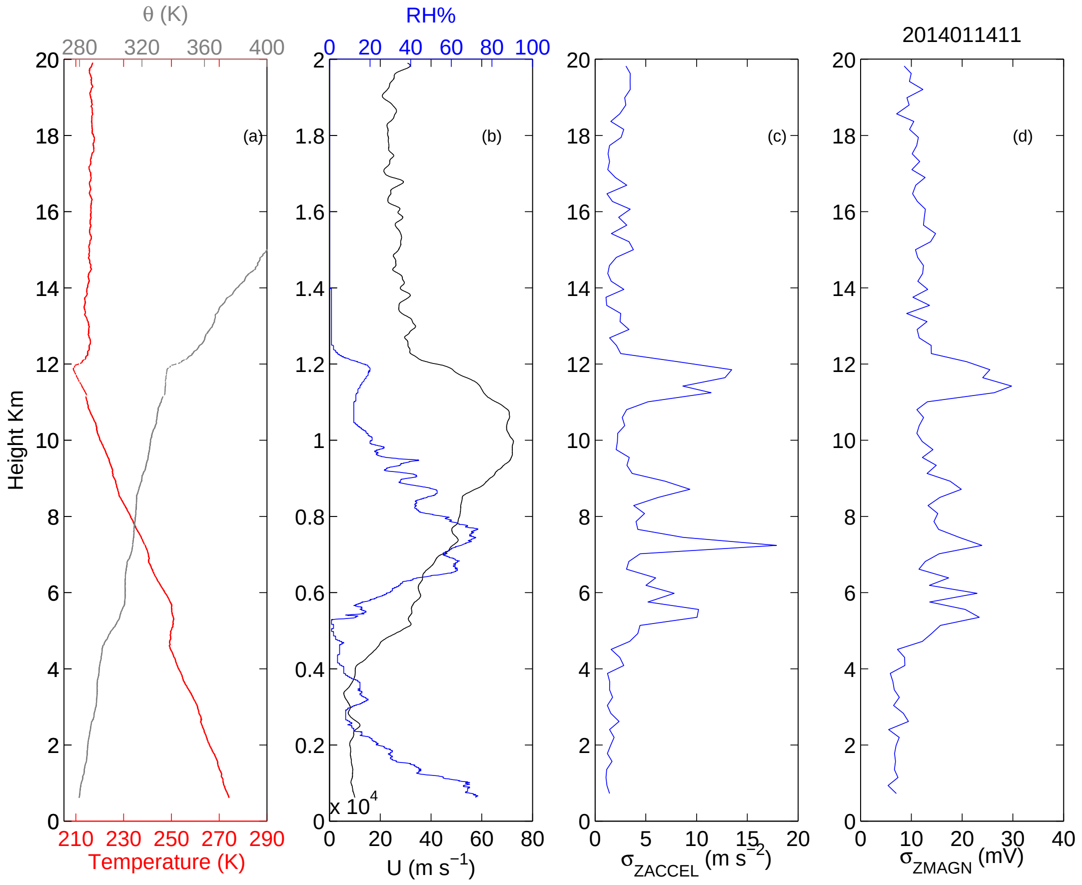

Figure 3.25 Vertical profiles of a) temperature and potential temperature θ (K) in red and grey respectively b) Relative humidity (%), and horizontal wind speed U (m s^{-1}) in blue and black respectively, (c) standard deviation of the Z orientated accelerometer (m s^{-2}) and (d) Standard deviation of the magnetometer voltage (mV) from an ascent RUAO on the 14th January 2014.

between 5 and 12 km, with evidence to suggest a tropopause fold at 5km given a low relative humidity and low temperature gradient. Both the accelerometer and magnetometer had standard deviations taken over 200 m. The two instruments detect turbulence within the jet stream, however the main difference is that the magnetometer's variability did not return to its sub jet stream values. This may be due to it either experiencing the resonant oscillatory state explored in section 3.3.4 or due to a thermal drift increasing the sensitivity of the magnetometer.

Figure 3.26 shows a good level of agreement between the variability in the accelerometer and magnetometer. A Pearson's correlation coefficient of $r = 0.81$ was found between the two instruments for the three ascents. Although a positive correlation was found there is a large amount of scatter. This is due to the magnetometer being a tilt sensing device and hence only providing quantitative information about the orientation of the radiosonde and hence its position, while the accelerometer however provides information regarding the radiosonde's change in direction and intensity of swing. The magnetometers are not as standardised as the accelerometer in that each has a different sensitivity and thermal drift (Harrison and Hogan, 2006). The accelerometers however are more consistent in manufacture, designed to have a given sensitivity. Given the problems demonstrated with the magnetometer, it was decided that the accelerometer gives more useful infor-

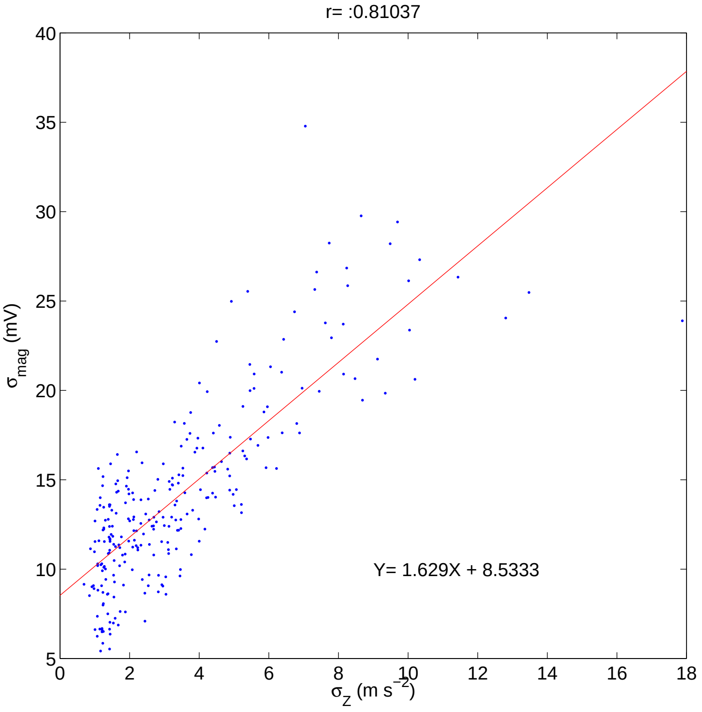

Figure 3.26 A scatter plot showing the standard deviation of the Z-orientated accelerometer (m s^{-2}) plotted against the standard deviation of the magnetometer (mV).

mation about atmospheric turbulence than the magnetometer. The data produced by the accelerometer was easier to use due to the direct calibration of output voltage in g which was reproducible between accelerometers. Although the short string does cause a resonant oscillation in the form of a conical pendulum, its effect can be removed by taking the variability of the accelerometer over a given height range, meaning it can still reliably be used for turbulence observation. In hindsight, the potential effect of shorter string lengths means that more experimental work should have concentrated on testing a variety of string lengths before selecting one for use on all launches in the campaign.

3.5 Modelling the motion of a radiosonde

In order to understand further how the radiosonde and the balloon would behave in the atmosphere, it is helpful to model how changes in the balloon's direction affects the radiosonde's motion beneath the balloon. The equation for a pendulum with a moving pivot in the (x,z) plane as shown in figure 3.27 is given by equation 3.4, which is derived in Trueba et al. (2003) as

$$\frac{\partial^2\theta_p}{\partial t^2}l + \frac{\partial\theta_p}{\partial t}\alpha + X''\cos(\theta_p) + (Z''+g)\sin(\theta_p) = 0, \tag{3.4}$$

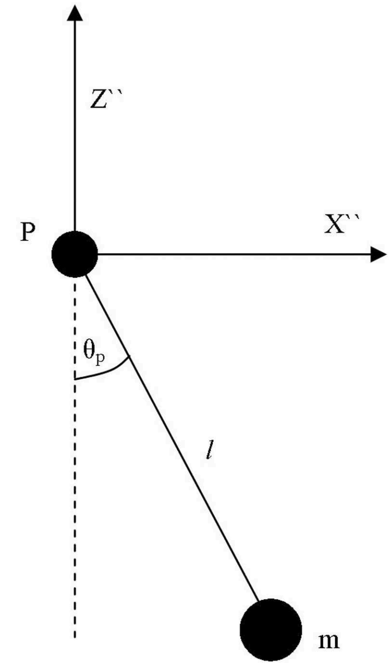

Figure 3.27 Diagram showing the pendulum described by equation 3.4, where P is the pivot, m is the mass, θ_p is the angle away from the vertical, l is the length of the rod between P and m, X'' and Z'' are the accelerations in the horizontal and vertical directions respectively.

where X'' and Z'' are the vertical accelerations of the pivot, α is the damping coefficient and θ_p is the angle of the pendulum mass away from the vertical. This produces a good approximation to what is expected of a pendulum mass being excited by a moving pivot. However in the real atmosphere the balloon is exposed to a 3-dimensional wind vector, hence this model is not sufficient for modelling the balloon and radiosonde. To model a moving pivot in 3D space is much more complex (Mitrev and Grigorov, 2008). Requiring matrix equations and transformations, an intermediate approach is to calculate the angle of the pendulum mass away from the vertical in the X and Y directions. This may be achieved by using equation 3.4 to calculate θ_p in the X direction and calculate ϕ_p the angle at which the pendulum is away from the vertical in the Y direction.

Modelling this system requires the use of two coupled differential equations which are constrained by l_x and l_y the length of the pendulum in the x and y planes respectively. A model for describing the motion of the radiosonde beneath a balloon could be represented by

$$\frac{\partial^2 \theta_p}{\partial t^2} l_x + \frac{\partial \theta_p}{\partial t}\alpha + X'' \cos(\theta_p) + (Z'' + g)\sin(\theta_p) = 0, \tag{3.5}$$

$$\frac{\partial^2 \phi_p}{\partial t^2} l_y + \frac{\partial \phi_p}{\partial t}\alpha + Y'' \cos(\phi_p) + (Z'' + g)\sin(\phi_p) = 0, \tag{3.6}$$

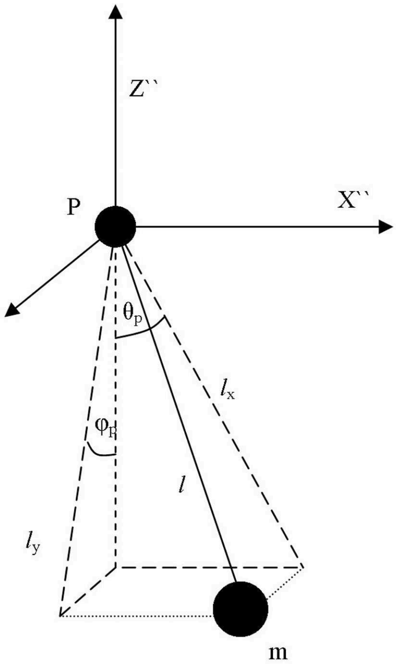

Figure 3.28 Diagram showing the 3D setup of a pendulum system using equations 3.5 and 3.6 to calculate both θ_p and ϕ_p along the X and Y components. l_x and l_y are the X and Y components of the pendulum length l, X",Y",Z" is the acceleration on the pivot in X,Y,Z directions respectively.

where

$$l_x = l\cos(\phi_p), \tag{3.7}$$

$$l_y = l\cos(\theta_p), \tag{3.8}$$

which constrains the problem so that

$$l = \sqrt{l_x^2 + l_y^2}. \tag{3.9}$$

This allows the pivot to be perturbed by 3D acceleration vectors, in a similar method to how the balloon will be affected by changes in wind direction in the atmosphere. Equations 3.5 and 3.6 were numerically integrated using a leap-frog second order numerical scheme with $\Delta t = 0.05$ s. This time-step was chosen to avoid numerical instability that can occur when using large time-steps. A Robert Asselin filter with strength 0.14 (Asselin, 1972) was added to damp computational nodes, which occurs when using such a numerical scheme. For initial experiments the damping coefficient was set to zero, and l=5 m was used as the approximate length between the centre of the balloon and the radiosonde package. To provide accelerations for each axis of these initial experiments, a 30 second time series of velocities sampled at 1 Hz was generated from a Gaussian distribution. The distribution was characterised with a standard deviation of 0.25m s^{-1} for both X' and Y'. X' and Y' were then re-sampled at 20 Hz using interpolation before the numerical gradient was taken to yield X" and Y".

Figure 3.29 shows how the differential equations can be used to model a pendulum bob beneath a pivot which is free to move in all dimensions. However for clarity the trajectory of the pendulum bob is shown in each plane of motion in figure 3.30. Before this model can be used to simulate how a real radiosonde will behave beneath a balloon, the effect of the balloon's size and the damping coefficient α need calculating. A turbulence velocity field also needs creating as well as the virtualisation of the accelerometer and magnetometer.

3.5.1 Modelling the size of the balloon

When a balloon is inflated with helium it can be approximated as a sealed gas parcel. As the balloon rises through the atmosphere the temperature and pressure drop, which causes the balloon to increase in volume. Ultimately this affects the size of l because as the radiosonde beneath swings, the whole balloon rotates as the anchorage point is forced to move, which can be seen in figure 3.31. Hence the pivot is at the centre of the balloon, a larger balloon has a larger radius yielding a larger l. To provide a good estimate of l,

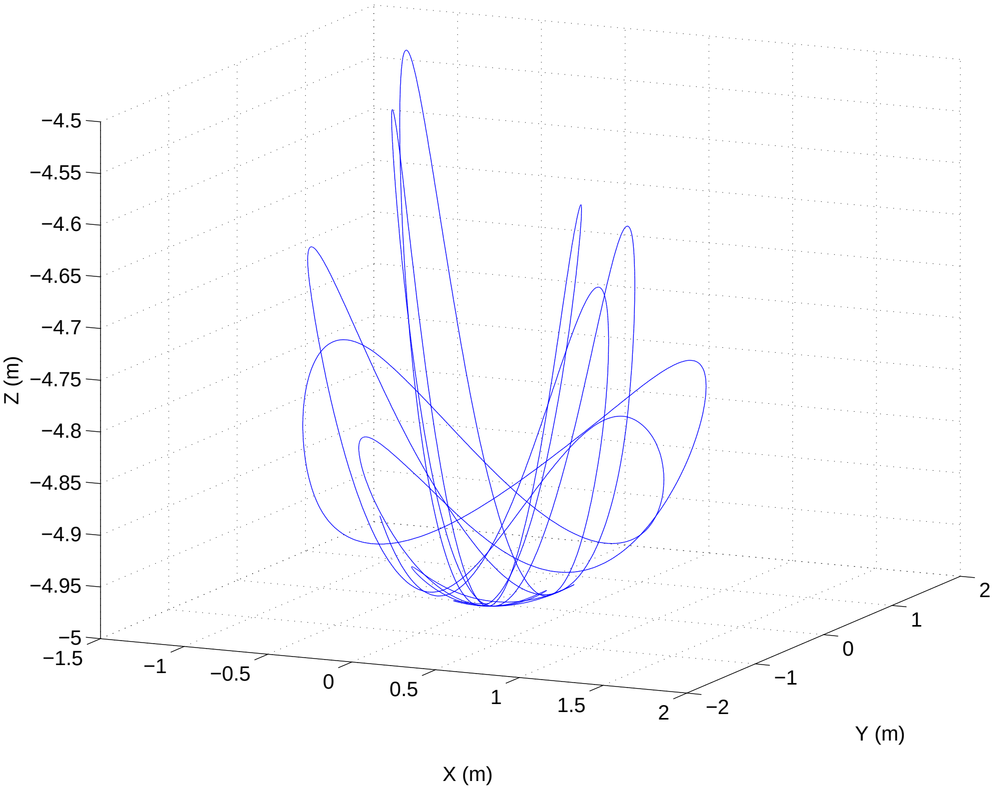

Figure 3.29 3D Trajectory of a pendulum bob beneath a pivot excited by X' and Y' random velocities with a normal distribution of 0.25 m s^{-1}. Distances shown are those of the pendulum mass with respect to the pivot.

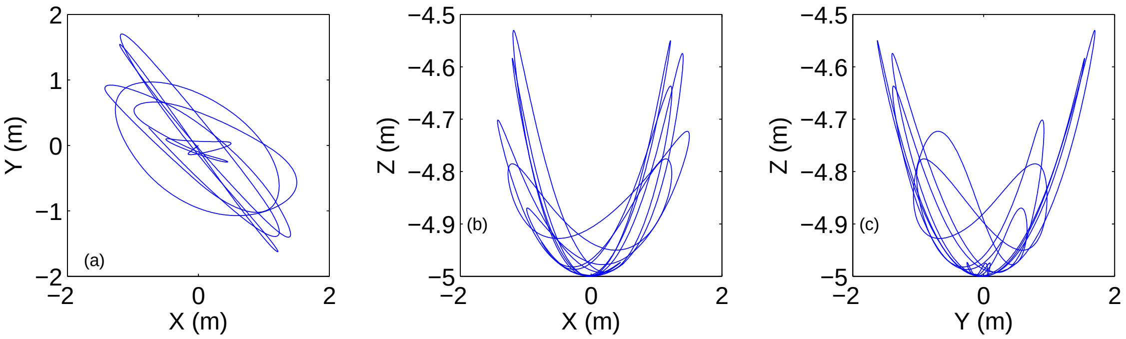

Figure 3.30 Trajectory of a pendulum bob beneath a pivot excited in both the X and Y directions shown in a) the X-Y plane ,b)the Z-X plane and c) the Z-Y plane. Distances shown are those of the pendulum mass with respect to the pivot.

the size of the balloon at a given temperature and pressure needs to be known. A model called the Mooney Rivlin model, detailed in Müller and Strehlow (2004) which is used to simulate the stress and strain on balloon rubber as it inflates is used. To begin simulating an inflating balloon, the pressure balance across an inflated balloon in the atmosphere needs addressing, it is given in Chapman (2012) as

$$P_{out} = P_{in} - \Delta P, \tag{3.10}$$

where P_{out} is the pressure of the environment and P_{in} is the pressure inside the balloon. ΔP is the pressure induced inwards by the balloon rubber and is modelled by the Mooney Rivlin model

$$\Delta P = 2\mu_r \frac{t_0}{r_0} \left(\left(\frac{r}{r_0} \right) - \left(\frac{r}{r_0} \right)^7 \right) \left(1 + \frac{1-\beta}{\beta} \left(\frac{r}{r_0} \right)^2 \right), \tag{3.11}$$

where μ_r is the shear modulus which for a weather balloon is approximated at 300 kPa and $\beta = 0.909$ (Chapman, 2012), r is the radius of the balloon at a given temperature and pressure, t_0 is the relaxed thickness of the balloon rubber approximated to be 0.21 mm. This was achieved by taking taking the mass of the balloon (200 g), the balloon rubber's density and taking the outer radius r_0 of the balloon as it becomes rigid under inflation, which was found to be 0.274 m. Hence the volume of the balloon could be calculated and by assuming a uniform distribution of rubber, the volume of balloon rubber could be subtracted from the volume of the balloon. This yields the volume from the internal walls of the balloon and from this the radius of the internal walls can be calculated. By using the internal and the external radius, the relaxed thickness t_0 was calculated. P_{out} can be input from either an existing radiosonde sounding or from a reference atmosphere such

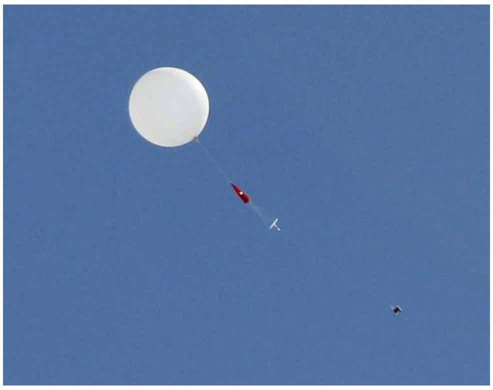

Figure 3.31 Image of Radiosonde mid swing taken above the NERC MST radar site at Aberystwyth Wales on the 3rd March 2015. Photographed by the author.

as the US standard atmosphere (US Standard Atmosphere, 1976). P_{in} can be calculated from knowing the balloon's volume at a given temperature, and the number of moles of gas within the balloon. Hence equation 3.10 can be rewritten as

$$P_{out} - P_{in} + 2\mu\frac{t_0}{r_0}\left(\left(\frac{r}{r_0}\right) - \left(\frac{r}{r_0}\right)^7\right)\left(1 + \frac{1-\beta}{\beta}\left(\frac{r}{r_0}\right)^2\right) = 0, \tag{3.12}$$

where

$$P_{in} = \frac{n_m R^* T}{\frac{4}{3}\pi r^3}. \tag{3.13}$$

n_m represents the number moles of gas present in the balloon. n_m was found to be 53.7 moles by calculating the amount of helium gas supplied into the balloon from the canister using the ideal gas law. This was achieved by noting the regulator pressure before and after the filling of the balloon. By using 3.13, and swapping the denominator for the volume of the canister and assuming that it and the temperature are fixed over the filling period, the drop in pressure then becomes proportional to the amount of moles transferred to the balloon. Here R^* is the ideal gas constant 8.314 m^3 Pa $\text{K}^{-1}\text{mol}^{-1}$. Hence r could be solved for equation 3.12 at a given pressure and temperature in the atmosphere. A pitfall of using this kind of model is that the rubber will continue stretching indefinitely unless a size at which it is to burst is assumed. Information regarding the average burst radius of a 200g balloon is not well documented, but is assumed to be approximately 1.5 m. To check this, a balloon was inflated using a compressor to see at which diameter the balloon burst. The last measurement which was made before burst estimated the balloon to be 1.46 m.

Using temperature and pressure data from a small selection of ascents to input into the balloon size model allowed the model to predict the maximum radius of the balloon before bursting. This, is shown in figure 3.32, the majority of the ascents burst when the balloon is predicted to have a radius of 1.6 m. This combined with information from the experiment in which a balloon was inflated gives a good level of confidence in the balloon radius at bursting point and in the balloon model to estimate balloon size during an ascent.

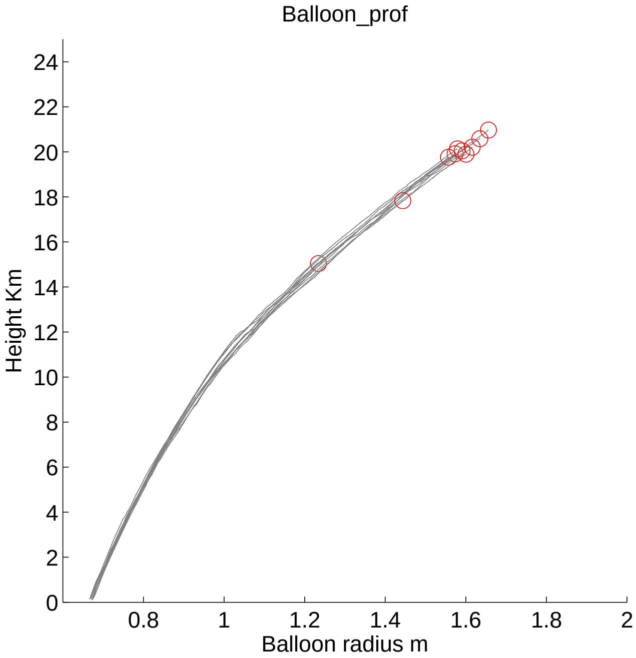

Figure 3.32 10 randomly selected radiosonde ascents from which pressure and temperature data were used to estimate the size of balloon with height. Red circles mark where the balloons burst.

3.5.2 Estimating the dampening coefficient

In order for the model to be as realistic as possible, a damping coefficient α is required in equations 3.6 and 3.5. The damping coefficient was calculated by using data collected during the prototype stage in section 3.4.1. The accelerometer package was agitated and then let to come to rest, and the data was filtered to give local maxima in the Z-axis accelerometer data. Hence α could then be found by fitting the following to the local maxima in the Z-axis accelerometer data

$$Z_{acc}(t) = \max(|Z_{acc}|)e^{-\alpha t}. \tag{3.14}$$

Figure 3.33 shows equation 3.14 fitted to the data, from which a damping coefficient of α=0.07 s^{-1} is calculated. However in flight the radiosonde is constantly ascending, which has not been emulated in this test. Another approach to estimating the in-flight dampening coefficient would be to use in flight accelerometer data and calculate the dampening coefficient. This can be achieved by fitting equation 3.14 to parts of the profiles where the subsequent magnitude of local maxima in the accelerometer were decreasing. By taking an average over multiple events in which this occurred, an $\alpha = 0.605 \pm 0.006\mathrm{s}^{-1}$ was found. This value is significantly higher than that found experimentally using the

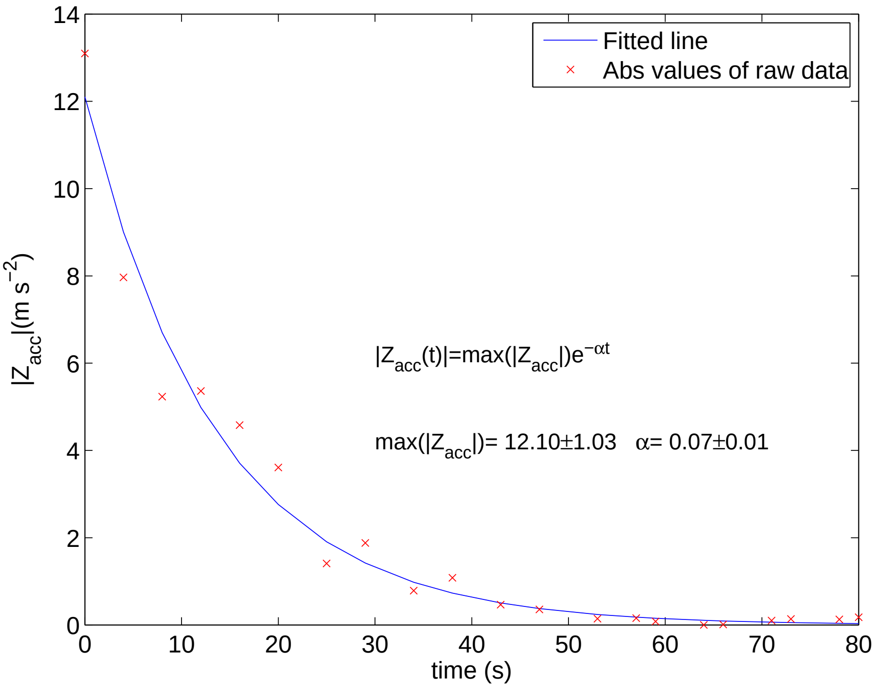

Figure 3.33 Absolute values of local minima and maxima accelerations measured from the Z-axis accelerometer $|Z_{acc}|$ (g) during prototype testing, in which the instrument package was agitated and allowed to come to rest, when suspended 4 m from a mast.

mast in the prototype testing. In total, 1606 dampening coefficients were used in this sample. There is high confidence in these in flight values due to the large sample size and small standard error.

3.5.3 Choosing a 3D velocity vector

In order to emulate how the instrument package will react on an encounter with turbulence, one needs to provide a 3D turbulence velocity field. As discussed in chapter 1 a turbulence velocity time series is characterised by a -5/3 law in the velocity spectra. From the three remote sensing methods discussed in chapter 2, data from a lidar would be most suitable due to a high vertical resolution of 30 m, and a 3D wind profile. However the variability is taken over time-scales of 30 minutes meaning they are not suitable due to poor temporal resolution. Another technique would be to take a vertical profile from a large eddy simulation. Danny (2009) used a Large Eddy Simulation (LES), which uses very fine spatial and temporal resolutions over small domains to effectively resolve turbulent eddies. However this would require firstly the acquisition and setup of a LES model, as well as the computational resources to run it, which is beyond the scope of this project. An alternative is to use data from a sonic anemometer. Sonic anemometers can be used to measure the small rapid fluctuations in wind speed in three dimensions at high frequency using ultrasound (Harrison, 2014). A Gill sonic anemometer stationed at the RUAO measures the 3D wind vector at 20Hz resolution. A time series from July 2013 was examined by truncating it into smaller 600 second time series. A FFT was used to generate a power spectrum, to which a power law could be fitted. Truncated time series which had a fitted power law of -5/3 were selected. These time series were treated as synthetic 3D vertical profiles of wind speed. Given the model operates on a time step of 0.05 s, the synthetic wind profile just needed differentiating to generate 3D accelerations.

3.5.4 Modelling the response of the magnetometer and accelerometer devices

To appreciate how the sensors behave within the model, their response based on the position, orientation and velocity of the virtual radiosonde is required. The position of the sensor package in relation to the moving pivot point within the balloon is given by:

$$s_x = l_x \sin(\theta_p), \tag{3.15}$$

$$s_y = l_y \sin(\phi_p), \tag{3.16}$$

$$s_z = l_y \cos(\phi_p), \tag{3.17}$$

where θ_p and ϕ_p are the angles of the pendulum away from the vertical in the X and Y directions respectively. Knowing the position of the instrument package allows its actual orientation from the vertical γ to be found using

$$\gamma = \tan^{-1}\left(\frac{s_z}{|s_x| + |s_y|}\right). \tag{3.18}$$

By knowing the virtual instrument package's angle of orientation, a virtual magnetometer voltage can be emulated using the relationship between the angle of the magnetometer, and its voltage change shown in figure 3.9. The accelerometer response is somewhat more complex to model, as the acceleration vector of the virtual radiosonde must first be calculated. The string is assumed taut so any acceleration on the balloon at that point must also be taken into consideration to give

$$X''_{sonde} = X'' + s''_x, \tag{3.19}$$

$$Y''_{sonde} = Y'' + s''_y, \tag{3.20}$$

$$Z''_{sonde} = Z'' + g + s''_z. \tag{3.21}$$

Where X''_{sonde},Y''_{sonde} and Z''_{sonde} are the accelerations of virtual radiosonde in the X,Y and Z directions respectively. Figure 3.12 shows that the accelerometer is in a fixed orientation so the three orthogonal accelerations calculated in equations 3.19 , 3.20 and 3.21 need reorientating onto the accelerometer's axis at that given orientation given by γ, θ_p and ϕ_p using

$$X''_{accel} = X''_{sonde}\cos(\theta_p) + Z''_{sonde}\sin(\theta_p), \tag{3.22}$$

$$Y''_{accel} = Y''_{sonde} cos(\phi_p) + Z''_{sonde}\sin(\phi_p), \tag{3.23}$$

$$Z''_{accel} = \sqrt{(X''_{sonde})^2 + (Y''_{sonde})^2}\sin(\gamma) + Z''_{sonde}\cos(\gamma), \tag{3.24}$$

where X''_{accel},Y''_{accel} and Z''_{accel} are the accelerations experienced along each axis of the virtual accelerometer. By applying this to the data after the model has been run it allows the simulation of motion sensing instruments on the virtual radiosonde.

3.5.5 Constructing the meteorological profile and running the model

As discussed in section 3.5.1, the pressure and temperature at a given point of a virtual ascent are important for calculating balloon size. The length of the 3D wind data time series is 600 s at 20 Hz sampling. With the assumption of a vertical ascent speed of a balloon of 5 m s^{-1} a temperature and pressure profile of height 3 km is needed. Given that this is exclusively in the troposphere and ignoring the thermodynamics of the boundary layer structure, the temperature profile can be represented by the dry adiabatic lapse rate. This means that the pressure could be found by numerically integrating the hydrostatic balance equation at each $\Delta t = 0.05$ which corresponds to a Δz of 0.25 m. The increased time step from the initial model used was short enough to circumnavigate issues of numerical stability yet long enough that the wind data would not need oversampling.

The model was run in the following fashion. First the meteorological profiles of temperature and pressure were constructed assuming a surface pressure of 1000 hPa and a temperature of 8^{o}C. This temperature was chosen as the temperature at which the constants used in the balloon rubber equations were calculated. The time series of wind data becomes the u, v and w components of the wind with height. These are then differentiated to give accelerations that will act on the balloon (It has been assumed that the balloon will mimic these accelerations through to the pivot point). The position of the virtual radiosonde with respect to the balloon is then calculated as it rises through the model atmosphere to 3km. After this equivalent values for the virtual instruments are created.

Figure 3.34 shows that the model makes a good approximation of the motions typical of the sonde beneath the balloon. Panel (d) shows regions of the ascent with high variability in horizontal wind. The highest horizontal wind variance is at 500 and 2000 m, it is in these regions where the turbulence intensity is highest. In panel (b) the virtual accelerometer gives a similar signal to that from actual observations of turbulence (figure 3.17, etc.) in these regions. Here the magnitude of the X and Y accelerometers have been combined, as the x and y axis of the accelerometers in relation to the X and Y axis are unknown on a real radiosonde. However, high variability is still witnessed in the combined axis values when encountering turbulence in heightened regions of σ_U. The

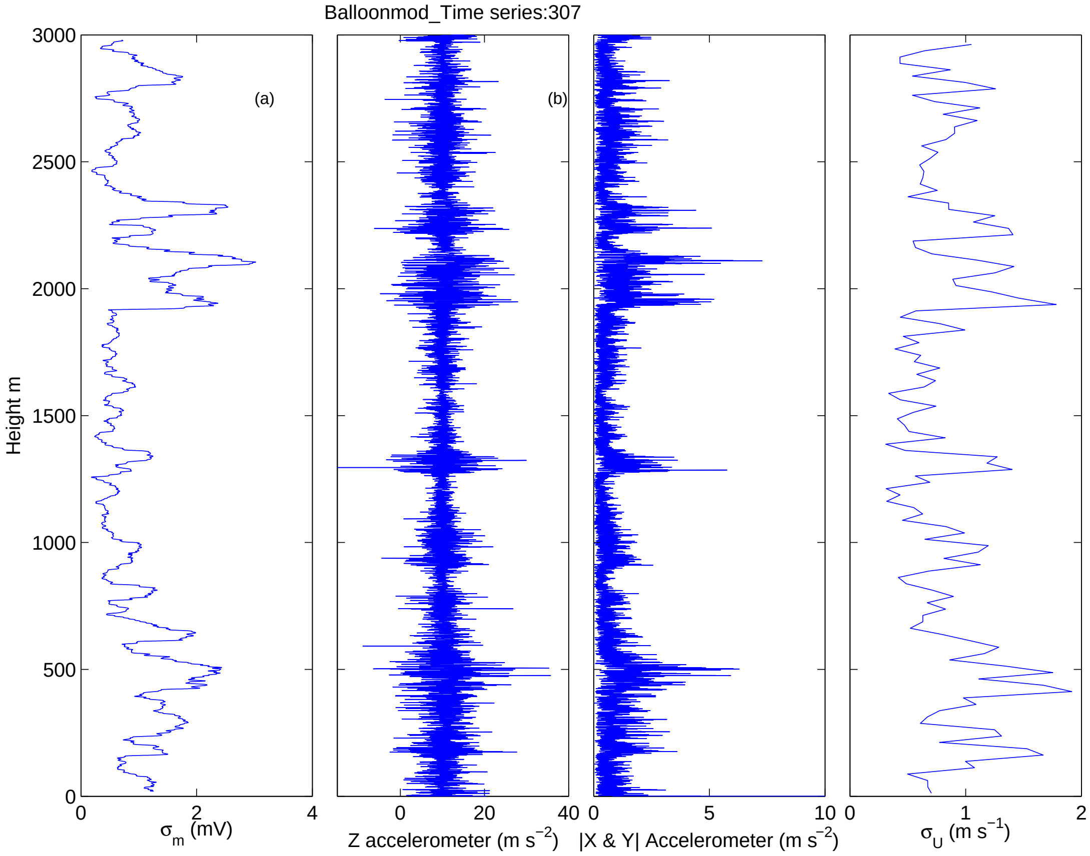

Figure 3.34 Vertical profiles of a) standard deviation of model magnetometer taken over 8 seconds (mV), b) Z-axis virtual accelerometer (m s^{-2}), c) combined magnitude of X and Y virtual accelerometers (ms^{-2}) and d) the standard deviation of the horizontal windspeed over 25 m σ_U (m s^{-1}).

standard deviation of the magnetometer however was smaller than observed in figure 3.8, for example. This could be due to the fact that the equation used to model the magnetometer being computed under laboratory conditions was not affected by the radiosonde's radio transmitter.

This model, whilst excellent in highlighting how the physics of a dynamic system which is the balloon and radiosonde work, is not perfect. Firstly if $\theta_p > 90^o$ or $\phi_p > 90^o$ the system becomes unstable due to equations 3.7 and 3.8 not being able to represent the l. Whilst this is incredibly unlikely[2] to happen to a balloon and radiosonde in the atmosphere it addresses the limits of the model. Secondly as discussed in section 3.4.3 the sonde can enter a resonant oscillatory mode where it exhibits the behaviour of a conical pendulum. This may not have been detected within the balloon model as centrifugal acceleration was not addressed directly. One method to include it would be to include an additional force and hence an acceleration in the Z-axis of the accelerometer in the latter stages of the model when sensors are virtualised. However further testing is needed to examine whether this added force would have feedback effects on the system. Technically the force should be taken up as tension in the balloon string, but given there are no fixed points in this system this may not be valid. Furthermore as it is still unknown what causes the resonant oscillation it is difficult to emulate the agitation needed on the balloon to get the desired resonant oscillatory effect.

3.6 Solar radiation sensor for cloud detection

Being able to detect turbulence is one thing, however having some indication of what kind of turbulence the radiosonde is ascending through is another. Here a brief description is given of how an optical measurement is added to the sensing package to gauge whether the radiosonde is in or above the clouds. Traditionally, methods of detecting clouds with radiosondes rely on the relative humidity sensors. The time response of a humidity sensor is not fast, it ranges from 5-10 seconds and becomes larger especially at low temperatures. This makes it difficult to infer a region of cloud from a region of enhanced RH alone. Here a passive optical sensor taking the form of a photodiode, described in Nicoll and Harrison (2012) is added to the motion sensing package. The photodiode is sensitive to light in the visible range with a spectral peak at 580 nm and has been calibrated against a standard pyranometer to give values of solar radiation in W m^{-2}. Cloud edges can

---

[2] Some radiosonde operators have reported radiosondes looping the balloon just after launch from ships in extreme conditions

be found by looking for increases in variability in the photodiode output, Harrison et al. (2016a) contains a more in depth discussion of using the photodiode to make observations of solar radiation.

Figure 3.35 shows standard meteorological data and solar radiation data from an ascent on the 23rd January 2013. As the balloon passes through the cloud, the variability from the photodiode increases sharply at 1600 m indicating a sharp cloud edge. In panel (a) the RH sensors are somewhat slower to respond. The large variability occurs due to the swinging of the radiosonde causing the photodiode to be constantly pointing in different directions, some in direct sunlight and others in the shadow of the balloon. This sensor will be used in the following chapter to identify regions of cloud.

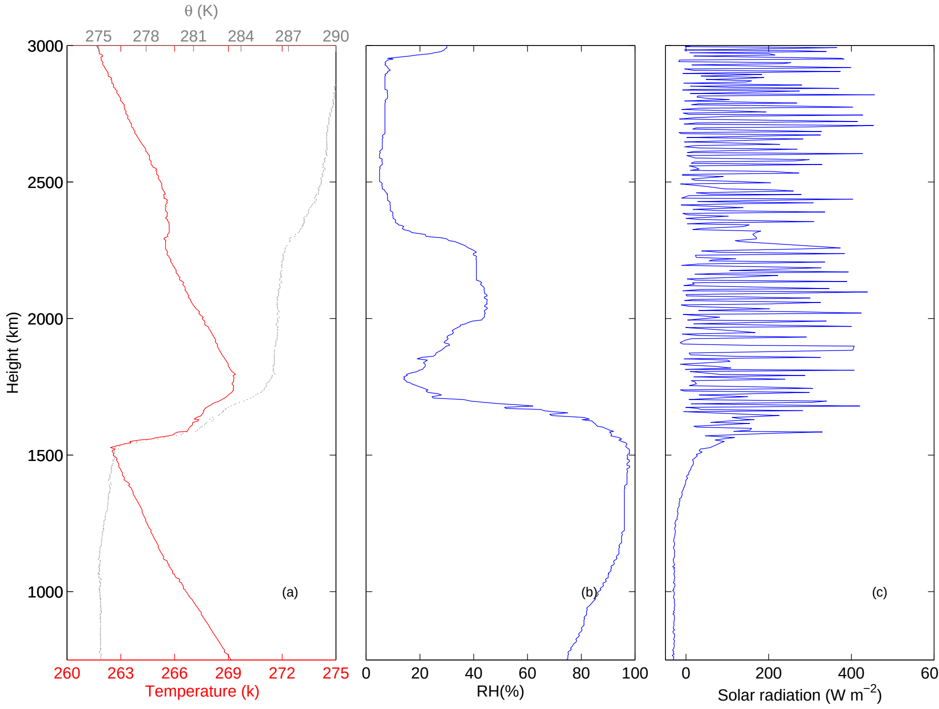

Figure 3.35 Vertical profiles of a) temperature and potential temperature θ (k) in red and grey respectively, (b) relative humidity (%) c) Solar radiation from the photodiode (W m^{-2}) between 750 and 3000m from an ascent made on 23rd January 2013 from RUAO.

3.7 Conclusions

It has been shown that a balloon and radiosonde form a dynamical system of a pendulum with a moving pivot which can move in all degrees of freedom. If the balloon is agitated by turbulence the radiosonde hanging below can swing. Two methods to measure the motion of the radiosonde have been tested and implemented, with the accelerometer technique preferred over that of the magnetometer. Due to better repeatability, less thermal drift and less susceptibility of the accelerometer to radio noise interference is observed. The string length between the radiosonde and the balloon was set to l=4 m to increase the pendulum system's sensitivity to turbulence. The magnetometer method suffered further from this as its variability increased with height. This was due to the radiosonde oscillating like a conical pendulum when not experiencing turbulence. The accelerometer did measure the oscillation, but by taking the standard deviation the effect could be removed. Lab calibration by orientating the accelerometer with respect to gravity showed the accelerometer produced repeatable results. A balloon model was created to attempt to understand more about the physics of the pendulum system. Much was learnt about the forces and factors that act on a radiosonde in flight by mathematically considering them.

Chapter 4

Comparisons of the accelerometer with remote sensing methods

In the previous chapter it was shown that atmospheric turbulence could be detected by a radiosonde. This was achieved by adding an accelerometer device to measure the motion of the radiosonde as the balloon is agitated by atmospheric turbulence. It is now important to understand how the accelerometer device responds to turbulence in comparison to current methods of turbulence observation. In chapter 2 many turbulence detection methods were discussed, here a comparison with three remote sensing methods will be shown. The first will be with a boundary layer lidar, the second with a zenith pointing Doppler radar and finally a comparison with an MST radar.

4.1 Comparing the accelerometer device against a Doppler lidar

In this section a comparison is made between a boundary layer Doppler lidar and the accelerometer sonde. This work is summarised in Marlton et al. (2015) but here a more in depth discussion of the work is undertaken. A Halo Photonics pulsed Doppler lidar was used to compare the accelerometer's response to turbulence. The instrument is situated within the meteorological enclosure at the Reading University Atmospheric Observatory (RUAO) (51.44^o N, 0.938^o W). Between October 2013 and March 2014, 13 flights were made from the RUAO whilst the lidar was operating. Turbulence comparisons with the Doppler lidar are limited to the boundary layer, meaning at best, a maximum of two km from the Earth's surface. If cloud is present, the lidar's beam becomes quickly attenuated, meaning it cannot penetrate the cloud base, therefore the height over which comparisons can be made is further reduced. The lidar uses a near-visible laser beam of 1.5 μm which is backscattered by aerosols. The shift in backscattered signal from the aerosol allows the lidar to infer information about the radial velocity along the beam.

The lidar at RUAO takes a vertical profile of the radial vertical velocity at near 1 Hz sampling. It can also make measurements of horizontal wind components using a Doppler Beam Swing (DBS) method, as described in Lane et al. (2013). The lidar makes two off-vertical radial velocity retrievals combined with the standard vertical retrieval. This allows the vertical wind component of the off vertical beams to be removed leaving both the u and v horizontal components for each beam respectively, so that

$$u = \left(V_x - V_z \cos(\psi)\right), \tag{4.1}$$

$$v = \left(V_y - V_z \cos(\psi)\right), \tag{4.2}$$

where V_x and V_y are the radial velocities along the off vertical beams in the x and y directions respectively and ψ is angle of the off vertical beams. For this campaign, the lidar was configured to make DBS wind profile measurements every 4 minutes.

4.1.1 Calculating turbulence properties using Doppler lidar

The eddy dissipation rate, ϵ may be calculated from the vertical wind velocity measured by the lidar. There are two methods through which this can be achieved. The first is to fit a power law to a power spectrum of the vertical velocity time series. ϵ is then calculated by fitting equation 1.2 to the power spectra, assuming a -5/3 law is present. An alternative method, described in (O'Connor et al., 2010), takes the integral of equation (1.2) over two length scales characterised by the lidar's sampling characteristics giving

$$\epsilon = 2\pi \left(\frac{2}{3\alpha_k}\right)^{\frac{3}{2}} \sigma_v^3 \left(L_0^{\frac{2}{3}} - L_1^{\frac{2}{3}}\right)^{-\frac{3}{2}}, \tag{4.3}$$

where σ_v is the standard deviation of the vertical velocity over N_s sampling periods α_k=0.55, which is Kolomogrov's constant. L_0 and L_1 are given by:

$$L_1 = Ut_d \tag{4.4}$$

$$L_0 = N_s U t_d \tag{4.5}$$

Where L_0 is an estimate of the length scale of the largest eddies in the inertial sub-range that the lidar can observe. L_1 corresponds to the smallest eddies that the lidar will be able to observe. U is the horizontal wind speed retrieved from the lidar's DBS wind profile. Finally t_d is the dwell time, the period over which the lidar takes the radial wind profile along the beam. O'Connor et al. (2010) advise calculating a spectrum where possible to complement the standard deviation method. Lidar data will be used for the 30 minutes centred about launch time. This minimises co-location effects, which occur as the radiosonde drifts away from the launch site. Data from the lidar's first three range gates were neglected as it contains instrumental noise. The signal to noise ratio (SNR) from the lidar is used to remove any spurious values, such as an inadvertently sampled cloud base.

4.1.2 Lidar comparison using standard deviation technique

ϵ was calculated using a 60 second window, using equation 4.3 to provide ϵ at 1 minute resolution at all available range gates. The length scales were calculated using a t_d of 1.2 seconds, with an N_s of 50 samples. If N_s was less than 25 the ϵ value would be removed. An average value of U was taken from the DBS profiles before and after the sample period in question.

The ϵ values were averaged temporally at each height gate, however, due to the logarithmic nature of the values, a geometric mean centred half an hour on launch time was taken. A geometric mean was then taken over the 210 m height windows, which equates to seven of the lidar's range gates. If less than 50% of the values at each range gate or over each height window were missing, then the value would be removed due to unfair representation of the atmosphere. The Z-axis accelerometer had a standard deviation taken over the same 210m. To refine the comparison, some ascents were removed as they presented unrealistic conditions, such as unnaturally large values of ϵ, in total 5 ascents were removed in this manner. For clarity, an unrealistic value of ϵ would be 1 $\mathrm{m^2s^{-3}}$. A realistic ϵ value within the boundary layer would be of the range 10^{-4} to 10^{-2} $\mathrm{m^2s^{-3}}$. The reason these unrealistic conditions occurred is unknown; it may be due to the fact a-5/3 law is assumed for all calculations. If equation 4.3 is being used when the -5/3 law is not present, then this may result in an incorrect ϵ. Given the low height of the boundary layer in the winter months this limited each ascent yielded only 2-3 data points.

Figure 4.2 shows the standard deviation of the accelerometer data, plotted against height averaged $\log_{10}(\epsilon)$ from the Doppler lidar. Error bars in figure 4.2 for ϵ were created

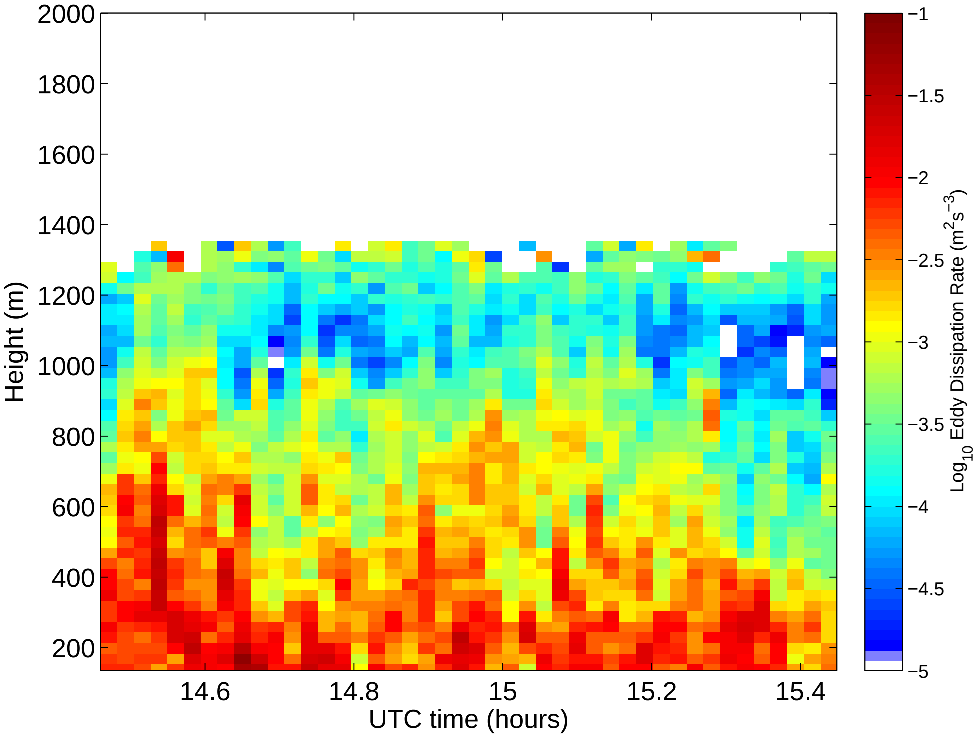

Figure 4.1 $\log_{10}\epsilon$ calculated from a Halo photonics pulsed Doppler lidar at RUAO using the velocity variance, technique between 1430 and 1530 UTC on 14th November 2013. Gaps where DBS sweeps were made have been removed.

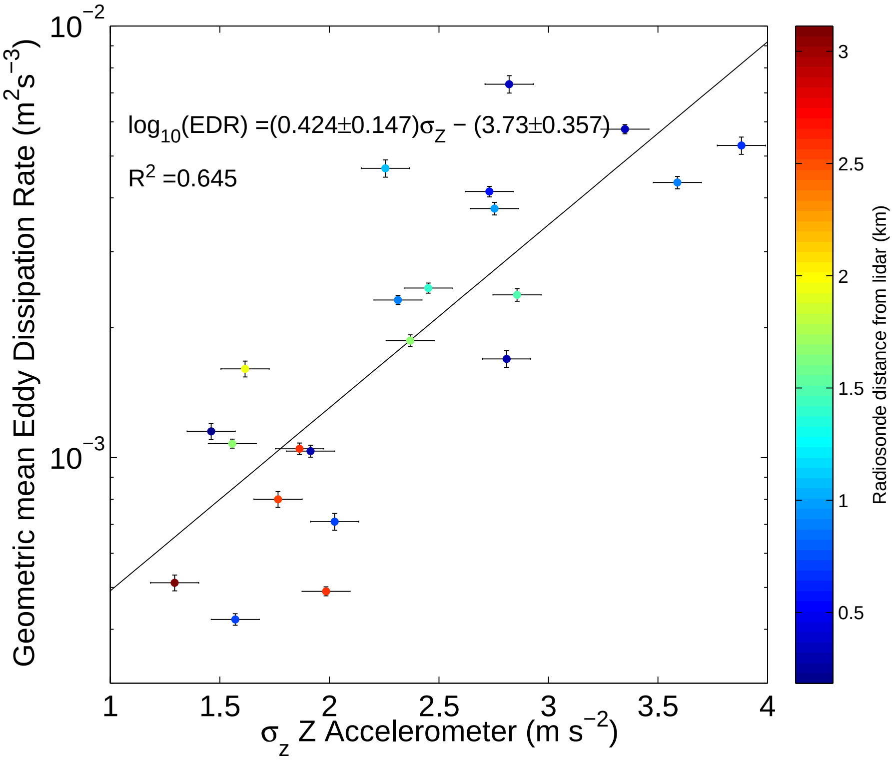

Figure 4.2 The lidar-derived geometric-mean eddy dissipation rate ϵ in ($\mathrm{m^2s^{-3}}$) plotted on a $\log_{10}$ scale against the standard deviation of the vertical accelerations over a 210 m height window from 9 flights through the boundary layer from RUAO. The coloured points show the distance of the radiosonde from the lidar at the time the height averaging was undertaken. Adapted from Marlton et al. (2015)

.

using the error analysis shown in O'Connor et al. (2010), which uses the signal to noise ratio of the return beam to generate an error. Due to the logarithmic nature of the data, errors were recalculated in terms of a fractional error. The error on the accelerometers is derived as the sensitivity at 1mV, which corresponds to 0.07 m s^{-2}. In the comparison, 5 ϵ values below that of 1×10^{-4} m^2s^{-3} were removed as the balloon did not show any response to a turbulence intensity this weak despite spanning two orders of magnitude. Without theoretical predictions of what should be expected, the lowest order statistical model is used. A least square first order fit was fitted to the data. The linear response was found to be $\log_{10}(\epsilon) = (0.424 \pm 0.147)\sigma_z - (3.73 \pm 0.357)$ and the goodness of fit was found to be $R^2 = 0.645$. The R^2 value demonstrates the validity of using such a statistical model. The reason for the scatter of points is most likely due to the lack of co-location between the radiosonde and lidar. It is apparent that the balloon will only react to turbulence above a certain intensity. From this comparison it would appear that an approximate figure for this turbulence threshold could be 3×10^{-4} m^2 s^{-3}. As previously mentioned, the downfall with this method is that it makes assumptions that a spectral law is present. Further work will focus on calculating ϵ from vertical velocity spectra.

4.2 Calibrating the accelerometer device against Doppler cloud radar

Between the 8th and 15th August 2014, an intensive observation period was carried out at the Atmospheric Radiation Measurement Mobile facility based in Hyytiala, Finland (61.83^oN,24.83^oE). At this temporary site, a suite of remote sensing instruments was available. The three radars used in this section are a Doppler zenith pointing Ka-band cloud radar, an X-band and a Ka-band scanning radar. The objective was to use the Doppler radars to calculate in-cloud turbulence parameters which could be compared with that from the accelerometer.

The zenith pointing Ka-band radar made constant vertical profiles of the atmosphere above. The two scanning radar cycled through different scanning configurations, meaning

Radar type	Operating frequency	Approximate Wavelength λ
Ka	35 GHz	10mm
X	9 GHz	3cm

Table 4.1 The two operating frequencies and wavelengths of the two radar types used at the ARM mobile facility at Hyytiala Finland.

they may not necessarily make a retrieval through the cloud that a radiosonde is traversing. Turbulence comparisons were made using the zenith pointing radar using the radial velocity along the beam. ϵ can be calculated using a similar method shown in section 4.1, however, as the radar has a larger beam width, a slightly different method, as shown in Bouniol et al. (2004), is used. Instead of bounding the inertial sub-range with length scales, it is bounded by wave number k, by

$$\epsilon = \left(\frac{2}{3\alpha_k}\right) \frac{\sigma_v^3}{\left(k_0^{-\frac{2}{3}} - k_1^{-\frac{2}{3}}\right)^{\frac{3}{2}}}, \tag{4.6}$$

where σ_v is the standard deviation of the vertical velocity over the sampling period and k_1 is the wave number equivalent to half the radar's operating wavelength. k_0 is the wave number equivalent to the length scale of advected air passing though the pulse volume over the sampling period and is given by

$$k_0 = \frac{2\pi}{2z_r \sin(\theta_b/2) + t_d|U|}, \tag{4.7}$$

where z_r is range from the radar, θ_b is the beam width of the radar and U is the horizontal wind speed which can be obtained from a NWP model (Bouniol et al., 2004). The ϵ values are provided by post processing from the radar.

4.2.1 Initial results from comparison with Doppler radar

In this section, two case studies of turbulence comparisons are shown; one through an ice cloud and one through a frontal cloud. The first case study was on the 9th August 2014 at 0745 UTC, through an ice cloud. The Ka-band radar reflectivity in the top panel of figure 4.3 shows an ice cloud between 6 km and 9 km. The ice cloud has a wide extent giving a high degree of certainty that the radiosonde passed through the cloud. The reflectivity is quite low throughout the ice cloud, peaking about the base. The vertical velocity indicates that the ice crystals and droplets within the cloud are falling towards the radar. Smith and Jonas (1996) discussed how turbulence could potentially occur at the base due to the evaporation or condensation of droplets and crystals. It was also found that cloud top turbulence can occur due to the radiative cooling of the cloud top.

Figure 4.4 shows that the radiosonde passed through the same ice cloud, indicated by the relative humidity in panel (a). The accelerometer aboard the radiosonde also encountered turbulence at similar height to the cloud edges shown in figure 4.3. At the

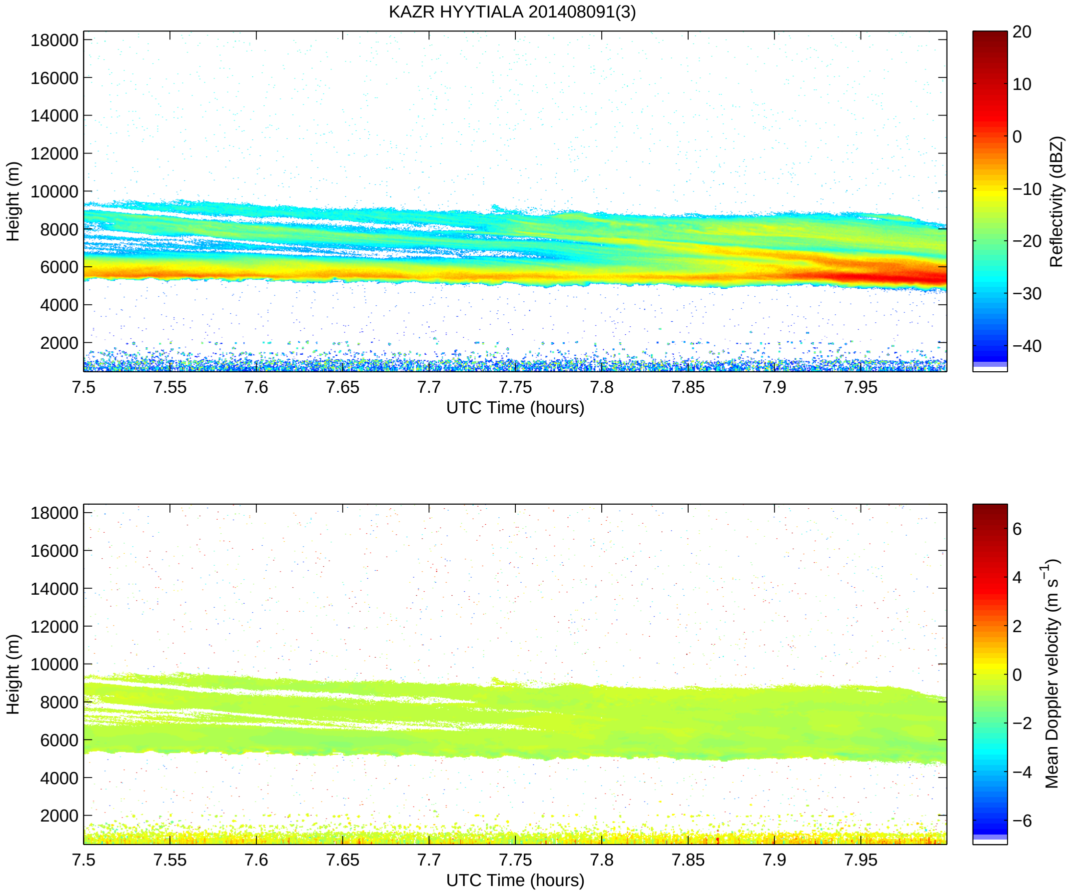

Figure 4.3 Radar reflectivity (dBZ) (top) and mean Doppler velocity (bottom) between 0730UTC and 800UTC from the zenith pointing Ka-band radar at Hyytiala, on 9th August 2014.

cloud base, both the sonde and the radar both registered turbulence; the accelerometer registered a standard deviation of 6 m s^{-2} and the radar registered an ϵ of magnitude 10^{-4}m^{2}s^{-3}. The accelerometer detected more intense turbulence at a lower altitude, but the radar can only see within the cloud and no comparison can be made. The centre of the cloud was relatively non-turbulent as indicated by the accelerometer values, and the radar reported $\epsilon = 10^{-8}$ to 10^{-6}m^{2}s^{-3} which are considered very small values of eddy dissipation rate. At the cloud top the accelerometer detects another region of turbulence, however, the radar cannot provide an eddy dissipation rate due to a lack of velocity information.

The next case study examined took place on the 12th August 2014, where a frontal cloud with precipitation passed over Hyytiala. In figure 4.5 the radar reflectivity shows the cloud spanning from approximately 2.5 km up to 10 km. The radar also picked up precipitation falling from the cloud base to the ground. Given how uniform the cloud was in the launch window shown, there is no doubt that the radiosonde traversed the cloud.

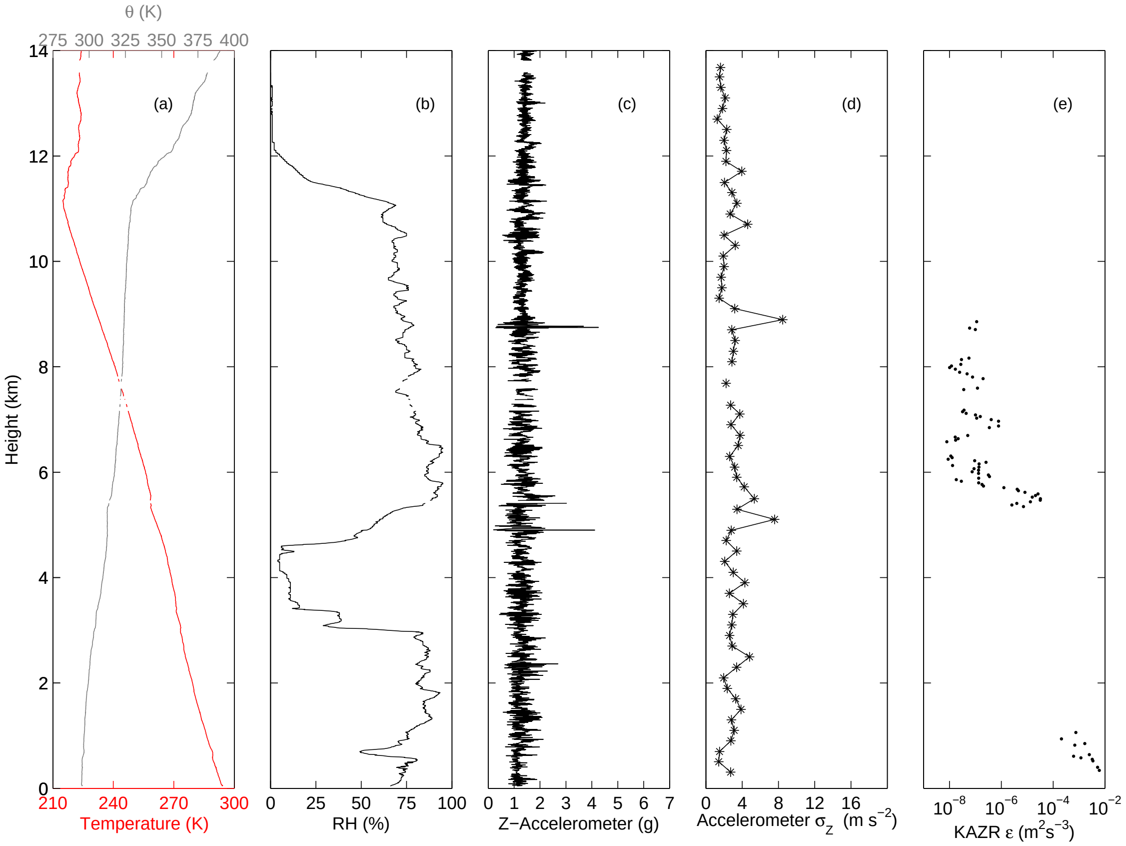

Figure 4.4 Vertical profiles of a) temperature and potential temperature (K) in red and grey respectively, b) relative humidity (%) c) Z-axis accelerometer (m s^{-2}), d) standard deviation of the Z-axis accelerometer over 200m for a accelerometer sonde ascent at 0745UTC on 9th August 2014 from Hyytiala. e) Radar derived ϵ (m^{2}s^{-3}) from a zenith pointing Ka-band radar based at the same location.

Radar reflectivity is significantly higher than shown in the previous example in figure 4.3. The mean Doppler velocity in the bottom panel is of particular interest. Firstly, between the ground and cloud base the large positive velocities are due to a phenomena known velocity aliasing, or Doppler folding. This aliasing occurs when the Doppler shift becomes so large, it appears that the target is moving in the opposite direction (Doviak and Zrnic, 2014). Above the cloud base the Doppler velocity shows that the majority of the droplets within the cloud are falling at a speed of 2 m s^{-1}. At heights between 7-8 km and above the Doppler velocity indicates a mix of both upward and downward velocities, implying turbulence near the cloud top. This may be due to in-cloud processes, such as embedded convection, and up-drafts and down-drafts which Houze Jr et al. (1976) showed are present in frontal clouds. Furthermore, there may be synoptic conditions which could also be causing turbulence (Keyser and Shapiro, 1986).

Figure 4.6 shows that upon entering the cloud at 2.5 km the balloon and radiosonde

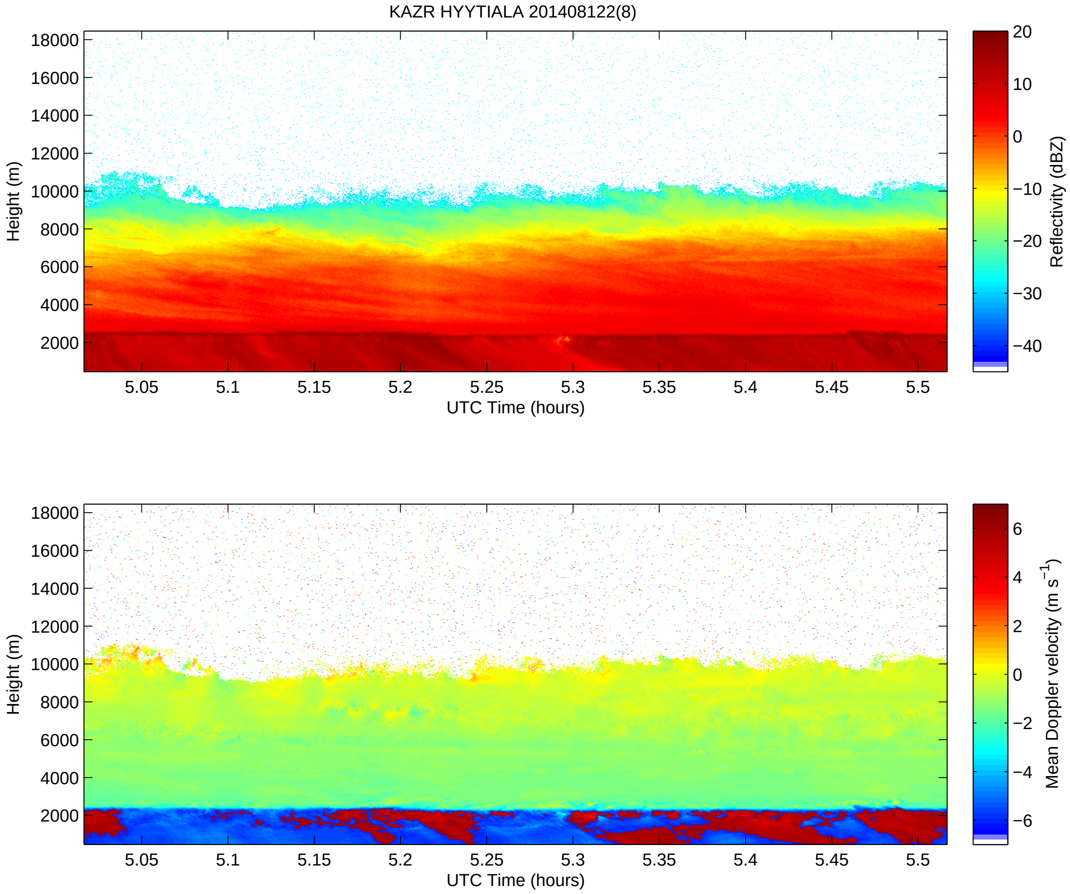

Figure 4.5 Radar reflectivity (dBZ) (top) and mean Doppler velocity (bottom) between 0500UTC and 0530UTC from the zenith pointing Ka-band radar at Hyytiala on 12th August 2014.

began to encounter turbulence. As the radiosonde ascended it progressively encountered more turbulence. The radar was able to provide a turbulence profile up to a height of 9 km. However, this profile seemed to vary more with height than the accelerometer measurements did. From the ground to the cloud base, the velocity information from the falling raindrops also provide an eddy dissipation rate. Due to the fall speed of the drops and the Doppler aliasing previously discussed, these values should be neglected. From the cloud base to 4 km, the radar indicates a decrease in turbulence intensity with height, contradicting the observations of the radiosonde. Above 4 km, the radar derived eddy dissipation rate begins to increase with height again. The eddy dissipation rates from the radar differ significantly and do not bear any resemblance to the turbulence observed by the radiosonde. This raises two questions; the first is why is there such a vertical extent of turbulence within the cloud? This topic will be discussed in chapter 5. Secondly, why is the radar producing such anomalous values of eddy dissipation rate? Examining the lidar calibration in section 4.1, an acceleration of >3 m s^{-2} would yield $\epsilon > 10^{-3}$ m^{2}s^{-3}. Nevertheless, something physical is needing to cause the sensor package

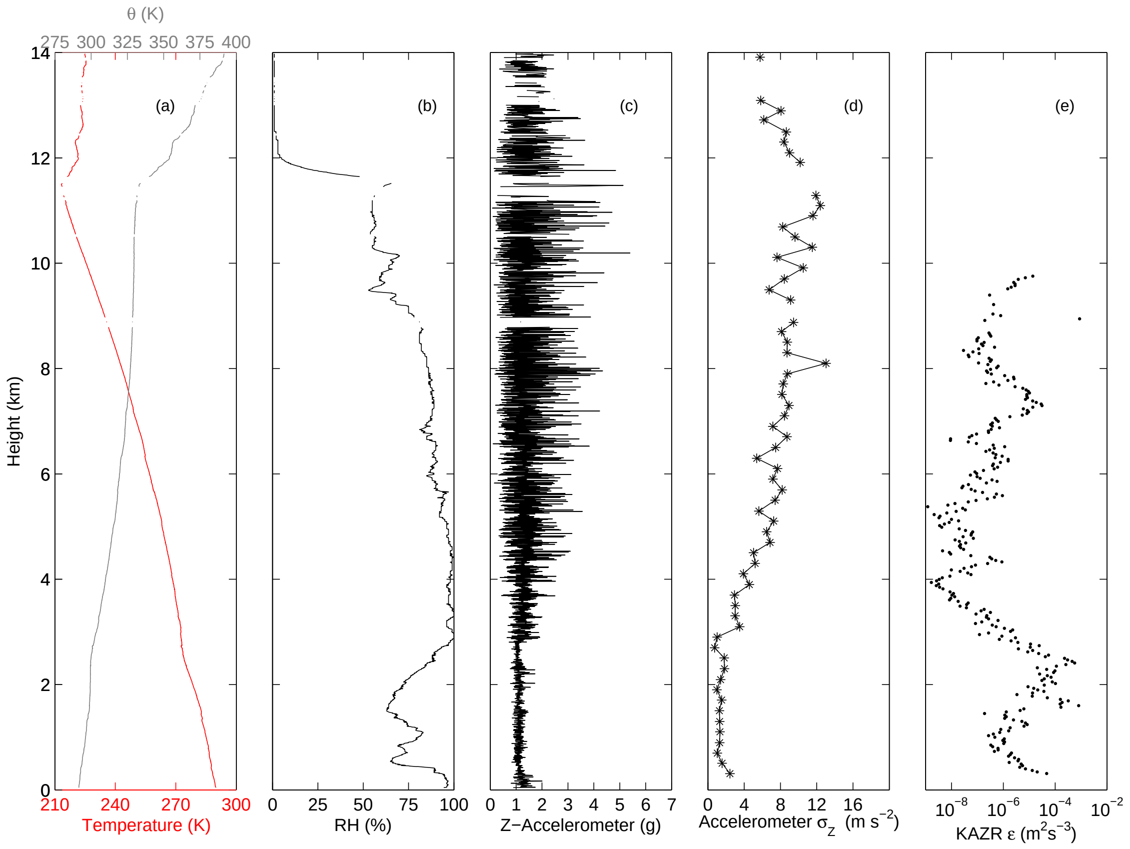

Figure 4.6 Vertical profiles of a)temperature and potential temperature θ (K) in red and grey respectively, b) relative humidity (%), c) Z-axis accelerometer (m s^{-2}), d) standard deviation of the Z-axis accelerometer over 200m for a accelerometer sonde ascent at 0516UTC on 12th August 2014 from Hyytiala. e) Radar derived ϵ (m^{2}s^{-3}) from a zenith pointing Ka-band radar based at the same location.

to swing. If it were due to hydrometeors colliding with the balloon, then substantial variability from the accelerometer would be detected from launch and would decrease with height. A final thought is how well is the radar resolving the turbulence? Could it be a case that larger hydrometeors have greater fall speeds, which are dominating the turbulence velocity spectra, meaning that the derived values of ϵ are smaller? The next section discusses how a hypothesis could be validated by using both the X-band and Ka band scanning radar to estimate the droplet size.

4.2.2 Droplet size effects on eddy dissipation rate calculations

Droplet sizes can be estimated from radar reflectivity in conjunction with the liquid water content (LWC) of the pulse volume, from the technique of Ellis and Vivekanandan (2011). The LWC can be found from a dual wavelength radar method (Hogan et al., 2005). This method uses the radar reflectivity from two different wavelength radars and standard meteorological data from a radiosonde. In this case, the scanning X and Ka band radars are used. The LWC is calculated using equation 3 from Hogan et al. (2005) which gives

$$LWC = \frac{1}{\kappa_{ka} - \kappa_X} \left(\frac{(Z_X(h+1) - Z_{ka}(h+1)) - (Z_X(h) - Z_{ka}(h)) - B}{2(z_r(h+1) - z_r(h))} - A_{ka} + A_X \right), \tag{4.8}$$

where Z_f is the radar reflectivity in dBZ of a given radar at height h. A_f are the attenuation coefficients of atmospheric gases at a given frequency, they are a function of temperature, pressure and relative humidity. A_f is calculated using an attenuation model described in Liebe (1985). B is a small correction factor due to the change of temperature with height, given by

$$B = 10log_{10} \left(\frac{|K_X(T(h+1))|^2}{|K_X(T(h))|^2} \frac{|K_{ka}(T(h+1))|^2}{|K_{ka}(T(h))|^2} \right), \tag{4.9}$$

where $K_f(T(h))$ is the dielectric constant of the radar frequency at a given temperature T, for a height h, where the radiosonde's temperature data was again used. The dielectric constant was calculated using equations shown in both Liebe (1985) and Hogan et al. (2005). Finally, the attentuation coefficient of liquid water was calculated using

$$\kappa_f = 4.343 \times 10^3 \frac{6\pi}{\lambda \rho_l} \Im(-K_f(T)), \tag{4.10}$$

where ρ_l is the density of liquid water and λ is the wavelength of the radar. $\Im(-K_f(T))$ is the imaginary part of the complex value $K_f(T)$. The median drop diameter (MDD) in mm was then calculated using equation 7 in Ellis and Vivekanandan (2011)

$$MDD = \sqrt[3]{\frac{2.15 \times 10^{-4} Z_{ka}}{LWC}} \tag{4.11}$$

where Z_{ka} is the radar reflectivity of the Ka-band radar in units of mm^{6}m^{-3}. As discussed earlier, the X and Ka band scanning radar repeatedly cycled through different scanning configurations. The zenith scanning part of the cycle occurred for 20 minutes approximately every two hours. The period where the scanning radar was in zenith mode and within 15 minutes of a launch time therefore, limits the number of ascents to three. Two of these occasions provided the two case studies previously shown: the third ascent not shown as it is similar to that depicted in figures 4.5 and 4.6. LWC and droplet size estimations were calculated over the 60 second time period closest to launch using 500 m height windows. As there was a small temporal shift, the 60 second profile closest to launch time was selected. Given the uniform structure of the clouds in figures 4.5 and 4.3 the effects of co-location are minimised.

Figure 4.7 shows radar derived profiles of droplet radius and radial velocity for the ascent made on the 9th August 2014. There is one data point at 6 km where the ice cloud is present, the lack of droplet estimations in this cloud is due to the nature of the two radar wavelengths. In figure 4.3 there is a high reflectivity from the Ka band radar, however, the X-band radar operates on a 3 cm wavelength and won't detect the ice cloud

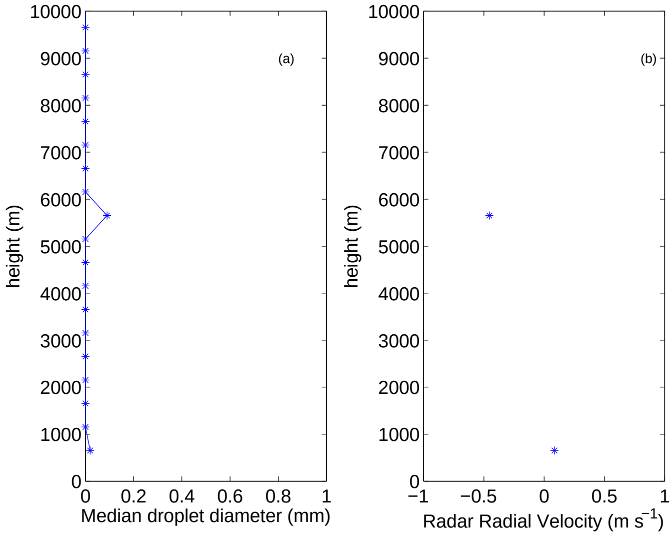

Figure 4.7 Vertical profiles of a) median droplet diameter (mm) and b) mean radial velocity (m s^{-1}), computed from an X and Ka band radar at 0745 UTC on 9th August 2014.

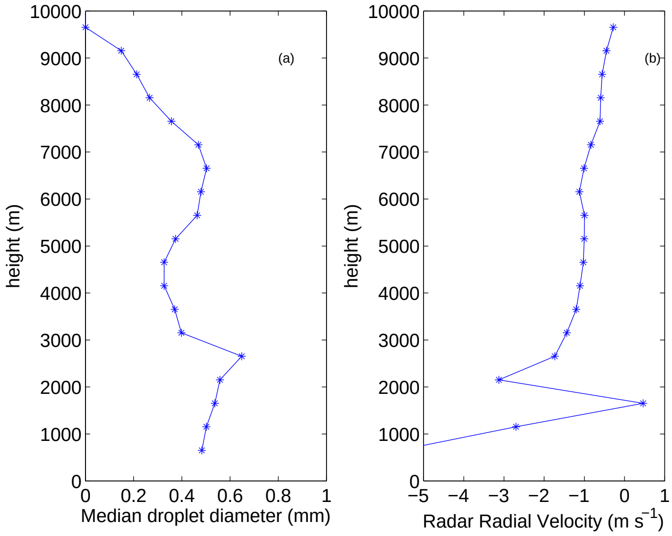

Figure 4.8 Vertical profiles of a) median droplet diameter (mm) and b) Mean radial velocity (m s^{-1}), computed from an X and Ka band radar at 0534 UTC on 12th August 2014.

if the hydrometeors have a radii significantly smaller than that of the radar's wavelength. If the X-band radar cannot observe the ice-cloud then it will be difficult to make droplet size calculations. From the single data point, the droplet's size is 0.1 mm with a fall speed of 0.5 m s^{-1} towards the ground. For this case study it would appear that the small size of hydrometeors does not affect turbulence measurements being made. The reason for this is that the low ϵ from the radar and low variability from the accelerometer sonde show weak to null turbulence anyway.

For the second case study, in figure 4.8, the size of droplets within the cloud, which starts at 2.5 km (see figure 4.5), is 0.4 mm in diameter and reduces towards the cloud top. The vertical radial velocity along the radar beam appears to decrease with height in the cloud. This is good evidence to suggest that droplet size, and hence terminal fall speed of the drops dominates the velocity spectra and yields smaller ϵ values. Further evidence to support this can be seen by comparing ϵ in figure 4.6 with the drop diameter and fall speed in 4.8. As drop size and fall speed decrease, the radar derived ϵ appears to increase. Velocity values from below the cloud base have been neglected due to the velocity aliasing issues. Confidence is given in calculated drop sizes using this method by comparing the expected terminal fall velocities in Lhermitte (2002) with those observed.

4.2.3 Doppler cloud radar conclusions

It is difficult to compare the turbulence measurements between an accelerometer sonde and a Doppler cloud radar. The most turbulent conditions occur within deep convective or frontal clouds, but, associated with these are larger droplets with faster fall velocities which dampens the velocity variance. Figures 4.7 and 4.8 show evidence that the larger droplets appear to yield smaller eddy dissipation rates as the velocity variance is dampened. In summary, the radar detects the cloud drops and not the turbulent air they pass through. Future work in this area of research should look at how the fall velocity of raindrops is perturbed by turbulence, a method by Meischner et al. (2001) used scanning radar and included a term to remove the droplet fall speeds.

4.3 Comparing the accelerometer sonde against a MST radar

To gain a better understanding of the turbulence that the balloon encounters in the free troposphere and stratosphere, a comparison with a remote sensing method which can make observations in these regions of the atmosphere is essential. During the course of Spring 2015, three Intense Observation Periods (IOP) were carried out spanning two days in which a total of 18 accelerometer ascents were made from the Natural Environment Research Council (NERC) Mesospheric Stratospheric and Tropospheric (MST) radar site located in Aberystwyth, Wales, United Kingdom (52.42° N, 4.01° W). The IOPs took place when a jet stream was forecast to be overhead. This section will discuss how the radar data can be used to give a turbulence metric for comparison with the 18 sondes launched.

4.3.1 NERC MST Radar operating principles

The NERC MST radar array consists of 2 by 2 grids of Yagi antennas, referred to as a quad, arranged in a 10 by 10 grid, giving a total of 400 antenna. By altering the power and phase of the transmitted pulse to each quad, the radar beam can be effectively steered. Using this method, the radar beam can be orientated in 17 configurations of varying zenith and azimuth, as shown in figure 4.9. By using the off vertical beams at different azimuth, a DBS method can be used to calculate the horizontal wind speed and direction. This enables the NERC MST radar to make constant wind observations between 2-20km, for which the technical specifications are given in table 4.2.

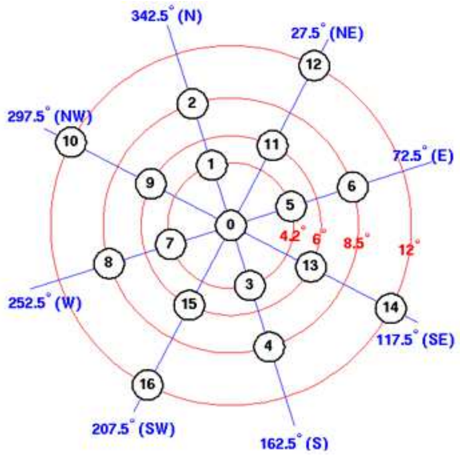

Figure 4.9 Polar diagram showing the azimuth and zenith beam configurations of the NERC MST Radar. The beam direction is given by the azimuthal component and the zenith (off vertical angle ψ) is given by the distance from the origin. Each beam configuration is given a number, which is shown here. Diagram from `http://mst.nerc.ac.uk/nerc_mstr_beam_dirs.html`.

At each range gate along each beam a 128 point time series is determined, allowing the calculation of a Doppler spectra of velocities. The Doppler spectra have Gaussian form, allowing a spectral width to be calculated. This is equal to the standard deviation,

Radar parameter	Value
Radar frequency	46.5 MHz
Radar wavelength	6.45 m
Range gate	150 m
Half power half beam width	1.5^o
Integrated dwell time	21 s

Table 4.2 Operational parameters of the NERC MST radar.

which is the radar's main measure of turbulence. The raw spectral width cannot be used in comparisons of turbulence, due to the effects of beam broadening. Beam broadening is the broadening of the Doppler spectra by perpendicular wind components to the beam, vertical wind shear across the beam, and turbulence (Dehghan et al., 2014). To make turbulence comparisons between the balloon and the radar, the unwanted effects of beam broadening need to be removed. For the comparison here, the $\psi = 6^o$ off vertical beams are used, with a correction applied to get σ_t^2, the spectral width due to turbulence. This is given in Dehghan and Hocking (2011) as

$$\sigma_t^2 = \sigma_{ms}^2 - \sigma_{br}^2, \tag{4.12}$$

where σ_{ms}^2 is the spectral width measured by the radar and σ_{br}^2 are the contributions to beam broadening estimated by

$$\begin{aligned}\sigma_{br}^2 \approx \frac{\nu^2}{\eta} U^2 \cos(\psi) - a_o \frac{\nu}{\eta} \sin(\psi(U \frac{\partial U}{\partial z} \zeta_r)) + b_o \frac{2 \sin^2 \psi}{8\eta} \left(\frac{\partial U}{\partial z} \right)^2 \\ + c_o (cos^2 \psi \sin^2 \psi) |U \xi_r| + d_o (\cos^2 \psi \sin^2 \psi) \xi_r^2,\end{aligned} \tag{4.13}$$

where

$$\zeta_r = 2\nu z_r \sin(\psi), \tag{4.14}$$

$$\xi_r = \left(\frac{dU}{dZ} \right) \frac{\Delta R}{\sqrt{12}}, \tag{4.15}$$

$$\eta = 4ln2. \tag{4.16}$$

ν is the one way half width of the radar beam, U is the horizontal wind speed, z_r is the range, ΔR is the range gate size, and a_0, b_0, c_0 and d_0 are constants given in Dehghan et al. (2014). It should be noted that this approximation is not perfect which will become apparent in the results section. This approximation was applied at the radar post processing stage for each of the four 6^o beams, which were then smoothed over a 1 hour moving window.

Another metric which can sometimes indicate turbulence is the aspect sensitivity, which is the signal strength difference between the vertical and off vertical beams. The theory is that a well mixed turbulent patch will have near identical signal returns, regardless of the zenith of the radar beam. Similarly, a highly stratified part of the atmosphere will have large values of aspect sensitivity as the vertical beam will have a high return compared to the off-vertical, which scatters signal away from the receiver. This is depicted in figure 4.10. However, if the turbulence is not fully resolved within the pulse volume, this may cause higher aspect sensitivity values. This makes aspect sensitivity more of a qualitative measure of turbulence rather than a quantitative measure.

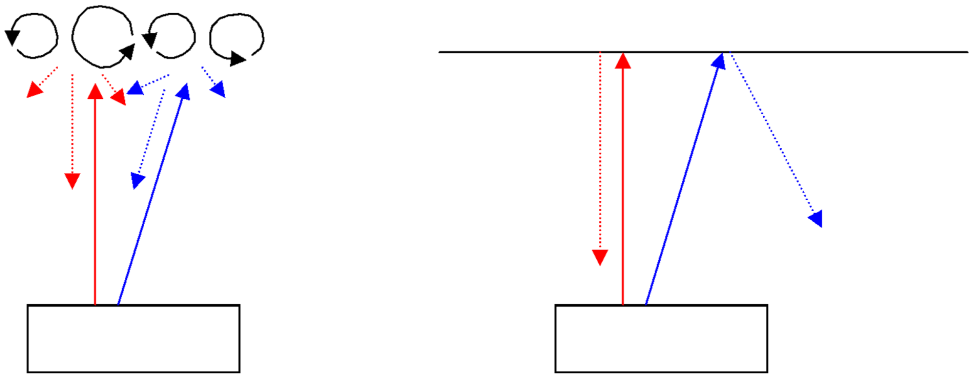

Figure 4.10 Low aspect sensitivity (left) The radar transmits along both beams (solid colors) the turbulence reflects an equal return signal (dashed lines). High aspect sensitivity (right): The radar transmits along both beams however the off vertical return beam (blue) is scattered away from the receiver by the stratified air.

4.3.2 Initial results from the NERC MST radar

The post processed spectral width data was selected to only use the $\psi = 6^o$ beams for the 1 hour centred around launch time of the accelerometer sonde. Although the beams point in four orthogonal directions, the fact that the turbulence is most likely isotropic means that they can be combined and treated as one beam. The analysis begins by showing the post processed data from the radar for one of the radiosonde ascents. At this stage the only filtering applied to the data is the removal of data points which have a reliability flag of 60% or less. For this comparison the accelerometer standard deviation was taken over the same 150 m range gates as the radar

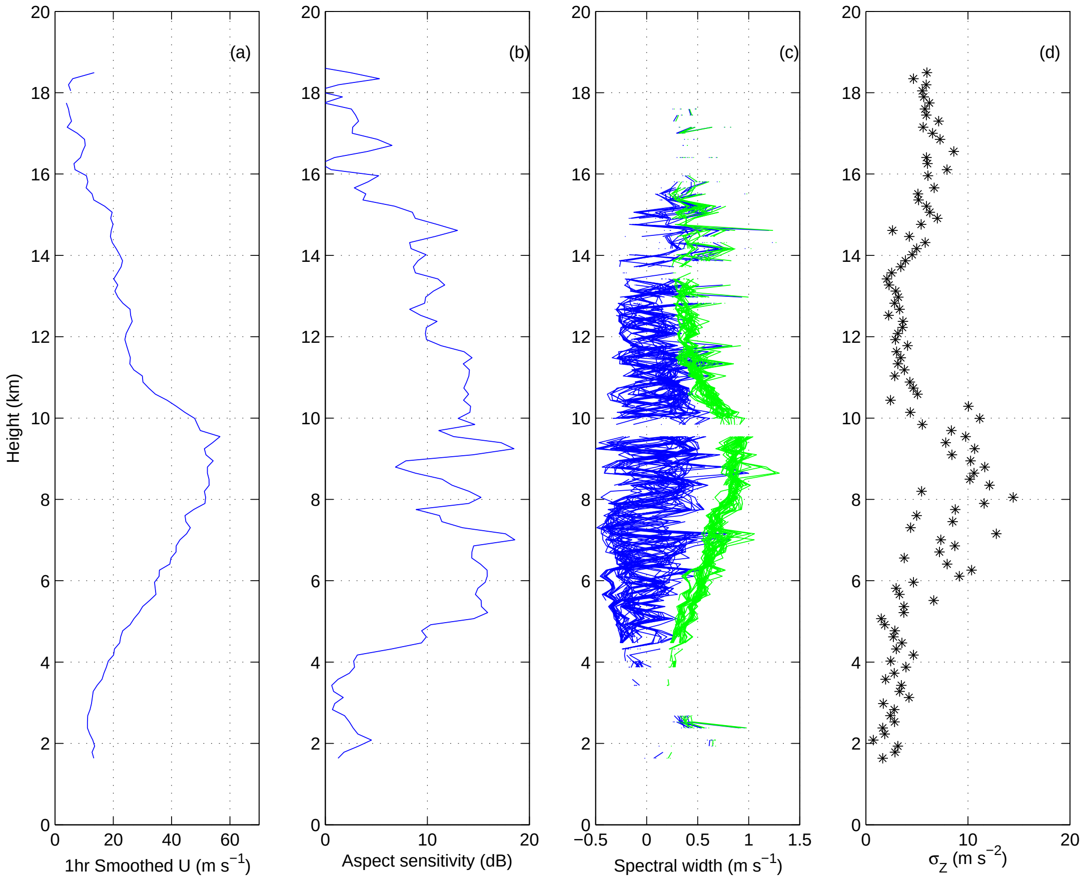

Figure 4.11 Vertical profiles of a) MST horizontal wind smoothed over 1 hour (m s^{-1}), b) 1 hour smoothed aspect sensitivity (dB) and c) individual uncorrected (green) and corrected beam broadened spectral width (blue) (m s^{-1}) over an hour centred on 1507 UTC on 28th April 2015 from the NERC MST radar. d) shows the standard deviation of the accelerometer σ_z (m s^{-2}) launched at the same time and place.

Figure 4.11 shows a jet stream with a core velocity of 50 m s^{-1}. The uncorrected spectral widths, shown in green, have a similar shape to the jet stream, indicating that the spectral widths are affected by beam broadening effects. The beam broadened corrected spectral widths are shown in blue. However, the values are inherently noisy and also include negative values of spectral width. This shows that equation 4.13 is not perfect at fully correcting for beam broadening. Physically speaking, a negative spectral width is impossible. Dehghan et al. (2014) state that large negative values are as likely as large positive values, and hence should be included in the hourly mean and incorporated into an error. Others have taken a median of the data, for example Nastrom and Eaton (1997), to alleviate the problem. Before embarking on a comparison, the data is further filtered.

The spectral widths are estimated from the velocity distributions by fitting a Gaussian to the distribution and approximating the spectral width from the fitted line. A Chi-squared test is carried out at the radar post processing stage to asses the goodness of the fit. Spectral widths were retained if a chi-squared value of less than 0.012 (Lee, C.F., 2015, personal communication) was present. This ensured that spectral widths were calculated from Gaussian distributions. The radar data also contained an upper and lower error on the corrected spectral width data. This allowed all remaining data to be weighted; the weighting was such that the range of the error above zero was divided by the range of the error. This effectively weights in favour of data which have been corrected and found to be positive. Data which has been over corrected has less weight. Spectral width values where the upper error was below zero had a weighting of zero. Likewise, spectral width values where the lower error was above zero had a weighting of 1. This method ensures that data points which have been poorly corrected for beam broadening are given less weighting when a time average is made. Next, a 1 hour weighted average of the data at each range gate centred on the time of launch was taken. This was done because the radiosonde takes an hour to ascend the vertical range of the radar. If less than 25% of the range gate points over the hour was present then the range gate was removed.

Figure 4.12 is the same as that shown in figure 4.11, but the spectral width is now a weighted average over an hour. It can be seen that the corrected spectral width and the accelerometer values follow a similar trend. Given there is still some variability across range gates, an average of the corrected spectral width was taken over 1.5 km. These are shown by the red squares in figure 4.12. A standard deviation of the accelerometer data was taken over the same 1.5 km height window and is plotted in red squares in panel (d). For this case, the two quantities both show similar trends in the amount of turbulence they are detecting.

Figure 4.13 shows data from the MST radar for a different ascent on the 3rd March 2015. The values of corrected spectral width and values of standard deviation from the accelerometer do not show the same level of agreement. Upon examination of panel a), it can be seen that there is a weak jet present. The MST radar observes an almost constant spectral width with height, compared with that of the radiosonde which observes increased turbulence at 8km. The reason for the lack of correlation here is almost certainly due to co-location issues. The previous comparisons with the lidar were only made in the first 1 km of the atmosphere. In contrast, the cloud radar was compared in large clouds where the radiosonde was advected with the cloud. Here, the radiosonde could be at least 50 km away by the time it reaches its burst height. The addition of orography surrounding the site also means that turbulence generated by mountain waves may be experienced by the

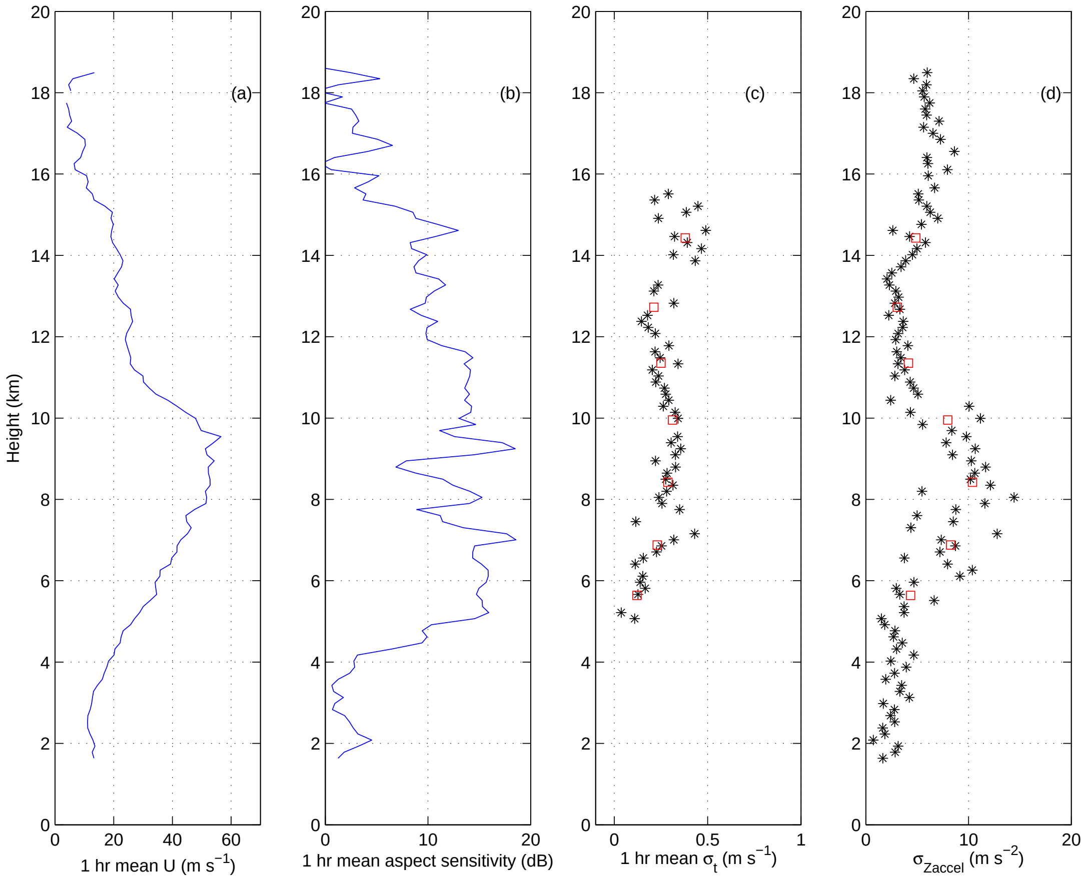

Figure 4.12 Vertical profiles of a) MST Horizontal wind smoothed over 1 hour (m s^{-1}), b) 1 hour smoothed aspect sensitivity (dB), c) 1 hour smoothed corrected beam broadened spectral width (m s^{-1}) over an hour centred on 1507 UTC on 28th April 2015 from the NERC MST radar. d) shows the standard deviation of the accelerometer (m s^{-2}) launched at the same time and place. (Red squares denote height averaging over 1.5km)

radiosonde downstream and not observed at the radar. Another contributing factor could be due to a sonde being advected in one convective cell, whilst the radar makes turbulence observations of different convective cells as they pass over the radar site, although this is unlikely to be a major contributor due to the IOPs occurring in winter months. To minimise the effects of local weather phenomena, only ascents that were flown into large scale jet streams were selected for the comparison. Jet streams are sufficiently large scale that the probability of the jet varying over such distances is unlikely.

The data from the MST radar and accelerometer were compared using the 1.5 km height averaged values for 12 of the 18 ascents. As a combined dataset, the ascents were filtered further by two criteria. Firstly, in figure 4.11 there are increased values of spectral width between 2 km and 4 km, which is present in some of the ascents. There does not appear to be a meteorological explanation for this and so could be due to a radar issue, thus data points below 4 km were removed. Secondly, data points considered spurious

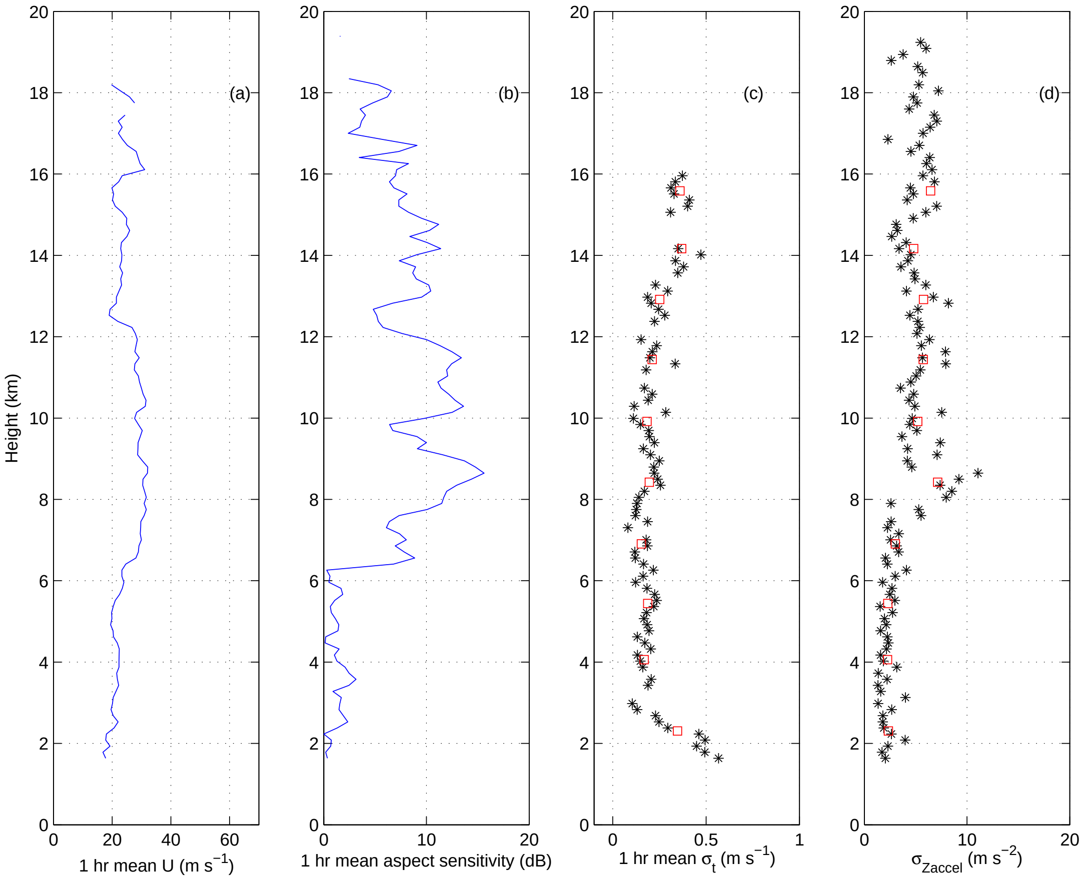

Figure 4.13 Vertical profiles of a) MST Horizontal wind smoothed over 1 hour (m s^{-1}), b) 1 hour smoothed aspect sensitivity (dB) and c) 1 hour smoothed corrected beam broadened spectral width (m s^{-1}) over an hour centred on 1758 UTC on 3rd March 2015 from the NERC MST radar. d) shows the standard deviation (m s^{-2}) of the accelerometer launched at the same time and place. (Red squares denote height averaging over 1.5km)

were associated with high aspect sensitivities > 15 dB. As previously discussed, high aspect sensitivities are associated with more stratified air and thus stumble into one of the issues of this radar. The radar pulse volume is much larger than that used in the two previous comparisons. It is 150 m in depth and has a radius of 250 m at mid tropospheric heights. This means that it is the pulse volume average of spectral width which is received by the radar. For example, there could be a thin layer of turbulence with a lengthscale of 60 m sandwiched by two stratified layers of air. It is not clear how the radar would interpret this: for example would the velocity distribution be narrowed to yield a smaller value of spectral width, yet maintain a high aspect sensitivity? Consequently, the higher aspect sensitivity values have been used to remove spectral width points that may be of a different origin.

The standard deviation of the accelerometer was plotted against the mean corrected spectral width over 1.5 km windows, as shown in figure 4.14. Error bars in figure 4.14 for

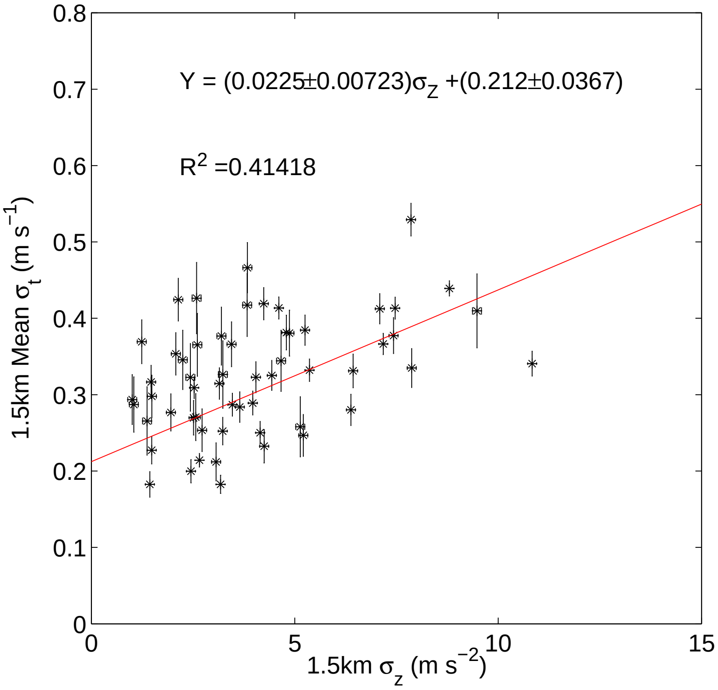

Figure 4.14 σ_Z accelerometer (m s^{-2}) over 1.5km plotted against MST radar 1.5km mean corrected spectral width σ_t (m s^{-1}). Error bars are calculated from the standard error in the mean of the spectral width.

the spectral width were calculated from the standard error of the mean spectral width. Some of the more scattered points appeared to have larger standard errors, so a weighted fit was applied. The weights were calculated by taking $1/E^2$, where E is the standard error. The fit is shown in figure 4.14, for which the 95% confidence intervals on the gradient show that there is a positive relationship between the two quantities. The R^2 value is somewhat lower than that with the lidar, but this is most likely due to the scatter of the data, given the co-location problems described.

4.3.3 Calculating ϵ from spectral width

The next natural step is to attempt to use the spectral width to calculate the ϵ. There are a few methods for this and a thorough discussion of these various methods is given in Hocking (1999). The first shown in Dehghan et al. (2014) calculates ϵ using

$$\epsilon = \frac{C_m \sigma_t^2}{T_{BV}}, \tag{4.17}$$

where T_{BV} is the Brunt-Vaisala period and C_m is a constant which can vary from 1.7 to 3.4 (Dehghan et al., 2014). Here C_m is taken to be 1.8 and the Brunt-Vaisala period is calculated from the radiosondes temperature profile. A second method, originally proposed by Labitt (1981), uses a hyper confluent geometric function to represent the spectral characteristic of the pulse volume. It takes into account the pulse volume and spectral width in calculating an eddy dissipation rate. Hence, ϵ can be calculated using

$$\epsilon = \left(\frac{\sigma_t^2}{1.828 F_\chi}\right)^{\frac{3}{2}} M^{-1}, \tag{4.18}$$

where F is the Gaussian confluent hyper-geometric function, described in Appendix A, and M is the beam width in m. ϵ was calculated using both of these methods, which are compared in figure 4.15. The Brunt-Vaisala method gives an ϵ lower than those used during the lidar calibration. It is hard to assess the presence of a linear trend given the size of the confidence intervals and their proximity to zero. The Labitt method also underestimates the intensity of turbulence, and more so when compared to the lidar calibration, however, a more justified linear trend is present.

An alternative method to calculate ϵ is the use of a -5/3 law. However, it is not possible to calculate the power spectrum directly from the radar as only a mean and standard deviation of the Doppler spectra are stored. Given two length scales and a standard deviation of the velocity field, it may be possible to calculate the ϵ using equation

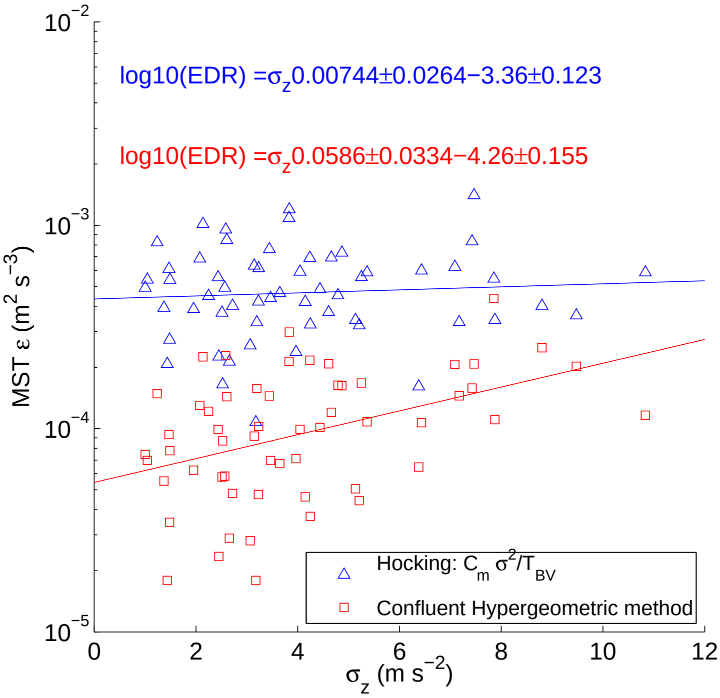

Figure 4.15 A composite plot showing the relationship between the standard deviation of the accelerometer and the Brunt-Vaisala method (blue) and the confluent hyper-geometric function (red) derived ϵ.

4.6, such as that used by Bouniol et al. (2004) or O'Connor et al. (2010) in section 4.2. The smallest length scale at which the NERC MST radar can detect turbulence is half the radar wavelength, 3.25 m. However L_0, the upper length-scale of detected eddies, is more difficult to define as it could be argued that it is the length of the wind run over the 21 second effective dwell time. This would give an outer length scale of 1-1.5 km in a modest jet stream. Alternatively, the outer length scale could be defined by a buoyancy driven length scale, such as a Thorpe length scale (Wilson et al., 2011) or by using an approximation similar to that given in Weinstock (1978), which estimates an upper limit to the inertial length scale. This equation is used for more point or low pulse volume measurements. The MST radar has a volume many orders of magnitude greater, for which the theoretical assumptions are less likely to be appropriate.

4.4 Conclusions

The accelerometer sonde has shown an increase in variability as a response to an increase in turbulence intensity, which has been independently observed by a Doppler lidar and MST radar. The standard deviation of the accelerometer showed a good correlation with the lidar derived ϵ. The standard deviation of the accelerometer also showed a relationship with the MST derived spectral width. Values from the MST radar were difficult to turn into ϵ as each method gave different values. It is beyond the scope of this thesis to seek an alternative method of calculating this value. The agreement with spectral width is enough to know the accelerometer responds to turbulence in the mid atmosphere. Comparisons with the cloud radar were difficult, as the cloud radar looks at the motion of cloud drops and not necessarily that of the turbulent air.

Chapter 5

Analysis of accelerometer data set

In the previous chapter, comparisons of the accelerometer sonde with different remote sensing methods of turbulence were undertaken, giving an insight into how the balloon-borne accelerometer reacts in-flight to turbulence. In this chapter, the quantification of the meteorological conditions that are sources of turbulence are undertaken. In total, 53 accelerometer sonde ascents were launched across the UK and Finland between October 2013 and December 2015. These 53 ascents have been grouped into a data set. An overview of the measurements will be given as well as considerations to which accelerometer values represent significant turbulence. A hypothesis will be tested as to whether simple metrics, such as the Ri number can be used as a universal indicator of turbulence. Detailed data analysis will also be undertaken. It will first examine notable case studies of turbulence observed in the presence of meteorological conditions such as: jet streams, in and near cloud, convection and gravity waves. Secondly, a qualitative analysis will be under taken to see if trends in these categories are more likely to give rise to turbulence.

5.1 Description of dataset

Accelerometer sondes were launched from three locations: the Reading University Atmospheric Observatory (RUAO), United Kingdom (51.44^o N , 0.98^o W), the ARM mobile facility based at the Hyytiala forestry station, Finland (61.83^o N, 24.28^o E), and the NERC MST radar site near Aberystwyth, United Kingdom (52.42^o N,4.01^o W). In this section a brief summary of the ascents made at each site is given in Tables 5.1, 5.2 and 5.3 respectively.

Table 5.1 shows all accelerometer ascents made from the RUAO. All ascents, with

Date	Time (UTC)	Ascent No.	Payload
10/10/2013	1113	1	Accelerometer and Solar radiation sensor(up)
15/10/2013	1354	1	Accelerometer and Solar radiation sensor(up)
28/10/2013	1258	1	Accelerometer and Solar radiation sensor(up)
31/10/2013	1519	1	Accelerometer and Solar radiation sensor(up)
05/11/2013	0903	1	Accelerometer and Solar radiation sensor(up)
12/11/2013	1059	1	Accelerometer and Solar radiation sensor(up)
14/11/2013	1458	1	Accelerometer and Solar radiation sensor(up)
16/12/2013	1430	1	Accelerometer and Solar radiation sensor(up)
07/01/2014	1433	1	Accelerometer and Solar radiation sensor(up)
14/01/2014	1149	1	Accelerometer and Solar radiation sensor(up)
23/01/2014	1125	1	Accelerometer and Solar radiation sensor(up)
19/02/2014	0937	1	Accelerometer and Solar radiation sensor(up)
26/02/2014	1348	1	Accelerometer and Solar radiation sensor(up)
26/02/2014	1548	2	Accelerometer and Solar radiation sensor(up)
20/03/2014	1326	1	Accelerometer and Solar radiation sensor(up)
20/03/2014	1520	2	Accelerometer and Solar radiation sensor(up)
20/03/2014	1707	3	Accelerometer and Solar radiation sensor(up)
06/06/2014	0957	1	Accelerometer and Solar radiation sensor(up)
08/10/2014	0907	1	Accelerometer and Solar radiation sensor(up)
08/10/2014	1213	2	Accelerometer and Solar radiation sensor(up)
08/10/2014	1546	3	Accelerometer, Solar radiation sensor (up), Point discharge sensor (MALFUNCTION)*
02/03/2015	1550	1	Accelerometer and Solar radiation sensor(up)
11/05/2015	1159	1	Accelerometer and Solar radiation sensor(up)
18/12/2015	1500	1	Accelerometer and Solar radiation sensor(up)*

Table 5.1 A table listing accelerometer sonde launches made from the RUAO between October 2013 and December 2015, showing time of launch and payload. * indicates an ascent not included in the main dataset (see text for details).

the exception of two, are included in the dataset. The reasoning for their exclusion is as follows. The ascent made on the 10th October 2014 included a prototype point discharge current[1] sensor , similar to those used by Simpson and Scrase (1937) and Weber and Few (1978) to measure intense electrification within cloud. This sensor was based on a surface instrument design in Marlton et al. (2013), but adapted for use on a radiosonde. The experimental sensor, on occasion, produced small negative voltages, which are problematic for the PANDORA board, causing sporadic voltage jumps across other logging channels. The ascent made on the 18th December 2015 was to target turbulence within a deep frontal cloud, to see if similar results obtained in figure 4.6 could be reproduced. Given the late time within the project at which this data was collected, it has not been added to the dataset, which will go on to be used for model comparisons.

---

[1] A point discharge current, or corona current, occur when the ambient electric field intensifies around a sharp protruding point. This causes a small current of 1μA to flow through the extremity.

Date	Time(UTC)	Ascent No	Payload
08/08/2014	0817	1	Accelerometer and Solar radiation sensor(up)
08/08/2014	1128	2	Accelerometer and Solar radiation sensor(up)
09/08/2014	0745	1	Accelerometer, Solar radiation sensor (down), Charge sensor
10/08/2014	0731	1	Accelerometer, Solar radiation sensor (down), Charge sensor
10/08/2014	1120	2	Accelerometer and Solar radiation sensor(up)
11/08/2014	2315	3	Accelerometer and Solar radiation sensor(up)
12/08/2014	0516	2	Accelerometer and Solar radiation sensor(up)
12/08/2014	1116	4	Accelerometer and Solar radiation sensor(up)
13/08/2014	1251	1	Accelerometer and Solar radiation sensor(up)
11/08/2014	1722	2	Accelerometer, Solar radiation sensor (down), Charge sensor and cloud sensor
14/08/2014	1730	2	Accelerometer, Solar radiation sensor (down), Charge sensor and cloud sensor

Table 5.2 A table listing accelerometer sonde launches made from the ARM mobile facility during August 2014, showing time of launch and payload.

Table 5.2 shows ascents made from the ARM mobile facility at Hyytiala. Apart from the standard accelerometer and solar radiation measurements, other sensors were mounted upon the radiosonde to provide active optical and electrical measurements of cloud, associated with the Biogenic Aerosols and their Effects on Cloud and Climate (BAECC) project. The cloud sensor uses high power modulated LEDs and a photodiode to make active optical measurements of cloud by backscatter as described in Harrison and Nicoll (2014). The charge sensor is described in Nicoll and Harrison (2011), and uses a spherical metal electrode attached to a high gain op-amp [2] circuit to allow small charges to be detected as it passes through clouds. The downward pointing solar radiation sensor uses a similar technology to the upward pointing solar radiation sensor, but measures the diffuse solar radiation in the atmosphere. The same theory can be applied to the data, as low variability in the sensor signal implies the radiosonde is in cloud.

Table 5.3 shows the accelerometer sonde launches made from the NERC MST radar site. The aim of this part of the campaign was twofold. First was to utilise the MST radar for turbulence comparisons, as shown in the previous chapter. Secondly, having 3-4 ascents a day enabled case studies, showing how turbulence develops over a short time period to be explored, particularly during the passage of a jet stream overhead.

In total, 52 of the 53 ascents were usable for further data analysis, with 51 being combined to form the dataset, used for comparisons in the next chapter. Sensors were

---

[2] An operational amplifier or op-amp is an electrical component which amplifies a voltage from a sensor or other output affectively increasing its sensitivity.

Date	Time (UTC)	Ascent No.	Payload
13/01/2015	1346	1	Accelerometer and Solar radiation sensor(up)
13/01/2015	1547	2	Accelerometer and Solar radiation sensor(up)
14/01/2015	0939	1	Accelerometer and Solar radiation sensor(up)
14/01/2015	1119	2	Accelerometer and Solar radiation sensor(up)
14/01/2015	1311	3	Accelerometer and Solar radiation sensor(up)
03/03/2015	1315	1	Accelerometer and Solar radiation sensor(up)
03/03/2015	1530	2	Accelerometer and Solar radiation sensor(up)
03/03/2015	1715	3	Accelerometer and Solar radiation sensor(up)
04/03/2015	0854	1	Accelerometer and Solar radiation sensor(up)
04/03/2015	1046	2	Accelerometer and Solar radiation sensor(up)
04/03/2015	1253	3	Accelerometer and Solar radiation sensor(up)
04/03/2015	1419	4	Accelerometer and Solar radiation sensor(up)
28/04/2015	1204	1	Accelerometer and Solar radiation sensor(up)
28/04/2015	1348	2	Accelerometer and Solar radiation sensor(up)
28/04/2015	1507	3	Accelerometer and Solar radiation sensor(up)
29/04/2015	0820	1	Accelerometer and Solar radiation sensor(up)
29/04/2015	0933	2	Accelerometer and Solar radiation sensor(up)
29/04/2015	1055	3	Accelerometer and Solar radiation sensor(up)

Table 5.3 A table listing accelerometer sonde launches made from the NERC MST radar site between January 2015 and April 2015, showing time of launch and payload.

carried aloft using 200 g balloons, which were filled to provide approximately 1250 g of lift, giving a burst height of approximately 20 km. For some of the multi sensor payloads used in Hyytiala, extra helium was provided to the balloon to grant an extra 100 g of lift to compensate for the extra payloads. The string length was set to 4 m for each launch, in accordance with the discussions in chapter 3. Although it was shown that this can cause an oscillatory effect, it did not seem to affect the standard deviation from the accelerometer. All radiosondes launched were equipped with a parachute to enable the safe descent of the payload back to Earth. The descent data was also recorded for the majority of ascents, but unlike Anderson (1957) it is not included in the analysis, as the radiosonde signal becomes weak and unusable. Radiosondes often travel horizontally up to ten times their vertical extent[3], which can mean by the time of descent the radio signal contains intermittent data, due to the weak signal. The radiosonde parachute system behaves differently as the radiosonde payload is pulling the parachute behind it, hence the dynamical response to turbulence is different. For the turbulence measurements analysed here, only the Z-axis accelerometer will be used, as it was found to be the most sensitive axis, as discussed in chapter 3.

---

[3] One radiosonde launched from RUAO was tracked some 230 km to just off the coast of Belgium before signal was lost.

5.2 Preliminary data analysis

In this section a preliminary analysis of the dataset as a whole is undertaken, regardless of meteorological conditions the radiosonde was experiencing. First, a decision is made over which accelerometer value constitutes significant turbulence. Then hypothesises that low thermal stability, high wind shear, and critical Richardson numbers are more likely to yield more turbulence, are investigated.

Figure 5.1 shows a histogram of raw Z-axis accelerometer data from the 51 ascents. The median of the distribution is 1.32 g. This value is expected when considering that if the radiosonde is in a non-oscillatory mode, then the Z-axis accelerometer reports approximately 1 g. When the balloon and radiosonde do enter an oscillatory mode, values up to 1.6 g can be induced, as shown in chapter 3. From the histogram it can be seen that approximately 1% of incidents are higher than the minimal ±5 g specification of the accelerometer. As the tail continues in a similar fashion past this point it can be considered that the accelerometer is still making reliable observations outside the minimal operating

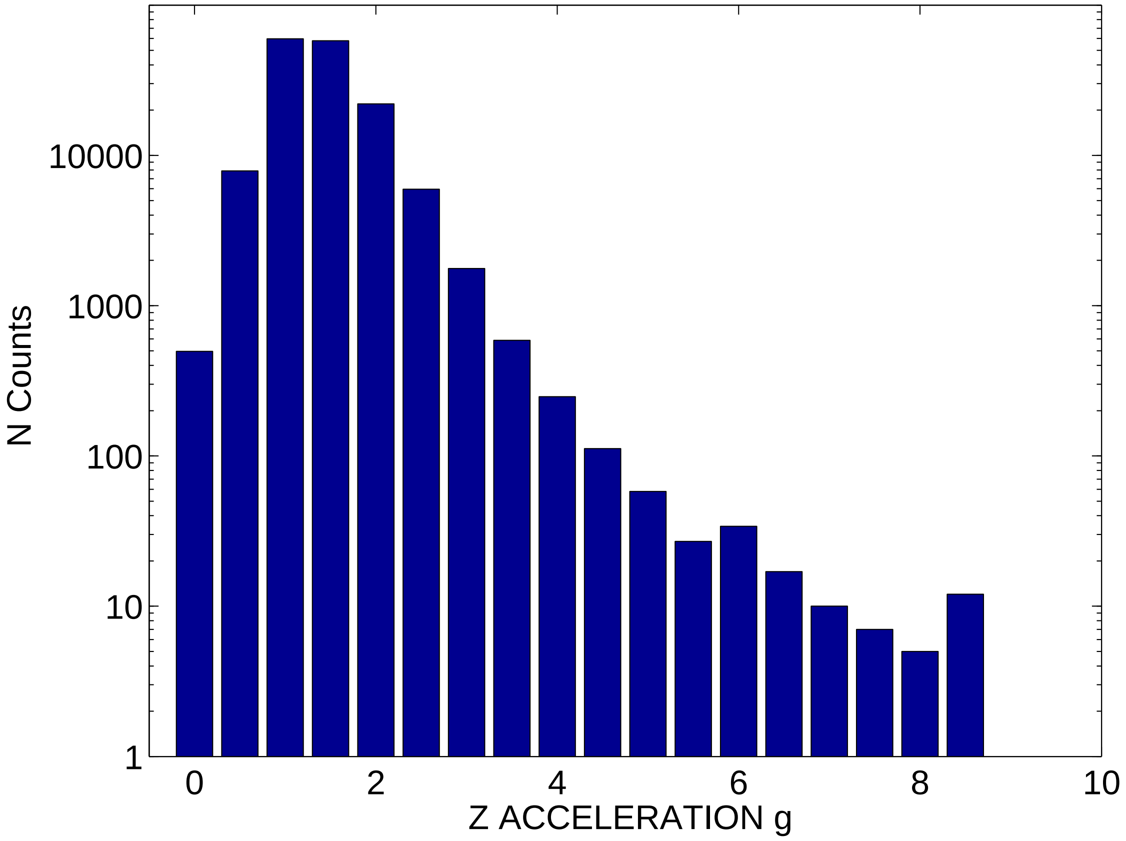

Figure 5.1 A histogram of 1 second values of g from the Z-axis of the accelerometer from 51 ascents, yielding 156885 values with an average ascent containing 3500-4000 values. The median of the distribution is 1.32 g.

range. The raw accelerometer data is affected by the oscillation, but the variance is not, therefore the remainder of the analysis will be concerned with the standard deviation of the accelerometer over 200 m, σ_z. This vertical window size is chosen, as it is similar to the 210 m height window used in the lidar comparison in chapter 4.

σ_z were only computed when 25% of the raw values over the 200 m window were present. σ_z for all ascents are shown in figure 5.2, with the peak of the distribution being approximately 2 m s^{-2}. In the previous chapter, the accelerometer's response to turbulence was compared with that of remote sensing methods. However, a σ_z threshold for what constitutes significant turbulence is still needed. The balloon may be experiencing small amounts of turbulence which are ubiquitous in the atmosphere, but at what point does that turbulence become significant? The first step is to perform a simple data analysis, which explores the distribution of the σ_z dataset.

Figure 5.3 shows that the data set is positively skewed with a skewness of 1.88, indicating that the data are not normally distributed. This is further reinforced, as the mean and median are not about the peak of the distribution, hence a standard deviation cannot be used to infer a significant turbulence threshold. Instead, the use of percentiles may yield a better approximation of when significant turbulence is detected. Figure 5.4 shows a cumulative frequency diagram of σ_z, the 75th percentile can be used to determine if a given σ_z represents significant turbulence. The 75th percentile is 4.97 m s^{-2} which, when examining figure 5.3, places a significant turbulence threshold at the point along the tail of the distribution.

A significant turbulence value of $\sigma_z > 5$ m s^{-2} would imply an $\epsilon > 0.025$ m^{2}s^{-3} if the relationship shown in figure 4.2 is extrapolated. Using table 2.2, this would yield a light-to-moderate turbulence value for an aircraft. Nevertheless, it should be discussed whether this frequency of turbulence is representative of its occurrence of turbulence in the atmosphere. Sharman et al. (2006) stated that $\epsilon > 0.025$ m^{2}s^{-3} occurred only during 1% of flight time for a fleet of B757 over a 3 month period over the United States. Schwartz (1996) showed that 16% of PIREPs from over the United States indicated greater than moderate/light turbulence. The automated B757 turbulence data is relatively unbiased, due to removal of human and aircraft factors. Some bias may remain, however, as aircraft are rerouted to avoid severe turbulence, this may have reduced the percentage of moderate or greater turbulence encounters. Furthermore, the PIREP study suffers from human subjectiveness in that null turbulence may not have been reported. The accelerometer dataset presented here is more biased to conditions where turbulence is likely by project

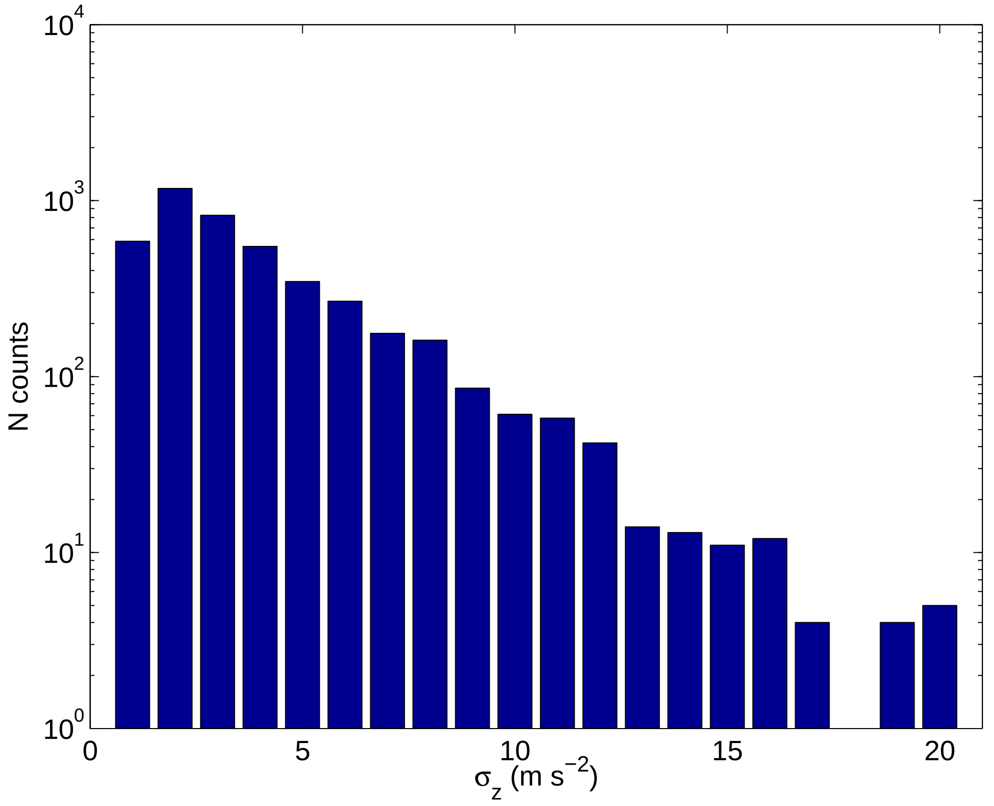

Figure 5.2 A histogram of σ_z from the Z-axis accelerometer from 51 ascents.

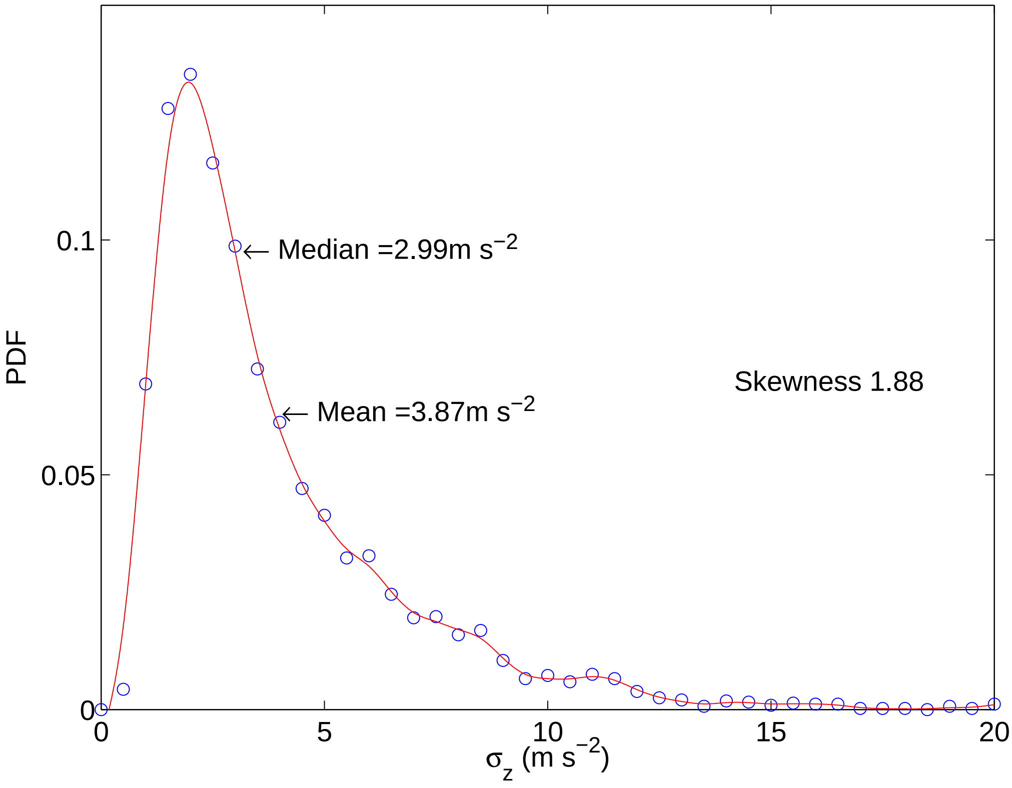

Figure 5.3 A probability density function of σ_z from the Z-axis from 51 ascents, mean, median and skew of the distribution have been annotated. Blue circles are the PDF bins and the red line is a fitted smoothing spline.

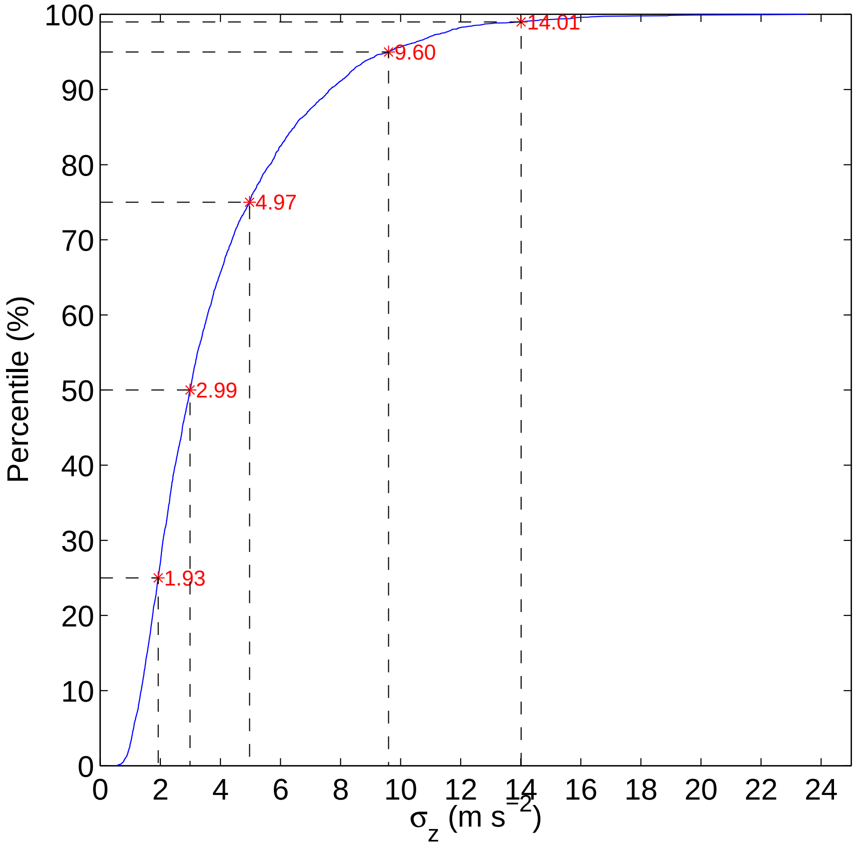

Figure 5.4 A cumulative frequency diagram of σ_z from the Z-axis accelerometer from 51 ascents, 25th, 50th, 75th, 95th and 99th percentiles have been marked along the curve.

design. Here, the aims of this project were to fly accelerometer equipped radiosondes through conditions where turbulence was anticipated. The analysis by Anderson (1957), using gust sondes, found that 77% of all descents contained a layer of turbulence, although the magnitude is not known. Given that this project is biased to flying accelerometer radiosondes through turbulence, the selected 75% percentile value of σ_z is a suitable threshold for significant turbulence. This is further reinforced with the estimation from the calibration with the lidar and MST radar in the previous chapter. For simplicity, rounding is applied to provide a σ_z threshold of 5 m s^{-2}.

Now that a value of σ_z that constitutes significant turbulence has been defined, the next section focuses on the properties of the vertical extent of detected turbulence. To calculate the vertical extent of each turbulent incident, subsequent $\sigma_z > 5$ m s^{-2} data records are concatenated together to give the vertical extent of turbulent motions. Figure 5.5 shows a histogram of depths of turbulent regions. It can be seen that the majority of turbulent layers are 200-400 m in depth. Some turbulent layers may be shallower than 200 m, but the use of a smaller sampling window may affect the σ_z calculation. Anderson

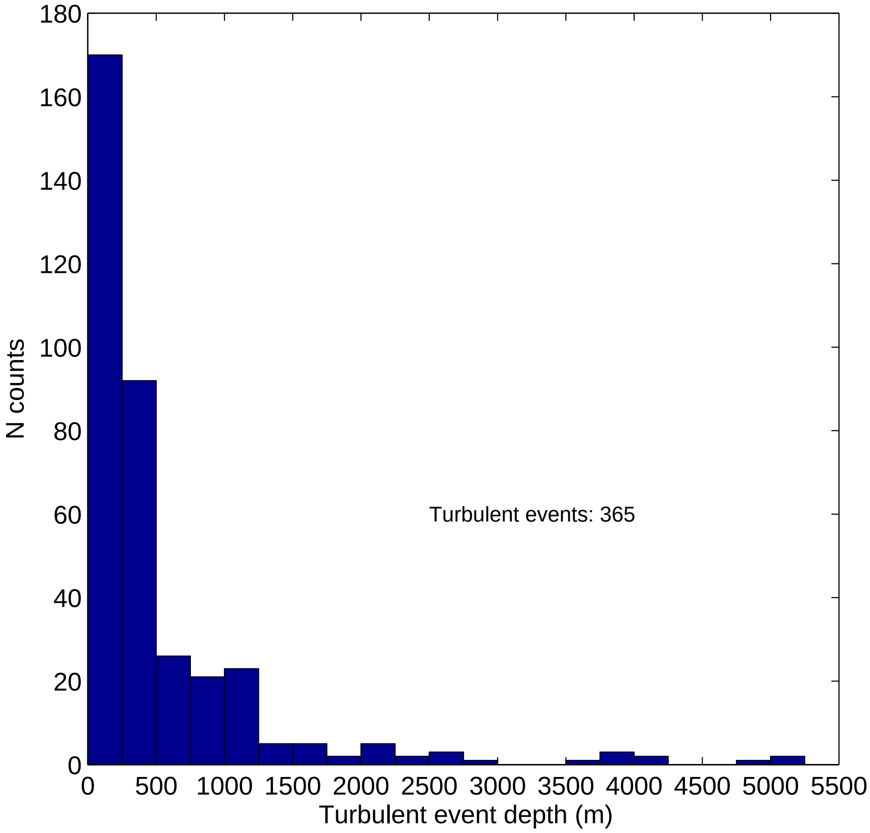

Figure 5.5 A histogram showing the depths of turbulent regions of the atmosphere where σ_z >5 m s^{-2} from 51 ascents.

(1957) found that 87% of identified turbulence patches were 400 m or less. Here 71% of turbulent patches are less than 400 m thick. It should be remarked again that this project targeted potential turbulence conditions, where the work of Anderson (1957) appears to be undertaken regardless of conditions and with a larger dataset.

The remainder of this section explores whether quantities such as the Richardson number, Brunt-Vaisala frequency, and vertical wind shear can be used to universally infer turbulence. The first quantity to be analysed is the Richardson number, Ri given by

$$Ri = \frac{N^2}{U_z}, \tag{5.1}$$

where N^2 is given by

$$N^2 = \frac{g}{\overline{T}}\theta_z, \tag{5.2}$$

where θ_z is the potential temperature gradient. Due to the instrumental noise encountered by both T and P, the resulting N^2 is noisy. Hence, θ is averaged over 200 m and a numerical gradient is taken from that to give θ_z. U_z is given by

$$U_z = \sqrt{\left(\frac{\partial u}{\partial z}\right)^2 + \left(\frac{\partial v}{\partial z}\right)^2}, \tag{5.3}$$

where the vertical derivatives of u and v are approximated by fitting a first order polynomial over the same 200 m height window that σ_z was computed from. To begin with, the Richardson number is examined, which is followed by an analysis of the N^2 and U_z components.

Figure 5.6 exhibits σ_z binned by Richardson number, no trend is clear but the largest range of σ_z are within the smallest positive Ri bin. This suggests that more intense turbulence is likely at low Richardson numbers. The notches within each box plot provide a confidence interval, so that multiple box plots can be examined visually, to access if they are significantly different. The confidence intervals reveal that σ_z values are not significantly greater than those at larger Richardson numbers. This suggests that, al-

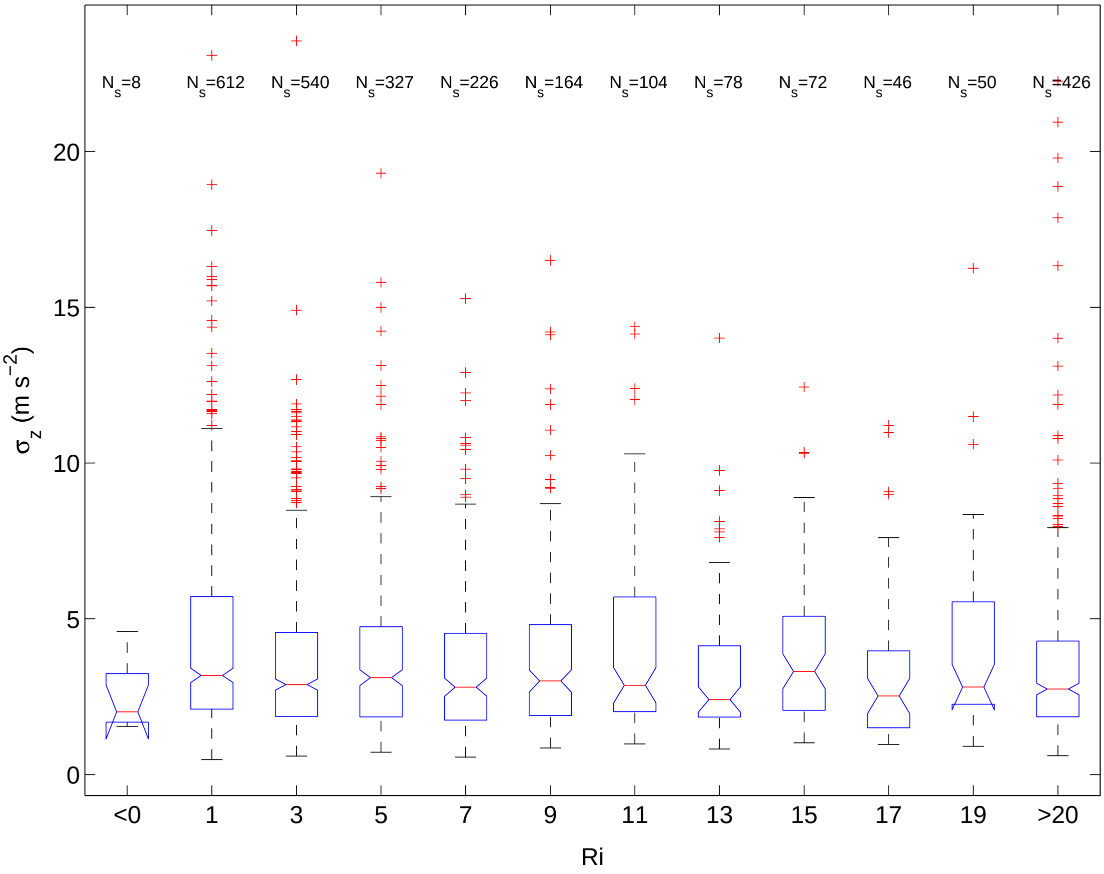

Figure 5.6 A box plot showing the distributions of σ_z (m s^{-2}) binned by Ri. The red line is the median, with the blue box representing inter quartile range ($q_3 - q_1$). Upper black stems represent the MIN($q_3 + 1.5(q_3 - q_1), \max(\sigma_z)$) and lower black stems represent the MAX($q_1 - 1.5(q_3 - q_1), \min(\sigma_z)$) red crosses show outliers which are data points that fall outside range given by the black stems.

though some of the largest σ_z values were observed at small Ri, there are also a lot of null turbulence observations. As there is no trend in the Ri data, it may be of more use to study the wind shear and thermal stability components separately. This is because the Richardson number cannot be used to infer all kinds of turbulence. The U_z data shall be the next avenue of examination.

σ_z was binned by U_z, and for each data bin, a box plot was produced to show the distribution of the data. Figure 5.7 shows that there is no relationship between U_z and the intensity of turbulence. Although the median value of the σ_z distributions does appear to increase somewhat, it is hard to conclude if a relationship is present with U_z. From the box plot notches in the binned data for a U_z of 0.035 s^{-1} it shows it to be significantly more turbulent than that of smaller U_z. However the subsequent larger bins have large confidence intervals and varying medians, making it hard to infer a trend. Furthermore, given the large amount of σ_z outliers for small U_z, it is unlikely that wind shear is a sole generator of turbulence. This is understandable, as the Richardson number criterion has both a buoyancy and shear term, which should ideally be at a critical ratio of 0.25. The numerator of the Richardson number, N^2 is now studied.

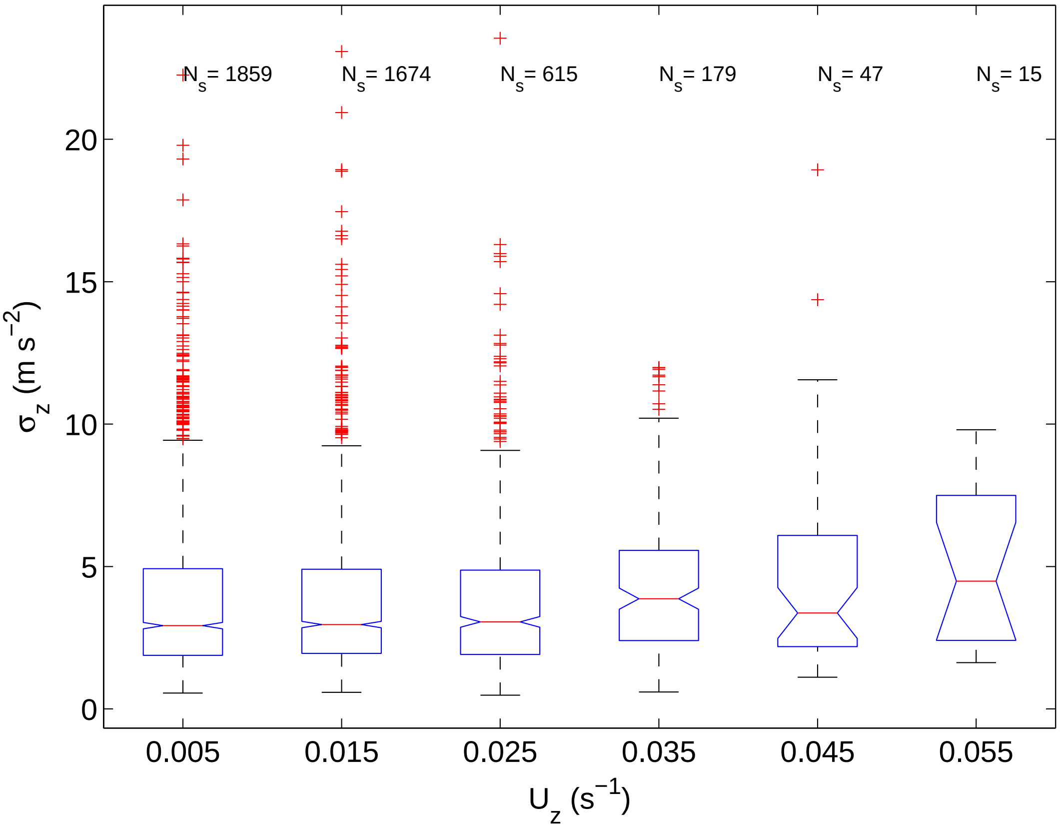

Figure 5.7 A box plot showing the distributions of σ_z (m s^{-2}) binned by U_z. For a full description of the box plot see figure caption 5.6.

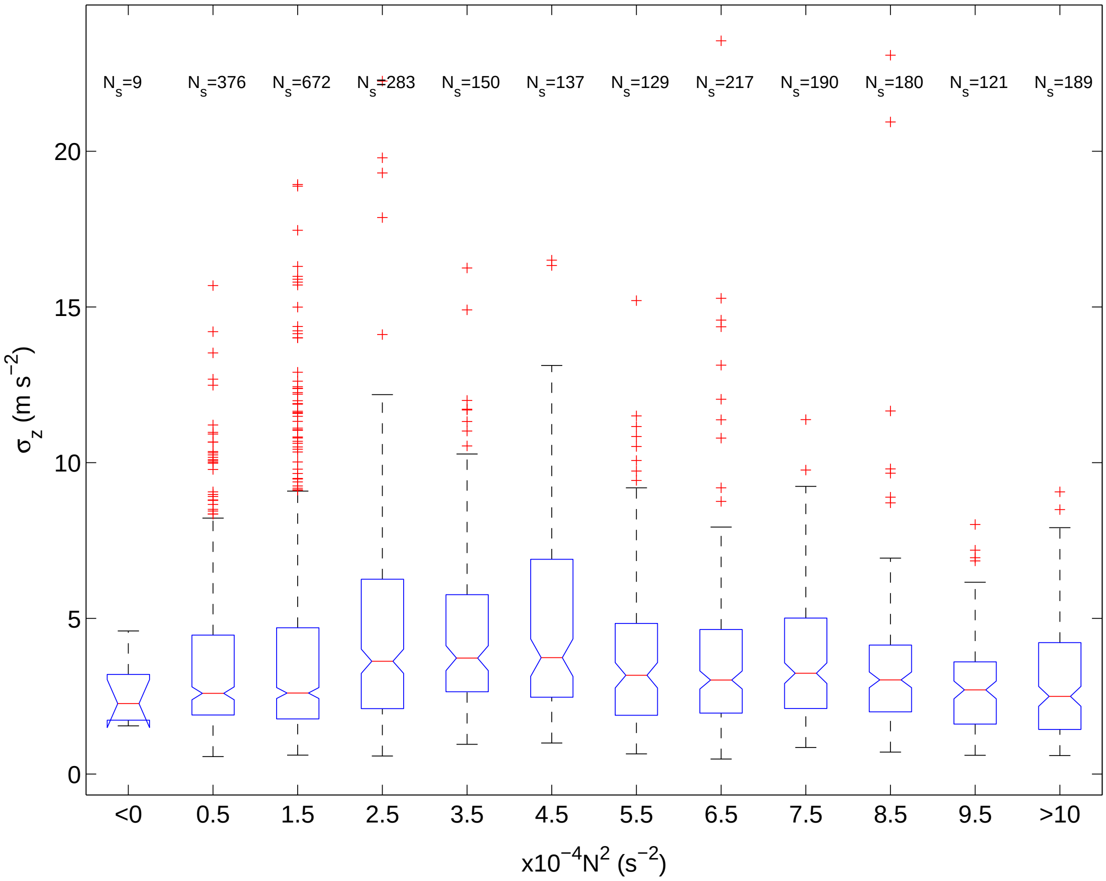

Figure 5.8 A box plot showing the distributions of σ_z (m s^{-2}) binned by N^2, for a full description of the box plot see figure caption 5.6.

Figure 5.8 shows a similar plot as shown in figure 5.7, but for N^2. There is a trend of increasing σ_z from a high N^2 of 1 to 2.5 $\times 10^{-4}$ s^{-2}, the latter value is a typical tropospheric value for N^2 (Ambaum, 2010). For N^2 values greater than 3.5×10^{-4}s^{-2}, σ_z values begin to drop, from this it could be concluded that greater than normal values of N^2 could yield more stratification and hence less turbulence. At less than nominal N^2 values, it appears that significantly smaller values of σ_z are observed, which shows that low thermal stability alone, is not enough to cause significantly more intense turbulence.

From the results of the analysis of Ri, N^2, and U_z over the whole dataset, there is little evidence to show that these quantities could be used as universal indicators of turbulence. This is due to there being many sources of turbulence in the atmosphere, some of which may not be represented by the Richardson number. Another problem lies in the uncertainty of these derived values which has been summarised in table 5.4. Uncertainties on directly measured values from the radiosonde were taken from the RS92 datasheet (Vaisala, 2013). Error propagation techniques in Hogan (2006) were used.

The uncertainty derived for Ri and U_z is quite small, where the errors are two mag-

Quantity	Uncertainty
ΔT	0.15 K
ΔP	0.4 hPa
Δu	0.15 m s^{-1}
Δv	0.15 m s^{-1}
$\Delta \theta$	0.2 K *
ΔU_z	8 $\times 10^{-5}$ s^{-1} **
ΔN	2 $\times 10^{-5}$ (s^{-1}) **
ΔRi	1% (fractional)

Table 5.4 A table showing the uncertainties associated with measured and derived quantities from the radiosonde. * Denotes an uncertainty which has propagated from uncertainties on direct measurements. ** Indicates an uncertainty that is based on the mean confidence intervals of first order polynomial fits to measured data from a randomly selected ascent.

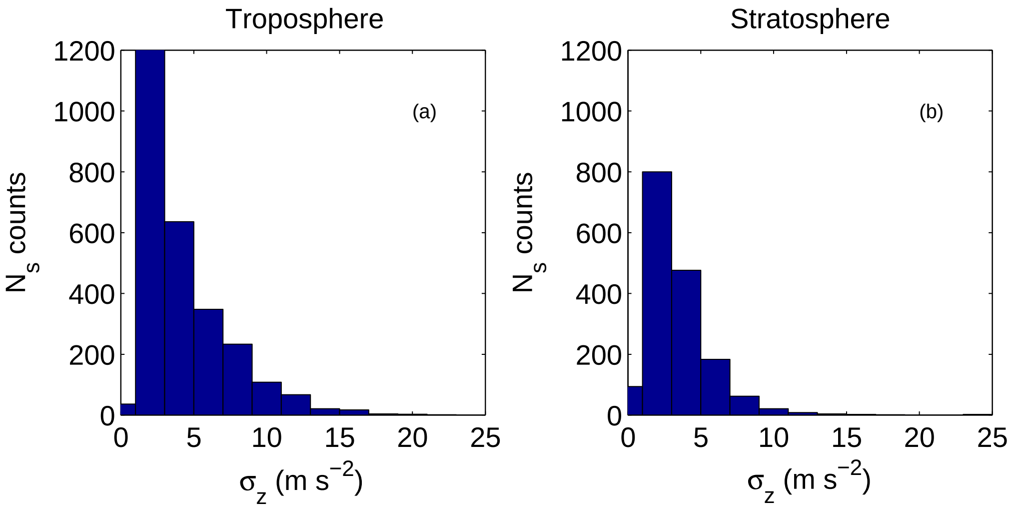

Figure 5.9 Histogram showing distribution of σ_z for a) tropospheric values, and b) stratospheric values.

nitudes smaller than the bin sizes. ΔN^2 is one order of magnitude smaller, which means there could be an uncertainty of up to a bin either way on calculated N^2. An en-masse approach to analysing this data set is not appropriate, and the dataset is best examined by performing a subset analysis of different meteorological conditions associated with turbulence generation. Hence, σ_z will be investigated in: jet stream conditions, the presence of convection, in and near clouds, and also when tropospheric gravity waves are present. The tropopause was defined thermodynamically as the point along the temperature profile where $dT/dZ <$ -2 K km^{-1} for 2 km (Santer et al., 2003). Using this definition, the dataset has been split into tropospheric and stratospheric data. Histograms of σ_z for both the troposphere and stratosphere are shown in figure 5.9. They have similar distributions, however one can see that the tropospheric distributions has a larger tail of σ_z events, this is expected as the stratosphere is generally less turbulent than the troposphere. In these next sections, jet stream, convective, in and near cloud and gravity wave turbulence will be explored.

5.3 Jet stream turbulence

In chapter 1, it was discussed that the jet stream was a main source of turbulence. This is due to the jet stream generating large wind shears and being a driver behind the development of extratropical weather systems, processes such as deformation (Holton, 2004), which have been shown to cause turbulence (Ellrod and Knapp, 1992) are also present. In this section, case studies of turbulence encounters in jet streams will be shown. A more quantitative assessment, taking into account all identified jet streams, is then undertaken. In this subset analysis, radiosonde metrics will be used to identify turbulence trends.

5.3.1 Case study 1: 28th April 2015

Figure 5.10 shows the horizontal wind component from the NERC MST radar, at Aberystwyth on 28th April 2015. The three pink lines indicate times when accelerometer sondes were launched. It can be seen that the intensity and position of the jet stream does not appear to change over the IOP. There is a slight drop of 10 m s^{-1} across the jet core, but apart from this the jet stream structure appears uniform. Figures 5.11, 5.12 and 5.13 show accelerometer ascents corresponding to each of the pink lines in figure 5.10 respectively.

In all three ascents, there is no cloud observed and no appreciable convection, which implies that any turbulence observed is most likely connected with the jet stream. In the first ascent made at 1204 UTC shown in figure 5.11, turbulence is observed in the shear region between 4 and 6 km. The source of the turbulence is likely due to the wind shear at this height. Turbulence would also be expected at 10 km in the other shear region, but the increased stratification above the tropopause may have suppressed turbulence generation. Figure 5.12 shows an accelerometer ascent made 2 hours later at 1348 UTC, from the same location. It can be seen that the meteorological conditions are very similar to the ascent made in figure 5.11, however more intense turbulence is present with a larger vertical extent between 4-10 km. In the final ascent made at 1507 UTC shown in figure 5.13, turbulence is still at the same intensity, and the meteorological conditions are

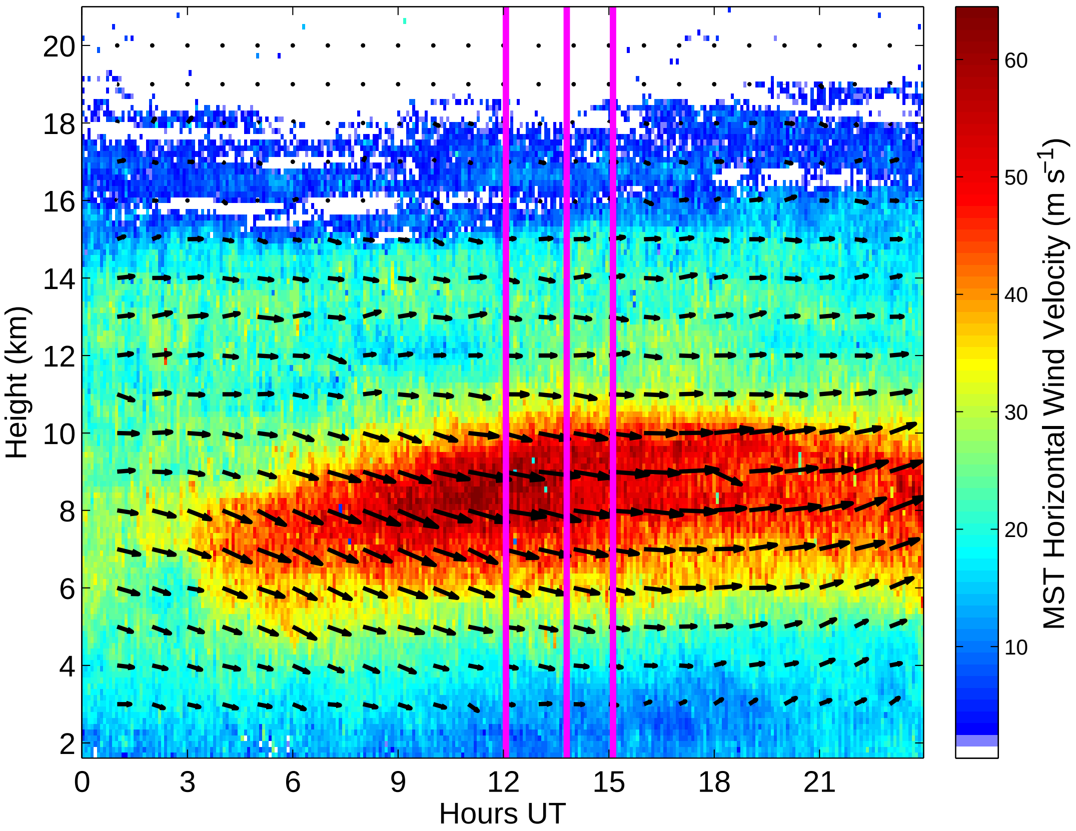

Figure 5.10 Horizontal wind magnitude from the NERC MST wind profiler at Aberystwyth, arrows indicate the direction and size of the wind vector, for the day of 28th April 2015. Pink lines indicate the time of radiosonde launches.

similar. In the two latter cases it is obvious that turbulence is being suppressed in the lower stratosphere due to the higher static stability. Turbulence in the lower jet region is understandable due to the shear region. However, a null region at the jet core is expected where the air should have a more laminar flow, in this case it is turbulent. Before drawing any further conclusions an examination the wind shear, stability and the Ri number from these ascents will be undertaken.

In figure 5.14 all three accelerometer ascents have been overlaid, see caption for legend. Panel (a) shows that the turbulent region appears to be building from within the shear region of the jet into the jet core. Examination of U_z, N, and Ri in panels (b-d) shows they are not significantly different on an ascent-to-ascent basis. The Richardson number in panel (d), despite being noisy, indicates that for all three ascents, there should be turbulence in the shear regions of the jet that do not reside in the lower stratosphere. The latter two σ_z profiles show agreement with this. There is no variation in θ with time in panel (e), further removing the possibility of frontal structure giving rise to the development of turbulence witnessed. Briefly summarising the analysis of the standard

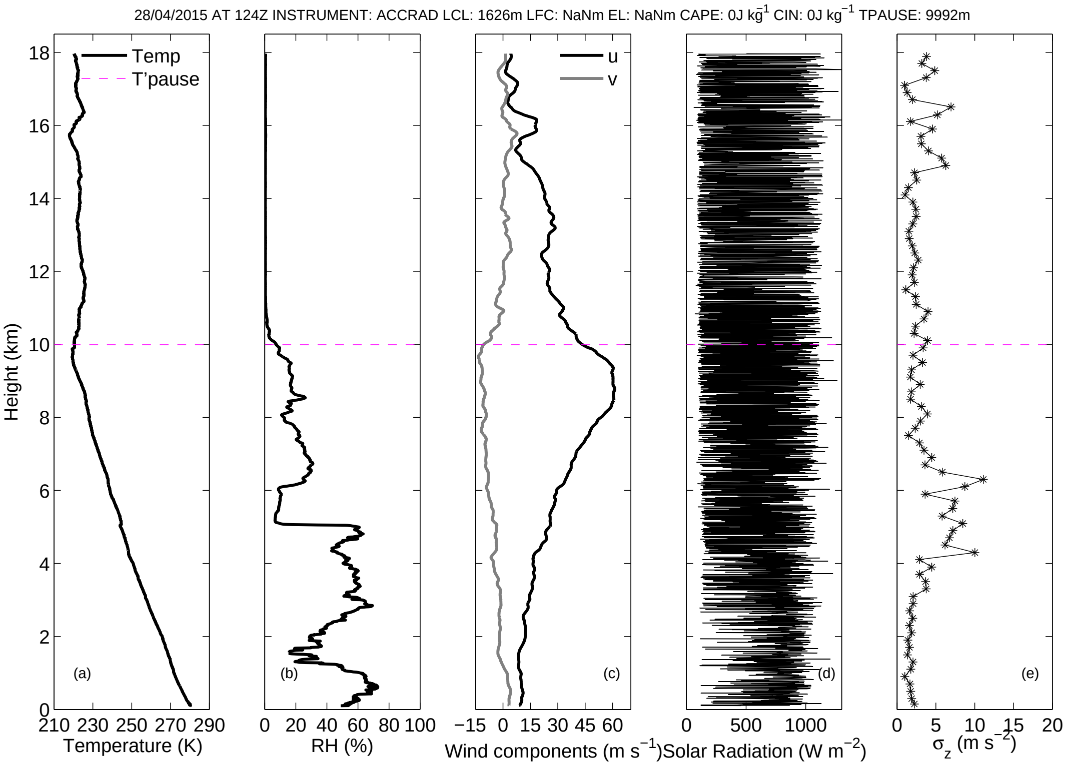

Figure 5.11 Vertical profiles of a) temperature (K) , b) RH (%) c) u and v wind components in black and grey respectively (m s^{-1}), d) Solar radiation from photodiode (W m^{-2}) and (e) σ_z (m s^{-2}) for an ascent at 1204 on 28th April 2015 from the NERC MST radar site at Aberystwyth. The purple line is the estimated tropopause height.

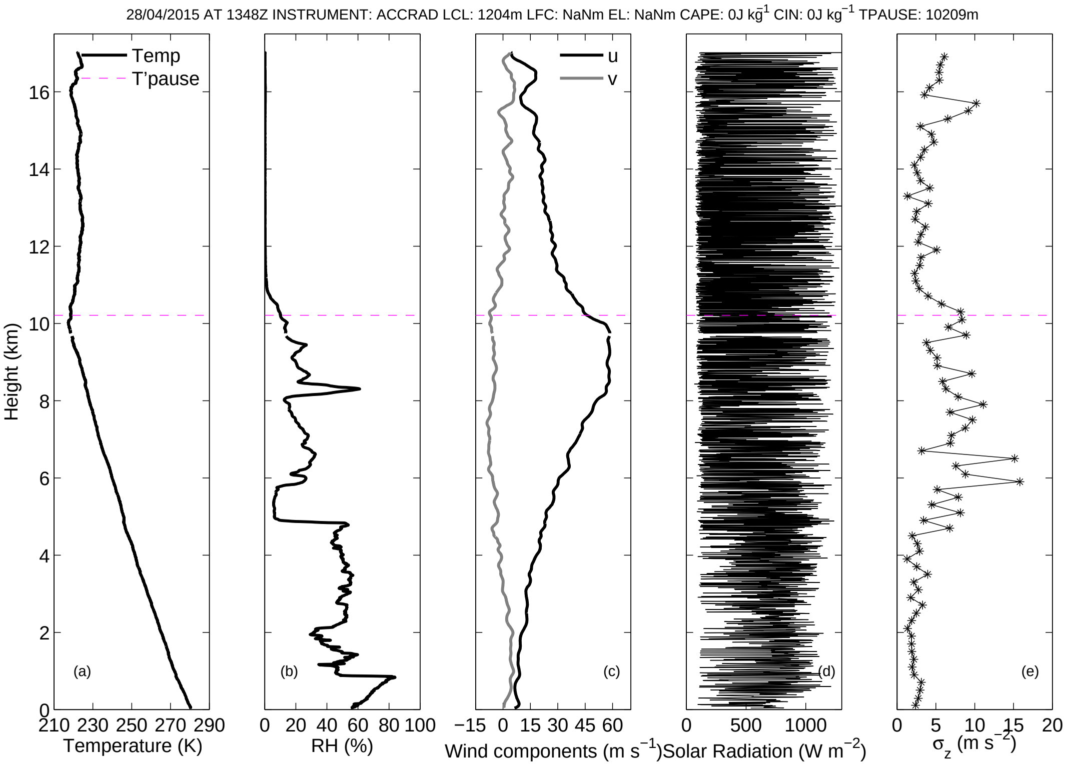

Figure 5.12 Vertical profiles of a) temperature (K) , b) RH (%) c) u and v wind components in black and grey respectively (m s^{-1}), d) Solar radiation from photodiode (W m^{-2}) and (e) σ_z (m s^{-2}) for an ascent at 1348UTC on 28th April 2015 from the NERC MST radar site at Aberystwyth. The purple line is the estimated tropopause height.

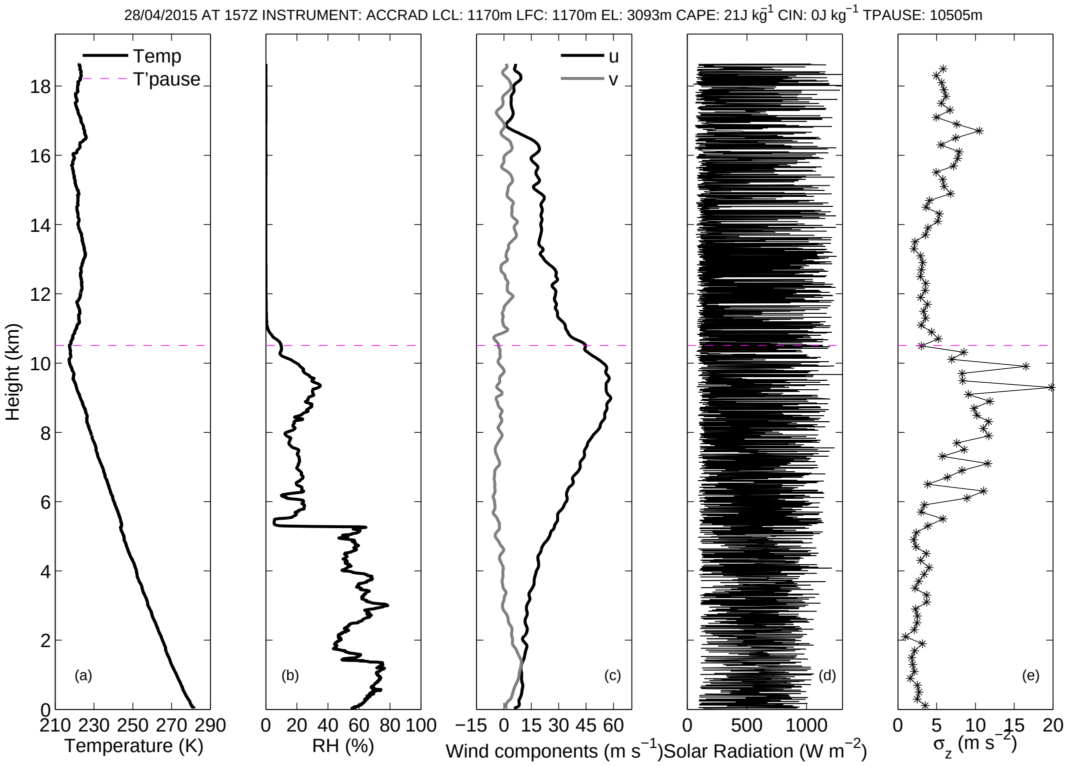

Figure 5.13 Vertical profiles of a) Temperature (K) , b) RH (%) c) u and v wind components in black and grey respectively (m s^{-1}), d) Solar radiation from photodiode (W m^{-2}) and (e) σ_z (m s^{-2}) an ascent at 1507UTC on 28th April 2015 from the NERC MST radar site at Aberystwyth. The pink line is the estimated tropopause height.

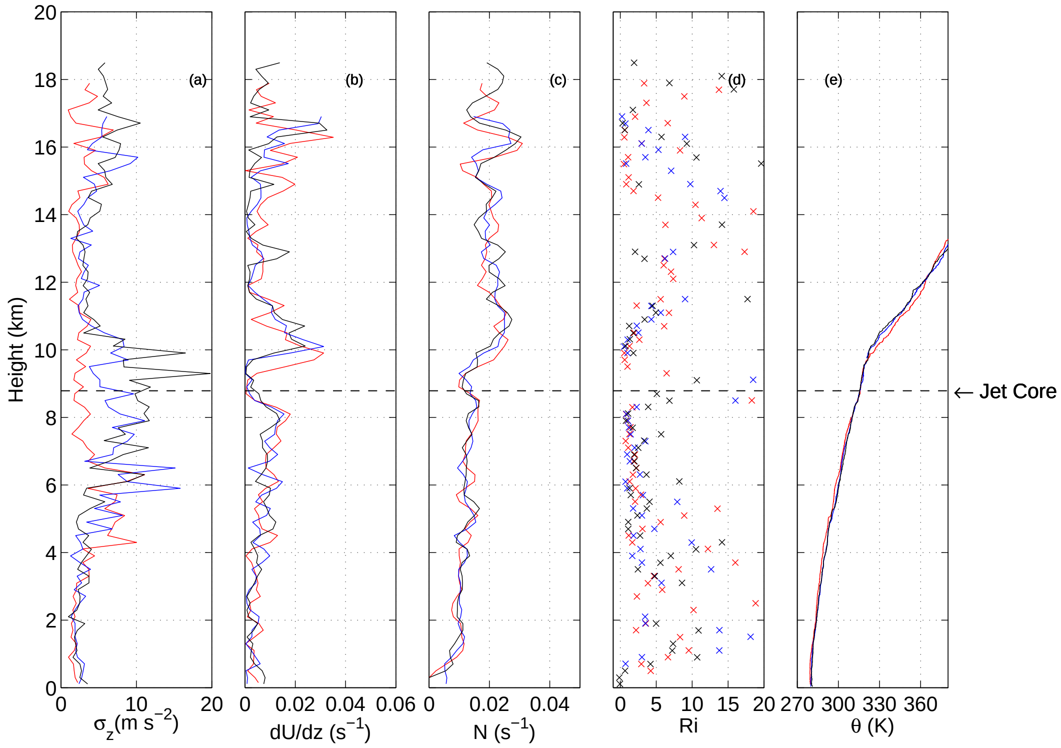

Figure 5.14 Vertical profiles of a) σ_z (m s^{-2}), b) U_z (s^{-1}), c) N (s^{-1}), d) Ri, and e) θ (K) for the 1204 (red) 1348 (blue) and 1507 (black) accelerometer launches from the NERC MST radar site on 28th April 2015.

meteorological parameters has shown that the turbulence is likely caused by the wind shear, although the reason for its temporal development is yet to be understood. Whilst a wealth of data can be obtained from a radiosonde's suite of instruments, there are limitations to the larger meteorological processes it can observe. The radiosonde is essentially taking Lagrangian measurements along a trajectory. Dynamical measurements, such as deformation are calculated on grids, a further analysis of this case study will continue in chapter 6, where other dynamical properties from a model can be used to infer information about the temporal evolution of turbulence.

5.3.2 Case study 2: 4th March 2015

The second case study to be examined is that of a jet stream with a tropopause fold, on the 3rd March 2015 from the NERC MST radar site. In this case study, a north-south jet stream is present, as shown in the radar data in figure 5.15. During the IOP, the jet stream's structure changes from a narrow fast jet to a less intense jet stream with a larger

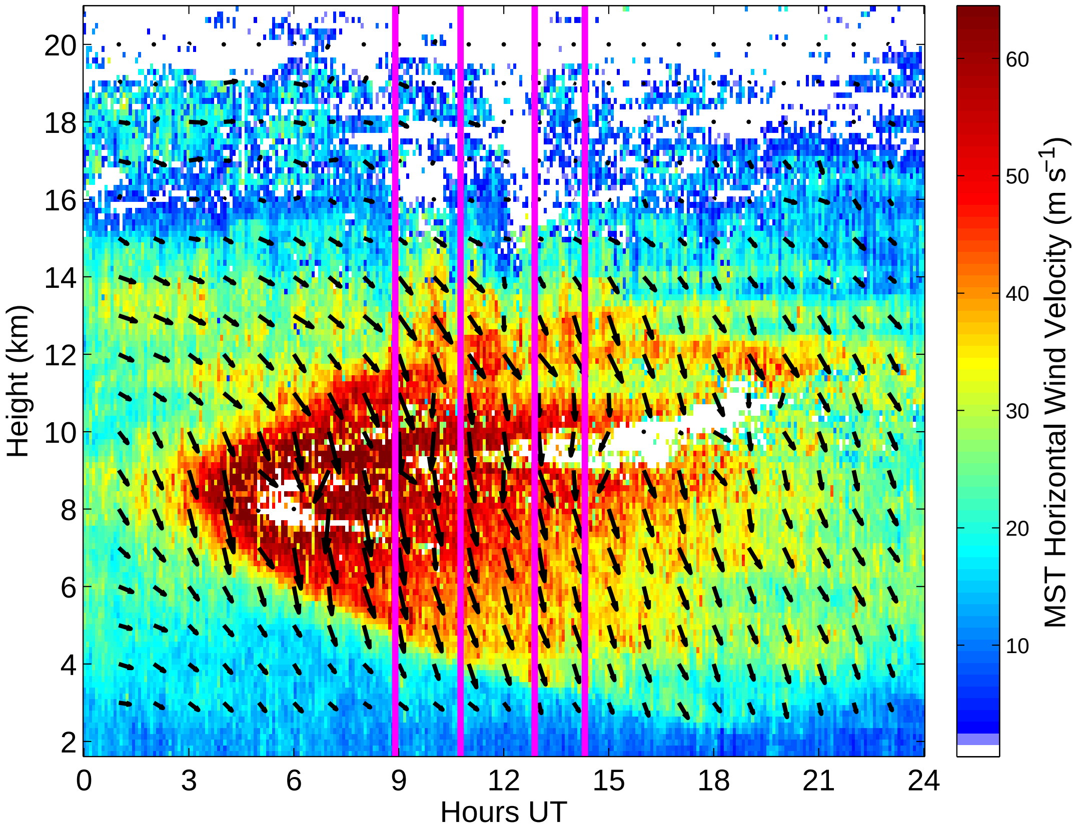

Figure 5.15 Horizontal wind magnitude from the NERC MST wind profiler at Aberystwyth, arrows indicate the direction and size of the wind vector, for the day of 4th March 2015. Pink lines indicate the time of radiosonde launches, white gaps within the jet stream are due to poor radar return, which can occur in very intense jet streams.

vertical extent. The bow shock shape depicted in figure 5.15 implies that a tropopause fold may be present over the radar site. Troposphere folds occur when the ageostrophic winds about the jet are combined with the frontal zone (Reid and Vaughan, 2004), causing a deep intrusion of stratospheric air into the troposphere, which has been associated with turbulence. Signatures of tropopause folds in radiosonde ascents are a large potential temperature gradient and a dew point depression > 45 K (Vaughan et al., 1994). The purple lines in figure 5.15 represent the times of radiosonde launches made on this day.

The radar site is situated in a valley meaning that under some conditions radiosonde reception can be patchy as the signal is blocked by mountains, a directional antenna boosts the reception but to limited affect. Hence the first ascent of the IOP at 0854 UTC only has data available up to 9 km which is shown in 5.16. Moderate σ_z is found in the lower shear region of the jet stream, at the same height as the tropopause fold. In panel (a), the temperature profile becomes shallow, which would correspond to a steep θ gradient and secondly RH is near 0% indicative of stratospheric air. Furthermore the proximity of this turbulent area to the cloud top at 2 km may indicate a contribution of cloud top turbulence. In the second IOP at 1046 UTC show in figure 5.17 the turbulence is mainly concentrated between 5-10 km, which could be due large values of U_z in the jet stream. As there is not much turbulence around 4 km as seen in the previous flight, this may be due to a reduction in the size of the wind shear in this region, or change in prominence of the tropopause fold which is likely still present, as evident in temperature and humidity profiles in panels (a) and (b) respectively.

Figure 5.18 shows the third ascent made at 1253UTC where the turbulence regions present in figure 5.17 have intensified, despite the reduction in jet stream speed and wind shear. The final ascent at 1419UTC is shown in figure 5.19, which demonstrates turbulence in the same location but of even higher intensity than the previous ascent, with yet another reduction in wind shear and wind speed. One noteworthy observation is the wave like properties in the wind profiles above the jet stream which are likely gravity waves. If these are gravity waves emitted from the upper regions of the jet stream, then the observed turbulence maybe caused by spontaneous imbalance of the jet stream as discussed in Knox et al. (2008) and McCann et al. (2012). As in the last case study, more information can be inferred by comparing vertical profiles of θ, N, U_z and Ri.

Figure 5.20 shows the 4 ascents overlaid, see figure caption for legend. It can be seen that during the IOP the turbulence intensified, and over a larger vertical extent. The wind shear is quite small when compared with that of the previous case study; the

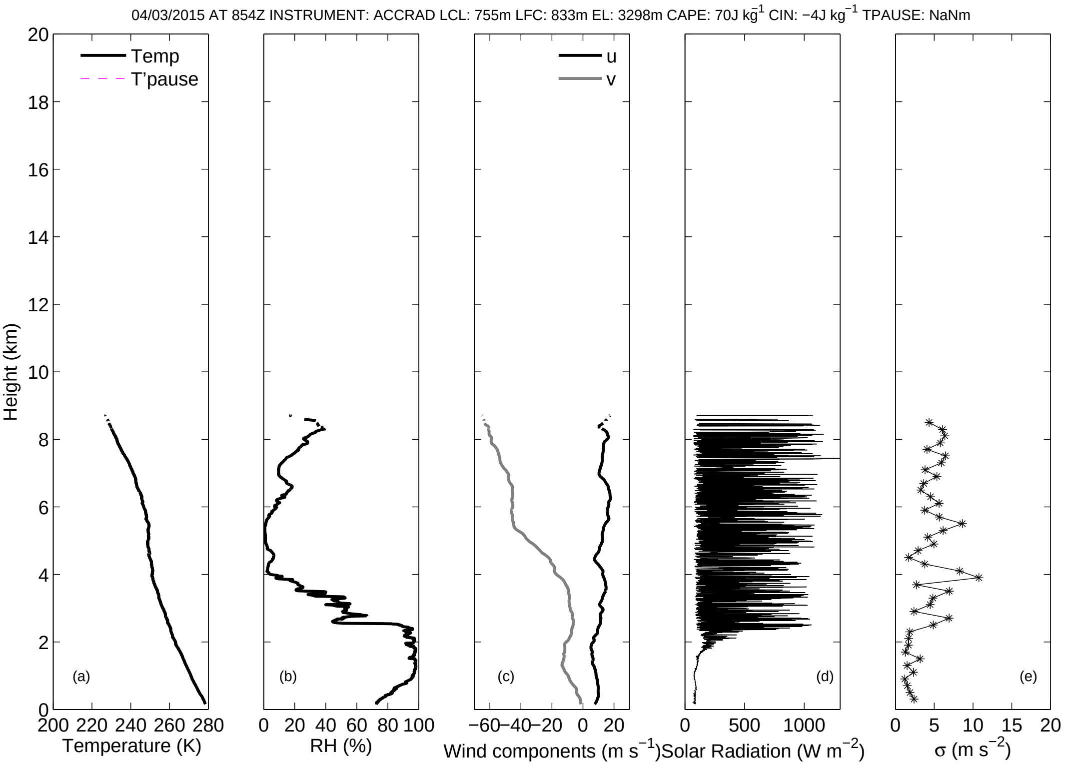

Figure 5.16 Vertical profiles of a) temperature (K) , b) RH (%) c) u and v wind components in black and grey respectively (m s^{-1}), d) Solar radiation from photodiode (W m^{-2}) and (e) σ_z (m s^{-2}) for an ascent at 0854UTC on 4th March 2015 from the NERC MST radar site at Aberystwyth. The purple line is the estimated tropopause height.

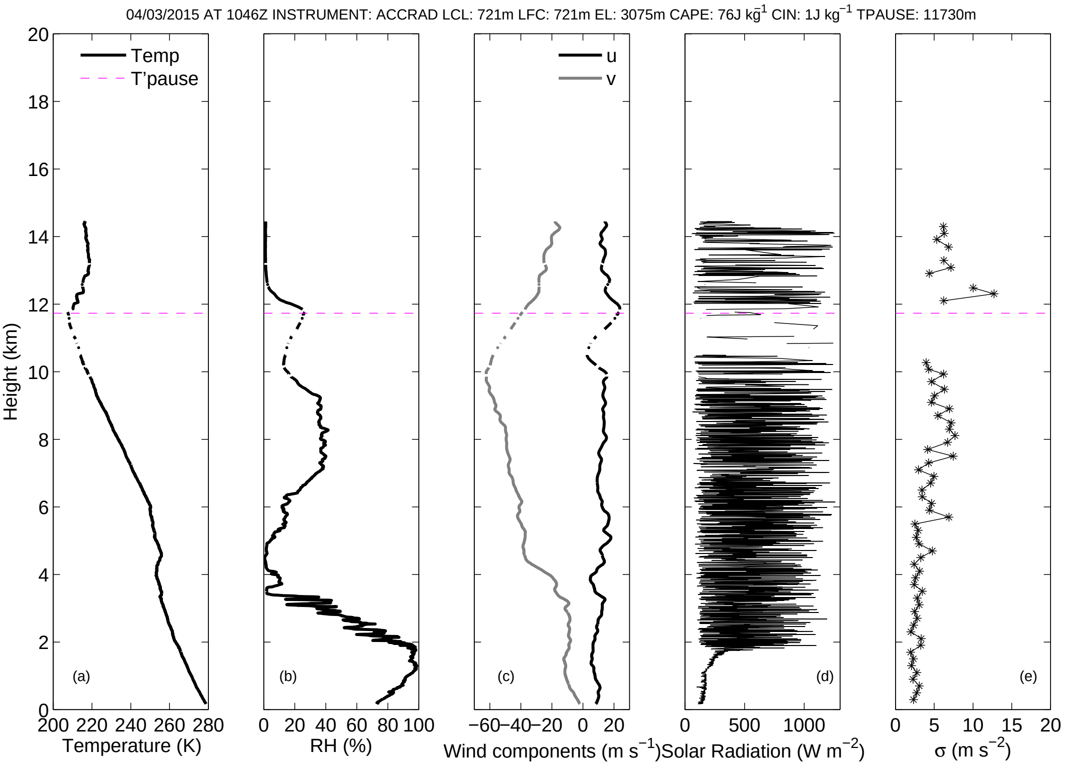

Figure 5.17 Vertical profiles of a) temperature (K) , b) RH (%) c) u and v wind components in black and grey respectively (m s^{-1}), d) Solar radiation from photodiode (W m^{-2}) and (e) σ_z (m s^{-2}) for an ascent at 1046UTC on 4th March 2015 from the NERC MST radar site at Aberystwyth. The purple line is the estimated tropopause height.

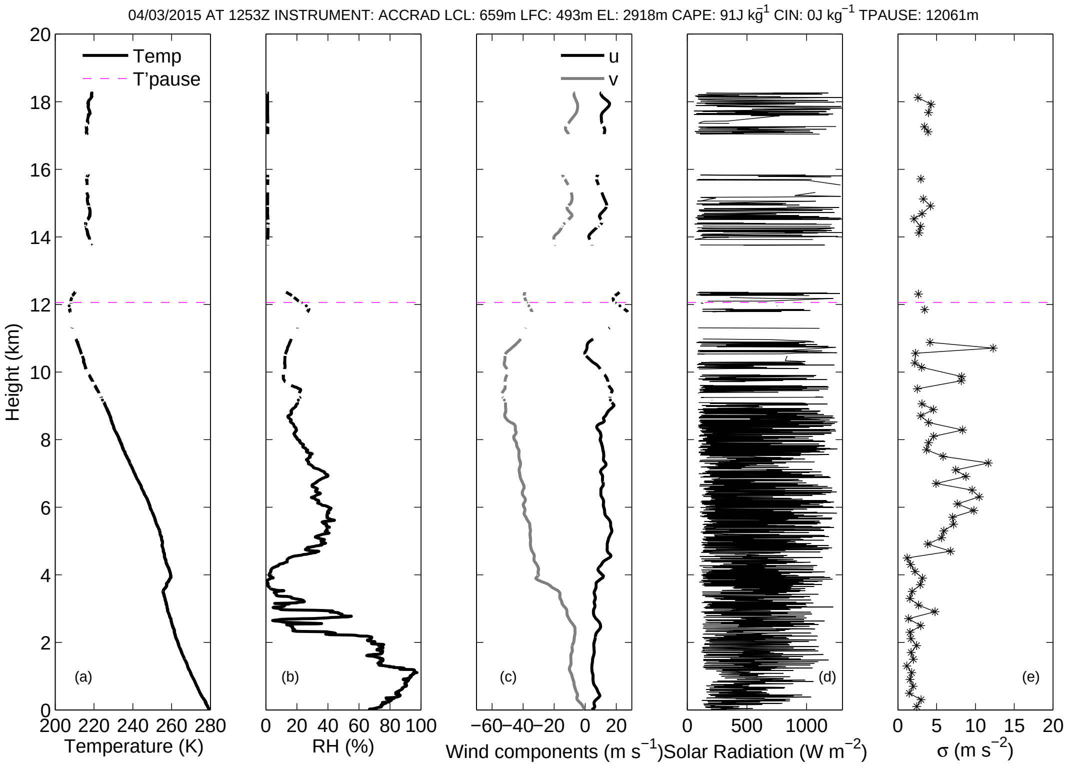

Figure 5.18 Vertical profiles of a) temperature (K) , b) RH (%) c) u and v wind components in black and grey respectively, d) Solar radiation from photodiode (W m^{-2}) and (e) σ_z (m s^{-2}) for an ascent at 1253UTC on 4th March 2015 from the NERC MST radar site at Aberystwyth. The purple line is the estimated tropopause height.

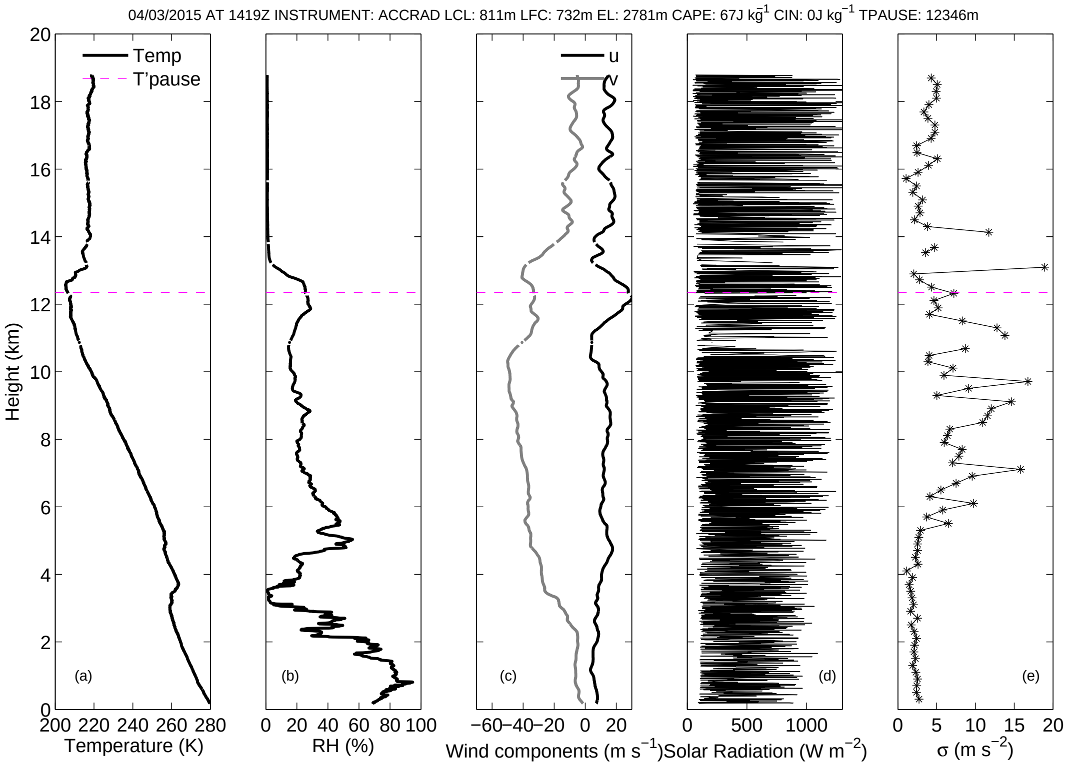

Figure 5.19 Vertical profiles of a) temperature (K) , b) RH (%) c) u and v wind components in black and grey respectively, d) Solar radiation from photodiode (W m^{-2}) and (e) σ_z (m s^{-2}) for an ascent at 1419UTC on 4th March 2015 from the NERC MST radar site at Aberystwyth. The purple line is the estimated tropopause height.

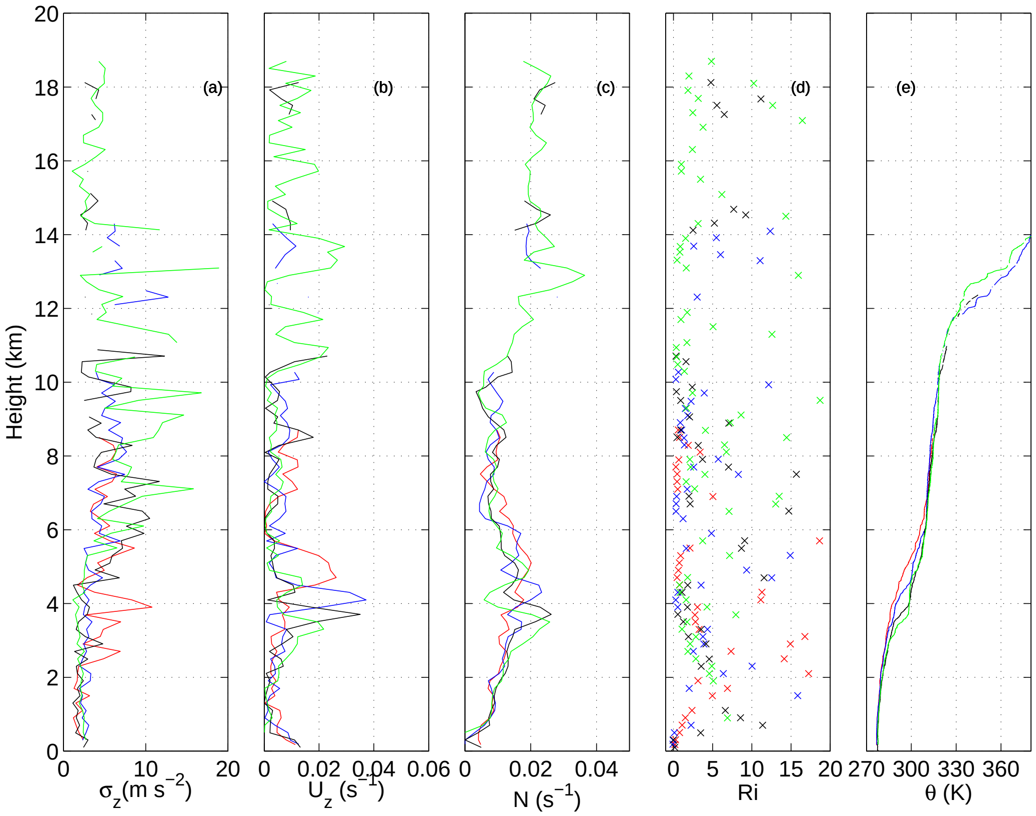

Figure 5.20 Vertical profiles of a) σ_z (m s^{-2}, b) U_z (s^{-1}), c) N (s^{-1}), d) Ri and (e) θ (K) for the 0854UTC (red), 1046UTC (blue), 1253UTC (black) and 1419UTC (green) accelerometer launches from the NERC MST radar site on 4th March 2015.

static stability appears to be lower, which could be another cause of increased turbulence within the jet stream especially between 6 and 10 km. In panel (c) a local maxima in N is present about 3-4 km which indicates the intrusion of stratospheric air in the form of a tropopause fold. This can also be seen in panel (e) where a change in the θ profile structure is seen indicating that the tropopause fold is dropping in height. This is in agreement with the jet stream structure shown in Shapiro (1976), although their aircraft observations are not in the same position across the jet core. Shapiro (1976) then state that their results are from a limited set of jet case studies, which may not offer a fair representation. In the first case study the turbulence could be caused by wind shear, however the temporal development of turbulence requires the help of quantities from a numerical model to explain. In the second case study a lower static stability across the jet core may lead to turbulence production, either by spontaneous imbalance due to the gravity waves emitted from the jet, or due to the tropopause fold making air in the jet less stable. There are many jet streams present in the radiosonde dataset. In the next section, a more quantitative analysis of accelerometer encounters with jet streams is undertaken.

5.3.3 A subset analysis of Jet stream ascents

Jet streams are defined by the Met Office (1991) glossary as a region of the atmosphere where wind speeds exceed 25 m s^{-1}. Endlich and McLean (1957) defined a jet stream should have a jet core speed in excess of 50 m s^{-1}. From the previous definitions, and from visual inspection of jet stream case studies undertaken here, a jet core was classified here as the height at which $U_{max} > 40$ m s^{-1}, but only if there was a standard deviation of the U profile > 10 m s^{-1}. Thus ensuring jet streams with an identifiable jet core are selected, on some occasions a strong uniform flow spanning the troposphere and lower stratosphere could be mistaken for a jet stream. The vertical extent of the jet core was classified as the region where the U does not fall below 10% of the jet core peak. The vertical extent of the jet was classified as the heights away from the jet core at which the horizontal wind speed first drops to below 25 m s^{-1}. To remove the effects of high frequency variations in U, this analysis was performed on 200m height averaged data using the same window as computations of σ_z.

Firstly, an analysis of the σ_z by maximum core speed is presented, to see if faster jet streams have larger turbulence associated with them. The reasoning behind this is firstly that U is often featured as a factor in turbulence diagnostics [Reap (1996),Vogel and Sampson (1996), etc]. Secondly, the speed of the jet is related to horizontal thermal gradients in a meridional sense which is another turbulence diagnostic (Audrey et al., 2011). Climate projections by Williams and Joshi (2013) show that intensification of this gradient in the Upper Troposphere and Lower Stratosphere (UTLS) due to climate change could lead to a more intense jet with more intense turbulence. Furthermore, faster jet streams are likely to have larger U_z which have been shown in one case study as a likely cause of turbulence.

In figure 5.21, it can be seen that there is little evidence of significant increase in σ_z with peak velocity of the jet stream. Although for the fastest jet streams, all σ_z values are over the 5 m s^{-1} threshold derived in earlier sections. The bulk of observed jet streams have a peak jet core about 50-70 m s^{-1}, for these values, there is a large variety of σ_z ranges, implying that while the presence of the jet stream is a source of turbulence, the turbulence intensity is not a strict function of the jet core speed. At slow jet core speeds (< 50 m s^{-1}) there are smaller ranges in σ_z, indicative that slower jet streams may have less intense turbulence. In the previous two case studies, a uniform jet structure and a jet structure which developed with a tropopause fold were shown. In the first, a large wind shear was shown to be a possible cause of turbulence, however, it did not explain the

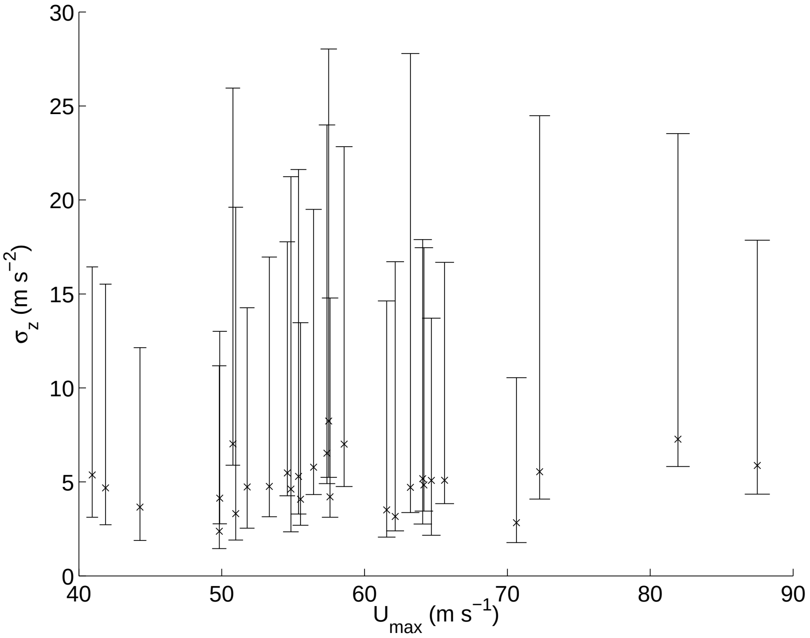

Figure 5.21 A plot showing the mean σ_z against peak wind speed U_{max} bars represent the range of σ_z for each jet stream with peak U_{max}.

temporal evolution. In the second ascent, a low N was associated with the large region of intense turbulence found above the tropopause fold. In this next part of the analysis, the amount of significant σ_z that can be attributed to either low N or large U_z will be examined. Threshold values for these two quantities are first required, $N = 0.01$ s^{-1} is considered a typical tropospheric value, with values less than this indicating unstable air, hence this value will be used as a stability threshold. For U_z, a value of 0.0125 s^{-1} is related to a moderate shear of 12.5 m s^{-1} km^{-1}. A contingency table was constructed to find significant turbulence, where one or both of these quantities could be attributed as a source of turbulence. Only σ_z values that were in jet regions were used in this analysis. Furthermore, σ_z values which were also related to convection or clouds were removed using definitions in sections 5.4 and 5.5.

	$\sigma_z > 5$ m s^{-1}	$\sigma_z < 5$ m s^{-1}
$N \leq 0.01$ s^{-1} and $U_z \geq 0.125$ s^{-1}	5 (1.2%)	3 (0.5%)
$N \leq 0.01$ s^{-1} and $U_z < 0.125$ s^{-1}	98 (24.4%)	69 (11.47%)
$N > 0.01$ s^{-1} and $U_z \geq 0.125$ s^{-1}	106 (26.4%)	149 (24.75%)
$N > 0.01$ s^{-1} and $U_z < 0.125$ s^{-1}	192 (47.9%)	381 (63.3%)
Total	401	602

Table 5.5 A contingency table showing counts of σ_z under different N^2 and U_z conditions within selected jet streams.

In table 5.5 it can be seen that approximately 24 % of significant turbulence could be attributed to low static stability and like wise another 26 % are attributed exclusively to high wind shears. There were a small handful of cases in which both low N and high U_z could have both been attributed to turbulence. 47% of significant turbulence could not be attributed to either. It should also be noted that 63% of null turbulence occurred in the presence of large N and low U_z. This reinforces that a proportion of turbulence being observed in jet streams is likely caused by processes which cannot be directly observed by radiosondes, such as horizontal wind gradients. Yet, it also shows that low static stability and high wind shears are a contributing factor for turbulence when a dataset has been refined to look at one phenomenon. In the latter case study, a tropopause fold was present, which could potentially play a role in the intensity of turbulence within a jet stream. One way of determining if a tropopause fold might be present is by examining σ_z by wind direction as tropopause folds are more likely to happen along a N-S orientated jet stream.

Figure 5.22 shows that there is no given jet stream direction that yields more intense turbulence, with the exception of easterly jet streams, which do not occur commonly in the atmosphere, hence no data is available in the dataset to assess this. As tropopause folds tend to occur along a north-south axis, there is little evidence from the directional

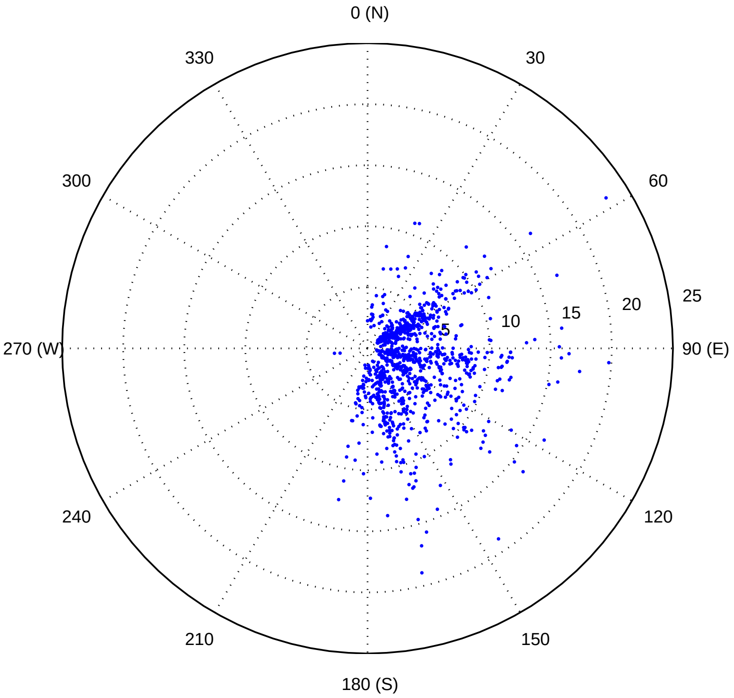

Figure 5.22 A Polar plot showing the wind bearing (deg) of all σ_z values within jet streams. The distance from the origin is the size of σ_z in (m s^{-2}).

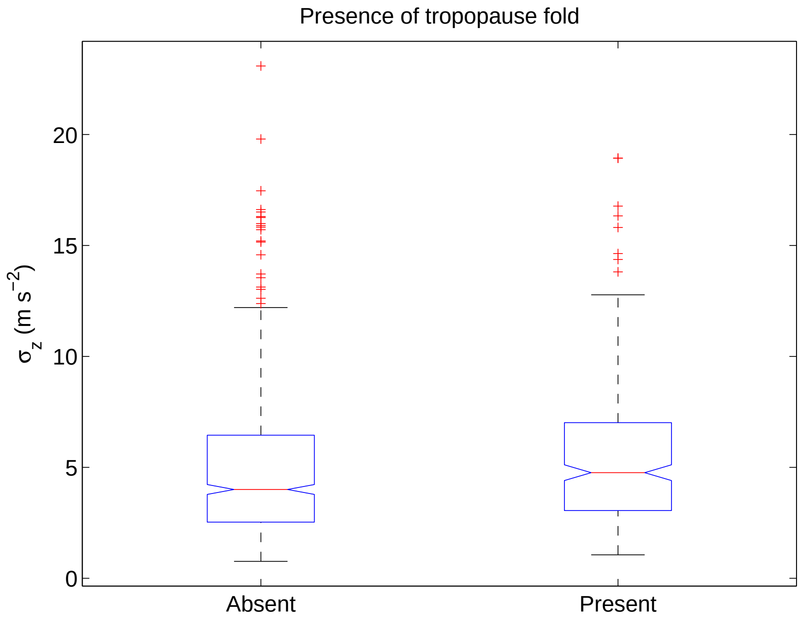

Figure 5.23 A box plot showing the distributions of jet stream σ_z (m s^{-2}) binned by presence of a tropopause fold. σ_z in jet streams without a tropopause fold present had a median of 4 m s^{-2}. A median σ_z of 4.76 m s^{-2} was recorded for jet streams with a tropopause fold present. For a full description of the box plot see figure caption 5.6

.

analysis that they may be associated with turbulence. To further check this, a diagnostic was run to find which jet streams had a tropopause fold, defined as having a region of both high $N > 0.02$ s^{-1} and $RH < 5\%$ present beneath the jet core. σ_z in jet streams that met this criteria were binned and compared with those which did not. The results are shown in figure 5.23, jet streams which did have tropopause folds present do have slightly larger σ_z values present. This is indicated by the different values of the interquartile range. The confidence intervals in both box plots do not overlap, also indicating jet streams with tropopause folds contain more intense turbulence. An example is shown in the second case study, summarised in figure 5.20. A tropopause fold alters the thermodynamic structure of the atmosphere, potentially making the air inside the jet stream more unstable than in the first case study summarised in figure 5.14.

5.3.4 Conclusions

In this section, two case studies of jet stream turbulence have been examined. In the first, turbulence was encountered in the lower boundary of the jet stream, which has been attributed to U_z. Turbulence was not found on the upper jet stream boundary, due to the stratification of the lower stratosphere. Although stability and shear conditions did not change significantly over the IOP, the spread and intensity of turbulence did. This indicates that a dynamical process, not directly observable by the radiosonde, could be causing this. In the next chapter, further analysis, utilising a model representing the state of the atmosphere, will be used to explore the temporal evolution of the turbulence. The model is run at multiple time steps allowing the evolution of turbulence to be examined. In the second case study, a jet stream with an evolving structure and tropopause fold was analysed. U_z was not as intense as in the previous study, but stability across the jet core was low. During the second IOP, turbulence intensity increased as jet speed and U_z decreased. Turbulence in the jet core could be attributed to the low static stability, which may be a side effect of the tropopause fold undercutting the jet. Alternatively, given the wavelike signatures in the wind profiles above the jet stream, turbulence may be created by breaking gravity waves emitted due to spontaneous imbalance or mountain waves. The temporal evolution of turbulence within the latter case study, if caused by the tropopause fold, could be occurring as the tropopause fold drops in height, as shown in panel (e) of figure 5.20. In the two case studies it was also shown that turbulence in jet streams has a life span of more than a couple of hours, however further anaylsis with other dynamic quantities are needed.

In the analysis of multiple jet stream ascents, it was found that faster jet streams did not necessarily lead to more intense turbulence. There was little preference for more intense turbulence along a given wind direction with the potential exception of easterly bearing jet streams, which have not been sampled. It was found 24% of jet stream turbulence could be attributed to low static stability and 26% could be attributed to high wind shears. Jet streams where tropopause folds are present were found to be more turbulent than those where a tropopause fold was not present. This could be due to the tropopause fold changing the thermodynamic structure of the jet above, making it more unstable. From this analysis it appears that less stability, either via a tropopause fold or spontaneous imbalance and large wind shear show attribution to just over half of significant turbulence observed. In the next chapter an exploration with a model will be used to examine further processes which could also cause turbulence.

5.4 Convective turbulence

Convection is well known to cause turbulence. This is due to warm air rising and reaching a equilibruim level (EL) where the air is forced to stop. Rising and falling air has been included in some turbulence diagnostics via a convergence term (Ellrod and Knapp, 1992), or by looking at vertical velocity (Sharman et al., 2006). Aircraft avoid large thunderclouds, as they contain turbulence generated from up drafts and down drafts, as well as possible damage from lightning and large hail stones. From a commercial aviation prospective, this makes thunderclouds easy to avoid. However, from a scientific perspective this means there are very few measurements of turbulence within cloud. In this section an analysis as to whether there is a relationship between CAPE and turbulence will be undertaken. First, two case studies will be examined, one in clear-air conditions which is of particular interest as aircraft would not avoid such an area in the absence of cloud. In the other case study in-cloud convective turbulence will be examined. In the second part of this section, an analysis of all ascents in which CAPE was present will be undertaken.

CAPE is calculated using (Wallace and Hobbs, 2006)

$$CAPE = R_d \int_{EL}^{LFC} \left(T_v' - T_v\right) d\log P, \tag{5.4}$$

where T_v is the observed virtual temperature, and T_v' is the virtual temperature of the air parcel if it were to follow the saturated adiabat from the lifting condensation level (LCL). R_d is the gas constant of dry air. The LCL is found using a Normand's rule or construction (Wallace and Hobbs, 2006). It can be computed by calculating the saturation mixing ratio

$$r_s = \epsilon_r \frac{e_s(T)}{P}, \tag{5.5}$$

at the surface. Where e_s the saturated vapour pressure and ϵ_r is the molecular weight ratio of water to dry air (Wallace and Hobbs, 2006). Next a line of constant r_s is computed with height on to θ co-ordinates from the surface value of r_s. The LCL is the height (in meters) where the θ co-ordinate of constant r_s is the same as the θ at the surface. At this point, T can be inferred from P and θ and a saturated adiabat, or line of constant θ_e is calculated. The hypothetical profile T_v' affectively follows this line. The Level of Free Convection (LFC) is the height at which $T_v' > T_v$. The EL is defined as the point when T_v' is significantly less than T_v. This is stressed due to the fact in some cases there can be points where $T_v' < T_v$ momentarily due to the uncertainty in the radiosonde's temperature sensors. The virtual temperature is given by

$$T_v = \frac{T}{1 - \frac{e}{P}\left(1 - \epsilon_r\right)}. \tag{5.6}$$

where e is the vapour pressure. To aid better explanation of the CAPE calculation, a tephigram is shown in figure 5.24, which shows the LCL, LFC and EL. CAPE is the region bounded by the red (Temperature) and green (saturated adiabat) lines constrained by the points EL and LFC.

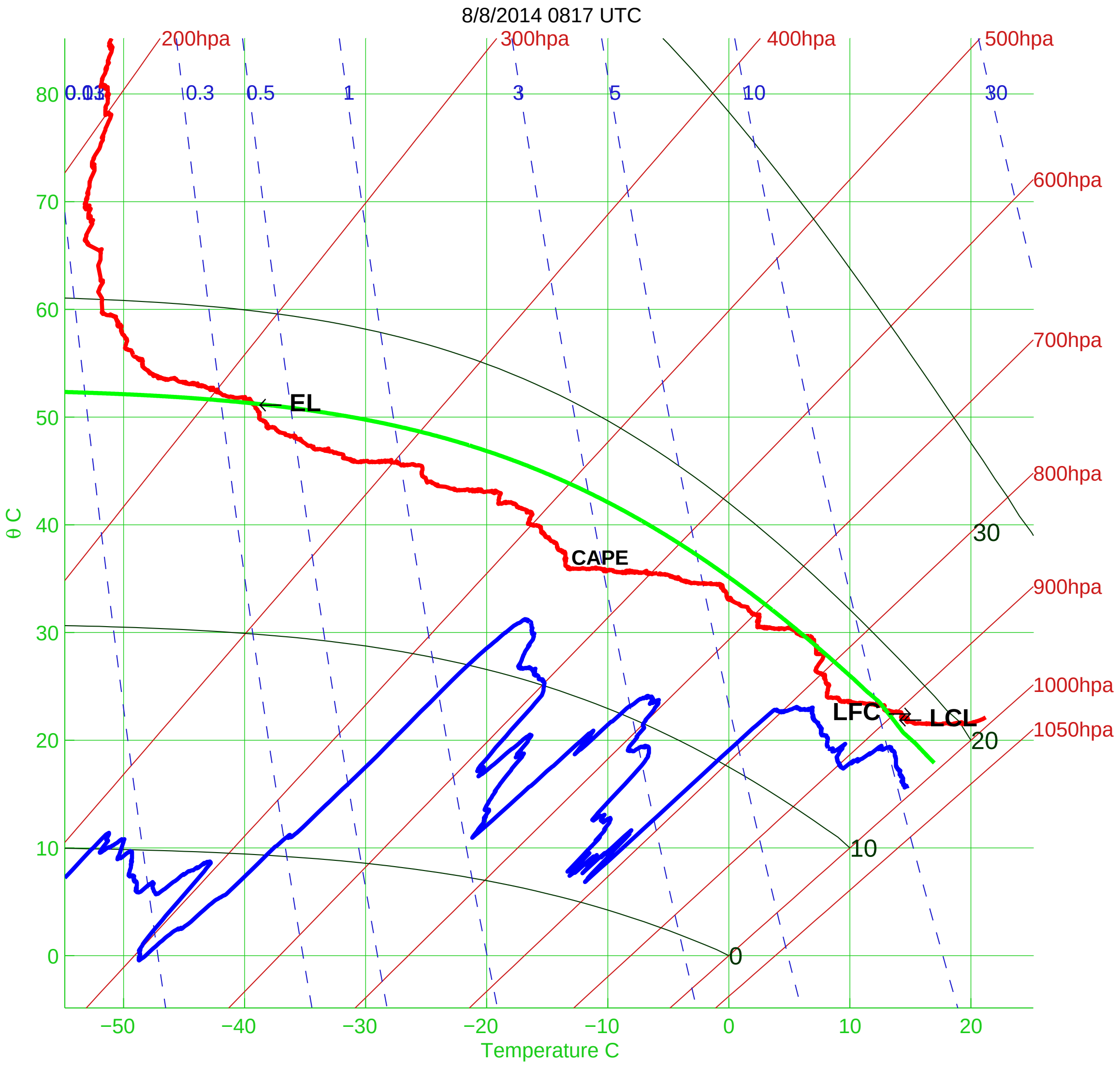

Figure 5.24 A tephigram showing dry and dewpoint profiles for at 0817 UTC on 8th August 2014. The LCL, LFC and EL have been marked, the region between the LFC and EL is used to calculate CAPE. Although the CAPE calculation is performed using T_v and T_v' which are slightly adjusted versions of T_{dry} (red) and the saturated adiabat (thick green) respectively, CAPE can be approximated as the region between them.

5.4.1 Clear air convection case studies

On the 8th August 2014, two accelerometer ascents were made, from the ARM base in Hyytiala Finland. The first was launched at 0817 UTC and is shown in figure 5.25, CAPE was calculated to be 585 J kg^{-1}, which implies moderate convection (Wallace and

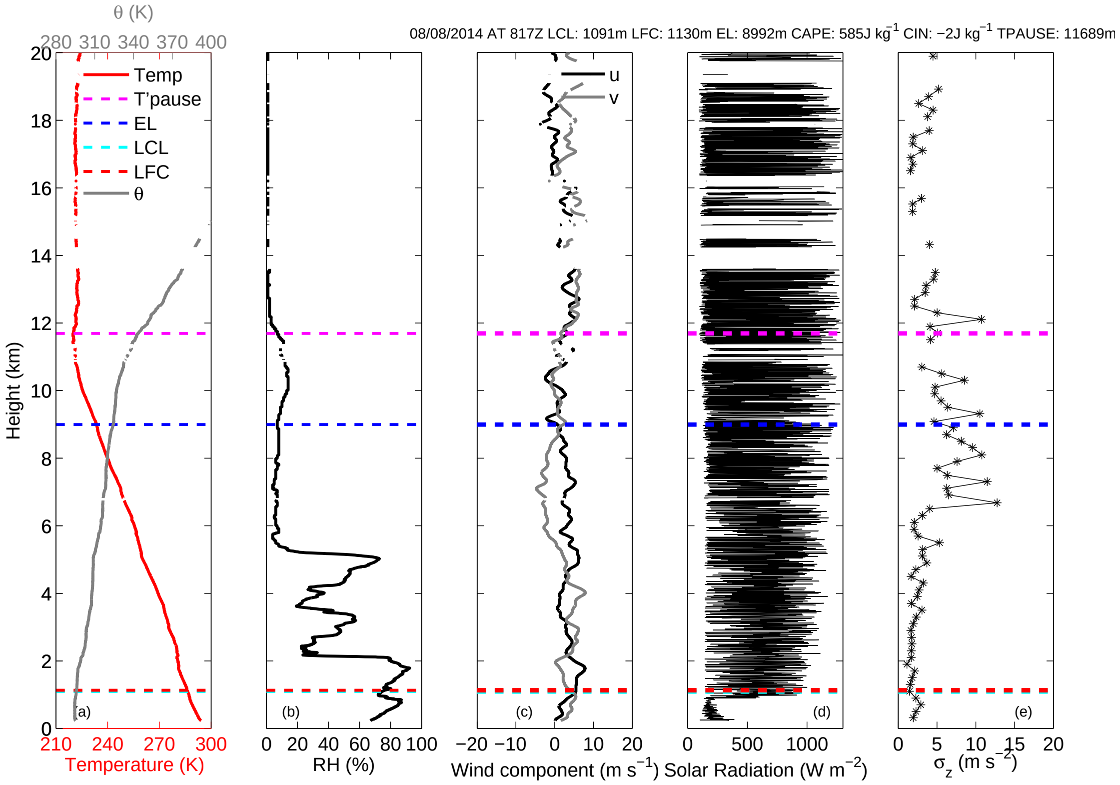

Figure 5.25 Vertical profiles of a) temperature and potential temperature θ (K) in red and grey respectively , b) RH (%) c) u and v wind components in black and grey (m s^{-1}), d) Solar radiation from photodiode (W m^{-2}) and (e) σ_z (m s^{-2}) over 200m for an ascent from Hyytiala ARM base at 0817UTC on 8th August 2014. Threspectivelye tropopause, EL, LFC and LCL heights are given by the coloured lines in the legend of panel (a).

Hobbs, 2006). The LFC and EL have been marked in red and blue respectively in figure 5.25. Strong turbulence is encountered just below the EL in panel (e), which could be caused by rising air displacing air at the EL. There is more clear air turbulence above the EL and this may be caused by air being forced through the EL and encountering another capping layer at the tropopause. Convection appears to be the dominant turbulence generation mechanism here, as wind shear appears minimal, as seen in panel (c).

A second ascent was made 3 hours later at 1126 UTC, shown in figure 5.26. The CAPE had diminished to 33 J kg^{-1}, but there is still significant turbulence in the same region. The turbulence is less intense and extensive in a vertical sense, likely due to the the much depleted CAPE. In both ascents, no appreciable cloud is present and wind shear is minimal, meaning turbulence generated here is most likely due to convection. In the second ascent, there is little CAPE and the turbulence observed may be from waves generated from the earlier convection.

A High Spectral Resolution Lidar (HSRL) was deployed at the site, which can observe the optical properties of aerosols and molecules in the atmosphere. The backscatter com-

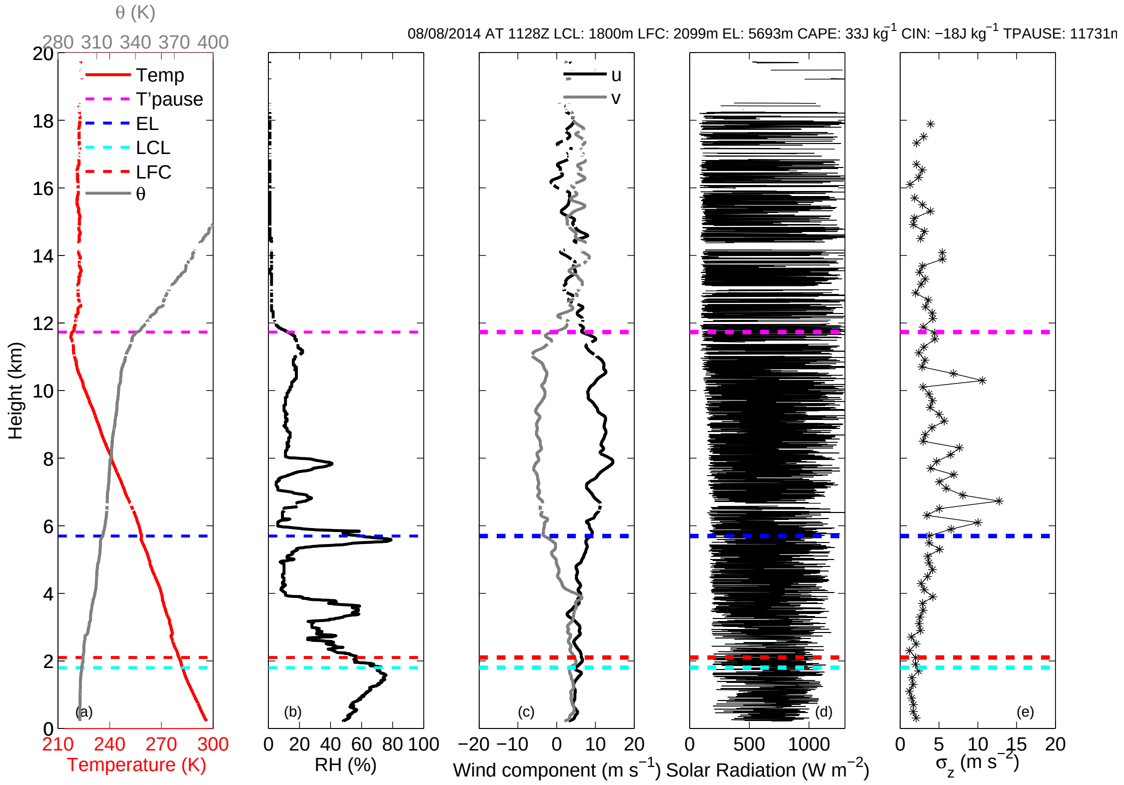

Figure 5.26 Vertical profiles of a) temperature and potential temperature θ (K) in red and grey respectively , b) RH (%) c) u and v wind components in black and grey respectively (m s^{-1}), d) Solar radiation from photodiode (W m^{-2}) and (e) σ_z (m s^{-2}) over 200 m for an ascent from Hyytiala ARM base at 1126UTC on 8th August 2014. The tropopause, EL, LFC and LCL heights are given by the coloured lines in the legend of panel (a).

ponent can be used to observe layers within the atmosphere, with aerosols and molecules acting as tracers. Figure 5.27 shows the backscatter from the HSRL for the morning of the 8th August. During the first ascent, there are wavelike properties above the environmental layer at 10 km, most likely small gravity waves being caused due to the convection below. In the second ascent, the waves appear to have broken down and the turbulent mixing is presented by a single layer, which is reflected in the turbulence sonde observations. This is an interesting case study, as it shows how convection can cause clear-air turbulence and also how turbulence is still present even after CAPE has dropped.

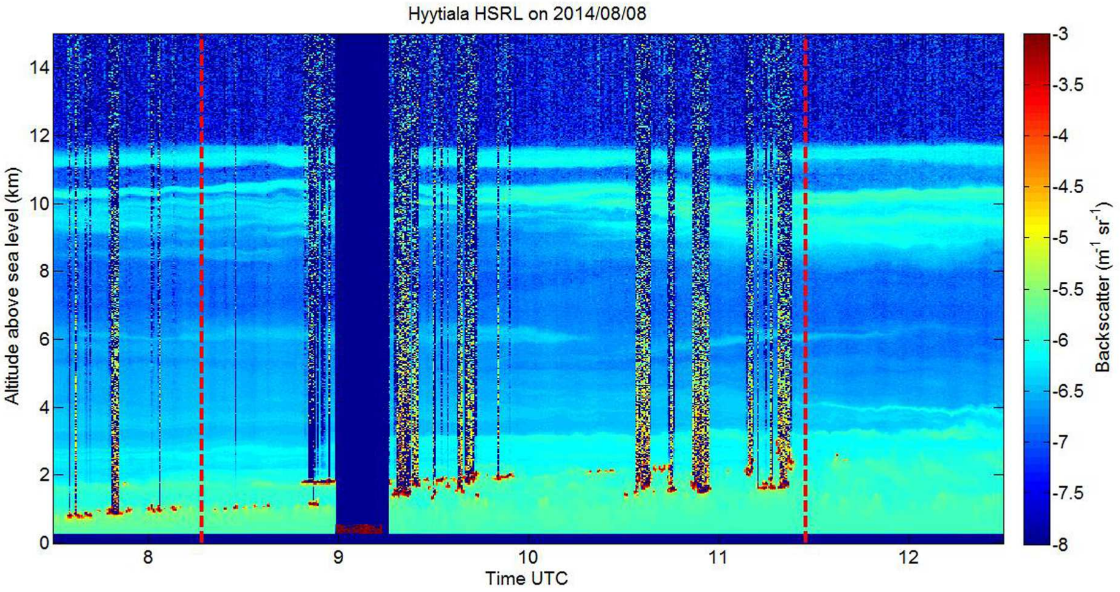

Figure 5.27 Shows the backscatter coefficient profile from the High Resolution Spectral Lidar between 0730 and 1230 UTC on 8th August 2014, at Hyytiala, Finland. Red dashed lines show the time of launch of the radiosondes used in figure 5.25 and 5.26.

5.4.2 In-cloud convection case study

Figure 5.28 shows an ascent into the leading edge of an approaching thunderstorm on the 14th August 2014 at Hyytiala. During the launch, the sound of thunder was audible however no precipitation was present at the time of launch, light precipitation followed after. The radiosonde was visually observed entering the cloud, the CAPE was calculated to be 450 J kg^{-1}. From panel (b) it can be seen that the relative humidity indicates cloud to the height of the tropopause. Panel (d) shows the downward pointing solar radiation sensor has increased variability, as the radiosonde exits the cloud above the environmental layer. σ_z shows a spike of turbulence just before the environmental layer. Most of the turbulence here is concentrated in the upper reaches of the cloud. This is likely due to air rising through the cloud being forced to stop causing turbulence above the EL and cloud top turbulence. There may be a contribution to turbulence from the evaporation from the cloud top.

In summary, when CAPE is large enough to generate a convective up-draft any turbulence related to this can be found within close proximity of the EL, where air reaches a natural barrier causing the air to become unstable and cause turbulence. Furthermore, the up-draft may be generating gravity waves, which ultimately break down and cause

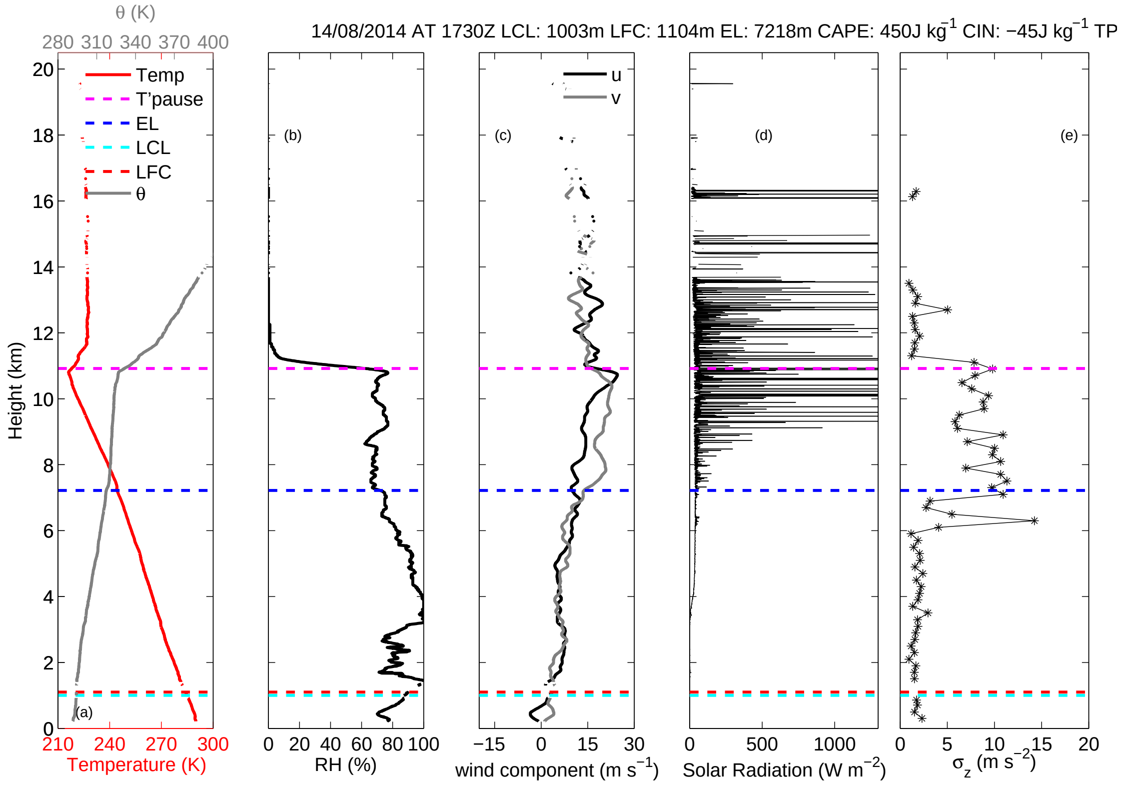

Figure 5.28 Vertical profiles of a) temperature and potential temperature θ (K) in red and grey respectively , b) RH (%) c) u and v wind components in black and grey respectively (m s^{-1}), d) Solar radiation from downward pointing photodiode (W m^{-2}) and (e) σ_z (m s^{-2}) for an ascent from Hyytiala ARM base at 1730UTC on 14th August 2014

further turbulence. Evidence of such waves was seen in figure 5.27, where waves in layers of aerosol above the EL were seen. The next step to embark on is a wider analysis of all ascents where convection was present, to see if a trend between CAPE and turbulence can be sought.

5.4.3 A subset analysis of convective ascents

In the previous section, case studies of individual convective turbulence were shown, here an examination of all convective ascents is undertaken as a whole. Given that in general, larger σ_z was found near the EL, an analysis which looks at the distributions of σ_z between the LFC and EL as a function of CAPE is needed. All ascents where the height difference between the LFC and the EL were $>$ 200m were selected. σ_z values between the LFC and EL were selected, and then given a normalised height co-ordinate to allow the cross comparison of many convective ascents by CAPE.

Figure 5.29 shows the vertical distribution of σ_z with height and each ascent is further classified by its CAPE along the x-axis. From this, it is possible to see that CAPE greater

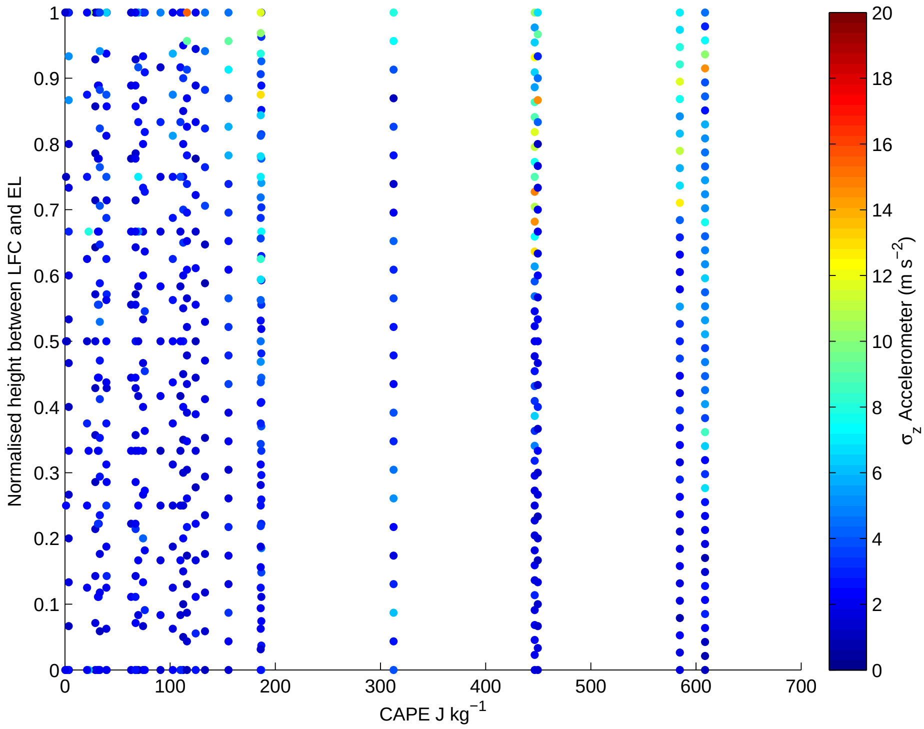

Figure 5.29 A plot showing the vertical distribution of σ_z for all ascents by the CAPE calculated for each ascent.

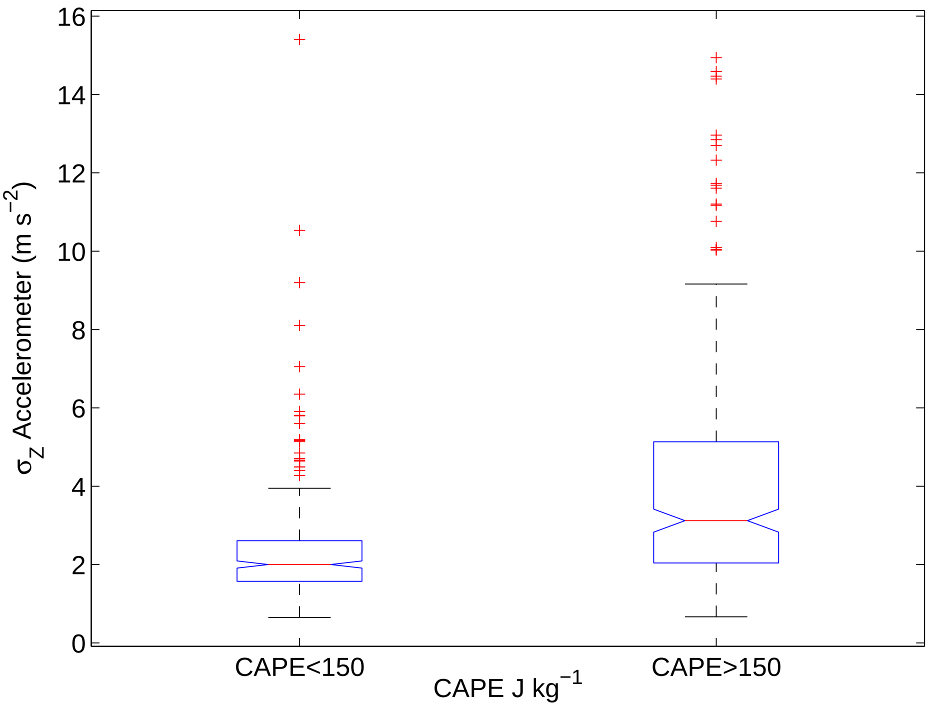

Figure 5.30 Box plots showing the distribution of σ_z (m s^{-2}) for ascents where CAPE< 150 J kg^{-1} and CAPE> 150 J kg^{-1}. For a full description of the box plot see figure caption 5.6.

than 150 J kg^{-1} is likely to cause turbulence; and of those large CAPE cases, it appears the more intense turbulence is observed in the top of the CAPE region. Figure 5.30 shows that ascents with larger values of CAPE $>$ 150 J kg^{-1} have significantly more intense turbulence than ascents with CAPE $<$ 150 J kg^{-1}.

To verify if the observation made in figure 5.29, that more turbulence is observed near the environmental layer, σ_z that was in regions of CAPE >150 J Kg^{-1} was retained for further analysis. It was then further split into two further subsets: one below and one above the normalised height of 0.5. Box plots of the two subsets are shown in figure 5.31. Turbulence is found to be more intense in the upper region of CAPE. This is likely due to the rising air being forced to stop at the EL, destabilising the air causing turbulence.

5.4.4 Conclusions

It can be seen that more intense turbulence is experienced in the upper convective regions, which is likely due to the rising air stopping at the equilibrium layer. Lane et al. (2003) undertook the modelling of a deep convective cloud to see where turbulence is most likely to form. It was found that turbulence was most likely 1 km above the cloud, due to stable air being displaced by rising air, which is in agreement with the case

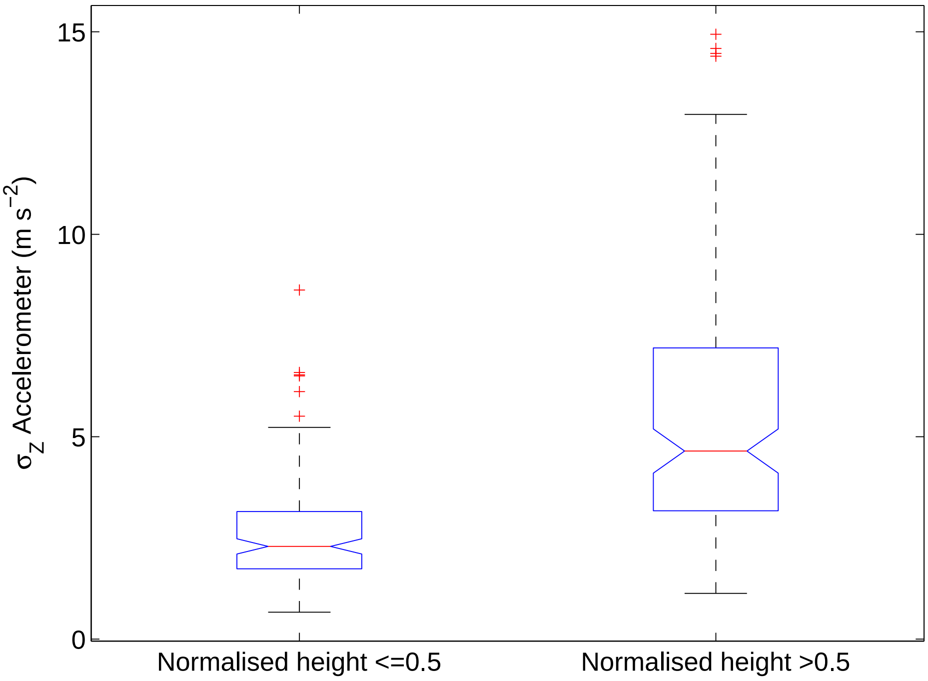

Figure 5.31 Box plots showing the distribution of σ_z (m s^{-2}) for ascents where CAPE was greater than 150 J kg^{-1} for both the lower and upper halves of the normalised convective regions. For a full description of the box plot see figure caption 5.6.

studies. Although the convective cases shown here are smaller in intensity, there is strong agreement between the literature and the results. More importantly, turbulence forecasts only use CAPE as a turbulence diagnostic and it could be improved by calculating positive CAPE regions within the model and selecting the upper extent, as a region of turbulence.

5.5 In-cloud and near-cloud turbulence

In chapter 4, two ascents through clouds were made in comparisons with doppler cloud radars. In those sections, the nuances of the different measurement techniques were discussed. In this section, there will be a focus on the causes of the observed in-cloud turbulence. There are many different types of cloud. One only needs to observe the sky and read Pretor-Pinney and Sanderson (2006) to be aware of this. Despite the many different variations of cloud, they are loosely grouped into three main categories from a turbulence perspective. The first are layer clouds, such as stratus, alto-stratus and high level cirrus clouds. These clouds often have well defined cloud edges and usually lack in-cloud processes that may cause appreciable turbulence. The second are frontal clouds, which produce a lot of precipitation and have many in-cloud processes (Houze Jr et al., 1976) as they bridge across adjacent air masses. The final cloud group is convective clouds, where turbulence occurs as warm moist air rises and condenses forming a cloud. Turbulence is formed by the displacement of stable air from the updraft. In the next section, a case study from each of these cloud groups will be undertaken to examine the turbulent structure. Then, in the final section a more quantitative analysis will be carried out to determine whether turbulence is more likely to occur in deeper clouds and whether turbulence is more likely at a cloud base or top.

5.5.1 In-cloud case studies

In the first case study, an examination of turbulence associated with a stratiform cloud encountered on the 28th October 2013, is undertaken. This is shown in figure 5.32, it can be seen that in panel (b), relative humidity is at its highest between 1 and 2 km, the photodiode in panel (d) shows that the variability in solar radiation increases across this layer. From these two instruments it can be stated that this cloud layer extends from 1-1.75 km. The solar radiation sensor has provided a useful method to interpret where cloud edges are; if just the RH profile was used, it would be difficult to infer the cloud edge. Above the cloud top, at 1750 m, there is a slight increase in σ_z, however it

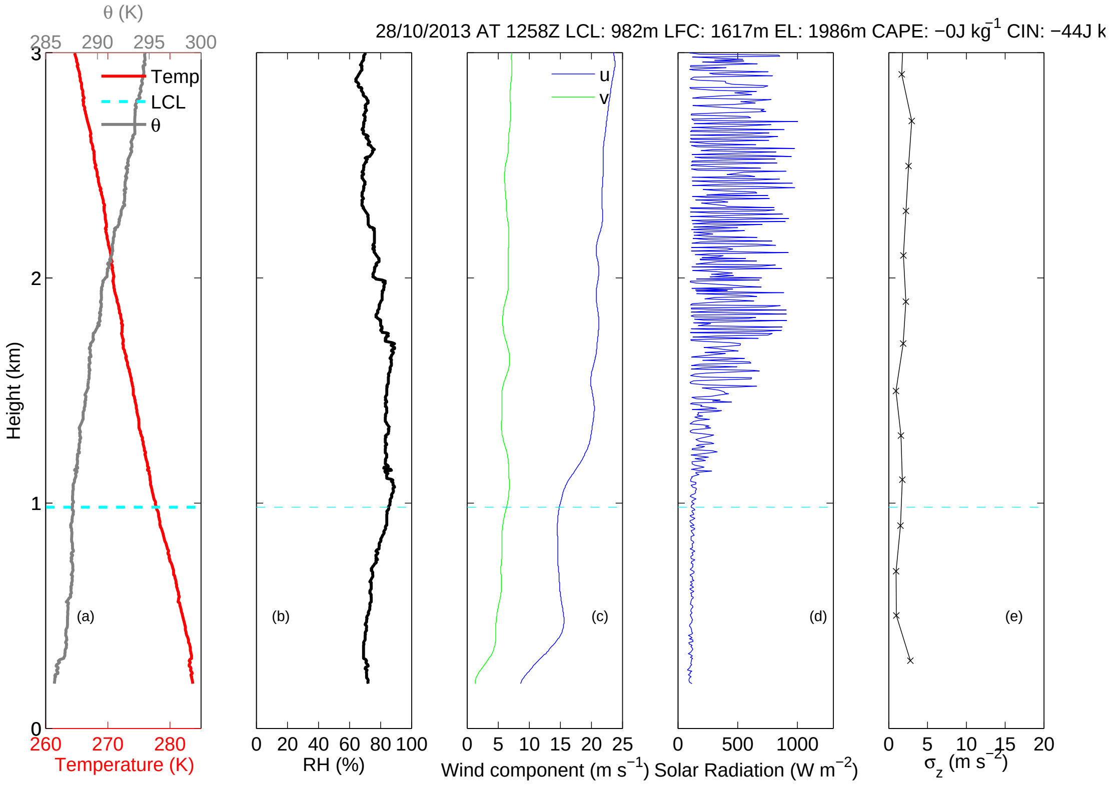

Figure 5.32 Vertical profiles of a) temperature and potential temperature θ (K) in red and grey respectively , b) RH (%) c) u and v wind components in black and grey respectively (m s^{-1}), d) Solar radiation from photodiode (W m^{-2}) and (e) σ_z (m s^{-2}) for an ascent from RUAO on 28th October 2013. The LCL is marked in light blue.

does not count as significant using the definitions set earlier in the chapter. The slight increase in turbulence at the cloud top could be due to radiative cooling and evaporation at the cloud top (Shao et al., 1997), which drives mechanisms for turbulence in the cloud. There is no evidence of turbulence generation from changes in the wind profile in panel (c). For clouds such as this, there are not many appreciable processes within the cloud which could generate turbulence. Hence the only turbulence present is from evaporation and radiative cooling at the cloud top, which can generate turbulence lower within the cloud.

In section 4.2.1 a case study of an ice cloud was shown where turbulence was found at the cloud boundaries. This is likely due to evaporation and radiative cooling from either ice crystals at the top, or droplets falling and evaporating from the base. The σ_z observed during this case study was indicative of light turbulence. In the second case study in that section, an accelerometer ascent was launched through a frontal cloud where turbulence was encountered throughout the depth of the cloud. To see if this was reproducible another ascent was made into similar synoptic conditions on the 18th December 2015, this ascent is shown in figure 5.33.

Panel (b) of figure 5.33 shows that the occluded front extended from a few hundred meters above the ground to the tropopause at 12.5 km. Due to the time of launch at 1515 UTC, during northern hemispheric mid winter, sunset made the solar radiation sensor redundant for cloud top detection. Turbulence was observed from the second layer of high RH in panel (b) and increased in intensity up to the cloud top. The turbulence is most likely cloud related as no jet stream is present. To see if the front had appreciable wind shears and low thermal stability, θ_z, U_z and ascent speed from the radiosonde are plotted in figure 5.34

Houze Jr et al. (1976) made case studies of several frontal systems and described that processes such as embedded convection, both up and down drafts, riming and aggregation, and evaporation of hydrometeors were all present. These in-cloud turbulence processes are all related to turbulence. Convection has already been discussed as a source of turbulence in the previous section. Up and down drafts within the cloud also cause turbulence, as air is forced to rise and fall. Evaporation of hydrometeors is also another cause of turbulence due to the state change. Riming occurs when ice comes into contact with supercooled water and aggregation occurs as hydrometeors collide, both due to turbulent mixing.

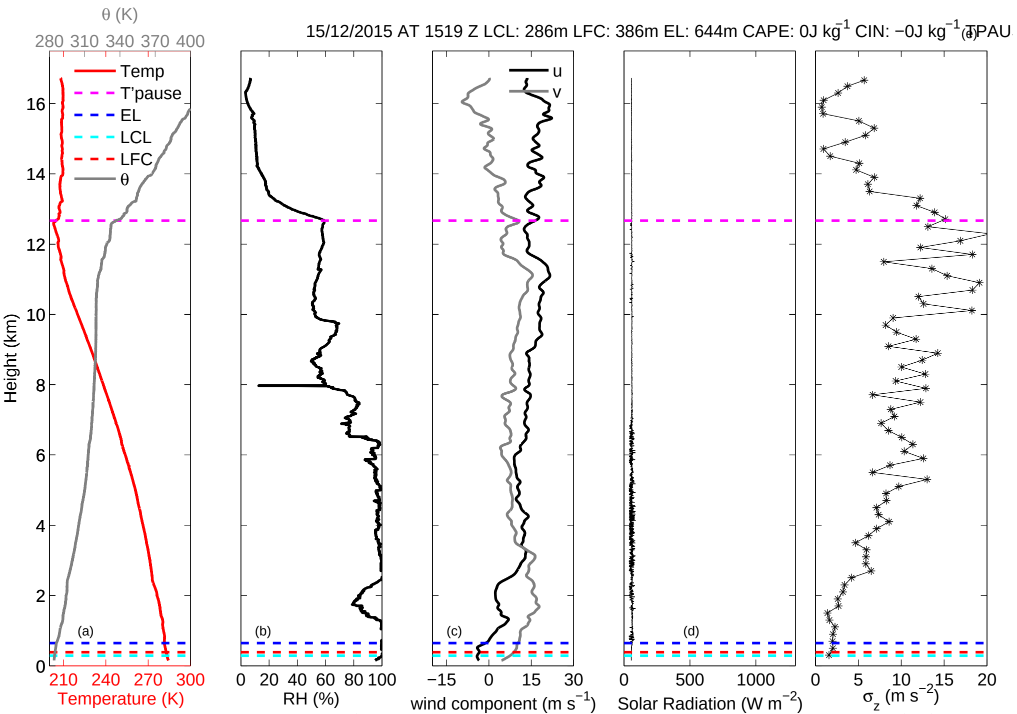

Figure 5.33 Vertical profiles of a) temperature and potential temperature θ (K) in red and grey respectively , b) RH (%) c) u and v wind components in black and grey respectively (m s^{-1}), d) solar radiation from photodiode (W m^{-2}) and (e) σ_z (m s^{-2}) for an ascent from RUAO on 15th December 2015.

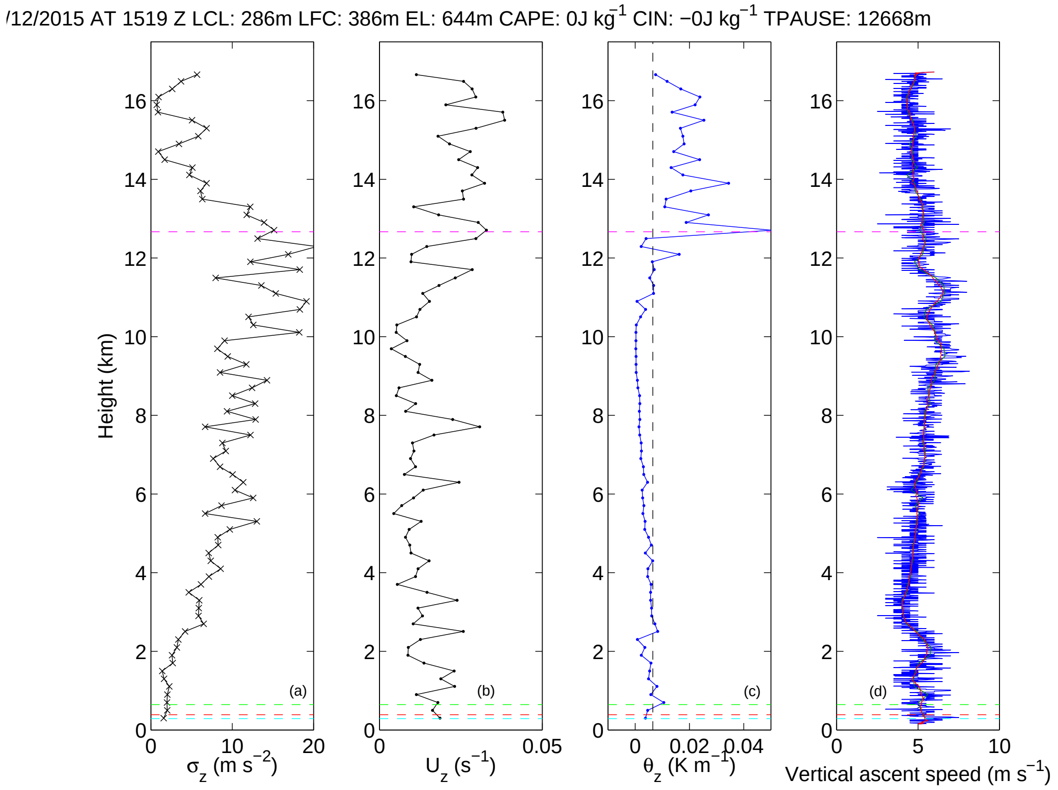

Figure 5.34 Vertical profiles of a) σ_z (m s^{-2}), b) vertical wind shear U_z (s^{-1}), c) potential temperature gradient θ_z (K m^{-1}) and d) the vertical ascent velocity (m s^{-1}) for an ascent at 1519 UTC on 15th December 2015.

Bond and Shapiro (1991) suggested that there could be low thermal stability along the front and high wind shears. In figure 5.34 the peak wind shears within the cloud are of magnitude 0.01 to 0.02 s^{-1}, indicating regions of moderate shear which has been discussed in Bond and Shapiro (1991). In the top of the cloud, between 6-10 km, there are values of θ_z of 0.002 K m^{-1} which is less than the standard lapse rate of 0.0065 K m^{-1}. The ascent velocity shown in panel (d) shows an increase in ascent velocity throughout the cloud to 9km, which is consistent with conceptual models of fronts in Houze Jr et al. (1976). Above this height, there is a small wave form in the ascent velocity which implies that gravity waves may be being produced within the front. Moore (1985) carried out some numerical simulations of thermal stability within a cold front and simulated how some gravity waves maybe produced in a front. From the radiosonde measurements, the front includes all the processes which are likely to cause turbulence, hence it is understandable why turbulence is experienced over the depth of the front.

The final case study will look at turbulence in a convective squall line. Figure 5.35 shows the accelerometer ascent into the leading edges of a thunderstorm, discussed in section 5.4.1. From the relative humidity and photodiode profiles, it can be seen that the

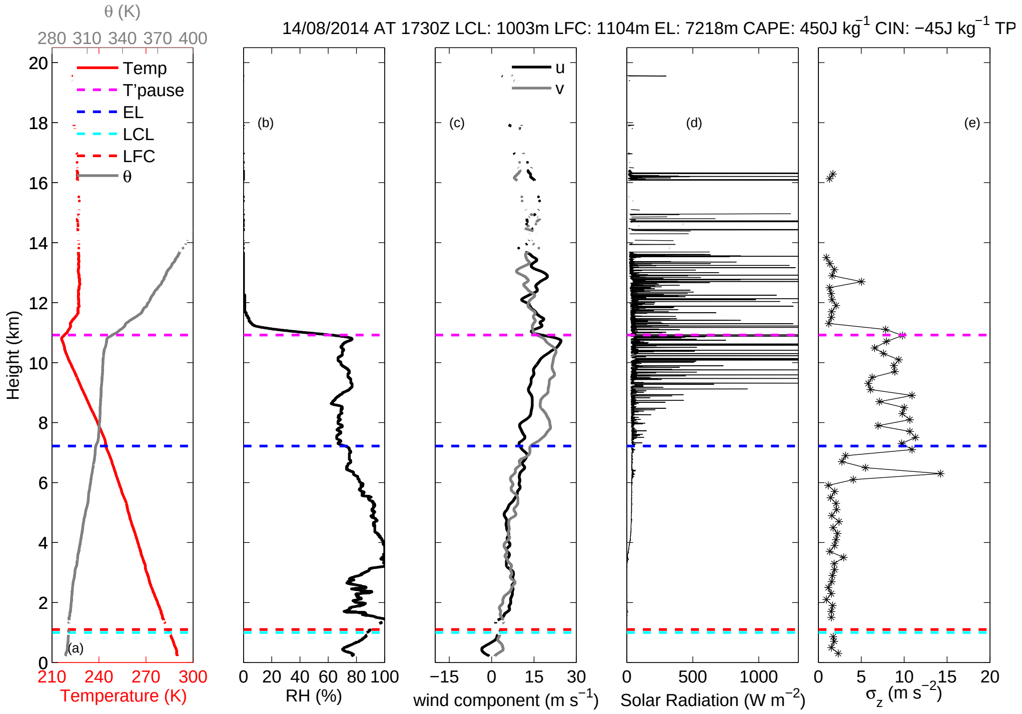

Figure 5.35 Vertical profiles of a) temperature and potential temperature θ (K) in red and grey , b) RH (%) c) u and v wind components in black and grey respectively (m s^{-1}), d) Solar radiation from photodiode (W m^{-2}) and (e) σ_z (m s^{-2}) over 200 m for an ascent from Hyytiala on 14th August 2014.

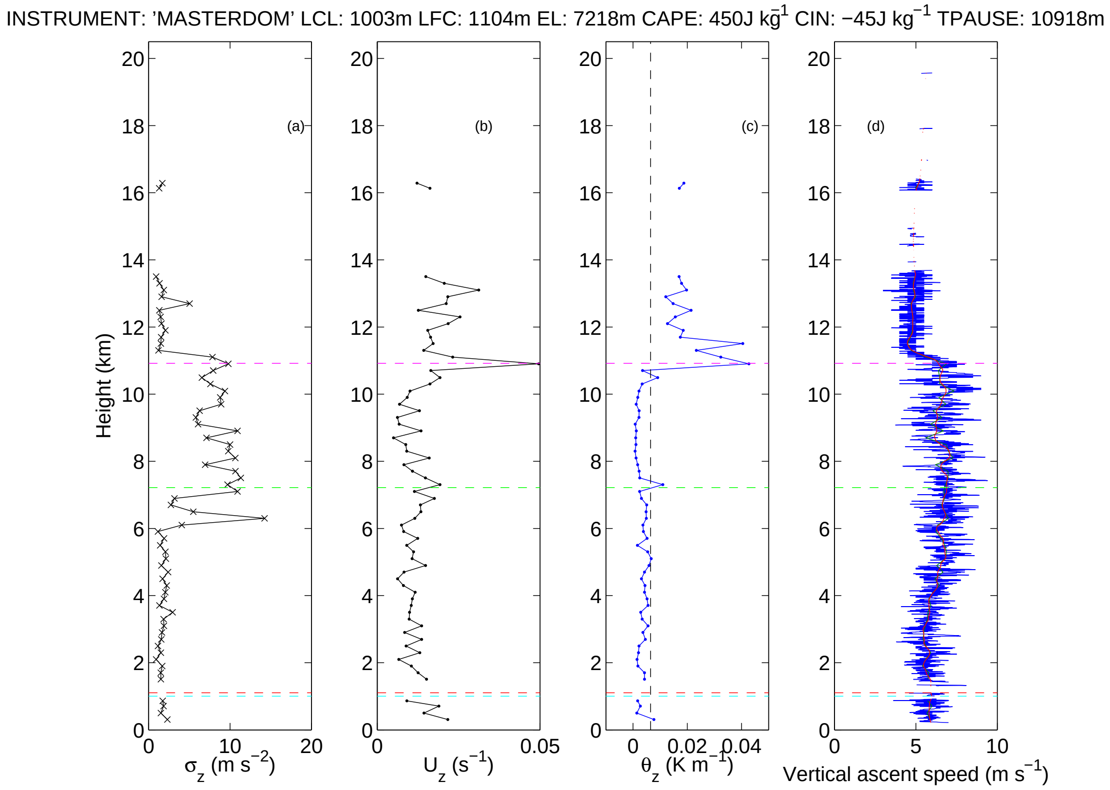

Figure 5.36 Vertical profiles of a) σ_z (m s^{-2}), b) vertical wind shear (s^{-1}), c) θ_z (K m^{-1}) and d) the vertical ascent velocity (m s^{-1}) for an ascent at 1730 UTC 14th August 2014 from Hyytiala.

radiosonde enters the cloud at 1.5 km and passes through the cloud top at 9 km. There is little turbulence within the majority of cloud, however, towards the cloud top strong convection is encountered by the radiosonde, typical of the earlier findings in the section on convection and in Meischner et al. (2001). Only light precipitation was experienced after the launch, which may be due to a lack of turbulence within the body of the cloud. As carried out for the frontal case study θ_z, U_z, and ascent speed have also been plotted. This is shown in figure 5.36 in panel (c), which shows θ_z is close to zero indicating low stability in the upper region of the cloud. For reference the normal atmospheric lapse rate is indicated by the dashed vertical line. This could be due to the air becoming unstable due to the rising air which is observed in panel (d) from the ascent speed. Although there is no jet present in figure 5.35, there is a 20 m s^{-1} shift in wind with height which may be causing wind shear in panel (b), contributing to turbulence. In conclusion, deeper clouds contain more processes, which are more likely to produce turbulence. With these deep clouds the above cloud turbulence can extend for a few km, often to the tropopause.

5.5.2 A subset analysis of ascents through cloud

It can be seen that both frontal clouds and convective clouds are more likely to produce turbulence. This is because of the more complex turbulence-producing meteorological processes present within the cloud. In this section, all clouds in the dataset will be analysed to see quantitatively if this is the case. This was undertaken by using the photodiode and standard meteorological instrumentation to estimate regions of cloud. To achieve this, cloud regions within the ascent stage of the flight were defined by finding the cloud top, as the height where the standard deviation from the solar radiation sensor was > 75 W m^{-2}. This value was chosen after examining the 95th percentile value of the solar radiation over 1 minute (Harrison et al., 2016a), as it passed through a cloud edge. The standard deviation at which the 95th percentile of the solar radiation sensor reached 37.5% of the final above cloud value was used. When multiple cloud tops were analysed it was found to be on average 75 W m^{-2}. A pseudo Relative Humidity (RH_s) profile, which used the RH with respect to water at temperatures >-20 C^o, and with respect to ice at lower temperatures was used. This is due to RH at such temperatures not being appropriate for cloud top detection. Regions of RH_s >85% were defined as cloud below the defined cloud top in a similar method described in Zhang et al. (2010). For night ascents, just the pseudo RH profile was used. Having defined in-cloud regions, near-cloud regions were defined as a region at the cloud base and top which extended 20% of the cloud depth away from each cloud boundaries. 20% was chosen after analysis of figure 5.34 which showed turbulence extending 2 km out of 9-10 km cloud. Using these definitions for cloud regions, each ascent can be analysed for regions of cloud and respective cloud edges. In total 44 in-cloud regions were identified. A 500 m split was used to divide the 44 cloud regions as this was the median depth of the cloud regions.

Figure 5.37 shows box plots of σ_z for clouds less than 500 m and greater than 500 m.

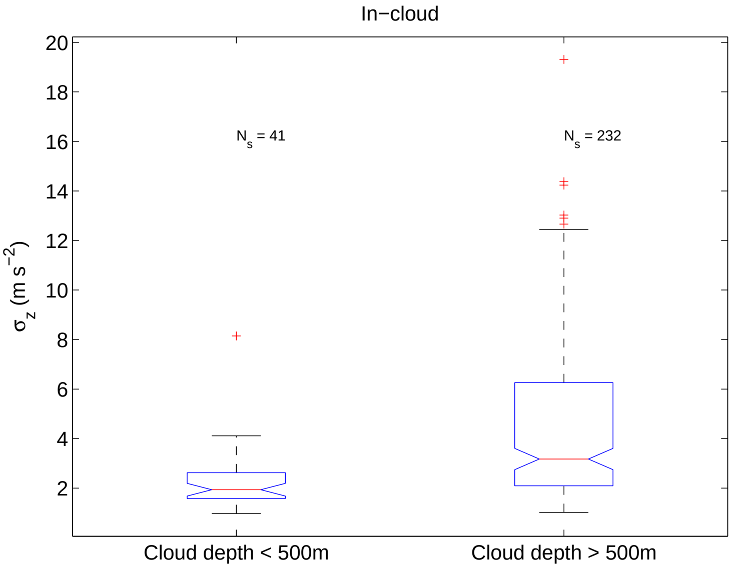

Figure 5.37 A box plot showing all in-cloud σ_z (m s^{-2}) binned by cloud depth. For a full description of the box plot see figure caption 5.6.

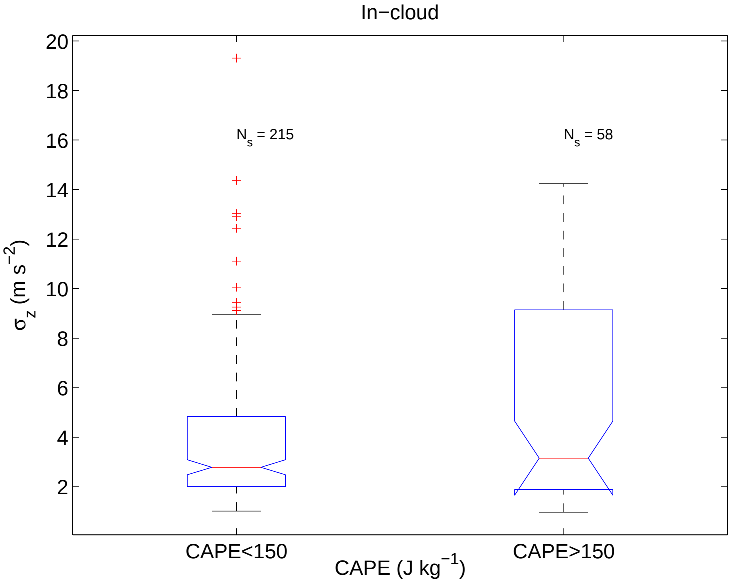

Figure 5.38 A box plot showing all in-cloud σ_z (m s^{-2}) binned by CAPE. For a full description of the box plot see figure caption 5.6.

The distribution of σ_z for the deeper cloud contains more values, as there is more data points associated with each cloud. It does however show that deeper clouds are associated with more intense turbulence. In the previous section, CAPE had been shown to be associated with turbulence in clear air and in-cloud, however this does not imply that convection is always the cause of turbulence within all clouds. Figure 5.38 shows box plots of distributions of convective and non convective clouds. Whilst a large inter quartile range of σ_z is encountered for clouds with convection present, it is not significantly different from non-convective clouds, due to the large confidence intervals. Next the intensity of σ_z at both upper and lower cloud boundaries will be examined.

Figure 5.39 shows that for deeper clouds, there is more likely turbulence about the cloud base, although it is not significantly different from smaller clouds. This could be due to larger clouds having evaporating precipitation, or due to the effects of down-drafts and up-drafts. Turbulence in the upper cloud boundaries shown in figure 5.40 is significantly greater than turbulence in cloud with depths of <500 m, this is likely due to the in-cloud processes, such as convection or up-drafts along a front displacing stable air above.

5.5.3 Conclusions

In this anaylsis of in and near cloud turbulence detected by the accelerometer sondes, it has been found that in-cloud turbulence is more intense within deeper clouds as deeper clouds contain more extensive in-cloud processes. This is summarised in table 5.6, which

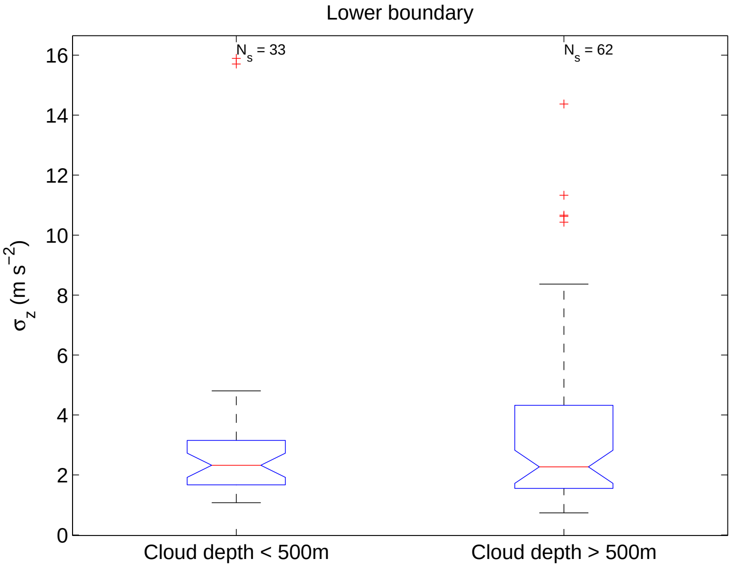

Figure 5.39 A box plot showing lower cloud boundary σ_z (m s^{-2}) binned by cloud depth. For a full description of the box plot see figure caption 5.6.

]

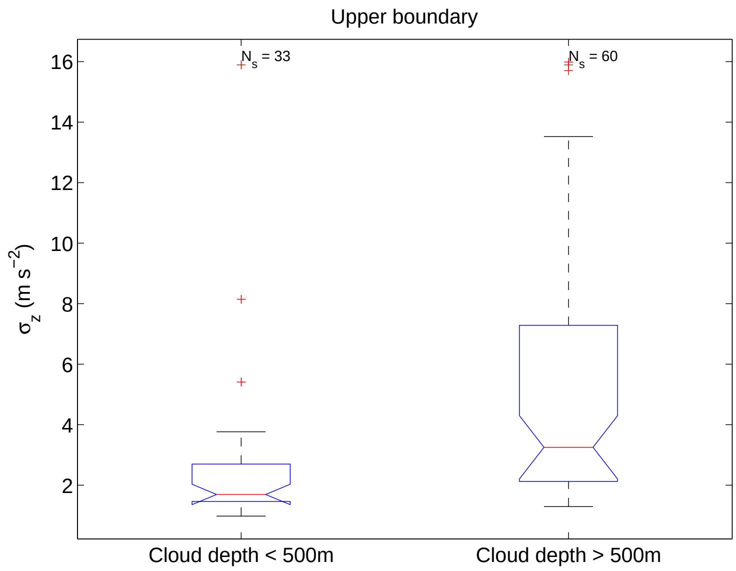

Figure 5.40 A box plot showing lower cloud boundary σ_z (m s^{-2}) binned by cloud depth. For a full description of the box plot see figure caption 5.6.

	In-cloud	Lower boundary	Upper boundary
Cloud depth $<$ 500m	1.5-3 m s^{-2}	1.5-3.5 m s^{-2}	1.5-3 m s^{-2}
Cloud depth $>$ 500m	2.5-7 m s^{-2}	1.5-4.5 m s^{-2}	2.5-7.5 m s^{-2}

Table 5.6 A table showing the first and third quartiles for in-cloud, lower boundary and upper boundary turbulence for shallow (<500 m) clouds and deep (>500 m) clouds.

shows that deeper clouds have more intense turbulence associated within them and near them. Frontal cloud turbulence is more likely to be observed across the depth of the cloud, and conceptual models shown in Houze Jr et al. (1976) and Bond and Shapiro (1991) support how conditions in fronts could cause turbulence. In convective clouds, turbulence is more likely to be observed in the cloud head where warm air in the up-draft is caused to stop at the EL, which causes turbulence in and above the cloud. However other conditions caused by frontal dynamics are not present, which means turbulence may not be experienced across the depth of the cloud. In the analysis of the near cloud turbulence, the near cloud turbulence was found to be more intense above deeper clouds.

5.6 Gravity wave turbulence

As discussed in chapter 1 breaking gravity waves can cause turbulence to form. So far in this chapter some limited evidence to suggest meteorological phenomena such as jet streams and fronts produce gravity waves has been shown. Gravity waves can be detected using the standard meteorological measurements from a radiosonde, and there has been a volume of work which has used temperature and wind component profiles to obtain the properties of inertia gravity waves in the stratosphere (Vincent and Alexander (2000) , Wang et al. (2005)). As shown in previous sections, and in figure 5.41, vertical velocities can be inferred from the radiosondes ascent speed and archived in addition to horizontal velocities. Vertical velocity variations in radiosonde profiles have previously been attributed to gravity waves (Shutts et al., 1988) and inclusions of ascent speeds as part of a gravity wave analysis in the lower stratosphere has been undertaken in Marlton et al. (2016).

Figure 5.41 shows an ascent from the the 3rd March 2015 from the MST radar site. Panel (a) shows the ascent velocity having a waveform property from the ground to the tropopause at 9 km. Given the geographic location it is likely that a mountain wave had developed over the Welsh mountains. In panel (d), at the tropopause there are increased values of σ_z which indicates the mountain wave is breaking against the tropopause causing turbulence with σ_z of up to 10 m s^{-2} observed. At 16-20 km another wave form is present in the ascent velocity and in the horizontal wind profiles, which are typical of

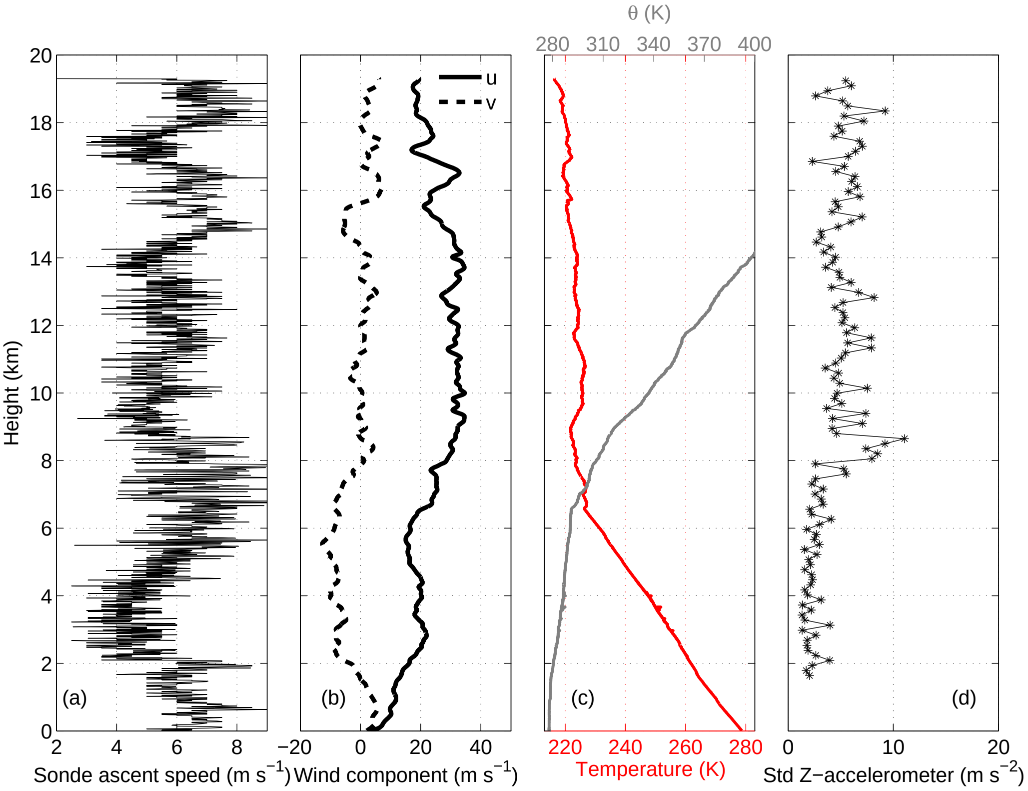

Figure 5.41 Vertical profiles of a) vertical ascent speed (m s^{-1}), b) u and v wind components (m s^{-1}) (c) temperature (K) (red) and Potential temperature (K) (grey), and d) σ_z (m s^{-2}) taken over 200 m from a Vaisala RS92 radiosonde ascent made from the Mesospheric, Stratospheric and Tropospheric (MST) Radar site at Aberystwyth, Wales, UK, on 3 March 2015. Adapted from Marlton et al. (2016).

inertia gravity waves. At this height, there is increase in σ_z indicative of wave breaking turbulence. Using the u and v wind components and T, a hodographic analysis can provide information about the frequency and propagation direction of the gravity waves (Wang et al., 2005). The u, v, and w components were used in a moving parcel analysis in Marlton et al. (2016). These methods are affected by non monochromatic gravity waves, as it is hard to resolve the components of each wave. This was addressed by Zink and Vincent (2001), who used a wavelet analysis to decompose each wave property in the lower stratosphere. One problem with performing such an analysis in the troposphere is the contamination of the wind profiles and temperature profile from features such as deep clouds, convection and jet streams. Hence, many of these analysis using this method (Zink and Vincent, 2001) (Murphy et al., 2014) have restricted their analysis to the lower stratosphere. Before undertaking a spectral analysis of ascent velocity data from all 51 ascents in the database, each ascent was checked by eye for the presence of a waveform. Nearly all waveforms that were not affected by other meteorological conditions were observed in the stratosphere, with the exception of the case study presented.

A Lomb periodogram, as described in section 3.3.4 was applied to the ascent data shown in figure 5.41 with a single sampling window spanning the height of the tropopause from the ground. The results of this are shown in figure 5.42, the peak of the periodogram approximates the vertical wave length to be approximately 6.2 km. This is characteristic of a mountain wave which often have long vertical wavelengths and propagate to the

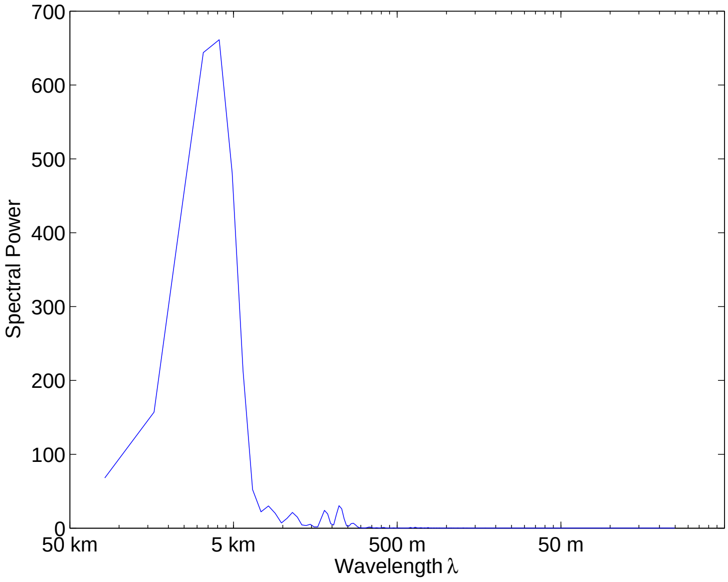

Figure 5.42 A lomb periodogram of the ascent velocity data between the surface and tropopause from a radiosonde ascent made on 3rd March 2015 shown in 5.41.

height of the tropopause (Holton, 2004).

5.7 Overview and Conclusions

In this section, the findings of the chapter will be at first summarised under the section headings. In the final part of this section, the turbulence intensities from the different sources of turbulence will be compared.

Preliminary data analysis

A σ_z of 5 m s^{-2} was found to constitute a value of significant turbulence. A bulk analysis of the dataset found that there were slight indications that σ_z may be more intense at higher U_z. Smaller distributions of σ_z were found when N^2 was signifying more stratification. The largest values σ_z were found at the lowest Ri number, although the confidence intervals for each distribution are such that no significant relationship can be inferred.

Jet stream turbulence

In the two IOPs examined, it was found that vertical wind shear and low thermal stability were associated with regions of turbulence. However, the presence of low thermal stability and wind shear did not always mean turbulence was observed. It was found that 51% of all significant turbulence within jet streams could be attributed to either high wind shears or low static stability. 63% of null turbulence occurred in the absence of low thermal stability and high wind shear. This means that not all turbulence generation is directly related to vertical wind shear and thermal stability. An investigation examined if a jet stream's intensity or direction yielded more turbulence, it did not find any tendencies in either quantity. In the second IOP, the structure of the atmosphere evolved due to a developing tropopause fold, this may explain the temporal evolution of turbulence. Following from this, it was shown that jet streams which had tropopause folds present contained more intense turbulence. The first IOP also presented a temporal evolution of turbulence, but no temporal evolution of the dynamical structure of the atmosphere was observed. This indicates that there are dynamical processes which cannot be observed directly by the radiosonde. An analysis using Numerical Weather prediction packages to investigate the evolution of dynamical processes, which may explain this evolution will be undertaken in the next chapter.

Convective turbulence

Turbulence was found to occur in the presence of convection inferred by CAPE. In conditions when CAPE $>$ 150 J kg^{-1}, turbulence was more likely to occur. Furthermore, turbulence was likely to occur in the upper half of positive regions where CAPE $>$ 150 J kg^{-1}. This is due to the rising air stopping at the equilibrium level

In-cloud and near-cloud turbulence

Case studies of three different cloud types were examined. In summary, stratiform clouds were found to have small amounts of turbulence about the cloud base and cloud top. Cloud top turbulence is caused due to the radiative cooling and evaporation along the cloud top. At the cloud base turbulence occurs due to the evaporation of hydrometeors. Frontal clouds were found to have turbulence spanning the depth of the cloud as opposed to convective clouds which have turbulence about the cloud top. Frontal clouds have more dynamical processes which span the depth of the cloud whereas the main source of turbulence within convective cloud is near the cloud top.

Using a cloud detection algorithm, 44 cloud regions were detected in the accelerometer sonde dataset. Clouds which were deeper than 500 m were found to be more turbulent than shallower clouds. This is because the deeper clouds have more in-cloud processes, which can cause turbulence. Although from the data collected, it was hard to infer whether convective clouds were more turbulent than frontal clouds.

Cloud boundaries were considered as the distance which is 20% of the cloud depth from the cloud edges. Deeper clouds were associated with more intense near cloud turbulence. Further to this, turbulence was more intense at the cloud top opposed to the cloud base.

Gravity wave turbulence

Some evidence for gravity waves was seen in both u and v components in a few ascents. These were emitted from jet streams and clouds. However, it is quite hard to isolate the waves characteristics due to contamination of the profiles from other meteorological phenomena. A gravity wave was found in the ascent velocity data which was successfully isolated. Given the geographical location of the launch and the vertical wave length, extracted using a spectral analysis, it is likely a mountain wave. Turbulence was observed in the wave breaking region near the tropopause.

Overview of different turbulence sources

Table 5.7 shows each turbulence category, along with the rubric used to categorise σ_z values and finally the percentage of the datasets significant σ_z in each category. It should be noted that as a categorisation rubric was not created for mountain wave turbulence, it has not been included in the table, however the range of σ_z observed as the mountain wave broke was found to be 4-10 m s^{-2} . Using the algorithms summarised in table 5.7, significant values of σ_z were assigned to one or more meteorological conditions. The table shows the % of each tropospheric $\sigma_z > 5$ m s^{-2} values assigned to each condition. 47% of significant σ_z in this dataset was found within jet stream regions, with 20% associated with clouds, 10% associated with convection and 7% with near-cloud turbulence. 23% of the values did not fit in the criteria. Some of this could be caused by gravity waves which were hard to identify. Furthermore some turbulence may still be observable even though the main turbulence mechanism has subsided. A good example of this is the second convective ascent shown in figure 5.26. Here, the CAPE has subsided yet there is still turbulence present, thus despite the turbulence being caused by convection it is not classified as convective turbulence. This demonstrates the difficulty in attempting to classify such a turbulence dataset.

Figure 5.43 shows the distributions of σ_z from the four different categories in table 5.7. Turbulence within the jet stream is significantly more intense than, in-cloud, near-cloud and convective turbulence. The next category with the most intense turbulence is in-cloud turbulence. Near-cloud and convective turbulence have similar turbulent intensities. In the next chapter, a numerical model that represents the atmosphere will be used to generate turbulence diagnostics described in chapter 2. Firstly, these diagnostics will be used to see if any can provide explanations of the temporal evolution of turbulence in the two jet stream IOPs. Finally, the described database of turbulence observations will be used to assess the skill of these turbulence diagnostics.

Meteorological phenomena	Condition	$\%\sigma_z > 5$ m s^{-2}
Jet	$U_{max} > 40$ m s^{-1} and $U > 25$ m s^{-1}	46.8
Convection	CAPE > 150 J kg^{-1}	9.7
Cloud	$RH > 85$ and $\sigma_{sw} < 75$ W m^{-2}	20.0
Near cloud	20 % of cloud depth at base and top of cloud	7.4

Table 5.7 A table summarising the meteorological condition and algorithm used to select that conditions as well as the percentage of significant turbulence from the data set of 802 significant turbulence values.

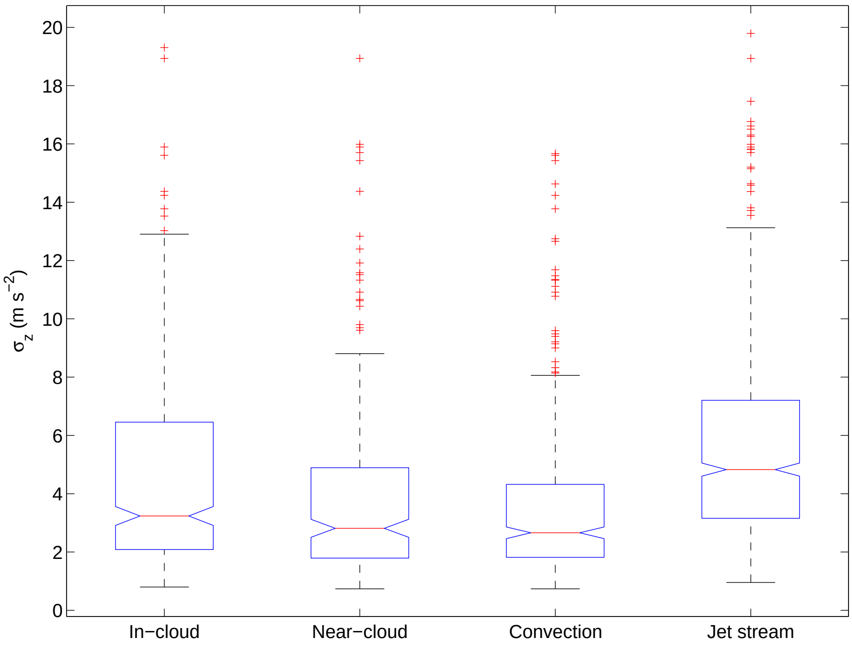

Figure 5.43 Box plot diagrams showing distributions of σ_z (m s^{-2}) for In-cloud, near-cloud, convective and jet stream turbulence. For a full description of the box plot see figure caption 5.6.

Chapter 6

Comparison of accelerometer observations of turbulence with diagnostics from a model

In this chapter the dataset of turbulence observations discussed in chapter 5 are compared with the turbulence diagnostics described in chapter 2. In chapter 1 it was discussed how aircraft rely on turbulent diagnostics so they can avoid turbulence. Here the skill of these diagnostics is assessed by comparing them against the accelerometer sonde observations. Furthermore the turbulent diagnostics can also be used to explain the temporal evolution of turbulence within the case studies in chapter 5. Before undertaking any comparisons, an appropriate atmospheric model, which provides a good representation of the large-scale atmospheric state, is selected for each accelerometer sonde ascent. Turbulence diagnostics discussed in chapter 2, are then calculated at the model time step corresponding to each accelerometer sonde ascent. Next turbulence diagnostics from chapter 2 are calculated for each selected time step. Firstly, the turbulence diagnostics will be used to unearth more information about the evolution of turbulence shown in the jet stream case studies shown in chapter 5. Secondly, the skill of the turbulence diagnostics will be examined by comparing them with the observations of turbulence from the accelerometer sonde dataset.

6.1 Selection of a model

To calculate turbulence diagnostics for the time of accelerometer sonde launch, an atmospheric model which represents the large-scale state of the atmosphere is needed. There are two options available for a model which represents the atmosphere, reanalysis data sets or operational weather forecasts. Reanalysis datasets are large datasets which assimilate atmospheric observations to approximate the state of the atmosphere at a given time. There are many reanalysis products available which are summarised in table 6.1. The 20th century analysis does not incorporate the time period over which the accelerometer sondes were launched, hence it is not considered further. The US NCAR analysis does include this period, but the horizontal and vertical resolution is rather coarse for calculating turbulence diagnostics for a comparison. This leaves both the ECMWF's ERA Interim reanalysis or the JMA's JRA-55 reanalysis. Both appear to have similar specifications, with the JRA-55 having a finer temporal and horizontal resolution, despite this the ERA-Interim reanalysis was chosen due to ease of access and technical support.

An alternative to reanalysis data is archived operational forecast data. An operational forecast is similar to reanalysis in that an analysis state of the atmosphere is created, but a forecast is then integrated forward from that analysis. The forecasts are archived at 1 hour intervals providing an increased temporal resolution over reanalysis packages. Being operational forecasts, they also have finer horizontal and vertical resolution as they utilise more powerful computing resources. Most current global forecasts have resolutions of $1/8^o$ horizontal resolution and 100 model levels. Here a global model is desirable as accelerometer sondes were launched from both the UK and Finland. Thus the ECMWF's operational global deterministic model was selected as a candidate model to calculate

Reanalysis package	Horizontal resolution	Model levels	Temporal resolution	Temporal coverage
20th Century analysis Compo et al. (2011)	2^o	28	6 hr	1871 - 2012
NCEP/NCAR Reanalysis 1 Kalnay et al. (1996)	2.5^o	17	6 hr	1948 - present
ERA-interim Dee et al. (2011)	0.7^o	60	6 hr	1979 - present
JRA-55 Kobayashi et al. (2015)	0.5^o	60	3 hr	1958 - present

Table 6.1 A table of current reanalysis data sets.

turbulence diagnostics. To evaluate which model best represented the atmosphere, the standard meteorological values of T,Z,u,v,q and RH from the radiosonde were compared at the appropriate grid points in both the ERA-interim, and the ECMWF deterministic global model. In the next section, the method to select the appropriate points in the model will be described.

6.1.1 Method to select grid points for model comparisons

Radiosondes provide vertical profiles of T, RH, P, u, v and Z. It is a common misconception that this represents the state of the atmosphere directly above the launch site. In many cases a radiosonde will travel ten times its vertical distant of travel horizontally. This is demonstrated in figure 6.1, which shows the trajectories of accelerometer sondes launched from the RUAO. The figure further demonstrates that during the course of the ascent the radiosonde may pass through several model grid squares. Thus a method which selects the appropriate grid points in the model along the radiosonde's trajectory, in both the horizontal and vertical sense, is needed. Here the nearest neighbour technique is affectively used where the radiosonde's GPS position is used to select the grid point in the model that the radiosonde passes through. The reason for using this method and not

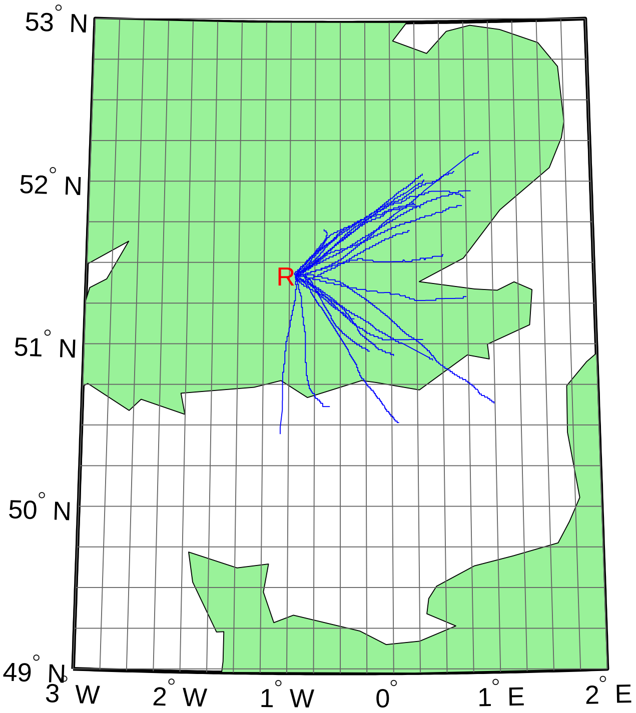

Figure 6.1 A map showing the trajectories of the 23 accelerometer ascents made from the Reading University Atmospheric Observatory (RUAO), marked by R. The grey lines mark the grid squares of a hypothetical model with a 0.25^o grid resolution.

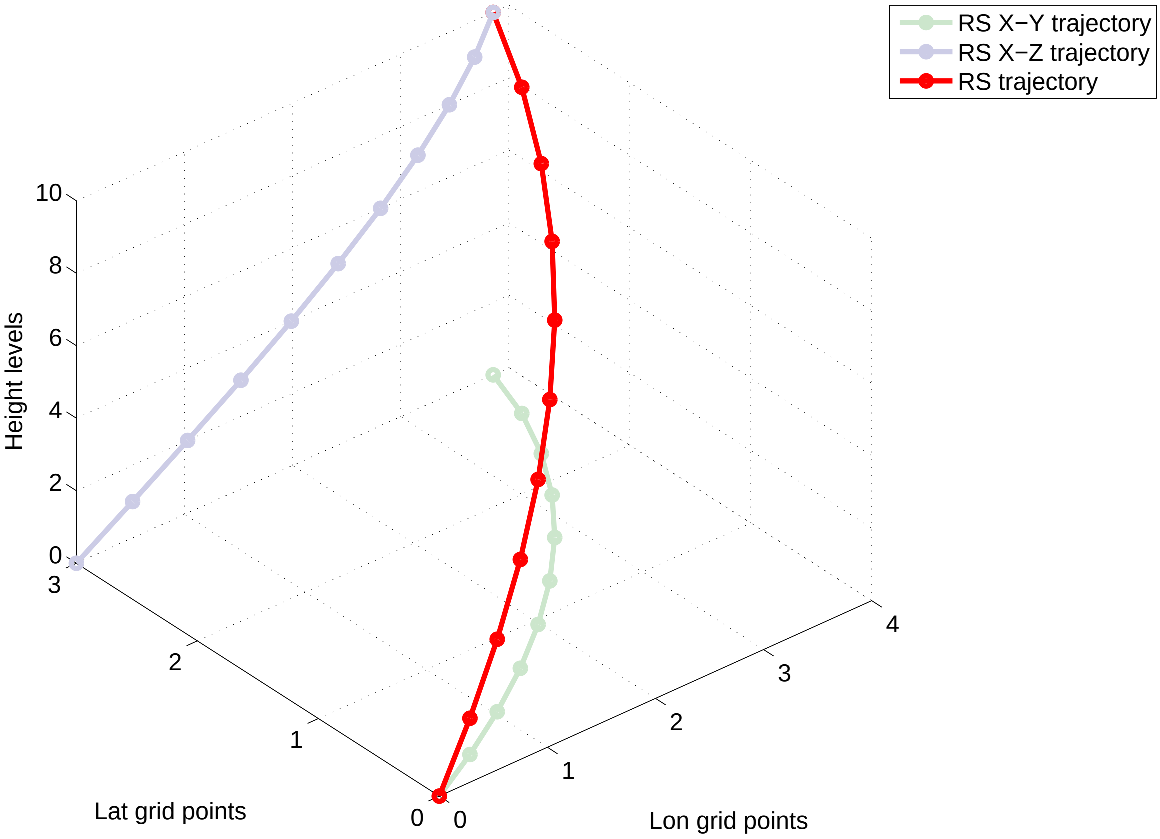

Figure 6.2 Diagram showing how a hypothetical radiosonde trajectory (red) launched from origin spans multiple grid squares and height levels in both the Z-X (blue) and X-Y (green) planes.

interpolation is that aviation turbulence forecasts are issued as gridded data (Gill, 2014) and verifications of these forecasts are made by placing observations in a grid square. The comparison between the radiosonde and the model was undertaken by first selecting a pressure surface within the model and matching it to the pressure height along the radiosonde's profile. The GPS location at the radiosondes matched pressure height was then used to select a grid point on the model pressure surface. The standard meteorological values from the model at that grid point were then extracted for a comparison with radiosonde data. If no GPS location data was available for that pressure surface, then the observation-model pair for that point was omitted. Furthermore, if the nearest radiosonde data record differed by more than 2.5 hPa from the pressure surface in question, the observation model pair was also omitted. 2.5 hPa was used as a threshold to avoid data that may be associated with a different pressure level being selected. A schematic in figure 6.2 shows how a hypothetical radiosonde ascent can be pegged to different grid squares and height levels. To provide a point to point comparison, no vertical averaging of the radiosonde data was undertaken. The time step of the model is selected as the time step closest to the time of the accelerometer sonde launch. In the next two sections a more in-depth description of the ERA-Interim reanalysis and the ECMWF deterministic model is undertaken, and the results of the aforementioned method for both models are shown.

6.1.2 ERA-Interim comparison with standard radiosonde data

The ERA-Interim analysis is described in detail in Dee et al. (2011). It has an 0.7 degree horizontal resolution and 60 model levels, it is based on the ECMWF's Information Forecast System (IFS) Cy31r2[1]. Pre-processing of the ERA-Interim data to 37 pressure levels between 1000 hPa and 1 hPa was undertaken by the ECMWF. The radiosondes used during this campaign usually reach heights of approximately 20 km, which equates to a pressure of 50 hPa, meaning that comparable model data are limited to the lower 30 pressure levels. ERA-Interim outputs the following radiosonde comparable fields: T,Z,u,v,q and RH. In total there were 1214 comparable observation-model pairs for the 51 ascents. In figure 6.3, the radiosonde observed values were plotted against the ERA-Interim values for each of the aforementioned fields. A linear fit was fitted to each observation-model field, to see if the relationship between the radiosonde data and model data followed a one to one relationship. A Pearson's correlation coefficient and RMSE was calculated between the radiosonde and ERA-Interim values, which are displayed on each plot. The ERA-Interim values of T, Z, u and v show a high level of agreement with the radiosonde observations. The model T comparison has a near 1:1 relationship with the radiosonde observations. The RMSE is 1.36 K, a portion of which could be due to an error on the radiosonde's temperature sensor (See table 5.4). Further uncertainty comes from the grid point representing an average 80 km across the pressure surface. Whilst Z has an almost 1:1 relationship, it has a RMSE of 64 m, this would appear large near the Earth's surface, but at higher altitudes of 100 hPa this could be a relatively small error. This is due to uncertainties which have propagated from the radiosonde's pressure sensors. To demonstrate this, one takes the hydrostatic equation

$$\frac{\Delta P}{\Delta Z} = -\frac{Pg}{RT}, \tag{6.1}$$

---

[1] More information can be found about the ECMWF's IFS versions at `https://software.ecmwf.int/wiki/display/IFS/Official+IFS+Documentation`.

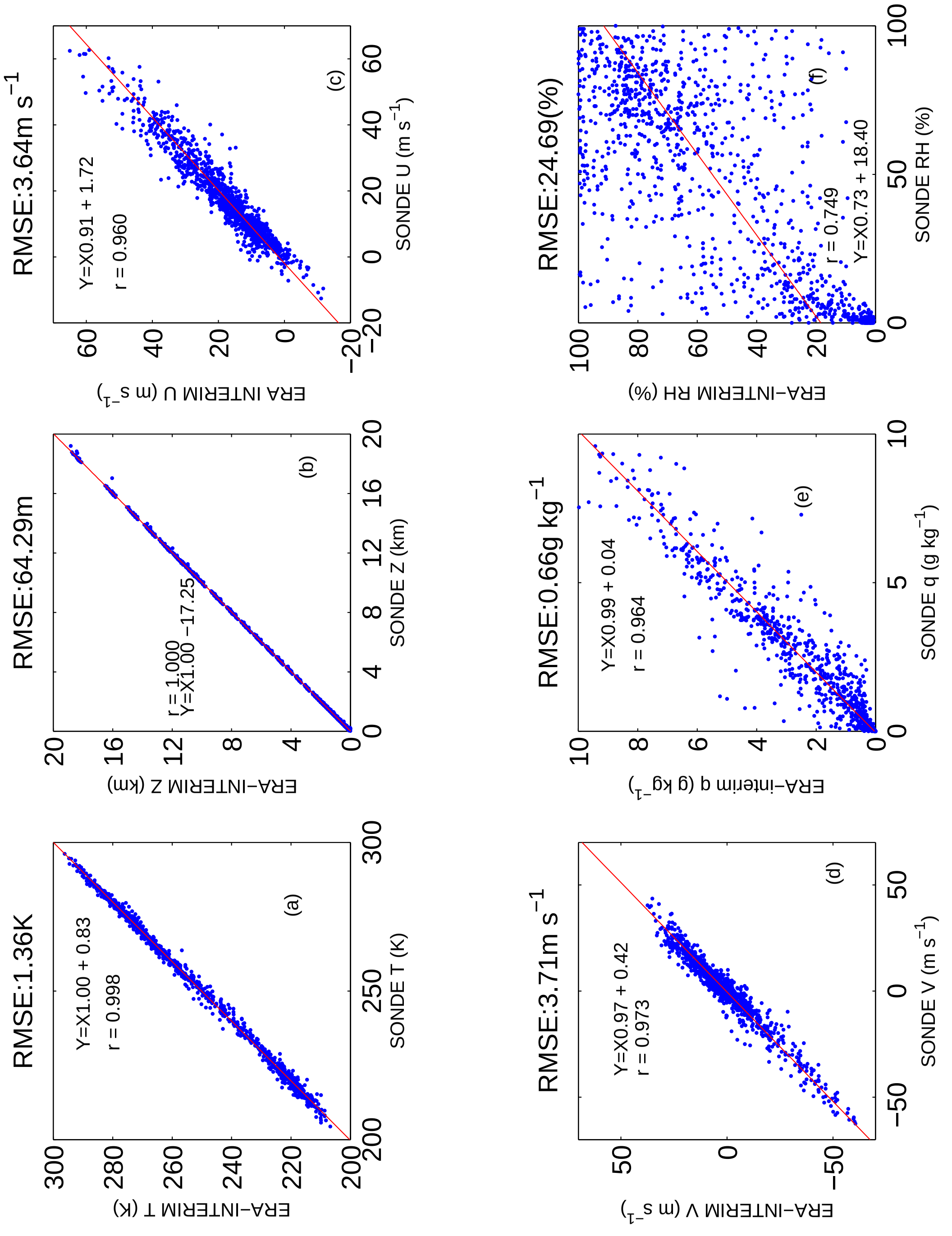

Figure 6.3 Radiosonde quantities plotted against ERA-Interim matched values from 51 ascents for a) temperature T (K), b) geopotential height Z (m), (c) zonal wind component u (m s^{-1}), (d) meridional wind component v (m s^{-1}), e) specific humidity q (g kg^{-1}) and (f) RH (%). The root mean square error (RMSE) is shown for each quantity.

and set ΔP to 0.4 hPa, which is the absolute error of the calibration accuracy of the radiosonde's pressure sensor(Vaisala, 2013). Then set P to 900 hPa and T to 283 K, the resulting ΔZ would be 3.6 m. However if P were set to 100 hPa and T to 221 K then ΔZ would equate to 25 m, explaining a proportion of the RMSE error encountered. The u and v wind components have observation-model ratios of 0.91 and 0.97 respectively, meaning that ERA-Interim is slightly under predicting wind speed. The RMSE calculated for both u and v are similar to those shown in Dee et al. (2011). The relationship between observed and model specific humidity has a 1:1 relationship. However, there is more scatter associated with this quantity yielding a RMSE of 0.66 g kg^{-1}. One reason for the more heightened discontinuity between the radiosonde and ERA specific humidity is down to humidity being a more localised parameter. If patchy cloud is present across the grid square, then ERA-Interim will take an average across the grid square, where the radiosonde will either traverse a cloud or it will not. This is more apparent when examining the RH values in panel (f) of figure 6.3, which shows a large amount of scatter, a correlation coefficient of 0.75 and the absence of a 1:1 relationship. There are many reasons for this, if a radiosonde ascends through a grid square where there is 50% cloud coverage, there is a 50% chance that the radiosonde will observe 100% RH. ERA-Interim on the other hand will combine satellite information in the data assimilation stage and through cloud schemes estimate the amount of cloud over the grid point and from this it will deduce an independent RH value. The RH value is independent as ERA's RH does not equate to ERA's specific humidity when converted. Miloshevich et al. (2009) found that the RS92 radiosonde had a bias in relative humidity measurements. This could cause an average error of 5%, which was not taken into account when undertaking the comparison between the radiosonde and ERA-Interim, however, is unlikely to be the sole reason for the large amount of scatter observed.

In summary, ERA-Interim makes a good approximation of the atmosphere, however there is disagreement involving relative humidity. This is likely due to the radiosonde making a point measurement, whereas ERA-Interim attempts to average cloud over the entire grid square. This should not be a problem as the majority of turbulence diagnostics do not have a humidity component.

6.1.3 ECMWF deterministic model comparison with standard radiosonde data

The ECMWF global deterministic model is described in detail in ECMWF (2014), it has 137 model levels and a horizontal resolution of 14 km. The data were extracted at 0.25 degree resolution equating to about 28 km, which has better horizontal and vertical resolution over the reanalysis packages but does not take advantage of the finer 14 km horizontal resolution. There has been little research on whether a high resolution forecast necessarily gives better turbulence forecasts. Sharman et al. (2006) successfully used a 20 km horizontal resolution to forecast turbulence over North America. Gill (2014) used a global model which had a 25 km resolution, hence this extracted resolution is on par with those used in other investigations. Unlike the ERA-Interim data the model data has not been processed on to pressure levels, therefore interpolation of the forecast data on to pressure surfaces is needed. One could calculate the turbulence diagnostics along the hybrid model levels, however the model levels are terrain following, which could cause unwanted artefacts in turbulence diagnostics across orography. For example calculating the horizontal temperature gradient would then include a contribution from the vertical temperature gradient. The pressure height at each point along the model level surface is a function of the surface pressure. An idealised pressure profile using a surface pressure of 1000 hPa was used as a guide to allow the forecast data to be re interpolated. This allowed the original resolution of the model levels, which is approximately 250 m for tropospheric heights, to be kept. Most commercial aircraft fly at a maximum cruising altitude of 12 km, thus it was decided pressure levels above 100 hPa could be excluded. As the boundary layer is of little interest in this study the model data was interpolated at a resolution of 50 hPa interval up to the 800 hPa surface, which gives 51 levels between 800 hPa and 100 hPa and an extra 4 levels between the surface and 800 hPa.

The deterministic model outputs T, Z, u, v and q. Figure 6.4 shows the result of the radiosonde model comparison for these quantities. RH is not output by the deterministic model so is not shown. The model-observation pairs have been selected using the same process as that used for selecting such pairs in the ERA Interim comparison above. In total 2608 observation pairs were compared. The model shows good agreement with the radiosonde observations, with the RMSE for T, Z, u ,v and q indicating that this agreement is stronger than that for the comparison with ERA-Interim data. This is likely due to the increased temporal and spatial resolution provided by the deterministic model. Furthermore the deterministic model uses the more advanced CY40R1 IFS system, which

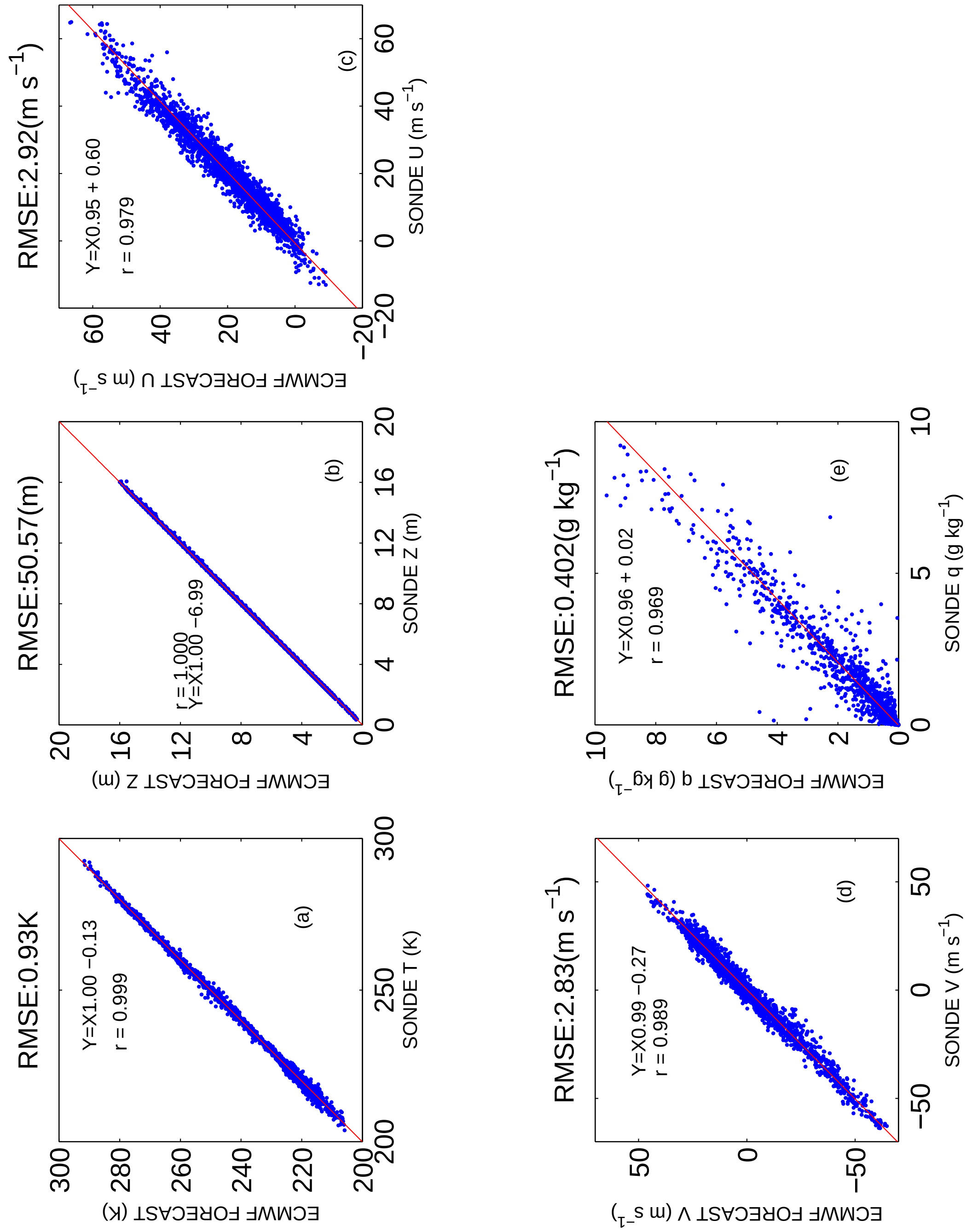

Figure 6.4 Radiosonde quantities plotted against ECMWF deterministic matched values from 51 ascents for a) temperature T (K), b) geopotential height Z (m), (c) zonal wind component u (m s^{-1}), (d) meridional wind component v (m s^{-1}) and e) specific humidity q (g kg^{-1}). RMSE values for each quantity are above each plot.

is likely to better represent the atmosphere. Specific humidity, although having a smaller RMSE, does appear to be underestimated in the deterministic model when comparing the slope of the relationship with that of ERA-Interim. However, as previously discussed, clear-air turbulence diagnostics don't include humidity variables so its accuracy is not paramount.

6.1.4 Conclusions

Quantity	ERA-Interim	ECMWF Deterministic
Average grid spacing	78.5 km	28 km
Usable height levels	20	50
Average grid spacing	500 m - 1 km	250 m
Time step (hours)	6	1
T sonde-model relationship	1.00	1.00
Z sonde-model relationship	1.00	1.00
u sonde-model relationship	0.91	0.95
v sonde-model relationship	0.97	0.99
q sonde-model relationship	0.99	0.96
RMSE T (K)	1.36	0.94
RMSE Z (m)	177	51
RMSE u (m s^{-1})	3.64	2.92
RMSE v (m s^{-1})	3.71	2.87
RMSE q (g kg^{-1})	0.66	0.37

Table 6.2 Table showing specifications of each model and assessment of their skill at representing the atmosphere the radiosonde traverses.

Two models which can give a reasonable estimate of the state of the atmosphere have been examined. Both are very good, but the deterministic model does perform slightly better and it has a finer spatial and temporal resolution than ERA-Interim. Table 6.2 shows the specifications for both ERA-Interim, and the ECMWF global deterministic model. The RMSE and the slope of the sonde-model relationship for each quantity compared is also shown. In conclusion, the ECMWF global deterministic forecast will be used for the turbulence diagnostic calculations.

6.2 Calculating turbulence diagnostics

Table 6.3 shows a list of the turbulence diagnostics calculated for this study, the majority of which were presented in table 2.4 in chapter 2. The Lighthill-Ford scheme (Knox et al., 2008), turbulent structure functions (Frehlich and Sharman, 2004) and Marroquins TKE closure method (Marroquin, 1998) are not calculated. Although it would have been ideal to include them they have been omitted for the following reasons. For the Lighthill Ford scheme a calibration of $\hat{a}$, in equation 2.36, is needed. However, this value has not been made publicly available. The structure function method requires a knowledge of the correction and reference structure functions D_{cor} and D_{ref} which, for this dataset are unknown. Finally the Marroquin TKE closure method also needs a pre calibration with observations to select suitable values of the Prandtl number Pr

and kinematic diffusivity K_m. The equation numbers in the table refer to the equation in appendix B which shows how each diagnostic is implemented on each pressure level. Many of the turbulent diagnostics require a horizontal gradient to be taken, which can be achieved by taking a numerical gradient across the pressure level. Padding is required along the edges of the grid to avoid incorrect gradients at the grid edge. The grid was padded by taking the 0^o longitudinal grid points and placing them at the opposite edge of the grid adjacent to the 360^o grid points and visa versa. The grid was then padded at both extremities in a latitudinal sense by placing the 0-180^o grid points between 180-360^o and visa versa. After the calculation of the turbulence diagnostics, the padding was removed.

Turbulence diagnostics for comparison were then selected from the model using the same method to select standard meteorological quantities as that described in section 6.1.1. Turbulence diagnostics were only calculated on the pressure levels between 800 hPa and 100 hPa. σ_z was recalculated from the raw accelerometer data with a 200 m height window centred on the selected grid points Z. An alternative method would have been to

Diagnostic	Symbol	Units	Equation no.
-ve Richardson number	$-Ri$		B.4
Colson Panofsky index	CP	knots^2	B.5
Knox 1997 index	$KX1$	s^{-2}	B.26
Relative vorticity squared	ξ^2	s^{-2}	B.10
North Carolina State University index 1	$NCSU1$	s^{-3}	B.23
Brown index	Φ	s $^{-1}$	B.11
Brown eddy dissipation rate	ϵ_{Brown}	m^{2}s^{-3}	B.13
Ellrod's turbulence index 1	$ET1$	s^{-2}	B.15
Ellrod's turbulence index 2	$ET2$	s^{-2}	B.16
U × Deformation	$UDEF$	m s^{-2}	B.21
Thermal gradient × Deformation	T_zDEF	K m^{-1}s^{-1}	B.22
Frontogenesis function	F	m^2 s^{-3} K^{-2}	B.8
Potential vorticity	$\|PV\|$	m^{2}s^{-1}K kg^{-1}	B.17
Negative absolute vorticity advection	$NAVA$	s^{-2}	B.24
Vertical wind shear	U_z	s^{-1}	B.3
Horizontal temperature gradient	$\|\nabla_H T\|$	K m^{-1}	B.18
Clark's CAT algorithm	$CCAT$	s^{-3}	B.27
Dutton empirical index	DUT	s^{-2}	B.28
Relative vorticity advection	$\|RVA\|$	s^{-2}	B.25
Wind speed	U	m s^{-1}	B.19
Wind speed × directional shear	$U\phi_z$	rad s^{-1}	B.20
Horizontal divergence	$\|\nabla_H\|$	s^{-1}	B.14
Flow Deformation	DEF	s^{-1}	B.9

Table 6.3 A table summarising the turbulence diagnostics calculated for comparisons with their corresponding symbol, units and equation number, for calculating on pressure levels in the appendix B.

re-interpolate the σ_z used in chapter 5. The meteorological indicators of cloud, near-cloud and convection were however re-interpolated onto the newly calculated height levels. As all the turbulence diagnostics in 6.3 are utilised for clear air turbulence prediction, it will be useful to remove regions of atmosphere in the verification stage where convection is present, or are in or near cloud. Before moving on to the verification section, an examination of a selection of turbulence diagnostics will be undertaken to explore the temporal evolution of turbulence observed in the case studies in section 5.3. The aim is to see if the turbulence diagnostics can provide any explanation of the temporal evolution of turbulence.

6.3 Case study comparison with model data

In chapter 5 two Intense Observation Periods (IOPs) where jet streams were present are shown. In summary it was found that the turbulence present could have been caused by either low vertical thermal stability or high vertical wind shear. There was no apparent evidence to conclude why the turbulence intensified over the course of the IOPs. During these case studies the wind profiler provided a time-altitude plot of wind speed. For each case study day, the wind field along the core of each jet stream will be examined, along with any turbulence diagnostics that may indicate why turbulence may be gaining intensity.

6.3.1 Case study 1: 28th April 2015

The first IOP to be studied was that during the 28th April 2015 over the MST Radar site at Aberystwyth. In section 5.3 it was shown that the structure of the jet stream was consistent during the IOP (see figure 5.10). There were also no significant changes in wind shear or thermal structure (see figure 5.14). In this section the horizontal components of the wind field are explored, before examining the turbulence diagnostics. Figure 5.10 shows that the jet core is at an altitude of approximately 8 km, which for this day over the area of study is at a pressure surface of 339 hPa. In figure 6.5 the horizontal wind field from the model is shown for the three time steps corresponding to the three launches. From panels (a)-(c), it can be concluded that the intensity of the jet core did not change substantially which is in agreement with figure 5.10. The core of the jet was moving eastwards during the course of the IOP, meaning that the last radiosonde ascent would have been made at the downstream edge of the jet core where horizontal wind gradients

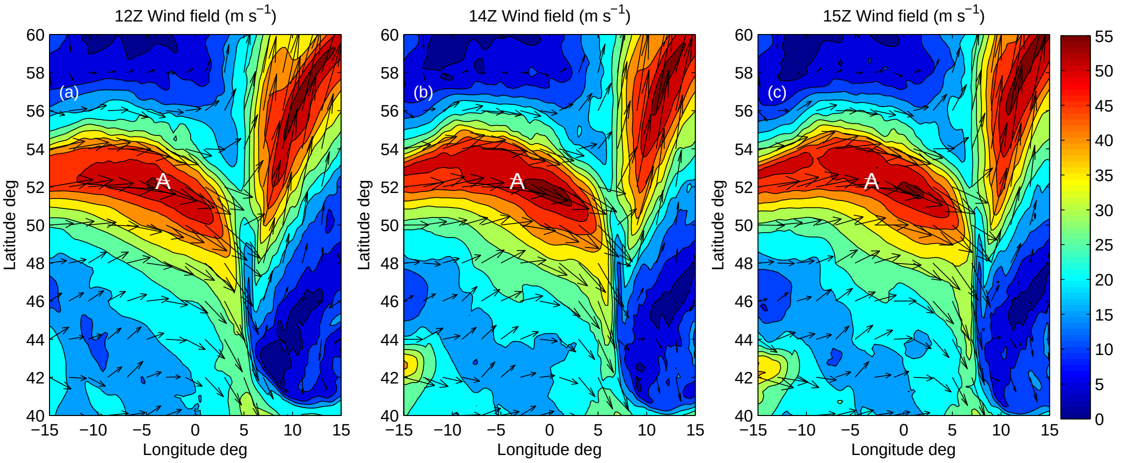

Figure 6.5 The 339 hPa wind field from the ECMWF deterministic model for a) 1200 UTC, b) 1400 UTC and c) 1500 UTC on 28th April 2015. The filled contours represent the magnitude of U (m s^{-1}) and the black arrows show both direction and magnitude. The white 'A' marks the radiosonde launch site at Aberystwyth.

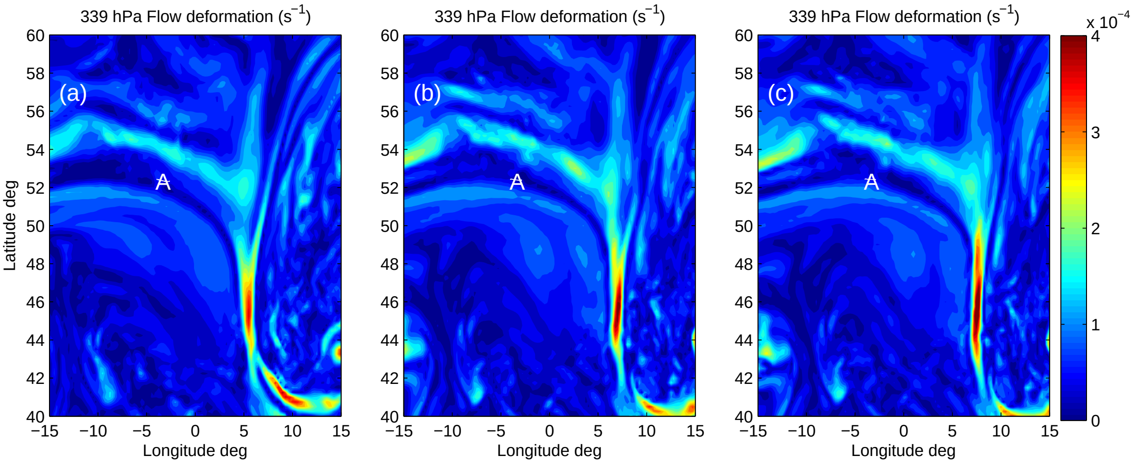

Figure 6.6 The 339 hPa deformation from the ECMWF deterministic model for a) 1200 UTC, b) 1400 UTC and c) 1500 UTC on 28th April 2015. The filled contours represent the magnitude of DEF in (s^{-1}), the white 'A' marks the radiosonde launch site at Aberystwyth.

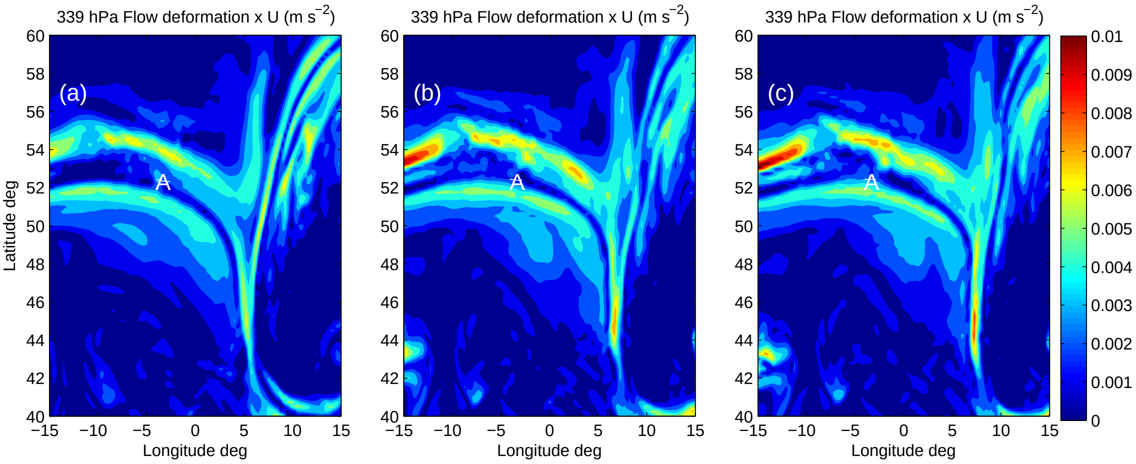

Figure 6.7 The 339 hPa $U\times$ deformation from the ECMWF deterministic model for a) 1200 UTC, b) 1400 UTC and c) 1500 UTC on 28th April 2015. The filled contours represent the magnitude of $UDEF$ in (m s^{-2}), the white 'A' marks the radiosonde launch site at Aberystwyth.

could intensify.

Deformation builds part of the underlying mechanics for several of the diagnostics computed here and it has been shown in previous cases to produce turbulence (Ellrod and Knapp, 1992), (Brown, 1973). Figure 6.6 shows the deformation for the same time steps and pressure level. During the course of the IOP, a region of deformation intensifies along the northern flank of the jet stream. On the southern flank of the jet stream, a less intense area of deformation begins to form over Aberystwyth which could be associated with the increased levels of turbulence. As deformation is often combined with other metrics, there are few reference values making it hard to infer a turbulence intensity. However, Sharman et al. (2006) tabulated turbulence thresholds for several turbulence diagnostics, including $U\times$ deformation which could be used to give an estimation.

Figure 6.7 shows the $U\times$ deformation ($UDEF$) on the 339 hPa pressure surface. As the IOP progresses, a region of $UDEF$ of 0.004 m s^{-2} begins to approach the observation site. Sharman et al. (2006) showed median values of 0.0017 and 0.0023 m s^{-2} for moderate and severe turbulence thresholds, which could imply a region of severe turbulence in the current case study. However, the following needs considering: are the climatological medians in Sharman et al. (2006) a comparable value? Firstly, the climatological medians are from 1 year worth of data over the US. The median values are calculated from all grid points where turbulence was observed by aircraft, whether a given diagnostic predicted turbulence or not, meaning there could be a bias to lower values if that diagnostic under predicts turbulence. Secondly, the horizontal resolution of the RUC model used by Sharman et al. (2006) is slightly finer and the vertical resolution is coarser when compared to the global ECMWF deterministic model. This may cause different values to be calculated and hence different distributions and medians for the two models. Finally, the suggested thresholds were for the mid-level RUC levels between heights of 3 and 7 km. To remedy this, a climatology for the deterministic model needed creating, so turbulence thresholds could be generated using a probability density function of ϵ observations. This was implemented by binning each diagnostic's values from across all pressure level surfaces, at all time steps (51 in total) to produce a Probability Density Function (PDF). This builds up a climatology of 10^9 turbulence diagnostic values which could be used to reliably infer statistical thresholds for turbulence intensity based on probability. Using the PDF estimates of ϵ from Sharman et al. (2014) of 7×10^{-2}, 7×10^{-4} and 4×10^{-5} for the turbulence probabilities of light, moderate, and severe turbulence, respectively, turbulence thresholds could be inferred from the PDFs of $UDEF$ and DEF from the model data.

Figure 6.8 shows turbulence thresholds for both DEF and $UDEF$, if the values found in figures 6.7 and 6.6 near point A are compared, it can be concluded that the approaching region of deformation could bring light to moderate turbulence. However, one caveat is that these probabilities are derived from ϵ which are computed from automated aircraft measurements, so some bias as to turbulence of aircraft length scales may be present. For completeness, thresholds for all turbulence diagnostics were calculated using the same method, with the results presented in table 6.4.

Another turbulence metric which appeared to vary over the IOP was the relative vorticity advection. As previously discussed, it is the leading order term in the Lighthill

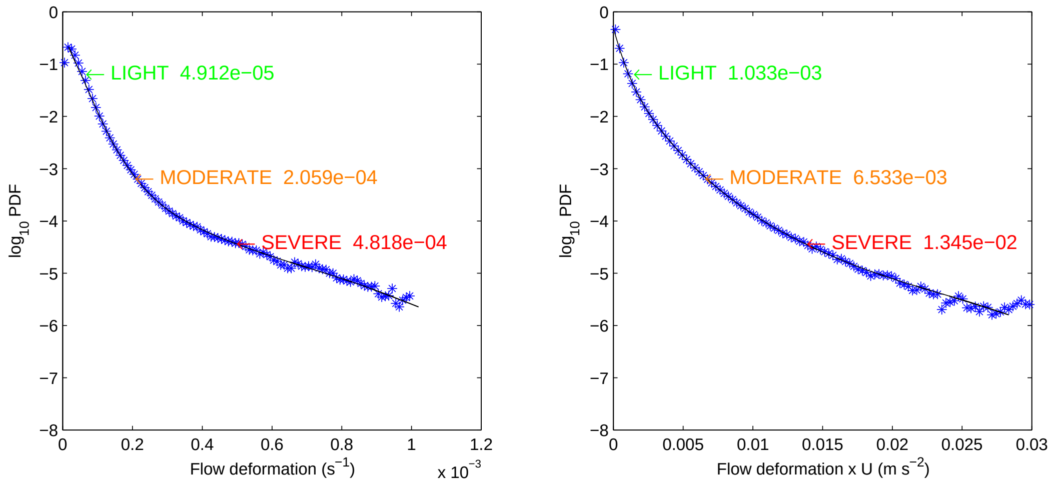

Figure 6.8 Probability Density Functions (PDF) of Deformation (s^{-1}) (left) and $U\times$ Deformation (m s^{-2}) (right) calculated from all forecast time steps at all selected pressure levels. Light, moderate and severe turbulence thresholds have been labelled using probability estimates from Sharman et al. (2014).

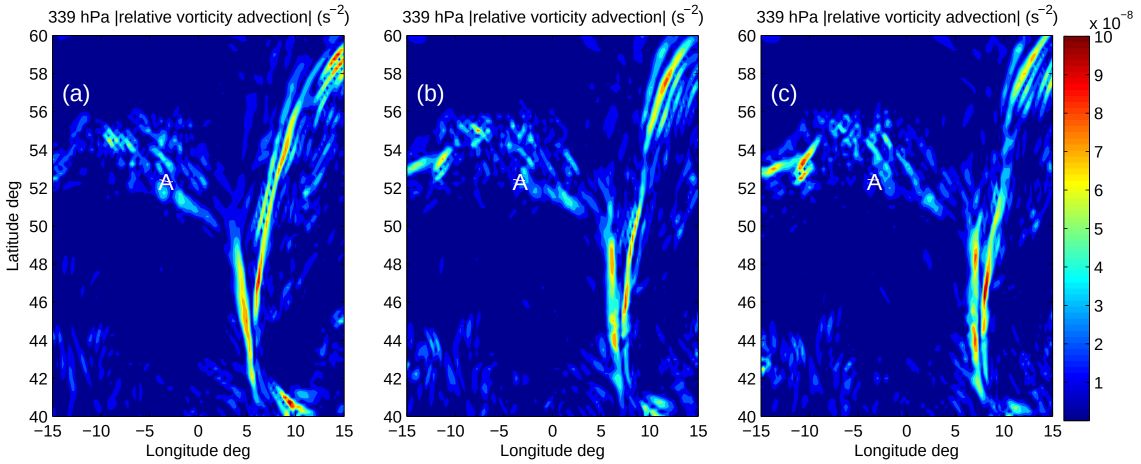

Figure 6.9 The 339 hPa RVA (s^{-2}) from the ECMWF deterministic model for a) 1200 UTC, b) 1400 UTC and c) 1500 UTC on 28th April 2015, the white 'A' marks the radiosonde launch site at Aberystwyth.

Turbulence diagnostic	Units	Light	Moderate	Severe
$-Ri$		-0.92	-0.56	2.37
U_z	$\times 10^{-3}\mathrm{s}^{-1}$	2.74	18.67	28.85
CP	kt^2	-0.37	1.70	25.81
F where +ve	$\times 10^{-3}\mathrm{m}^2\mathrm{s}^{-3}\ \mathrm{K}^{-2}$	-2.01	4.77	32.03
Φ	$\times 10^{-5}\mathrm{s}^{-1}$	6.67	24.00	40.31
ϵ_{brown}	$\times 10^{-10}\mathrm{J\ kg}^{-1}\ \mathrm{s}^{-1}$	3.21	20.18	53.19
$ET1$	$\times 10^{-7}\mathrm{s}^{-2}$	4.34	23.52	53.96
$ET2$	$\times 10^{-7}\mathrm{s}^{-2}$	4.28	32.32	74.09
DEF	$\times 10^{-5}\mathrm{s}^{-1}$	4.96	20.48	36.01
$\lvert PV\rvert$	$\times 10^{-6}\ \mathrm{m}^2\mathrm{s}^{-1}\mathrm{K\ kg}^{-1}$	2.23	17.60	22.42
ξ^2	$\times 10^{-9}\mathrm{s}^{-2}$	6.01	34.24	86.02
$\lvert\nabla_H T\rvert$	$\times 10^{-5}\ \mathrm{K\ m}^{-1}$	1.37	5.16	9.47
U	$\mathrm{m\ s}^{-1}$	6.00	64.88	88.39
$U\phi_z$	$\mathrm{rad\ s}^{-1}$	1.59	8.62	13.98
$UDEF$	$\times 10^{-4}\mathrm{m\ s}^{-2}$	9.94	63.13	124.80
T_zDEF	$\times 10^{-7}\ \mathrm{K\ m}^{-1}\mathrm{s}^{-1}$	1.14	10.50	19.32
$\lvert\nabla_H\rvert$	$\times 10^{-5}\mathrm{s}^{-1}$	2.43	12.05	23.29
$NCSUI1$	$\times 10^{-9}\mathrm{s}^{-3}$	-1.34	1.27	14.78
$NAVA$ (where +ve)	$\times 10^{-9}\ \mathrm{s}^{-2}$	7.14	53.19	125.30
$\lvert RVA\rvert$	$\times 10^{-8}\mathrm{s}^{-2}$	1.04	67.18	150.10
$KX1$	$\times 10^{-8}\mathrm{s}^{-2}$	1.37	5.15	9.24
$CCAT$	$\times 10^{-8}\mathrm{s}^{-3}$	1.92	12.73	32.95
DUT	s^{-2}	15.80	84.90	178.30

Table 6.4 A table showing thresholds for light, medium and severe turbulence calculated from global ECMWF data for all 51 forecast time steps on all selected pressure levels based on been placed on probability distributions of ϵ from Sharman et al. (2014).

Ford radiation term. Regions of high relative vorticity advection could be the sources of breaking gravity waves which could cause turbulence in their vicinity. Figure 6.9 shows the relative vorticity advection over the IOP. In the region surrounding Aberystwyth, there is a swathe of sporadic cells of relative vorticity advection. The intensity of these cells is in the region of $4\times 10^{-8}\mathrm{s}^{-2}$ which, when consulting table 6.4, implies light to moderate turbulence, in agreement with the deformation diagnostics. What makes the results from this diagnostic interesting is the sporadic nature of the cells that are being advected by the flow. As there are effective patches passing over the IOP area, it can explain why turbulence may be observed in some ascents and not in others. Furthermore, gravity waves could radiate out from any of these small cells causing turbulence in their vicinity. In brief conclusion, the temporal evolution of turbulence is likely a combination of deformation which increases as the southern flank of the jet passes over the IOP, and the relative vorticity advection which is a proxy for Lighthill-Ford radiation of turbulent gravity waves in the center of the jet. The effects of the increase in deformation are easier to see as the turbulence detected by the radiosonde also increases with the approach of the deformation region. The relative vorticity advection whilst appears to be sporadic, shows enough variability to generate increased regions of random patches of turbulence.

6.3.2 Case study 2: 4th March 2015

In the second case study on the 4th March 2015, shown in section 5.3, a jet stream with an evolving structure was studied. There was also evidence to support the presence of a tropopause fold, which could have explained the evolution of turbulence observed. There were also gravity waves present at the top of the jet stream in the latter ascent, which could suggest turbulence due to Lighthill Ford radiation of gravity waves. The analysis begins by looking at the wind field over the Aberystwyth radar site. Figure 6.10 shows the evolution of the wind field on the 339 hPa surface on the 4th March 2015 for the time of each ascent. The jet stream core was at 8 km so data from the 339 hPa pressure surface is used. The jet stream is orientated in a N-S direction in agreement with MST radar observations in figure 5.15. During the course of the IOP the jet stream propagates eastwards. During the first ascent at 0900 UTC the ascent traverses the core of the jet stream, in the subsequent ascents the trailing flank of the jet stream is sampled. In this region the jet is becoming less intense which is also observed in section 5.3, which further shows the wind field does not appear to change direction over Aberystwyth. However in the area from -15^o to -5^o longitude surrounding Aberystwyth there is a 90 degree shift in wind direction. Apart from this wind shift there are no other indications in the wind field of anything that could be causing increased turbulence. Turbulence diagnostics which did show signs of the evolution of turbulence over this IOP will now be shown, starting by examining the Brown index, Φ.

Figure 6.11 shows the Brown index on the 339 hPa pressure surface for each ascent. The Brown index is a deformation and vorticity based diagnostic, which shows an increase in magnitude between the first and final ascent of the IOP. In the model data for the first three ascents there is little difference in the Brown index. For the final ascent the Brown index increases, which is indicative of values of light to moderate turbulence. This increase in the Brown index is in agreement with observations of turbulence in figure 5.20 which shows the most intense turbulence during the last ascent. The Brown eddy dissipation rate is a product of the Brown index, ϵ_{brown} and U_z. ϵ_{brown} is shown in figure 6.12, where this diagnostic does not show turbulence at all over Aberystwyth, let alone show the temporal evolution of turbulence. Given that the Brown index did indicate turbulence, it is likely that the U_z value derived was not indicative of turbulence. The U_z on the 339

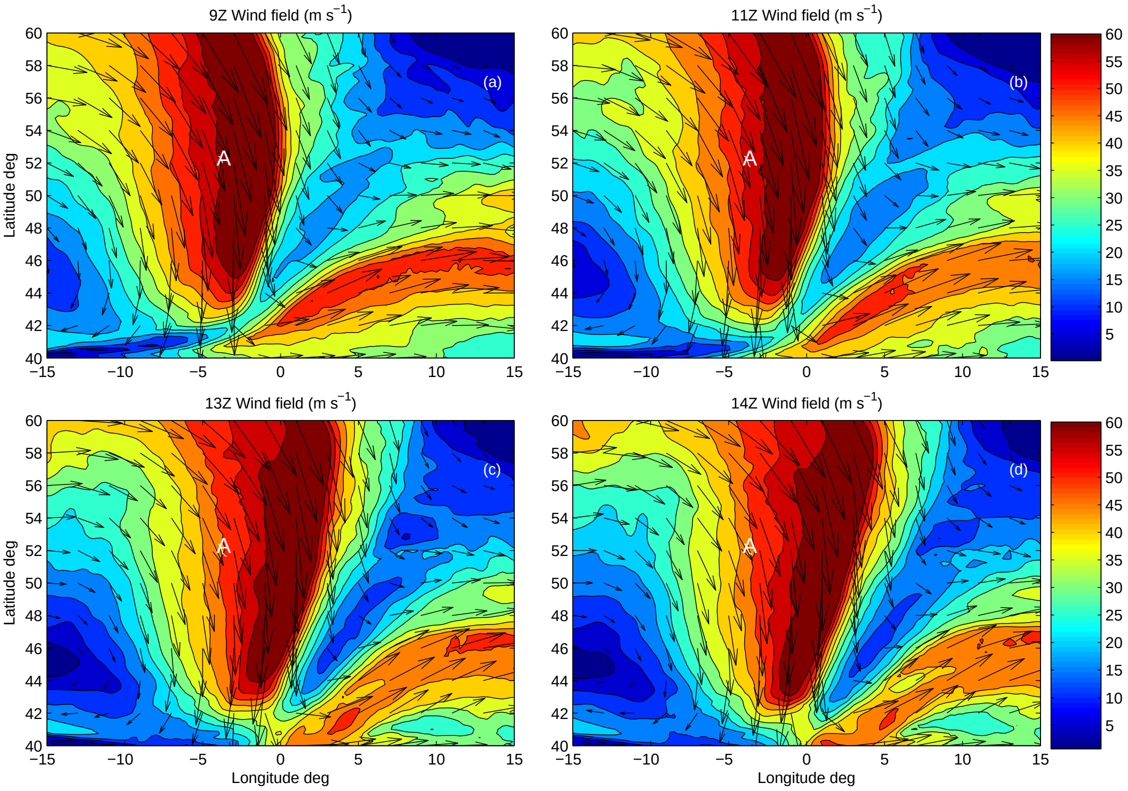

Figure 6.10 The 339 hPa wind field from the ECMWF deterministic model for a) 0900 UTC, b) 1100 UTC, c) 1400 and d) 1500 UTC on 4th March 2015. The filled contours represent the magnitude of U in (m s^{-1}) and the black arrows show both direction and magnitude. The white 'A' marks the radiosonde launch site at Aberystwyth.

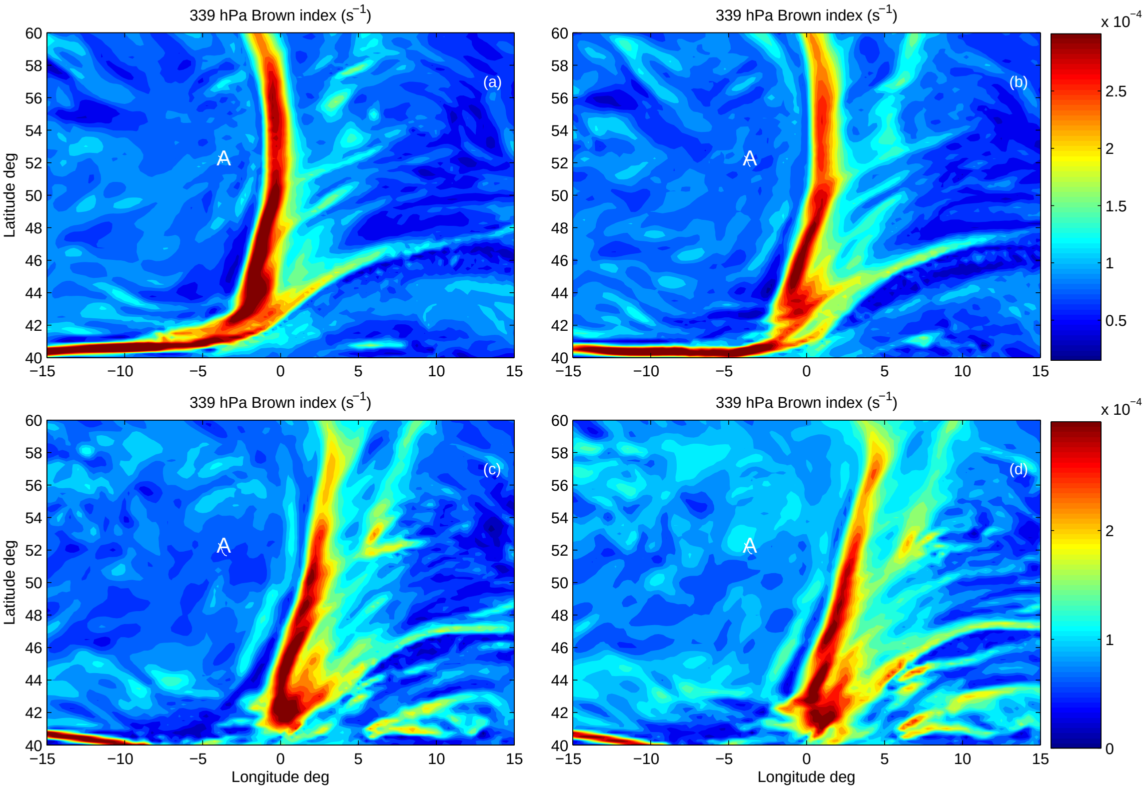

Figure 6.11 A contour plot of the 339 hPa Brown index, Φ, (s^{-1}) from the ECMWF deterministic model for a) 0900 UTC, b) 1100 UTC, c) 1400 and d) 1500 UTC on 4th March 2015. The white 'A' marks the radiosonde launch site at Aberystwyth.

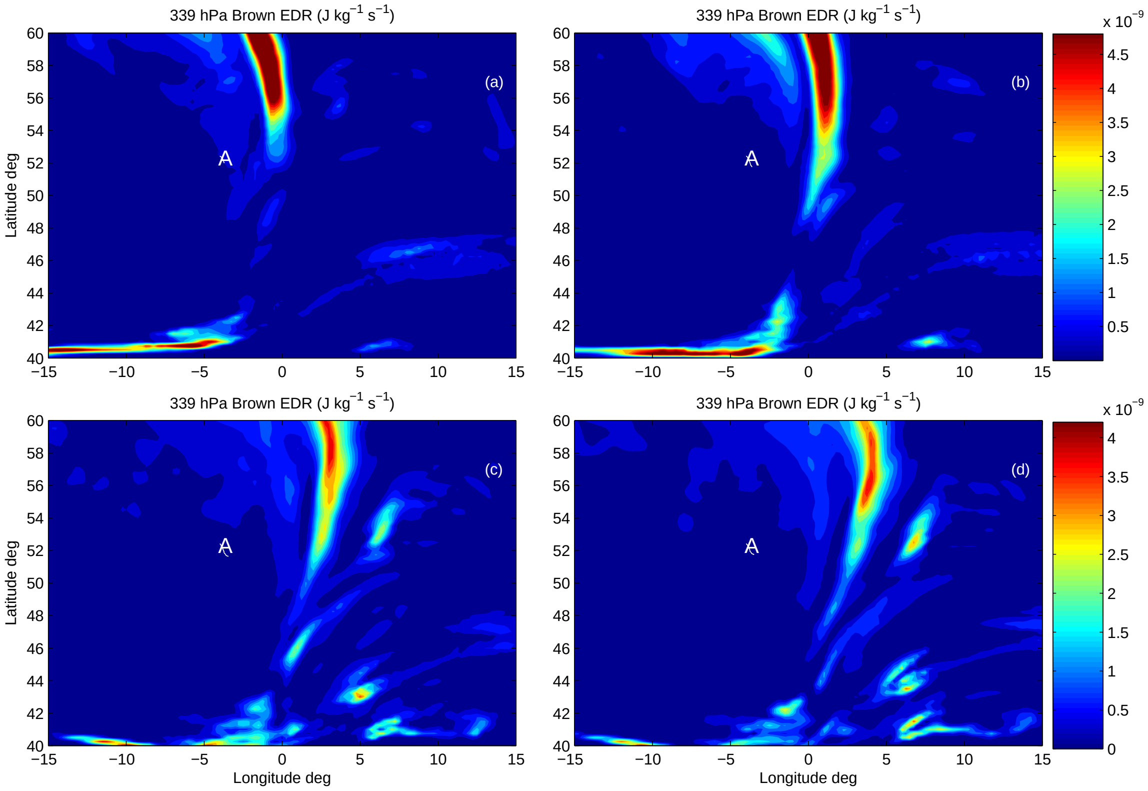

Figure 6.12 Contour plots of the 339 hPa ϵ_{Brown} (m^{2}s^{-3}) from the ECMWF deterministic model for a) 0900 UTC, b) 1100 UTC, c) 1400 and d) 1500 UTC on 4th March 2015. The white 'A' marks the radiosonde launch site at Aberystwyth.

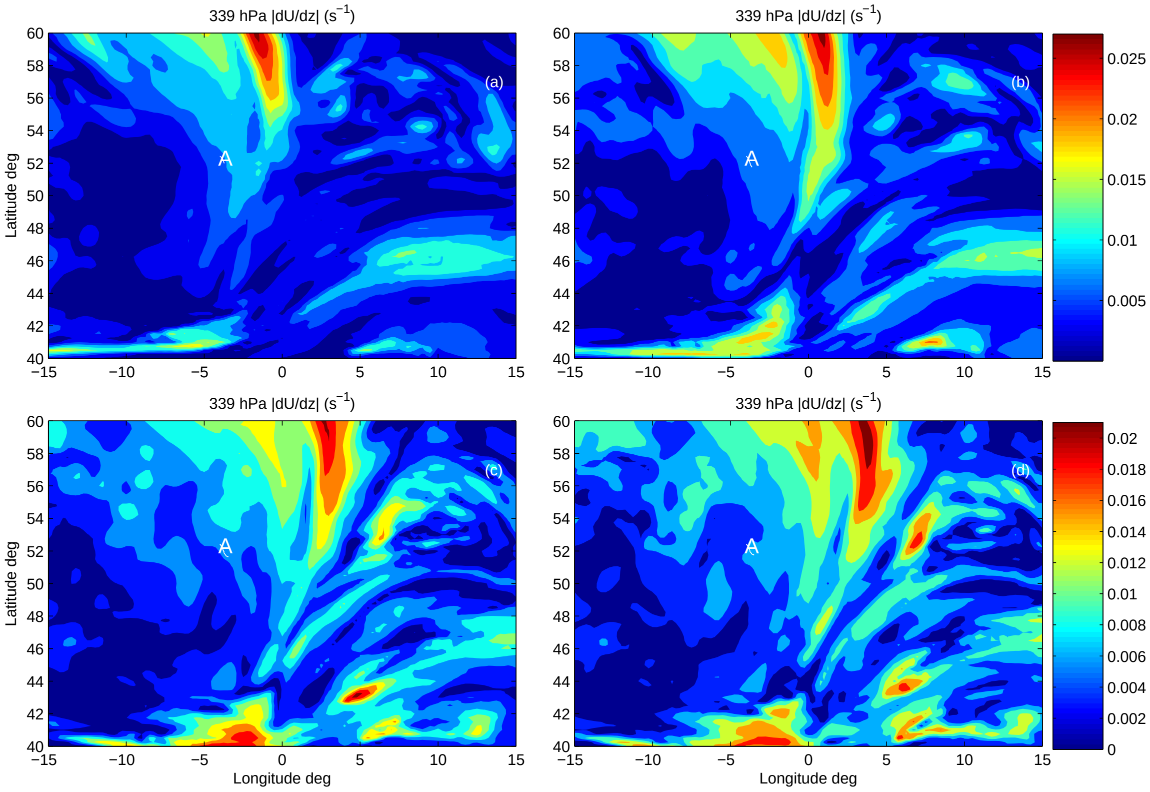

Figure 6.13 Contour plots of the 339 hPa U_z (s^{-1}) from the ECMWF deterministic model for a) 0900 UTC, b) 1100 UTC, c) 1400 and d) 1500 UTC on 4th March 2015. The white 'A' marks the radiosonde launch site at Aberystwyth.

hPa pressure surface for the four ascents is shown in figure 6.13. The values of U_z are of magnitude 0.0075 s^{-1} and do not appear to vary over the course of the IOP. Neither do there appear to be large values of U_z in the range of the observation site which could be related to the turbulence. The approximated light turbulence threshold value for U_z is 0.0027 s^{-1}. This is shown in table 6.4, which statistically indicates the presence of light turbulence, although the 0.0075 s^{-1} values is somewhat less than that of moderate turbulence.

Another deformation based diagnostic is the deformation × the vertical thermal gradient shown in figure 6.14 for each of the four ascents. It appears to intensify over the launch site during the IOP, and it is similar to the Brown index which increases during the final ascent in panel (d). The values shown in panel (d) over Aberystwyth are again in the light to moderate turbulence ranges when examining values in table 6.4. It appears that in this case study, the deformation of the flow could be the reason for the development of turbulence in combination with the developing tropopause fold detected. The relative vorticity advection does not appear to show any variability, or have values which would be classified as turbulent and is not shown.

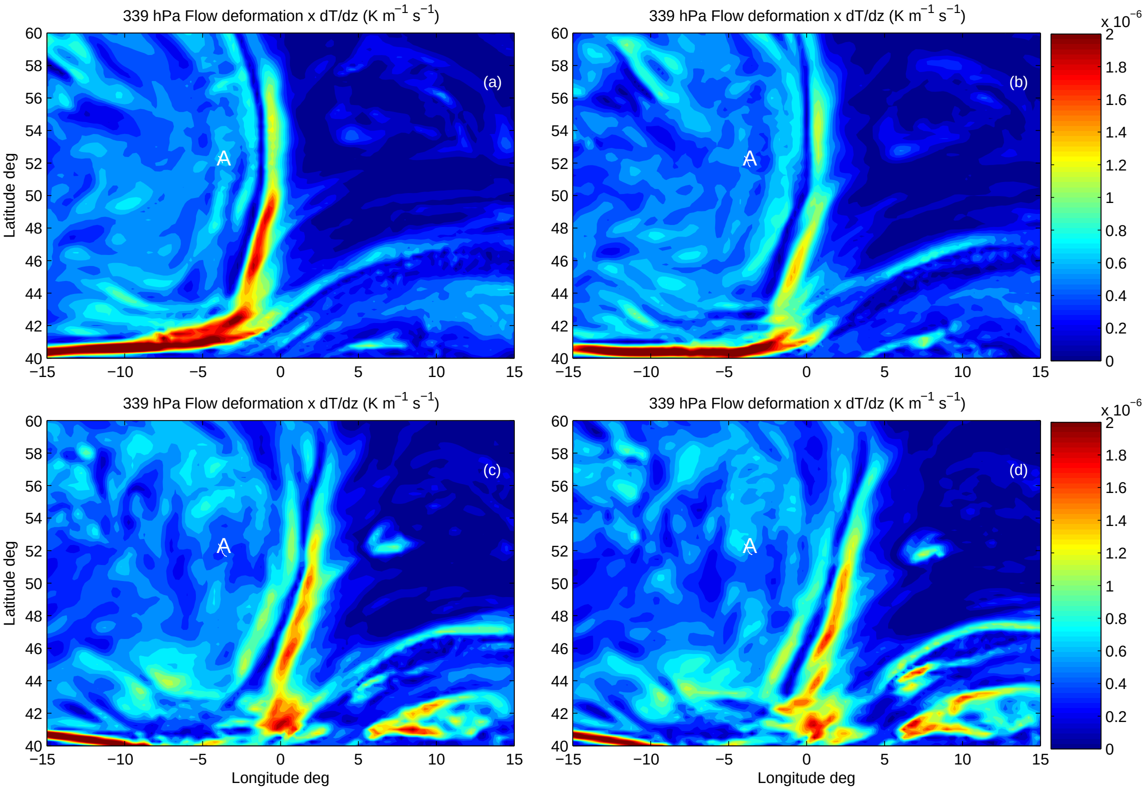

Figure 6.14 Contour plots of the 339 hPa T_zDEF (K m^{-1} s^{-1}) from the ECMWF deterministic model for a) 0900 UTC, b) 1100 UTC, c) 1400 and d) 1500 UTC on 4th March 2015. The white 'A' marks the radiosonde launch site at Aberystwyth.

6.3.3 Conclusions

In conclusion, two case studies of IOP's were examined to determine whether the turbulence diagnostics are able to improve the understanding of the temporal evolution of turbulence observed. In regions where the magnitude of deformation increases the observations of turbulence increase. In the first IOP regions of relative vorticity advection did also suggest that there could be Lighthill-Ford radiation of gravity waves which could lead to turbulence. Given the sporadic structure of the relative vorticity advection, this could also explain the temporal evolution of turbulence. In the second case study, the deformation gave a likely explanation of the development of turbulence. At the pressure level examined it was found that U_z didn't explain the temporal evolution of turbulence. Hence diagnostics which combine DEF and U_z may not predict turbulence. The T_zDEF did show a temporal evolution of turbulence. Relative vorticity advection was not present in significant values over Aberystwyth during the second IOP, so the suggestion made in section 5.3, that turbulence in the second IOP could be caused by Lighthill-Ford radiation, is unlikely. Given the qualitative findings within this section, it is expected that deformation diagnostics could perform best when the turbulence diagnostics are compared with in-situ observations of turbulence from the radiosonde in the next section.

6.4 Turbulence diagnostics verification

In this section the radiosonde observations of turbulence shall be used to assess the skill of the turbulence diagnostics shown in table 6.3. At first a technique to carry out the verification of each turbulent diagnostic will be discussed and then two comparisons will be undertaken. The first comparison will verify all the accelerometer data collected in clear-air and the second shall be further filtered to use only clear-air turbulence observations on days where a jet stream is present. The reason for doing this is that most clear-air turbulence diagnostics, such as deformation, are associated with large scale phenomena such as jet streams, which the turbulence diagnostics have been developed for.

6.4.1 Verification technique

In the atmospheric sciences there are many techniques to assess the skill of a forecast. Earlier in section 6.1 standard meteorological variables, such as T from the radiosonde were compared with T from a model. In that case both the model and radiosonde presented values with the same unit, meaning they could be compared directly. Here the radiosonde outputs a turbulent observation of σ_z in m s^{-2} and each diagnostic has its own units, meaning they cannot be compared in the same way that T could be compared. Most common verification methods use a contingency table, such as table 6.5, to assess a series of observation forecast pairs. A contingency table contains the total of hits, HH, where turbulence is forecast and observed. Another outcome is false alarms, FA, where turbulence is predicted but not observed, and there are also unforcasted turbulence incidents, HN, which is when turbulence is observed but not forecast. Finally there are cases where no turbulence is forecast or observed, NN. A method which is commonly used to assess the skill of a forecast using the data from a contingency table is to examine the false alarm rate (FAR) and the hit rate (HR), as is described in Brown et al. (1997) and used in Sharman et al. (2006) and Gill (2014). HR, the hit rate is the probability of all observed turbulence being predicted by the forecast and is given by

$$HR = \frac{HH}{HH + HN}. \tag{6.2}$$

NP, the null positive, is the probability of all null turbulence events being diagnosed by the forecast and is given by

$$NP = \frac{NN}{FA + NN}. \tag{6.3}$$

The false alarm rate, FAR, is given by

$$FAR = \frac{FA}{FA + NN}, \tag{6.4}$$

which is the probability of a forecast predicting turbulence when none is observed. A perfect forecast would have a HR=1 and FAR=0. These two values can be used to assess the skill of the forecast. The next step is to choose thresholds for both the accelerometer and the turbulence diagnostics in question. In chapter 5 a σ_z value of >5 m s^{-2} was chosen to indicate significant turbulence, and this is the value used here. The selection of a forecast threshold is somewhat more different. In table 6.4 thresholds for turbulence intensities were generated from a probability distribution, which gives 3 thresholds to verify at. However, what is often done in verification process is to use many thresholds,

	Turbulence observed	Null Turbulence
Turbulence forecast	HH	FA
No Turbulence forecast	HN	NN

Table 6.5 An example contingency table for summarising a series of turbulence observation-forecast pairs, definitions are described in the main text.

from 100 thresholds to as many as there are exclusive turbulence diagnostic values in the observation-forecast series. Contingency tables at each threshold are created, and from this a series of HR and FAR is produced and plotted as a curve. This curve is called Receiver Operating Characteristic (ROC) curve and has been used by many to assess the skill of a turbulence diagnostic (Sharman et al., 2006), (Gill, 2014), (Knox et al., 2008). ROC curves for two hypothetical forecasts are shown in figure 6.15. The blue ROC curve is that from a forecast with a good level of skill. As a rule of thumb, the closer the curve passes to the point (0,1) the more skilful the forecast. The red ROC curve closely follows the black dashed line which follows a 1:1 line which indicates no skill. A way to quantify this skill is to work out the Area Under the Curve (AUC). An area under the curve of 0.5 represents no skill and an AUC of 1 is that of a forecast with perfect skill. The AUC can be calculated by numerically integrating the ROC curve.

A ROC analysis will be performed for the turbulence observation pairs, for each turbulence diagnostic in table 6.3. Thresholds were derived by taking all the exclusively individual diagnostic values for each diagnostic. Two analysis will be performed, with the first using all the clear-air data from the observation-forecast pairs. The meteorological

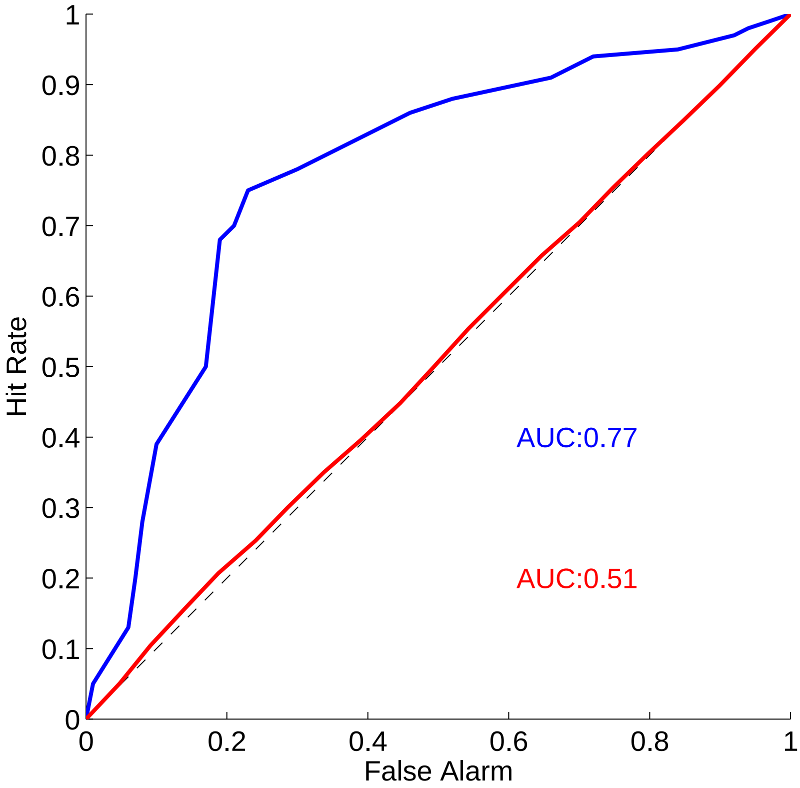

Figure 6.15 ROC curves of two hypothetical forecasts, the red curve is a forecast with no skill and blue curve represents a forecast with a good level of skill.

instruments on the radiosonde will allow the filtering out of observation forecast pairs where cloud was present to ensure all turbulence comparisons are made in clear air. The second, will use the meteorological information from the radiosonde to further retain days where jet streams were the dominant feature. The analysis performed here only looks at the selected grid point and does not include information from the surrounding grid points.

6.4.2 ROC Results

Figure 6.16 shows ROC curves for the 6 highest performing diagnostics when only clear air observation-forecast pairs were used. The highest performing diagnostic here is the wind speed, with an AUC of 0.675, this is likely due to the fact that the majority of clear-air turbulence detected is associated with the jet stream. $UDEF$ was the next most skilful forecast with an AUC of 0.653. Given that deformation proved to be a useful tool in understanding the evolution of turbulence in the case studies above, it is understandable how a combination of wind speed and deformation diagnostics performs well. The Ellrod T2 and T1 indices have AUCs of 0.628 and 0.619 respectively, and are both also based on deformation. The next best performing diagnostic was the relative vorticity advection,

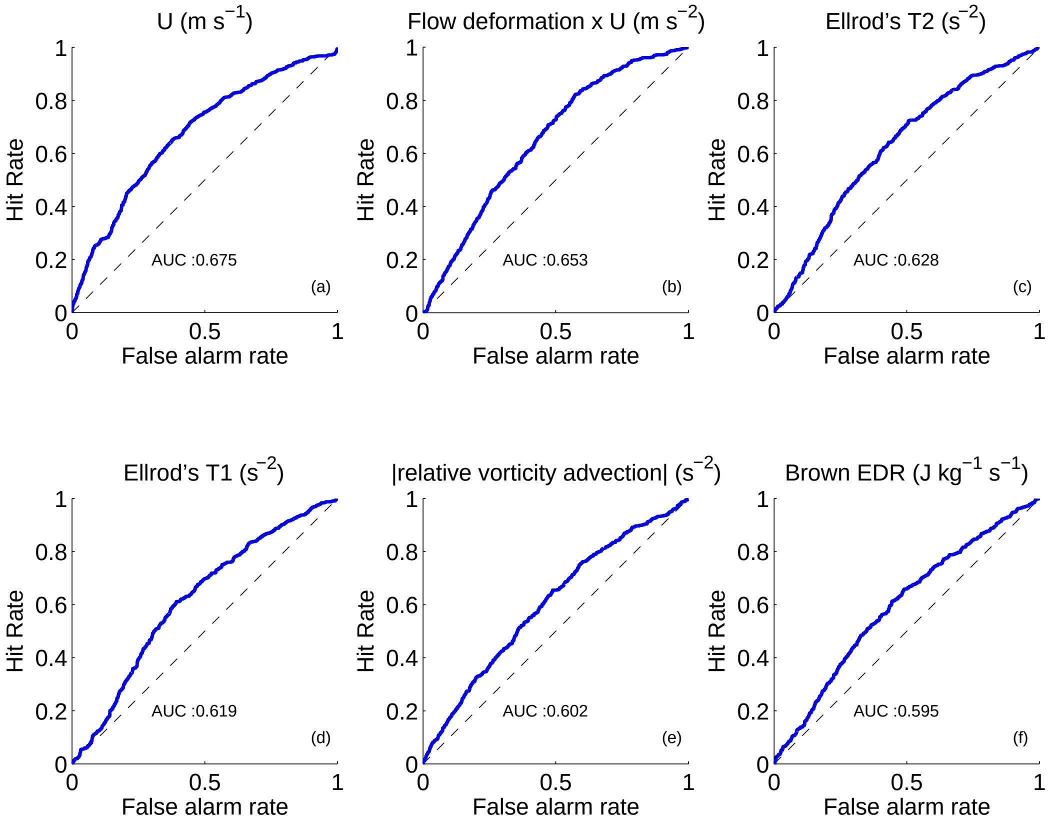

Figure 6.16 ROC curves for a) U, b) $UDEF$, c) Ellrod's T2, d) Ellrod's T1, e) RVA and f) ϵ_{brown} for observation - forecasts pairs in clear air.

with an AUC of 0.602 which, as discussed previously, is the leading term of the Lighthill Ford radiation term for turbulence. In one case study this was shown to be a potential cause of atmospheric turbulence, though it wasn't in the latter. This may explain why the skill wasn't as high as other diagnostics. The ϵ_{brown} diagnostic had an AUC of 0.595, and it is also deformation based. A full list of each turbulence diagnostic and its AUC is shown in column three of table 6.6. The majority of turbulence diagnostics had AUCs between 0.6 and 0.5. This is not a particularly high skill when compared to the AUCs of tuned turbulence forecast systems such as those of the GTG (Sharman et al., 2006) or ULTURB (McCann et al., 2012) with AUCs of approximately 0.85. The Colson Panofsky index, negative absolute vorticity advection and PV diagnostics showed no forecast skill. PV may have shown no skill as it increases in magnitude at the tropopause regardless of turbulence. A component of PV is the absolute vorticity which is also used in the negative absolute vorticity advection diagnostic, which may be an additional factor reducing the performance of the PV diagnostic. The Colson Panofsky index does not use absolute vorticity and still performs badly, so it is unlikely that the absolute vorticity is responsible for the poor skill of these diagnostics. The NCSU1 and the frontogenesis function had AUCs less than 0.5, indicating that if their thresholds were reversed they may provide a forecast with some level of skill.

The previous analysis discusses all clear-air observation-forecast pairs, whereas the next analysis considers clear-air observation-forecast pairs, but only on days where the jet stream was the dominant meteorological phenomenon. The 6 most skilful diagnostics are shown in figure 6.17. The two most skilful diagnostics remain U and $UDEF$, with their AUCs having increased to 0.732 and 0.668 respectively. The third most skilful diagnostic is the $-Ri$ which has an increased its AUC by 0.06. The increase could be due to the improved performance of the U_z diagnostic, which has an increased AUC to 0.613. The Ellrod T2 diagnostic is slightly less skilful than in the first experiment but not significantly. The Ellrod T1 is the 6th most skilful with an increased AUC to 0.621. The relative vorticity advection has an improved AUC by 0.02 and is the fifth most skilled diagnostic. The full list of results is found in column 4 of table 6.6. Some of the turbulence diagnostics discussed here increased by small margins, and so it is therefore useful to know if these are significant increases. Furthermore, for turbulent indices that have AUC close to 0.5 it is important to know if they are significantly different from 0.5. An AUC which is significantly less than 0.5 can be inverted, providing a forecast with some skill, but the forecast threshold needs to be inverted. For example, a turbulence diagnostic with an AUC of 0.4, with a threshold of $x > 5$, would then perform better at $x < 5$. To

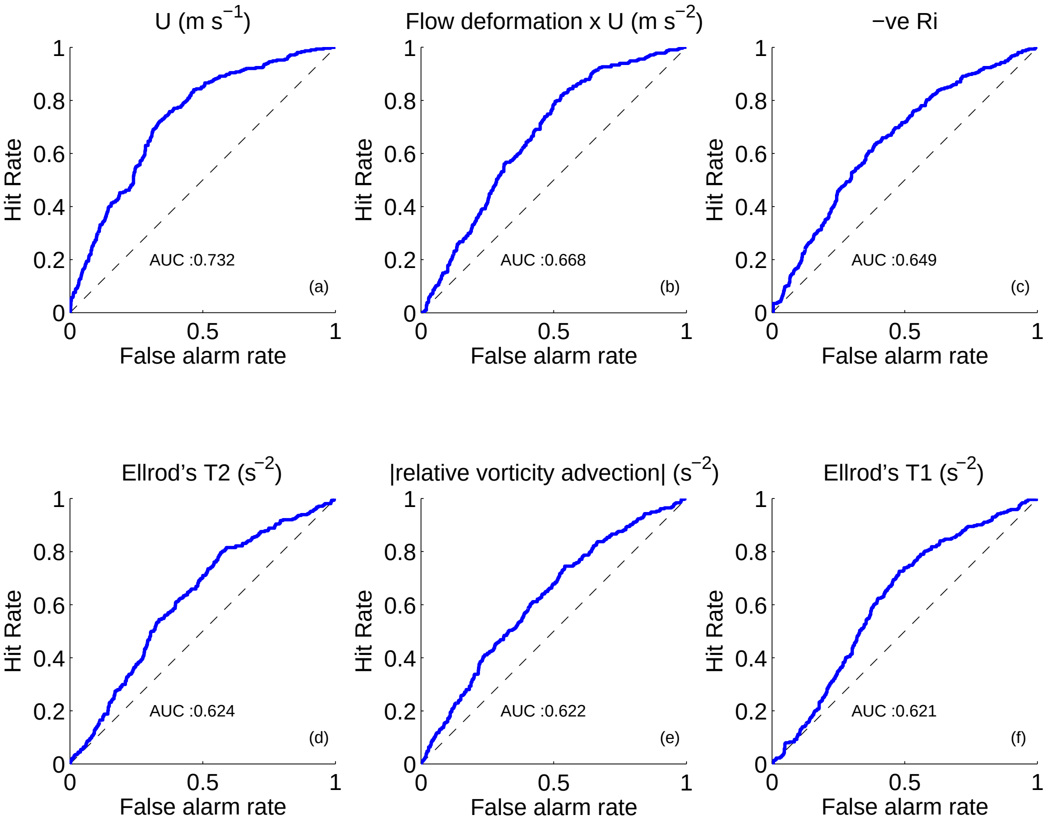

Figure 6.17 ROC curves for a) U, b) $UDEF$, c) $-Ri$, d) Ellrod's T2, e) RVA and f) Ellrods T1 for observation - forecasts pairs in clear air on jet stream days.

calculate confidence intervals on the ROC curves, boot strapping (Bertail et al., 2009) was undertaken to create 10 alternative ROC curves using randomly sampled observation forecast pairs from the existing dataset.

Table 6.6 shows the results of the ROC analyses ranked by the results of the second experiment. The majority of the 23 turbulence diagnostics statistically showed some level of skill for the second experiment, with the exception of the Brown index. PV, NCSU1 and the frontogenesis function. These have AUC significantly less than 0.5 meaning that if the thresholds were reversed they could provide some skill. Twelve of the turbulence diagnostics showed an increase in skill during the second experiment, with nine being significant increases. If the three diagnostics with AUCs less than 0.5 are removed, then 11 had decreases in skill with only two diagnostics showing a significant decrease in skill when the data was filtered further. For the filtered experiment, an optimal threshold was calculated by finding the threshold point closest to the point (1,0), which allows the best forecast threshold for significant turbulence to be known. In summary, if the turbulence diagnostics with an AUC greater than 0.6 are examined, the best turbulence diagnostics are U, $UDEF$, $-Ri$, Ellrod T2, RVA, Ellrod T1, U_z and ϵ_{brown}. Four of these diagnostics are deformation based, which is in agreement with findings in the case studies, with five

Diagnostic	Units	Exp. 1 AUC	Exp. 2 AUC	Optimal threshold
U	m s^{-1}	0.675±0.022	0.732±0.008	>35.2573
$UDEF$	m s^{-2}	0.653±0.021	0.668±0.016	> 0.0014
$-Ri$		0.592±0.016	0.649±0.021	>-5.245
$ET2$	s^{-2}	0.628±0.024	0.624±0.013	> 3.726e-07
$\|RVA\|$	s^{-2}	0.602±0.012	0.622±0.012	>9.8827e-09
$ET1$	s^{-2}	0.619±0.014	0.621±0.008	>3.012e-07
U_z	s^{-1}	0.583±0.019	0.613±0.006	> 0.0070
ϵ_{brown}	m^{2}s^{-3}	0.595±0.016	0.613±0.008	>1.5126e-10
DUT	s^{-2}	0.582±0.015	0.598±0.013	>22.0602
T_zDEF	K m^{-1} s^{-1}	0.585±0.028	0.580±0.008	>2.323e-07
$U\phi_z$	rad (s^{-1})	0.553±0.012	0.570±0.005	>1.549
$KX1$	s^{-2}	0.542±0.018	0.560±0.012	>1.6289e-08
$\|\nabla_H\|$	s^{-1}	0.545±0.026	0.546±0.018	>2.5539e-05
$CCAT$	s^{-3}	0.565±0.020	0.539±0.009	>7.0333e-09
DEF	s^{-1}	0.582±0.019	0.537±0.008	>5.2487e-05
CP	knot^2	0.510±0.020	0.531±0.007	>-162.2705
ξ^2	s^{-2}	0.572±0.029	0.526±0.013	>9.7652e-10
$\|\nabla_H T\|$	K m^{-1}	0.536±0.021	0.521±0.008	>1.3887e-05
$NAVA$	s^{-2}	0.517±0.017	0.513±0.006	> 4.0524e-09
Φ	s^{-1}	0.553±0.024	0.494±0.007	<8.2372e-05
$\|PV\|$	m^{2}s^{-1}K kg^{-1}	0.507±0.025	0.483±0.014	< 1.2152e-06
$NCSUI1$	s^{-3}	0.461±0.012	0.458±0.007	<7.336e-18
F	m^2 s^{-3} K^{-2}	0.446±0.018	0.431±0.015	<-1.8417e-06

Table 6.6 A table of all turbulence diagnostics showing the AUC with %95 confidence intervals for both clear air cases and for the filtered case studies, with the diagnostics being ranked in descending order of skill. An optimal threshold for turbulence is given in the last column.

of these diagnostics also using the vertical wind shear. In conclusion, the wind speed is the best diagnostic for predicting turbulence. The diagnostics which are the most skilful when looking at turbulence around jet streams are those that use deformation or wind shear or a combination of both. The relative vorticity advection also performed well. Sharman et al. (2006) found the frontogenesis function, NCSU1 and the Ellrod T1 to be the most skilful, with U and $UDEF$ also being shown to be skilful. However this is different from the results shown here, the reasons for which are likely to be as follows. Firstly, the analysis performed by Sharman et al. (2006) was made using aircraft with the majority of observations being made at cruising altitudes, which may incur a bias towards turbulence observations being made over a narrow vertical range of the atmosphere. This is different to the analysis performed here which was equally distributed over the majority of the troposphere's vertical depth. Secondly, the geographical location may have some effect. Kim et al. (2011) undertook a similar analysis over south east Asia and found that the Colson Panofsky index, negative Richardson number and Ellrod's T1 performed best, which is different to Sharman et al. (2006). Gill (2014) only looked at the Ellrod T1 and Dutton index globally and found the AUC varied from 0.5 to 0.78 dependent on latitude. This implies there may be some geographical dependence on a turbulence index skill so the results shown here may only be applicable to northern Europe. Such variability with geographic location may be due to climatological positions of jet streams, or potentially due to significant orography upstream of a particular region. Finally, weather balloons and planes do respond to turbulence on different length scales. This may explain why the diagnostics skill is not as high, the diagnostics used here have been formulated using aircraft observations, which are affected by larger length scale turbulence.

6.5 Conclusions

In this chapter a method to select an appropriate model of the atmosphere which can represent the conditions when turbulence sondes were launched has been discussed. Using the ECMWF global deterministic model to calculate turbulence diagnostics allowed the temporal evolution of turbulence to be investigated. It was found that deformation based diagnostics were able to reproduce the evolution of turbulence in both case studies. In the first case study, relative vorticity advection was also shown to be sporadic enough to cause a temporal evolution of turbulence. In the second part of this chapter two comparisons between the accelerometer observations and turbulent diagnostics were carried out. One using just clear-air measurements and a second using clear-air measurements on days where a jet stream was present. For the first comparison U was found to be the best turbulence diagnostic. For the second comparison nine turbulence diagnostics were shown to significantly increase in skill, showing that filtering of the diagnostics is needed to ensure that they are forecasting turbulence in conditions they are optimised for. The best turbulence diagnostics based on the second experiment were found to be: U, $UDEF$, $-Ri$, Ellrod T2, RVA, Ellrod T1, U_z and ϵ_{brown}. Many of these diagnostics use a combination of deformation and vertical wind shear. There is much application for this section of work as the findings can be used to improve aviation forecasts. There are also possibilities of using the model to impart more information about whether more intense turbulence measurements are made into the flanking or receding parts of a jet stream. Furthermore the comparison was undertaken on a point to point basis, which does not take into account any adjacent grid squares which may be predicting turbulence, a future comparison could take these into account.

Chapter 7

Conclusions and recommendations for future work

In this chapter the main findings for each thesis objective described in chapter 1 are first summarised. For each section the findings are discussed further in terms of limitations, implications for the scientific community and suggestions for further improvement, or new lines of investigation.

7.1 Thesis objectives and findings

The main findings for each objective are:

(a) To further develop a balloon borne turbulence sensor that can be used to make standardised measurements of atmospheric turbulence

- Chapter 3 described a magnetometer device used in Harrison and Hogan (2006) and Harrison et al. (2009) which measured the swing of the radiosonde as the balloon encountered turbulence. Although it had been demonstrated to make observations of turbulence, it was unsuitable for generating a large dataset of standardised turbulence measurements as it was not quantitative enough. This was due to each magnetometer device having inconsistent sensitivities, caused by the radiosonde's transmitter and being vulnerable to thermal drifts. Furthermore an oscillatory effect, present when using a shorter string for higher sensitivity and safety, causes difficulty in interpreting the magnetometer results.

- To improve on the problems encountered with the magnetometer, an accelerometer was successfully used to measure the swing of the radiosonde beneath the balloon in turbulence (Marlton et al., 2015). The main advantages being: the accelerometer is unaffected by the radiosonde transmitter, it has a high level of reproducibility between devices and provides an output voltage proportional to units of acceleration. The accelerometer detects the oscillation on the shorter string, but by taking the standard deviation, σ_z, the effects of the oscillation are removed. The accelerometer device was combined with a solar radiation sensor providing additional information to detect if the accelerometer sonde was in cloud.

- A theoretical model to represent the balloon rising through a turbulent atmosphere was also implemented. It used balloon size estimates, a synthetic wind field from a sonic anemometer and two coupled 2D pendulum equations. It produced similar results to those obtained from the test flights.

(b) Compare turbulence measurements from the accelerometer sonde against those from remote sensing techniques.

- A relationship between the standard deviation of the accelerometer and the lidar derived eddy dissipation rate was found. The accelerometer sonde's σ_z was compared over a range of ϵ of 10^{-3} to 10^{-2} m^2s^{-3}. Due to the small co-location error, as the comparisons were made in the first 1 km of the atmosphere, there is high confidence in this calibration.

- Comparisons were made between the accelerometer sonde and a zenith pointing Ka-band radar. Unfortunately due to the intensity of the clouds sampled, a reliable relationship could not be made as the falling droplets dominated the velocity spectra, yielding very small ϵ estimates. This was verified using a dual band radar technique to estimate the droplet size.

- A final comparison was made with the NERC MST wind profiler at Aberystwyth where the σ_z was compared with the radar's spectral width. A relationship between the two quantities was found, indicating turbulence detected by the accelerometer sonde in the free troposphere is also observed by another instrument. However the ϵ could not be reliably calculated from the radar's spectral width.

(c) Analyse observations of the turbulent structure of the atmosphere in different meteorological conditions.

- By carrying out a statistical analysis of all the data and considering the findings made in chapter 4 it was found that $\sigma_z > 5\text{m s}^{-2}$ was indicative of significant turbulence.

- Using the meteorological data from the radiosonde it was possible to attribute sections of the atmosphere to different meteorological conditions that are likely to cause turbulence. From the 51 accelerometer ascents in the dataset, the meteorological data from the radiosonde was used to attribute 77% of the incidents where $\sigma_z > 5\text{m s}^{-2}$ were caused by jet streams, convection or being in or near cloud. σ_z data from jet streams was found to be the most turbulent, followed by in-cloud, near cloud and convective turbulence.

- 50% of turbulence in jet streams could be attributed to either low thermal stability or high wind shear. However, having either of these two quantities did not always mean turbulence would be present. When looking at 3-4 accelerometer sonde profiles made over a period of 6 hours, turbulence evolved temporally. In one such case a tropopause fold could have caused the evolution in turbulence intensity. In the other IOP the radiosonde's meteorological data was unable to explain the temporal evolution of turbulence. Hence turbulence may be caused by a process not directly observable by the radiosonde.

- For ascents with a positive CAPE present, a CAPE > 150 J kg^{-1} was found to produce more intense turbulence within the positive CAPE region. Furthermore, turbulence was more intense near the environmental layer, where rising air displaces stable air.

- Deeper clouds were found to be more turbulent than shallow clouds. This is due to deeper clouds having more internal mechanisms which can produce turbulence. In convective clouds, turbulence was found near the cloud top as rising air destabilises air close to the top. In frontal clouds turbulence is present across the depth of the cloud. The likely reason for this is that frontal clouds have more in-cloud and frontal processes than in just convective clouds. However, it was difficult to infer whether convective clouds were more intensely turbulent than frontal clouds.

- A mountain wave was also observed in one ascent from the accelerometer dataset.

Turbulence was encountered at the tropopause which is likely a critical level for the mountain wave. In the critical region turbulence values of σ_z=10 m s^{-2} were observed, which is indicative of moderate turbulence, given the findings in chapter 4 and the statistical analysis in chapter 5.

(d) Use the accelerometer dataset to compare turbulence diagnostics from a numerical model.

- The ECMWF global deterministic model was selected as the numerical model to best represent the atmosphere for calculating turbulence diagnostics for each radiosonde launch time. By using turbulence diagnostics derived from this data, it was possible to explain the temporal evolution of turbulence during the IOPs in chapter 5. Increasing regions of deformation based diagnostics provided the best indicators of the temporal evolution of turbulence.
- By filtering all the radiosonde turbulence data to remove in-cloud turbulence, each CAT diagnostic could be compared against the accelerometer observations. The wind speed magnitude, deformation based diagnostics, and relative vorticity advection were found to produce the best predictors of turbulence in clear air.
- The data was further filtered to only include days where jet streams were present, so as to remove the affects of convection. This improved the skill of several diagnostics to yield that U, $U \times DEF$, the Richardson number, the two Ellrod indices, and relative vorticity advection were the best predictors for clear air turbulence in the presence of a jet stream.

7.2 A method to detect atmospheric turbulence with a radiosonde

Earlier research shows that balloons can be used as a platform to make observations of turbulence, but, until now, the potential of the technique had not been fulfilled. One of the aims of this project was to build up a large database of standardised turbulence measurements to allow comparison with other turbulence observations and predictors. The magnetometer lacked ascent-to-ascent reproducibility and was affected by the radio transmitter and the radiosonde's oscillation due to string length. This project started using the magnetometer due to the development made 10 years previously when Harrison and Hogan (2006) first flew motion sensors on a balloon. When designing disposable equipment for radiosondes, keeping the cost of the sensor package low is important. As only a small quantity of sensors were required for the work in Harrison and Hogan (2006), non-surface mount components were used. At the time a none surface mount accelerometer would have cost £ 15. The cost of the magnetometer and associated components were originally substantially cheaper. Furthermore, there were further concerns about the sensitivity and durability of the accelerometer in flight. In recent years the price of accelerometer technology has dropped five fold. Combined with the outsourcing of the manufacture of printed circuit boards in larger quantities, this has allowed accelerometers to be used at the cost of £1 each, making them not only technically superior as explained, but more financially viable.

The implication for the scientific community is that an inexpensive disposable turbulence sensor can be flown on widespread standard operational radiosondes or during research flights. For this to be implemented, two things would require further exploration, which are the effects of the balloon-radiosonde configuration on the accelerometer response and interfacing the accelerometer for use with other radiosonde manufacturers. This project uses a 4 m string length attached to a 200 g balloon. Different meteorological organisations use different size balloons, and different radiosonde manufacturers employ different string lengths (Luers and Eskridge, 1998). As discussed the string length can affect how the motion sensing package beneath responds to turbulence. If, for example, a meteorology agency wished to use the accelerometer on their balloon configuration, a calibration experiment would be required between the current configuration and the desired one. This could be achieved with simultaneous flights of the two configurations. Accelerometer data from both ascents could be compared to find a relationship so that the new configuration can relate further findings to the findings of this project.

Secondly the next generation of radiosondes are replacing their predecessors, for example the Vaisala RS41 model is set to become the new workhorse radiosonde of many meteorological organisations. The RS41 includes a new interface, designed to allow easier addition of custom sensors for relaying sensor data to the ground station. This has been partly a result of the University of Reading's collaborations with Vaisala. The new radiosondes also utilise the latest technology to run from lower voltage power supplies, meaning that some of the sensors described here will require upgrading to run from lower voltage power supplies. International research groups have expressed interest in the accelerometer so these steps will ultimately be undertaken in the future. To meet these needs a commercialisation project may be needed.

7.3 Accelerometer comparisons with turbulence remote sensing methods

The accelerometer device was compared against three different remote sensing techniques with differing levels of success. The lidar comparison was successful in demonstrating that the variability of the accelerometer could be compared with ϵ derived from a Doppler lidar. The main disadvantage was that the comparison was made mostly in the boundary layer. As has been shown, the larger values of σ_z are observed in the mid troposphere and it is unknown whether the lidar-accelerometer relationship would hold if extrapolated.

One method to make turbulence comparisons in the mid troposphere was to compare the accelerometer against a Ka-band Doppler cloud radar. However, the technique used was not appropriate for observing turbulence in intense clouds as the fall of the droplets dominated the turbulent spectra. An alternative method would have been to use the Ka-band scanning radar to make observations of turbulence using the method shown in Meischner et al. (2001). In this method the effects of droplet fall speed and wind shears across the pulse volume are taken into account. The problem using this method is ensuring that the radar scans the same piece of cloud that the radiosonde traverses. Future work would try to make use of the existing available scanning radar measurements made at the Hyytiala ARM site during the campaign there. Alternatively a new project could seek to launch radiosondes in the vicinity of scanning radar.

Finally the comparison with the MST radar showed that the accelerometer and the MST radar's spectral width did both respond to turbulence, however ϵ could not be reliably inferred from the radar data. Both, the Brunt-Vaisala and Labitt methods appear empirical at attempting to represent turbulence within the pulse volume. Further work needs to be undertaken by the MST radar user community to reliably infer ϵ from the spectral width. It is possible that the accelerometer sonde may play a role in this development, as it is one of the first campaigns where intense in-situ observations were undertaken spanning the majority of the radar's operating range.

The implication of the remote sensing findings in this section is that it adds a further level of credibility to the turbulence observations made by the accelerometer. The comparisons between remote sensing methods of turbulence detection and accelerometer measurements go some way towards calibrating the accelerometer observed turbulence. One method of turbulence observation that the accelerometer sonde has not been compared against is that of aircraft measurements. This could be achieved by comparing existing measurements of turbulence with nearby aircraft measurements or pilot reports. Finally an ideal situation would be to launch balloons in close proximity to a suite of wind profilers, cloud radars and lidars, within close proximity of a major flight lane. This would mean that multiple turbulence observations of the same air space could be made, so that for example, biases in turbulence observations may be identified.

7.4 Investigating meteorological sources of turbulence

In chapter 5 an analysis of the accelerometer sonde turbulence dataset as a whole is undertaken, and a statistical threshold value of $\sigma_z > 5\text{m s}^{-2}$ was set as a significant turbulence threshold. From the 51 accelerometer ascents in the dataset, the meteorological data from the radiosonde was used to classify that 77% of the significant turbulence data was attributed to one of either jet streams, convection or being in or near cloud. The analysis managed to subset the majority of observed turbulence into these categories, but it would not be complete without a discussion of the 23% of unclassified significant turbulence events. It can be said that throughout the duration of the project most types of turbulence have been sampled, however as the measurement campaigns were not targeted at turbulence from one particular source, it is difficult to make any meteorological deductions across the dataset as a whole, e.g. does a larger wind shear yield more turbulence? This is a simple example of the difficulties in categorising such a dataset. Whilst regions of cloud and convection were simpler to identify, jet streams were more difficult. This is due to the variability in the structure of the wind profiles, which can add some ambiguity to the jet detection algorithm. One could slacken the criteria but then run the risk of categorising regions of the turbulence incorrectly.

Furthermore there are identified regions of turbulence that have not been categorised possibly due to turbulence caused by a gravity wave from an unknown source, such as distant convective thunderstorms, or orography. Alternatively the turbulence being observed may be a residual from an atmospheric event that took place before the radiosonde ascent and has dissipated. An example of this is the second convective case study ascent at Hyytiala on 8th August 2014 shown in figure 5.26. Had the previous ascent not occurred, then there would have been no knowledge of the convection that led to the generation of the turbulence observed.

The implications of this data set are that these accelerometer radiosondes can be launched into most meteorological conditions and are able to produce useful observations of the vertical structure of atmospheric turbulence. The sub-setting of data shows how through some filtering, one can focus on particular meteorological conditions. For example it was found that in regions of strong CAPE more intense turbulence was observed. This finding could be used to design a turbulence diagnostic which forecasts turbulence near the environmental layer during the presence of significant CAPE. It is clear that the legacy of this dataset can continue through more investigations focussing on turbulence produced by a particular mechanism. It also demonstrates how further field use of these accelerometer radiosondes can be used as a tool when investigating a particular turbulence mechanism. Further lines of enquiry with this dataset could include:

- An investigation of the effectiveness of the Thorpe analysis by examining detected turbulent overturns with observed regions of turbulence.
- Investigating whether an approaching flank of a jet stream has different turbulent properties to that of the receding flank of a jet stream?
- Could information about cloud structures from cloud radars be used to explain more of the turbulence found within clouds?
- Could one attribute unclassified regions of turbulence to turbulent sources using ray tracing techniques such as those used in Marks and Eckermann (1995)

7.5 Comparing the accelerometer to model predictions of turbulence

Standard meteorological data from radiosondes was compared against the standard model outputs to select an atmospheric model which best represented the atmosphere. This shows how a data set of radiosondes independent of the data assimilation systems can be used to verify how good an atmospheric model is at representing the atmosphere.

Turbulence diagnostics were calculated for the time of launch for all the radiosondes. By qualitatively examining the evolution of turbulence diagnostics across a pressure surface, as opposed to the vertical, provides a new dimension to the analysis of the radiosonde data during IOPs. For the two case studies examined, deformation based diagnostics explained the temporal evolution of turbulence observed. There is much potential to further classify the turbulence data by synoptic situations as depicted by the models, for example to help investigations of intensifying or receding jet streams.

Wind speed, wind shear, deformation based, and relative vorticity advection diagnostics were found to the best predictors of turbulence. The analysis here used a point by point verification. Often spatial verification is undertaken, including averaging in a temporal and spatial sense. Hence, if turbulence diagnostics are incorrect by one grid square, the forecast is still acknowledged for some level of skill.

The broader implications of this work are that accelerometer sondes have been clearly demonstrated to measure turbulence, their use can have social and economic impacts by yielding information about the skill of turbulence diagnostics, and an increased knowledge of the turbulent structure of our atmosphere.

Appendices

Appendix A

Gaussian confluent hyper geometric function

The confluent hyper-geometric function mathematically represents the velocity perturbations due to turbulence with in the pulse volume (Labitt, 1981) and (Hocking, 1999). The confluent geometric function χ can be computed as a sum of an infinite series (Weisstein, 2002) and is given by

$$\chi(p, q; r, s) = \sum_{n=0}^{\infty} \frac{(p)_n (q)_n}{(r)_n} \frac{s^n}{n!} \tag{A.1}$$

where p,q,r and s are real values. χ converges if $r \geq 0$ and that for all values $|s| \leq 1$ and $r - p - q > 0$. $(p)_n$,$(q)_n$ and $(r)_n$ are increasing factorials which can be calculated using the Gamma functions Γ

$$(p)_n = \frac{\Gamma(p+n)}{\Gamma(p)}. \tag{A.2}$$

for example. For use in making estimations of ϵ, then the coefficients of χ are given as follows, with M equal to the half radar beam width in meters and $Q = 75$ m equal to half the MST radars vertical pulse length. If $M > Q$

$$F = \chi\left(-\frac{1}{3}, \frac{1}{2}; \frac{5}{2}; 1 - \frac{Q^2}{M^2}\right), \tag{A.3}$$

else if $Q > M$ then

$$F = \chi\left(-\frac{1}{3}, 2; \frac{5}{2}; 1 - \frac{M^2}{Q^2}.\right), \tag{A.4}$$

Having both forms of this equation is important as the beam width M increases as a function of height. Values for equations are taken from Hocking (1999).

Appendix B

Turbulence diagnostics discretisation

This appendix describes how each turbulence diagnostic listed in 6.3 is calculated along pressure surfaces of the global deterministic model. The Appendix is structured so simpler diagnostics are introduced first which can then be used in more complex diagnostics. First the method to calculate the numerical horizontal gradients in the x and y directions is shown as follows.

$$a_x = \frac{a_{i+1,j} - a_{i-1,j}}{2\Delta x}, \tag{B.1}$$

$$a_y = \frac{a_{i,j+1} - a_{i,j-1}}{2\Delta y}, \tag{B.2}$$

where a is a variable such as the wind component or temperature across the pressure surface, a_x is the horizontal gradient of a in the x (longitudinal) direction, and a_y is the horizontal gradient of a in the y (latitudinal) direction. i and j are the index of the variable a on the gridded pressure surface and, Δx and Δy are the horizontal resolution of the model which is approximately 28 km.

Magnitude of vertical wind shear, U_z (s^{-1}).

The magnitude of vertical wind shear U_z has been used by many investigators (Sharman et al., 2006), (Williams and Joshi, 2013), it is given by

$$U_z = \left(\left(\frac{\Delta u}{\Delta Z} \right)^2 + \left(\frac{\Delta v}{\Delta Z} \right)^2 \right)^{0.5}, \tag{B.3}$$

where $\Delta u = u_{k+1} - u_{k-1}$, $\Delta v = v_{k+1} - v_{k-1}$ and $\Delta Z = Z_{k+1} - Z_{k-1}$. Where the subscript denotes the pressure level k, u and v are the zonal and meridional wind components and Z is the geopotential height on the pressure surface.

Negative Richardson number, $-Ri$.

The Richardson number was proposed by Richardson (1920). Sharman et al. (2006) proposed multiplying the Richardson number by -1 to provide a diagnostic which increases with turbulence intensity, the $-Ri$ number is calculated using

$$-Ri = -\frac{\frac{g}{T_k}\frac{\Delta\theta}{\Delta Z}}{\left(U_z\right)^2}, \tag{B.4}$$

where T_k is the temperature on the pressure surface, $\Delta\theta = \theta_{k+1} - \theta_{k-1}$ and g is the acceleration due to gravity 9.81 m s^{-2}.

Colson-Panofsky index, CP (kt^2).

The Colson-Panofsky, CP, index is given in Colson and Panofsky (1965) and is calculated using

$$CP = 3.77\left(\frac{\Delta Z}{2}\right)^2 U_z \left(1 - \frac{Ri}{0.5}\right). \tag{B.5}$$

Frontogenesis function, F (m^2 s^{-3} K^{-2}).

The Frontogenesis function is given by

$$F = \frac{D|\nabla\theta|}{Dt}, \tag{B.6}$$

which Sharman et al. (2006) showed could be written using the thermal wind relationship as

$$F = \frac{D}{Dt}\left[\left(\frac{\partial u}{\partial\theta}\right)^2 + \left(\frac{\partial v}{\partial\theta}\right)^2\right]. \tag{B.7}$$

Sharman et al. (2011) then showed that by expansion, manipulation and removal of small terms F can be calculated using

$$F = \frac{\Delta u}{\Delta\theta}\left(\frac{\Delta u}{\Delta\theta}u_x + \frac{\Delta v}{\Delta\theta}u_y\right) + \frac{\Delta v}{\Delta\theta}\left(\frac{\Delta u}{\Delta\theta}v_x + \frac{\Delta v}{\Delta\theta}v_y\right), \tag{B.8}$$

where u_x, u_y, v_x and v_y are the horizontal numerical gradients of the wind components.

Flow Deformation, DEF ($\mathbf{s^{-1}}$).

The flow deformation is the magnitude of the shearing and stretching terms and is given in Ellrod and Knapp (1992) by

$$DEF = \left((v_x + u_y)^2 + (u_x - v_y)^2\right)^{0.5}. \tag{B.9}$$

Relative vorticity squared, ξ^2 ($\mathbf{s^{-2}}$).

Relative vorticity is given in Sharman et al. (2006) by

$$\xi^2 = (v_x - u_y)^2. \tag{B.10}$$

Brown index, Φ ($\mathbf{s^{-1}}$), and Brown eddy dissipation rate, ϵ_{brown} ($\mathbf{m^2s^{-3}}$).

The Brown index, Φ is given in Brown (1973) which combines ξ through absolute vorticity ζ, and DEF to give

$$\Phi = \left(0.3\zeta^2 + DEF^2\right)^{0.5}, \tag{B.11}$$

where $\zeta = \xi + f$. f is the Coriolis parameter and is calculated using

$$f = 2\Omega \sin(lat), \tag{B.12}$$

where Ω is the angular speed of the Earth's rotation given by $2\pi/86400$ s^{-1} and lat is the latitude in degrees. Following this the Brown eddy dissipation rate, ϵ_{brown} is given in Brown (1973) by

$$\epsilon_{brown} = \frac{\Phi}{24} U_z^2. \tag{B.13}$$

Horizontal divergence, ∇_H ($\mathbf{s^{-1}}$).

The horizontal divergence ∇_H is given in Ellrod and Knapp (1992) by

$$\nabla_H = u_x + v_y. \tag{B.14}$$

Ellrod turbulence indices, $ET1$ (s^{-2}) and, $ET2$ (s^{-2}).

The Ellrod T1 index is given in Ellrod and Knapp (1992) by

$$ET1 = U_z DEF, \tag{B.15}$$

and the Ellrod T2 index is given in Ellrod and Knapp (1992) as

$$ET2 = U_z(DEF - \nabla_H). \tag{B.16}$$

Potential Vorticity, PV (m^{2}s^{-1}K kg^{-1}).

Potential vorticity was used a turbulence diagnostic by Sharman et al. (2006) and is calculated by

$$PV = |\zeta g \frac{\Delta\theta}{\Delta P}|, \tag{B.17}$$

Where $\Delta P = P_{k+1} - P_{k-1}$ where k denotes the pressure level.

Magnitude of horizontal temperature gradient, $|\nabla T|$ (K m^{-1}).

The horizontal temperature gradient was used by Audrey et al. (2011) and is given by

$$|\nabla T| = \left(T_x^2 + T_y^2\right)^{0.5}. \tag{B.18}$$

Wind speed, U (m s^{-1}).

The magnitude of the horizontal wind speed is given by

$$U = (u^2 + v^2)^{0.5}. \tag{B.19}$$

Wind speed times directional shear, $U\phi_z$ (rad s^{-1}).

The wind speed times directional shear is used by Williams and Joshi (2013) and is calculated by transferring the wind components at each pressure level into a complex number of the form $u + iv$ thus

$$U\phi_z = U_{(k)} arg\left(\frac{u_{k+1} + iv_{k+1}}{u_{k-1} + iv_{k-1}}\right), \tag{B.20}$$

where i is the $\sqrt{-1}$.

Flow deformation times wind speed, $UDEF$ (m s^{-2}).

The flow deformation times wind speed is given in Reap (1996) by

$$UDEF = U \times DEF. \tag{B.21}$$

Flow deformation times vertical temperature gradient, T_zDEF (K m^{-1}s^{-1}).

The flow deformation times the vertical temperature gradient is given in Reap (1996) by

$$T_zDEF = DEF|\frac{\Delta T}{\Delta Z}| \tag{B.22}$$

where $\Delta T = T_{k+1} - T_{k-1}$.

North Carolina State University index 1, $NCUS1$ (s^{-3}).

This diagnostic was originally formulated in Kaplan et al. (2006), but the formulation shown here is that of Sharman et al. (2006) given by

$$NCSU1 = \frac{1}{\max(Ri, 10^{-5})} \max\left(uu_x + vv_y, 0\right) \left(\xi_x^2 + \xi_y^2\right)^{0.5}, \tag{B.23}$$

where ξ_x and ξ_y are the numerical gradient of ξ in the x and y directions respectively.

Negative absolute vorticity advection, $NAVA$ (s^{-2})

The negative absolute vorticity equation is given in Sharman et al. (2006) by

$$NAVA = \max\left(u\zeta_x - v\zeta_y, 0\right), \tag{B.24}$$

where ζ_x and ζ_y are the numerical gradients of ζ in the x and y directions respectively.

Relative vorticity advection, RVA (s^{-2}).

The relative vorticity advection is given as the leading order term in the Lighthill Ford radiation scheme shown in Knox et al. (2008) by

$$RVA = u\zeta_x + v\zeta_y. \tag{B.25}$$

Knox 1997 diagnostic, $KX1$ (s^{-2}).

The turbulence diagnostic used by Knox (1997) is implemented using

$$KX1 = f\left(f\left(1 - \frac{1}{Ri}\right) + \xi\right). \tag{B.26}$$

Clarks CAT algorithm, $CCAT$ (s^{-3}).

The Clark's CAT algorithm is described in Vogel and Sampson (1996) and is given by

$$CCAT = \left|\frac{g}{T_k}\frac{\zeta}{f}\left(U\left(\left(\frac{\Delta T}{\Delta Z}\right)_x + \left(\frac{\Delta T}{\Delta Z}\right)_y\right)\right)\right|, \tag{B.27}$$

where $(\Delta T/\Delta Z)_x$ and $(\Delta T/\Delta Z)_y$ are the horizontal gradients of the vertical temperature gradient in the x and y directions respectively

Dutton's empirical index, DUT (s^{-2}).

Duttons empirical index is given in Dutton (1980) by

$$DUT = 1.25\left(\frac{\Delta U}{\Delta X}10^5\right) + 0.25\left(1000U_z\right)^2 + 10.5, \tag{B.28}$$

where

$$\frac{\Delta U}{\Delta X} = \frac{\left(uvu_x - u^2u_y + v^2v_x - uvu_y\right)}{U^2}. \tag{B.29}$$

Appendix C

Sensor calibration co-effcients

This appendix explains shows the coefficients applied to the PANDORA voltage channels to get a) accelerometer values in (g) for each axis, and b) derive the solar radiation from the photodiode voltage. Firstly the voltage counts need converting to mV using

$$V = \frac{V_c}{65536} \times 5000 \tag{C.1}$$

where V_c is the digital voltage count from the PANDORA system and V is the sensor output voltage in mV.

a)Accelerometer coefficients

The accelerations in g for each accelerometer axis X,Y and Z can be calculated using

$$X_{acc} = \frac{V_{xa} - 1683}{185}, \tag{C.2}$$

$$Y_{acc} = \frac{V_{ya} - 1643}{193}, \tag{C.3}$$

$$Z_{acc} = \frac{V_{za} - 1674}{-190}, \tag{C.4}$$

where V_{xa}, V_{ya} and Z_{za} are the logged voltages in mV from each axis of the accelerometer.

b)Solar radiation sensor coefficients

To calculate the solar radiation from the photodiode voltage, one must first convert it to current generated by the diode, given by

$$i_{pd} = \frac{(2 \times V_{pd}) - 1.2}{8200}, \tag{C.5}$$

Then the solar radiation can be calculated using the calibration used in Nicoll and Harrison (2012) to get SR, the solar radiation in W m^2, which is

$$SR = 1681588 \times i_{pd} - 6.346. \tag{C.6}$$

REFERENCES

Ambaum, M.H.P. *Thermal physics of the atmosphere*, volume 1. John Wiley & Sons, 2010.

Analog Devices. *Small low power, 3 axis , ± 5g Accelerometer*, 2009. Rev.0.

Anderson, A.D. Free-air turbulence. *Journal of Meteorology*, 14(6):477–494, 1957.

Asselin, R. Frequency filter for time integrations. *Monthly Weather Review*, 100(6): 487–490, 1972.

Audrey, C., Christine, L., Yves, B., and Francois, B. Aeronautical diagnostics for Clear-Air Turbulence forecast at Meteofrance in the context of DELICAT European project. In *Journal of Physics: Conference Series*, volume 318, page 072007. IOP Publishing, 2011.

Axford, D.N. On the accuracy of wind measurements using an inertial platform in an aircraft, and an example of a measurement of the vertical mesostructure of the atmosphere. *Journal of Applied Meteorology*, 7(4):645–666, 1968.

Banakh, V.A., Smalikho, I.N., Köpp, F., and Werner, C. Measurements of turbulent energy dissipation rate with a CW Doppler lidar in the atmospheric boundary layer. *Journal of Atmospheric and Oceanic Technology*, 16(8):1044–1061, 1999.

BBC Archive. 1966: Passenger jet crashes into mount fuji, 1966. URL `http://news.bbc.co.uk/onthisday/hi/dates/stories/march/5/newsid_2515000/2515321.stm`.

Bertail, P., Clémençcon, S.J., and Vayatis, N. On bootstrapping the ROC curve. In *Advances in Neural Information Processing Systems*, pages 137–144, 2009.

Bond, N.A. and Shapiro, M.A. Research aircraft observations of the mesoscale and microscale structure of a cold front over the eastern pacific ocean. *Monthly weather review*, 119(12):3080–3094, 1991.

Bouniol, D., Illingworth, A.J., and Hogan, R.J. Deriving turbulent kinetic energy dissipation rate within clouds using ground based radar. In *Proceedings of ERAD*, volume 281, 2004.

Brown, B.G., Thompson, G., Bruintjes, R.T., Bullock, R., and Kane, T. Intercomparison of in-flight icing algorithms. Part II: Statistical verification results. *Weather and Forecasting*, 12(4):890–914, 1997.

Brown, E.N., Friehe, C.A., and Lenschow, D.H. The use of pressure fluctuations on the nose of an aircraft for measuring air motion. *Journal of Climate and Applied Meteorology*, 22(1):171–180, 1983.

Brown, R. New indices to locate clear-air turbulence. *Meteorology Magazine*, 102:347–361, 1973.

Browning, K.A. Structure of the atmosphere in the vicinity of large-amplitude Kelvin-Helmholtz billows. *Quarterly Journal of the Royal Meteorological Society*, 97(413): 283–299, 1971.

Campistron, B., Bernard, S., Bénech, B., Ardhuin-Girard, F., Dessens, J., Dupont, E., and Carissimo, B. Turbulent dissipation rate in the boundary layer via UHF wind profiler Doppler spectral width measurements. *Boundary-layer meteorology*, 103(3): 361–389, 2002.

Chapman, M. Weather balloon physics, 2012. URL `http://www.zmatt.net/weather-balloon-physics/`.

Clayson, C.A. and Kantha, L. On turbulence and mixing in the free atmosphere inferred from high-resolution soundings. *Journal of Atmospheric and Oceanic Technology*, 25 (6):833–852, 2008.

CNN News. American airlines flight diverted, 2016. URL `http://edition.cnn.com/2016/01/24/us/american-airlines-flight-turbulence-diverted/`.

Colson, D. and Panofsky, H.A. An index of clear air turbulence. *Quarterly Journal of the Royal Meteorological Society*, 91(390):507–513, 1965.

Compo, G.P., Whitaker, J.S., Sardeshmukh, P.D., Matsui, N., Allan, R.J., Yin, X., Gleason, B.E., Vose, R.S., Rutledge, G., Bessemoulin, P., et al. The twentieth century reanalysis project. *Quarterly Journal of the Royal Meteorological Society*, 137(654): 1–28, 2011.

Cornman, L.B., Morse, C.S., and Cunning, G. Real-time estimation of atmospheric turbulence severity from in-situ aircraft measurements. *Journal of Aircraft*, 32(1):171–177, 1995.

Counihan, J., Hunt, J.C.R., and Jackson, P.S. Wakes behind two-dimensional surface obstacles in turbulent boundary layers. *Journal of Fluid Mechanics*, 64(03):529–564, 1974.

Curran, J.K. Comparative turbulence for a Canberra and a Vulcan flying together at low altitude. *Aeronautical Research Council Current Papers*, (1244):30, 1973.

Danny, E.S. Turbulence kinetic energy and dissipation rate estimated from a virtual wind profiler and verified through large-eddy simulations. In *34th Conference on Radar Meteorology*, 2009.

Dee, D.P., Uppala, S.M., Simmons, A.J., Berrisford, P., Poli, P., Kobayashi, S., Andrae, U., Balmaseda, M.A., Balsamo, G., Bauer, P., et al. The ERA-Interim reanalysis: Configuration and performance of the data assimilation system. *Quarterly Journal of the Royal Meteorological Society*, 137(656):553–597, 2011.

Dehghan, A. and Hocking, W.K. Instrumental errors in spectral-width turbulence measurements by radars. *Journal of Atmospheric and Solar-Terrestrial Physics*, 73(9): 1052–1068, 2011.

Dehghan, A., Hocking, W.K., and Srinivasan, R. Comparisons between multiple in-situ aircraft turbulence measurements and radar in the troposphere. *Journal of Atmospheric and Solar-Terrestrial Physics*, 118:64–77, 2014.

Doviak, R.J. and Zrnic, D.S. *Doppler Radar & Weather Observations*. Academic press, 2014.

Dutton, M.J.O. Probability forecasts of clear-air turbulence based on numerical-model output. *Meteorological Magazine*, 109(1299):293–306, 1980.

Ecklund, W.L., Carter, D.A., and Balsley, B.B. A UHF wind profiler for the boundary layer: Brief description and initial results. *Journal of Atmospheric and Oceanic Technology*, 5(3):432–441, 1988.

ECMWF. IFS Documentation CY40R1 Parts I-VII. 2014. URL `https://software.ecmwf.int/wiki/display/IFS/CY40R1+Official+IFS+Documentation`.

Ellis, S.M. and Vivekanandan, J. Liquid water content estimates using simultaneous S and Ka band radar measurements. *Radio Science*, 46(2), 2011.

Ellrod, G.P. and Knapp, D.I. An objective clear-air turbulence forecasting technique: Verification and operational use. *Weather and Forecasting*, 7(1):150–165, 1992.

Endlich, R.M. The mesoscale structure of some regions of clear-air turbulence. *Journal of Applied Meteorology*, 3(3):261–276, 1964.

Endlich, R.M. and McLean, G.S. The structure of the jet stream core. *Journal of Meteorology*, 14(6):543–552, 1957.

Federal Aviation Association. *Aviation Weather Services, Advisory Circular AC 00-45G, Change 1*, 2010. URL `http://www.faa.gov/documentLibrary/media/Advisory_Circular/AC-0045G_chg1_fullDocument.pdf`. Rev.0.

Frehlich, R. and Sharman, R. Estimates of turbulence from numerical weather prediction model output with applications to turbulence diagnosis and data assimilation. *Monthly Weather Review*, 113:2308–2324, 2004.

Gavrilov, N.M., Luce, H., Crochet, M., Dalaudier, F., Fukao, S., et al. Turbulence parameter estimations from high-resolution balloon temperature measurements of the MUTSI-2000 campaign. In *Annales Geophysicae*, volume 23, pages 2401–2413, 2005.

Gill, P.G. Objective verification of World Area Forecast Centre clear air turbulence forecasts. *Meteorological Applications*, 21(1):3–11, 2014.

Gill, P.G. and Buchanan, P. An ensemble based turbulence forecasting system. *Meteorological Applications*, 21(1):12–19, 2014.

Golding, W.L. Turbulence and its impact on commercial aviation. *Journal of Aviation/Aerospace Education & Research*, 11(2), 2002.

Harrison, R.G. Inexpensive multichannel digital data acquisition system for a meteorological radiosonde. *Review of scientific instruments*, 76(2):026103, 2005.

Harrison, R.G. *Meteorological Measurements and Instrumentation*. John Wiley & Sons, 2014.

Harrison, R.G. and Hogan, R.J. In situ atmospheric turbulence measurement using the terrestrial magnetic field-A compass for a radiosonde. *Journal of Atmospheric and Oceanic Technology*, 23(3):517–523, 2006.

Harrison, R.G. and Nicoll, K.A. Note: Active optical detection of cloud from a balloon platform. *Review of Scientific Instruments*, 85(6):066104, 2014.

Harrison, R.G., Heath, A.M., Hogan, R.J., and Rogers, G.W. Comparison of balloon-carried atmospheric motion sensors with Doppler lidar turbulence measurements. *Review of Scientific Instruments*, 80(2):026108, 2009.

Harrison, R.G., Nicoll, K.A., Ulanowski, Z., and Mather, T.A. Self-charging of the Eyjafjallajökull volcanic ash plume. *Environmental Research Letters*, 5(2):024004, 2010.

Harrison, R.G., Nicoll, K.A., and Lomas, A.G. Note: Programmable data acquisition system for research measurements from meteorological radiosondes. *Review of Scientific Instruments*, 83(3):036106, 2012.

Harrison, R.G., Marlton, G.J., Williams, P.D., and K.A., Nicoll. Coordinated weather balloon solar radiation measurements during a solar eclipse (IN PRES). *Philosophical Transactions of the Royal Society A*, 2016a.

Harrison, R.G., Marlton, G.J, Williams, P.D., and Nicoll, K.A. Coordinated weather balloon solar radiation measurements during a solar eclipse. *Philosophical Transactions of the Royal Society A: Mathematical, Physical and Engineering Sciences*, 2016b.

Hitschfeld, W.F. The invention of radar meteorology. *Bulletin of the American Meteorological Society*, 67(1):33–37, 1986.

Hocking, W.K. On the extraction of atmospheric turbulence parameters from radar backscatter Doppler spectraI. Theory. *Journal of Atmospheric and Terrestrial Physics*, 45(2-3):89–102, 1983.

Hocking, W.K. The dynamical parameters of turbulence theory as they apply to middle atmosphere studies. *Earth, planets and space*, 51(7-8):525–541, 1999.

Hogan, R.J. How to combine errors. 2006. URL `http://www.met.rdg.ac.uk/~swrhgnrj/combining_errors.pdf`.

Hogan, R.J., Gaussiat, N., and Illingworth, A.J. Stratocumulus liquid water content from dual-wavelength radar. *Journal of Atmospheric and Oceanic Technology*, 22(8): 1207–1218, 2005.

Hoinka, K.P. The tropopause: Discovery, definition and demarcation. *Meteorologische Zeitschrift*, 6(6):281–303, 1997.

Holton, J.R. *An introduction to dynamic meteorology 4th edition*. Academic press, 2004.

Hooper, D.A. and Thomas, L. Aspect sensitivity of VHF scatterers in the troposphere and stratosphere from comparisons of powers in off-vertical beams. *Journal of Atmospheric and Terrestrial Physics*, 57(6):655–663, 1995.

Houze Jr, R.A., Locatelli, J.D., and Hobbs, P.V. Dynamics and cloud microphysies of the rainbands in an occluded frontal system. *Journal of the Atmospheric Sciences*, 33 (10):1921–1936, 1976.

Illingworth, A.J., Hogan, R.J., O'connor, E.J., Bouniol, D., Delanoë, J., Pelon, J., Protat, A., Brooks, M.E., Gaussiat, N., Wilson, D.R., et al. Cloudnet: Continuous evaluation of cloud profiles in seven operational models using ground-based observations. *Bulletin of the American Meteorological Society*, 88(6):883–898, 2007.

Kaimal, J.C and Finnigan, J.J. *Atmospheric boundary layer flows: their structure and measurement*. Oxford University Press, 1994.

Kalnay, E., Kanamitsu, M., Kistler, R., Collins, W., Deaven, D., Gandin, L., Iredell, M., Saha, S., White, G., Woollen, J., et al. The NCEP/NCAR 40-year reanalysis project. *Bulletin of the American meteorological Society*, 77(3):437–471, 1996.

Kantha, L. and Hocking, W. Dissipation rates of turbulence kinetic energy in the free atmosphere: MST radar and radiosondes. *Journal of Atmospheric and Solar-Terrestrial Physics*, 73(9):1043–1051, 2011.

Kaplan, M.L., Charney, J.J., Waight III, K.T., Lux, K.M., Cetola, J.D., Huffman, A.W., Riordan, A.J., Slusser, S.D., Kiefer, M.T., Suffern, P.S., et al. Characterizing the severe turbulence environments associated with commercial aviation accidents. A real-time turbulence model (RTTM) designed for the operational prediction of hazardous aviation turbulence environments. *Meteorology and Atmospheric Physics*, 94(1-4):235–270, 2006.

Kennedy, P.J. and Shapiro, M.A. The energy budget in a clear air turbulence zone as observed by aircraft. *Monthly Weather Review*, 103(7):650–654, 1975.

Kennedy, P.J. and Shapiro, M.A. Further encounters with clear air turbulence in research aircraft. *Journal of the Atmospheric Sciences*, 37(5):986–993, 1980.

Keyser, D. and Shapiro, M.A. A review of the structure and dynamics of upper-level frontal zones. *Monthly Weather Review*, 114(2):452–499, 1986.

Kim, J.H., Chun, H.Y., Sharman, R.D., and Keller, T.L. Evaluations of upper-level turbulence diagnostics performance using the Graphical Turbulence Guidance (GTG) system and pilot reports (PIREPs) over East Asia. *Journal of Applied Meteorology and Climatology*, 50(9):1936–1951, 2011.

Knox, J.A. Possible mechanisms of clear-air turbulence in strongly anticyclonic flows. *Monthly weather review*, 125(6):1251–1259, 1997.

Knox, J.A. The breakdown of balance in low potential vorticity regions: Evidence from a clear air turbulence outbreak. In *Preprints, 13th Conf. on atmospheric and oceanic fluid dynamics, Breckenridge, CO, American Meteorology Society*, pages 64–67, 2001.

Knox, J.A., McCann, D.W., and Williams, P.D. Application of the Lighthill-Ford theory of spontaneous imbalance to clear-air turbulence forecasting. *Journal of the Atmospheric Sciences*, 65(10):3292–3304, 2008.

Kobayashi, S., Ota, Y., Harada, Y., Ebita, A., Moriya, M., Onoda, H., Onogi, K., Kamahori, H., Kobayashi, C., Endo, H., et al. The JRA-55 reanalysis: general specifications and basic characteristics. *Journal of the Meteorological Society of Japan. Series II*, 93 (1):5–48, 2015.

Koch, S.E. and Dorian, P.B. A mesoscale gravity wave event observed during CCOPE. Part III: Wave environment and probable source mechanisms. *Monthly weather review*, 116(12):2570–2592, 1988.

Koch, S.E, Jamison, B.D., Lu, C, Smith, T.L., Tollerud, E.I., Girz, C., Wang, N., Lane, T.P., Shapiro, M.A., Parrish, D.D., et al. Turbulence and gravity waves within an upper-level front. *Journal of the atmospheric sciences*, 62(11):3885–3908, 2005.

Kolmogorov, A.N. The local structure of turbulence in incompressible viscous fluid for very large reynolds numbers. In *Dokl. Akad. Nauk SSSR*, volume 30, pages 301–305. JSTOR, 1941.

Kopeć, J.M., Haman, K.E., and Bajer, K. Prediction of clear-air turbulence induced by short gravity waves. In *Journal of Physics: Conference Series*, volume 318, page 072011. IOP Publishing, 2011.

Köpp, F., Schwiesow, R.L., and Werner, C. Remote measurements of boundary-layer wind profiles using a CW Doppler lidar. *Journal of climate and applied meteorology*, 23(1):148–154, 1984.

Kronebach, G.W. An automated procedure for forecasting clear-air turbulence. *Journal of Applied Meteorology*, 3(2):119–125, 1964.

Labitt, M. Coordinated radar and aircraft observations of turbulence. Technical report, DTIC Document, 1981.

Lane, S.E., Barlow, J.F., and Wood, C.R. An assessment of a three-beam doppler lidar wind profiling method for use in urban areas. *Journal of Wind Engineering and Industrial Aerodynamics*, 119:53–59, 2013.

Lane, T.P., Sharman, R.D., Clark, T.L., and Hsu, H.M. An investigation of turbulence generation mechanisms above deep convection. *Journal of the atmospheric sciences*, 60 (10):1297–1321, 2003.

Lane, T.P., Sharman, R.D., Trier, S.B., Fovell, R.G., and Williams, J.K. Recent advances in the understanding of near-cloud turbulence. *Bulletin of the American Meteorological Society*, 93(4):499, 2012.

Lesieur, M. *Turbulence in fluids 4th edition*. Springer Science & Business Media, 2012.

Lester, P.F. *Turbulence: A new perspective for pilots*. Jeppesen Sanderson, 1994.

Lewis, J.M. Ooishi's observation: Viewed in the context of jet stream discovery. *Bulletin of the American Meteorological Society*, 84(3):357–369, 2003.

Lhermitte, R.M. *Centimeter & millimeter wavelength radars in meteorology*. Lhermitte publications Miami, Florida, 2002.

Liebe, H.J. An updated model for millimeter wave propagation in moist air. *Radio Science*, 20(5):1069–1089, 1985.

Lohou, F., Campistron, B., Druilhet, A., Foster, P., and Pages, J.P. Turbulence and coherent organizations in the atmospheric boundary layer: A radar-aircraft experimental approach. *Boundary-Layer Meteorology*, 86(1):147–179, 1998.

Lomb, N.R. Least-squares frequency analysis of unequally spaced data. *Astrophysics and space science*, 39(2):447–462, 1976.

Luers, J.K. and Eskridge, R.E. Use of radiosonde temperature data in climate studies. *Journal of climate*, 11(5):1002–1019, 1998.

MacCready, P.B. Turbulence measurements by sailplane. *Journal of Geophysical Research*, 67(3):1041–1050, 1962.

Maccready, P.B. Universal turbulence indicator, September 13 1966. US Patent 3,272,973.

Mancuso, R.L. and Endlich, R.M. Clear air turbulence frequency as a function of wind shear and deformation. *Monthly Weather Review*, 94(9):581–585, 1966.

Marks, C.J. and Eckermann, S.D. A three-dimensional nonhydrostatic ray-tracing model for gravity waves: Formulation and preliminary results for the middle atmosphere. *Journal of the atmospheric sciences*, 52(11):1959–1984, 1995.

Marlton, G.J., Harrison, R.G., and Nicoll, K.A. Note: Atmospheric point discharge current measurements using a temperature-compensated logarithmic current amplifier. *Review of Scientific Instruments*, 84(6):066103, 2013.

Marlton, G.J., Harrison, R.G., Nicoll, K.A., and Williams, P.D. Note: A balloon-borne accelerometer technique for measuring atmospheric turbulence. *Review of Scientific Instruments*, 86(1):016109, 2015.

Marlton, G.J, Williams, P.D., and K.A., Nicoll. On the detection and attribution of gravity waves geneerated by the 20 March 2015 solar eclipse (IN PRES). *Philosophical Transactions of the Royal Society A*, 2016.

Marroquin, A. An advanced algorithm to diagnose atmospheric turbulence using numerical model output. In *Conference on Weather Analysis and Forecasting*, volume 16, pages 79–81. American Meteorological Society, 1998.

McCann, D.W., Knox, J.A., and Williams, P.D. An improvement in clear-air turbulence forecasting based on spontaneous imbalance theory: the ULTURB algorithm. *Meteorological Applications*, 19(1):71–78, 2012.

McLean Jr, J.C. Comments on the problem of turbulence in aviation. 1987.

Meischner, P., Baumann, R., Höller, H., and Jank, T. Eddy dissipation rates in thunderstorms estimated by doppler radar in relation to aircraft in situ measurements. *Journal of atmospheric and oceanic technology*, 18(10):1609–1627, 2001.

Met Office. *Meteorological Glossary, 6th Edition.* Her Majesties Stationary Office, 1991.

Miles, J.W. On the stability of heterogeneous shear flows. *Journal of Fluid Mechanics*, 10(04):496–508, 1961.

Miloshevich, L.M., Vömel, H., Whiteman, D.N., and Leblanc, T. Accuracy assessment and correction of Vaisala RS92 radiosonde water vapor measurements. *Journal of Geophysical Research: Atmospheres*, 114(D11), 2009.

Mitrev, R. and Grigorov, B. Dynamic behaviour of a spherical pendulum with spatially moving pivot. *Zeszyty Naukowe Politechniki Poznanskiej, Budowa Maszyn i Zarzadzanie Produkcja*, 9:81–91, 2008.

Moore, G.W.K. The organization of convection in narrow cold-frontal rainbands. *Journal of the Atmospheric Sciences*, 42(17):1777–1791, 1985.

Müller, I. and Strehlow, P. *Rubber and rubber balloons: paradigms of thermodynamics.* Springer Science & Business Media, 2004.

Murphy, D.J., Alexander, S.P., Klekociuk, A.R., Love, P.T., and Vincent, R.A. Radiosonde observations of gravity waves in the lower stratosphere over Davis, Antarctica. *Journal of Geophysical Research: Atmospheres*, 119(21), 2014.

Nastrom, G.D. and Eaton, F.D. Turbulence eddy dissipation rates from radar observations at 5–20 km at White Sands Missile Range, New Mexico. *Journal of Geophysical Research: Atmospheres (1984–2012)*, 102(D16):19495–19505, 1997.

Nicholls, S. Measurements of turbulence by an instrumented aircraft in a convective atmospheric boundary layer over the sea. *Quarterly Journal of the Royal Meteorological Society*, 104(441):653–676, 1978.

Nicoll, K.A. and Harrison, R.G. Charge measurements in stratiform cloud from a balloon based sensor. In *Journal of Physics: Conference Series*, volume 301, page 012003. IOP Publishing, 2011.

Nicoll, K.A. and Harrison, R.G. Balloon-borne disposable radiometer for cloud detection. *Review of Scientific Instruments*, 83(2):025111, 2012.

O'Connor, E.J., Illingworth, A.J., Brooks, I.M., Westbrook, C.D., Hogan, R.J., Davies, F., and Brooks, B.J. A method for estimating the turbulent kinetic energy dissipation rate from a vertically pointing Doppler lidar, and independent evaluation from balloon-borne in situ measurements. *Journal of Atmospheric and Oceanic Technology*, 27(10): 1652–1664, 2010.

Ottersten, H. Mean vertical gradient of potential refractive index in turbulent mixing and radar detection of CAT. *Radio Science*, 4(12):1247–1249, 1969.

Painting, D.J. AMDAR reference manual. *World Meteorological Organization Tech. Rep. WMO*, (958):84, 2003.

Paluch, I.R. and Baumgardner, D.G. Entrainment and fine-scale mixing in a continental convective cloud. *Journal of the atmospheric sciences*, 46(2):261–278, 1989.

Pfotzer, G. History of the use of balloons in scientific experiments. *Space Science Reviews*, 13:199–242, 1972.

Pick, W.H. and Bull, G.A. A note on bumpiness cranwell, lincolnshire during the period 1st December 1925 to 30th April 1926. *Meteorological Office Proffesional Notes*, 4(46): 1–7, 1926.

Press, W.H. *Numerical recipes 3rd edition: The art of scientific computing*. Cambridge university press, 2007.

Pretor-Pinney, G. and Sanderson, B. *The cloudspotter's guide: The science, history, and culture of clouds*. Taylor & Francis, 2006.

Readings, C.J. Some aspects of the Cardington research programme. *Quarterly Journal of the Royal Meteorological Society*, 99(422):764–767, 1973.

Reap, R.M. Probability forecasts of clear-air turbulence for the contiguous US National Weather Service Office of Meteorology Technology. *Procedures Bulletin*, 430:15, 1996.

Reid, H.J. and Vaughan, G. Convective mixing in a tropopause fold. *Quarterly Journal of the Royal Meteorological Society*, 130(599):1195–1212, 2004.

Reiter, E.R. Nature and Observation of High-level Turbulence Especially in Clear Air. Technical report, DTIC Document, 1962.

Reiter, E.R. and Burns, A. The structure of clear-air turbulence derived from TOPCAT aircraft measurements. *Journal of the Atmospheric Sciences*, 23(2):206–212, 1966.

Reiter, E.R. et al. The dependence of the richardson number on scale length. *Atmospheric science paper; no. 111.*, 1967.

Renard, C. On the use of sounding balloons for meteorological observations at great heights. *Monthly Weather Review*, 31:570–571, 1903.

Reynolds, O. An experimental investigation of the circumstances which determine whether the motion of water shall be direct or sinuous, and of the law of resistance in parallel channels. *Proceedings of the royal society of London*, 35(224-226):84–99, 1883.

Reynolds, O. On the dynamical theory of incompressible viscous fluids and the determination of the criterion. *Proceedings of the Royal Society of London*, 56(336-339):40–45, 1894.

Richardson, L.F. The supply of energy from and to atmospheric eddies. *Proceedings of the Royal Society of London. Series A, Containing Papers of a Mathematical and Physical Character*, 97(686):354–373, 1920.

Richardson, L.F. *Weather prediction by numerical process*. Cambridge: University Press, 1922.

Rogers, R.R. and Tripp, B.R. Some radar measurements of turbulence in snow. *Journal of Applied Meteorology*, 3(5):603–610, 1964.

Santer, B.D., Sausen, R., Wigley, T.M.L, Boyle, J.S., AchutaRao, K., Doutriaux, C., Hansen, J.E., Meehl, G.A., Roeckner, E., Ruedy, R., et al. Behavior of tropopause height and atmospheric temperature in models, reanalyses, and observations: Decadal changes. *Journal of Geophysical Research: Atmospheres*, 108(D1), 2003.

Sato, T. and Woodman, R.F. Fine altitude resolution observations of stratospheric turbulent layers by the Arecibo 430 MHz radar. *Journal of the Atmospheric Sciences*, 39 (11):2546–2552, 1982.

Schwartz, B. The quantitative use of PIREPs in developing aviation weather guidance products. *Weather and Forecasting*, 11(3):372–384, 1996.

Shao, Q., Randall, D.A., Moeng, C.H, and Dickinson, R.E. A method to determine the amounts of cloud-top radiative and evaporative cooling in a stratocumulus-topped boundary layer. *Quarterly Journal of the Royal Meteorological Society*, 123(544):2187–2213, 1997.

Shapiro, M.A. The role of turbulent heat flux in the generation of potential vorticity in the vicinity of upper-level jet stream systems. *Monthly Weather Review*, 104(7): 892–906, 1976.

Shapiro, M.A. Further evidence of the mesoscale and turbulent structure of upper level jet stream-frontal zone systems. *Monthly Weather Review*, 106(8):1100–1111, 1978.

Sharman, R., Tebaldi, C., and Brown, B.G. An integrated approach to clear-air turbulence forecasting. In *Preprints, 8th Conference on Aviation, Range, and Aerospace Meteorology*, 1999.

Sharman, R., Tebaldi, C., Wiener, G., and Wolff, J. An integrated approach to mid-and upper-level turbulence forecasting. *Weather and forecasting*, 21(3):268–287, 2006.

Sharman, R., Wiener, G., and Prestopnik, J. Technical Description Document (TDD) for the Graphical Turbulence Guidance Product v2.5 (GTG2.5). Technical report, 2011.

Sharman, R.D., Cornman, L.B., Meymaris, G., Pearson, J., and Farrar, T. Description and derived climatologies of automated in situ eddy-dissipation-rate reports of atmospheric turbulence. *Journal of Applied Meteorology and Climatology*, 53(6):1416–1432, 2014.

Sherman, D.J. The Australian implementation of AMDAR/ACARS and the use of derived equivalent gust velocity as a turbulence indicator. *Structures Report*, (418), 1985.

Shipley, S.T., Tracy, D.H., Eloranta, E.W., Trauger, J.T., Sroga, J.T., Roesler, F.L., and Weinman, J.A. High spectral resolution lidar to measure optical scattering properties of atmospheric aerosols. 1: Theory and instrumentation. *Applied optics*, 22(23):3716–3724, 1983.

Shupe, M.D., Brooks, I.M., and Canut, G. Evaluation of turbulent dissipation rate retrievals from Doppler cloud radar. *Atmospheric Measurement Techniques*, 5(6):1375–1385, 2012.

Shutts, G.J., Kitchen, M., and Hoare, P.H. A large amplitude gravity wave in the lower stratosphere detected by radiosonde. *Quarterly Journal of the Royal Meteorological Society*, 114(481):579–594, 1988.

Simpson, G. and Scrase, F.J. The distribution of electricity in thunderclouds. *Proceedings of the Royal Society of London. Series A, Mathematical and Physical Sciences*, pages 309–352, 1937.

Smith, S.A. and Jonas, P.R. Observations of turbulence in cirrus clouds. *Atmospheric research*, 43(1):1–29, 1996.

Thorpe, S.A. Turbulence and mixing in a scottish loch. *Philosophical Transactions of the Royal Society of London A*, 286(1334):125–181, 1977.

Trueba, J.L., Baltanás, J.P., and Sanjuán, M.A.F. A generalized perturbed pendulum. *Chaos, Solitons & Fractals*, 15(5):911–924, 2003.

US Standard Atmosphere. *US standard atmosphere.* National Oceanic and Atmospheric Administration, 1976.

Vaisala. *Vaisala Datasheet RS92-SGP* , 2013. URL `http://www.vaisala.com/Vaisala%20Documents/Brochures%20and%20Datasheets/RS92SGP-Datasheet-B210358EN-F-LOW.pdf`.

Vaughan, G., Price, J.D., and Howells, A. Transport into the troposphere in a tropopause fold. *Quarterly Journal of the Royal Meteorological Society*, 120(518):1085–1103, 1994.

Vincent, R.A. and Alexander, M.J. Gravity waves in the tropical lower stratosphere: An observational study of seasonal and interannual variability. *Journal of Geophysical Research: Atmospheres*, 105(D14):17971–17982, 2000.

Vogel, G.N. and Sampson, C.R. Clear Air Turbulence Indices Derived from US Navy Numerical Model Data: A Verification Study. Technical report, DTIC Document, 1996.

Vrancken, P., Wirth, M., Rempel, D., Ehret, G., Dolfi-Bouteyre, A., Lombard, L., Gaudo, T., Rees, D., Barny, H., and Rondeau, P. Clear air turbulence detection and characterisation in the DELICAT airborne LIDAR project. In *25th International Laser Radar Conference (ILRC)*, 2010.

Wallace, J.M. and Hobbs, P.V. *Atmospheric science: an introductory survey.* Academic press, 2006.

Wang, L., Geller, M.A., and Alexander, M.J. Spatial and temporal variations of gravity wave parameters. Part I: Intrinsic frequency, wavelength, and vertical propagation direction. *Journal of the atmospheric sciences*, 62(1):125–142, 2005.

Weber, M.E. and Few, A.A. A balloon borne instrument to induce corona currents as a measure of electric fields in thunderclouds. *Geophysical Research Letters*, 5(4):253–256, 1978.

Weinstock, J. On the theory of turbulence in the buoyancy subrange of stably stratified flows. *Journal of the atmospheric sciences*, 35(4):634–649, 1978.

Weisstein, E.E. Hypergeometric function, 2002. URL `http://mathworld.wolfram.com/HypergeometricFunction.html`.

White, A.B., Lataitis, R.J., and Lawrence, R.S. Space and time filtering of remotely sensed velocity turbulence. *Journal of atmospheric and oceanic technology*, 16(12): 1967–1972, 1999.

Williams, P.D. and Joshi, M.M. Intensification of winter transatlantic aviation turbulence in response to climate change. *Nature Climate Change*, 3(7):644–648, 2013.

Wilson, R., Luce, H., Dalaudier, F., and Lefrère, J. Turbulence patch identification in potential density or temperature profiles. *Journal of Atmospheric and Oceanic Technology*, 27(6):977–993, 2010.

Wilson, R., Luce, H., Dalaudier, F., et al. Can one detect small-scale turbulence from standard meteorological radiosondes? *Atmospheric Measurement Techniques*, 4:795–804, 2011.

Wilson, R., Luce, H., Hashiguchi, H., Shiotani, M., and Dalaudier, F. On the effect of moisture on the detection of tropospheric turbulence from in situ measurements. *Atmospheric Measurement Techniques*, 6(3):697–702, 2013.

Worthington, R.M., Palmer, R.D., and Fukao, S. An investigation of tilted aspect-sensitive scatterers in the lower atmosphere using the MU and Aberystwyth VHF radars. *Radio Science*, 34(2):413–426, 1999.

Zhang, J., Chen, H., Li, Z., Fan, X., Peng, L., Yu, Y., and Cribb, M. Analysis of cloud layer structure in Shouxian, China using RS92 radiosonde aided by 95 GHz cloud radar. *Journal of Geophysical Research: Atmospheres*, 115(D7), 2010.

Zink, F. and Vincent, R.A. Wavelet analysis of stratosphere gravity wave packets over Macquarie Island 1. Wave parameters. *Journal of geophysical research*, 106(D10):10275–10288, 2001.